

NAVAL POSTGRADUATE SCHOOL

Monterey, California



THESIS

THE SOUTH CHINA SEA THERMOHALINE
STRUCTURE AND CIRCULATION

by

Binbing Ma

September 1998

Thesis Advisor:
Second Reader:

Peter C. Chu
Pierre-Marie Poulain

Approved for public release; distribution is unlimited.

Reproduced From
Best Available Copy

19981103 065
590

REPORT DOCUMENTATION PAGE

Form Approved OMB No. 0704-0188

Public reporting burden for this collection of information is estimated to average 1 hour per response, including the time for reviewing instruction, searching existing data sources, gathering and maintaining the data needed, and completing and reviewing the collection of information. Send comments regarding this burden estimate or any other aspect of this collection of information, including suggestions for reducing this burden, to Washington Headquarters Services, Directorate for Information Operations and Reports, 1215 Jefferson Davis Highway, Suite 1204, Arlington, VA 22202-4302, and to the Office of Management and Budget, Paperwork Reduction Project (0704-0188) Washington DC 20503.

1. AGENCY USE ONLY <i>(Leave blank)</i>	2. REPORT DATE	3. REPORT TYPE AND DATES COVERED	
	September 1998	Master's Thesis	
4. TITLE AND SUBTITLE THE SOUTH CHINA SEA THERMOHALINE STRUCTURE AND CIRCULATION			5. FUNDING NUMBERS
6. AUTHOR(S) Binbing Ma			
7. PERFORMING ORGANIZATION NAME(S) AND ADDRESS(ES) Naval Postgraduate School Monterey CA 93943-5000			8. PERFORMING ORGANIZATION REPORT NUMBER
9. SPONSORING/MONITORING AGENCY NAME(S) AND ADDRESS(ES)			10. SPONSORING/MONITORING AGENCY REPORT NUMBER
11. SUPPLEMENTARY NOTES The views expressed in this thesis are those of the author and do not reflect the official policy or position of the Department of Defense or the U.S. Government.			
12a. DISTRIBUTION/AVAILABILITY STATEMENT Approved for public release; distribution is unlimited.		12b. DISTRIBUTION CODE	
13. ABSTRACT <i>(maximum 200 words)</i> The minimum curvature with spline method was used to establish a three-dimensional monthly-varying gridded data from the Navy's Master Oceanographic Observation Data Set (approximate 189,000 profiles), covering the area of 5°N - 25°N and 105°E - 125°E and from the surface to 400 m depth. For temperature, profiles were binned into 204 monthly data sets from 1968 to 1984 (17 years). Because of the paucity of salinity data, salinity profiles were binned into 12 climatological monthly data sets, and the monthly climatological mean was computed. After the gridded data set had been established, both composite analysis and the Empirical Orthogonal Function (EOF) analysis were used to identify the major thermohaline features. The first EOF mode accounts for 26.7% of the variance and represents the seasonal variation. The second EOF mode accounts for 17.7% of the variance and represents the interannual SCS warming/cooling phases. Furthermore, the P-vector method was used to invert three-dimensional velocity fields from the analyzed temperature and salinity data. Important dynamical processes, including the Kuroshio intrusion, the western boundary current (counter-current), the cross basin current (under counter-current), the mesoscale eddies, and the basin gyre are identified.			
14. SUBJECT TERMS Water mass, thermohaline structure, seasonal variation, circulation			15. NUMBER OF PAGES 271
			16. PRICE CODE
17. SECURITY CLASSIFICATION OF REPORT Unclassified	18. SECURITY CLASSIFICATION OF THIS PAGE Unclassified	19. SECURITY CLASSIFICATION OF ABSTRACT Unclassified	20. LIMITATION OF ABSTRACT UL

Approved for public release; distribution is unlimited.

**THE SOUTH CHINA SEA THERMOHALINE STRUCTURE
AND CIRCULATION**

Binbing Ma

Lieutenant Commander, Taiwan R.O.C. Navy
B.S., Chinese Naval Academy, 1988

Submitted in partial fulfillment
of the requirements for the degree of

MASTER OF SCIENCE IN PHYSICAL OCEANOGRAPHY

from the

NAVAL POSTGRADUATE SCHOOL

September 1998

Author:

Binbing Ma

Binbing Ma

Approved by:

Pete Chu

Peter C. Chu, Thesis Advisor

Pierre-Marie Poulain

Pierre-Marie Poulain, Second Reader

Roland W. Garwood, Jr., Chairman
Department of Oceanography

ABSTRACT

The South China Sea (SCS), the largest marginal sea in the West Pacific Ocean, is separated from adjacent oceans by a chain of islands. The deepest water is confined to a bowel-type trench, and the maximum depth is approximately 5,000 m. Most of the existing studies on the seasonal and interannual variability have been based only on surface temperature data. However a primary need is an understanding of the three-dimensional thermohaline circulation. The minimum curvature with spline method was used to establish a three-dimensional monthly-varying gridded data from the Navy's Master Oceanographic Observation Data Set (approximate 189,000 profiles), covering the area of 5°N - 25°N and 105°E - 125°E and from the surface to 400 m depth. For temperature, profiles were binned into 204 monthly data sets from 1968 to 1984 (17 years). Because of the paucity of salinity data, salinity profiles were binned into 12 climatological monthly data sets, and the monthly climatological mean was computed. After the gridded data set had been established, both composite analysis and the Empirical Orthogonal Function (EOF) analysis were used to identify the major thermohaline features. The first EOF mode accounts for 26.7% of the variance and represents the seasonal variation. The second EOF mode accounts for 17.7% of the variance and represents the interannual SCS warming/cooling phases. Furthermore, the P-vector method was used to invert three-dimensional velocity fields from the analyzed temperature and salinity data. Important dynamical processes, including the Kuroshio intrusion, the western boundary current (counter-current), the cross basin current (under counter-current), the mesoscale eddies, and the basin gyre are identified.

TABLE OF CONTENTS

I. INTRODUCTION	1
II. THE SOUTH CHINA SEA OCEANOGRAPHY	7
A. WATER MASSES	7
B. MONSOON EFFECT ON CURRENT SYSTEM	9
1. Summer Monsoon	9
2. Winter Monsoon	10
C. MESOSCALE EDDIES	11
D. AN AIR-SEA FEEDBACK SCENARIO	12
III. MASTER OCEANOGRAPHIC OBSERVATION DATA SET (MOODS) . . .	19
IV. ESTABLISHMENT OF GRIDDED DATA	25
V. COMPOSITE ANALYSIS	31
A. ANNUAL MEAN	31
B. SEASONAL VARIATION	33
1. Temperature	33
2. Salinity	35
VI. EMPIRICAL ORTHOGONAL FUNCTION (EOF) ANALYSIS	63
A. THERMAL VARIABILITY	63
B. PRINCIPAL EOF MODES	65
1. The EOF 1 Mode	65

2. The second EOF Mode	67
C. TEMPORAL VARIABILITIES	68
1. First Principal Component	69
2. Second Principal Component	70
VII. THE SOUTH CHINA SEA CIRCULATION	77
A. GEOSTROPHIC VELOCITY INVERTED FROM DENSITY FIELD ..	77
B. SEASONAL VARIATION OF SOUTH CHINA CIRCULATION ..	80
1. General Description	80
2. Surface Circulation	80
3. Sub-Surface (75 m)	82
4. Intermediate level (400m)	82
5. Kuroshio Intrusion Through the Luzon Strait	83
VIII. CONCLUSIONS	97
A. CLIMATOLOGICAL MEAN THERMOHALINE FEATURES	97
B. SEASONAL THERMOHALINE VARIABILITY	98
C. KUROSHIO INTRUSION	99
D. INTERANNUAL SCS WARMING/COOLING PHASES	99
E. MULTI-EDDY STRUCTURE	100
APPENDIX A. MONTHLY TEMPERATURE ANOMALY	101
APPENDIX B. MONTHLY SALINITY ANOMALY	161
APPENDIX C. EOF 3~6 FOR TEMPERATURE ANOMALY	221

APPENDIX D. THE CIRCULATION PATTERNS	229
LIST OF REFERENCES	249
INITIAL DISTRIBUTION	253

LIST OF FIGURES

Figure 1. Bathymetry of the South China Sea	4
Figure 1.2 Observational Surface Currents of the Southeast Asia Waters in April	5
Figure 2.1 Distribution of water masses at the sea surface and bottom layer in the northern South China Sea	14
Figure 2.2 Mean Atmospheric Surface Streamline Analysis for summer monsoon	15
Figure 2.3 Observational Summer Surface Circulation of the Southeast Asia Waters ..	16
Figure 2.4 Mean Atmospheric Surface Streamline Analysis for winter monsoon	17
Figure 2.5 Observational Winter Surface Circulation of the Southeast Asia Waters ...	18
Figure 2.6 An Air- Sea Feedback Scenario for the SCS Warm-Core Eddy Life Cycle ..	19
Figure 3.1 The Spatial distribution of MOODS temperature profiles	23
Figure 3.2 The Spatial distribution of MOODS salinity profiles	24
Figure 3.4 The temporal distribution of MOODS	25
Figure 3.4 The temporal distribution of MOODS in 1968	25
Figure 4.1a Cross-sections through surfaces produced with splines in tension	31
Figure 4.1b Cross-sections through continental shelf and slope produced with splines in tension	32
Figure 5.1a The annual mean temperature field from surface to 100 meters	40
Figure 5.1b The annual mean temperature field from 125 to 400 meters	41
Figure 5.2a The zonal cross-section view of annual mean temperature from Latitude 14°N to Latitude 19°N	42

Figure 5.2b The zonal cross-section view of annual mean temperature from Latitude 20°N to Latitude 25°N	43
Figure 5.3a The annual mean salinity field from surface to 100 meters	44
Figure 5.3b The annual mean salinity field from 125 to 400 meters	45
Figure 5.4a The zonal cross-section view of annual mean salinity from Latitude 14°N to Latitude 19°N	46
Figure 5.4b The zonal cross-section view of annual mean salinity from Latitude 20°N to Latitude 25°N	47
Figure 5.5a Monthly mean temperature anomalies at surface from January to June	48
Figure 5.5b Monthly mean temperature anomalies at surface from July to December ..	49
Figure 5.6a Monthly mean temperature anomalies at 75 meters from January to June ..	50
Figure 5.6b Monthly mean temperature anomalies at 75 meters from July to December	51
Figure 5.7a The zonal cross-section view of monthly mean temperature anomalies at 19°N from January to June	52
Figure 5.7b The zonal cross-section view of monthly mean temperature anomalies at 19°N from July to December	53
Figure 5.8a Monthly mean temperature anomalies at 200 meters from January to June ..	54
Figure 5.8b Monthly mean temperature anomalies at 200 meters from July to December	55
Figure 5.9a Monthly mean salinity anomalies at surface from January to June	56
Figure 5.9b Monthly mean salinity anomalies at surface from July to December	57
Figure 5.10a Monthly mean salinity anomalies at 75 meters from January to June	58
Figure 5.10b Monthly mean salinity anomalies at 75 meters from July to December ..	59
Figure 5.11a The zonal cross-section view of monthly mean salinity anomalies at 19°N from January to June	60

Figure 5.11b The zonal cross-section view of monthly mean salinity anomalies at 19°N from July to December	61
Figure 5.12a Monthly mean salinity anomalies at 200 meters from January to June	62
Figure 5.12b Monthly mean salinity anomalies at 200 meters from July to December ..	63
Figure 6.1 EOF1 Temperature anomalies	74
Figure 6.2 EOF2 Temperature anomalies	76
Figure 6.3 The first six principal components for 1968-1984	78
Figure 7.1 Thermal wind relation at two different depth and β spiral turning angle	87
Figure 7.2a Surface Circulation from January to June	88
Figure 7.2b Surface Circulation form July and December	89
Figure 7.3a Sub-Surface (75 meters) Circulation from January to June	90
Figure 7.3b Sub-Surface (75 meters) Circulation form July and December	91
Figure 7.4a Intermediate Level (400 meters) Circulation from January to June	92
Figure 7.4b Intermediate Level (400 meters) Circulation form July and December	93
Figure 7.5 Temperature and Salinity data from surface to 400 meters used for the computation of east-westgeostrophic velocity along 120.5°E	94
Figure 7.6a The monthly zonal velocity in 120°E from January to June	95
Figure 7.6b The monthly zonal velocity in 120°E form July and December	96
Figure 7.7 The Mass Transport (Sv) at the Luzon strait	97

ACKNOWLEDGEMENTS

I would like to acknowledge the unfailing support of C. W. Fan and Yuchun Chen for their programming assistance. Special thanks to Dr. Peter C. Chu for his guidance and patience and to Dr. Pierre-Marie Poulain for his valuable comments. This work was funded by the Naval Oceanographic Office, the Office of Naval Research NOMP Program, and the Naval Postgraduate School.

I. INTRODUCTION

The South China Sea (SCS), the largest marginal sea in the West Pacific Ocean, is separated from adjacent oceans by a chain of islands. It contains the broad shallow Sunda Shelf on the south, a shelf extending from the Gulf of Tonkin to the Taiwan Strait on the north, a deep sea basin in the center, and the Dangerous Ground with numerous reef islands over the southeast (Figure 1.1). It has a bottom topography that makes it a unique semi-enclosed ocean basin that is overlaid by a pronounced monsoon surface wind. Extensive continental shelves (less than 100 m deep) are found on the western and southern parts, while steep slopes with almost no shelves are found in the eastern part of SCS. The deepest water is confined to a bowel-type trench and the maximum depth is approximately 5,000 m.

The SCS's physical oceanographic condition has been investigated for several decades. Studies show that eddies in the SCS are predominantly cyclonic in winter and anti-cyclonic in summer, with sizes ranging from small to meso-scale, and are both cold and warm [Huang et al., 1994]. A survey by Wyrtki [1961] revealed complex temporal and spatial features of the surface currents in both the SCS and the surrounding waters. By April, the northeast monsoon has decayed and the main SCS current consists of two large cyclonic eddies in the western SCS, one in the north and the other in the south (Figure 1.2). With the beginning of the southwest monsoon in May and June, a wind drift current is formed off the coast of Vietnam. The westward intensification of this current is clearly visible. The wide uniform drift in the northern SCS shows a deflection of the current to the right of the wind. A large

part of the water passes south of Taiwan and into the root of the Kuroshio. The southern SCS is occupied by an anticyclonic eddy.

Based on limited data sets, studies show that eddies in the SCS are predominantly cyclonic in winter and spring and anti-cyclonic in summer, with sizes ranging from small to meso-scale [Huang et al., 1994]. Both cold and warm eddies exist in the SCS. Dale [1956] and Uda and Nakao [1972] reported a cold eddy off the central Vietnamese Coast in summer, and Nitan [1970] found a cold eddy located to the northwest of Luzon. Reports from the South China Sea Institute of Oceanology [SCSIO, 1985] indicate that in the central SCS a warm-core eddy appears in summer and winter, but it is more closer to Vietnam in summer at the surface. In addition, a cold-core eddy was detected in the central SCS from the 29th December 1993 to 5th January 1994 according to analysis of the TOPEX/ POSEIDON data [Soong, et al., 1995].

Recently, Chu et al. [1997a] and Chu and Chang [1997] identified a central SCS surface warm-core eddy in mid-May from a more complete historical data set - the U.S. Navy's Master Observational Oceanographic Data Set (MOODS). From the composite analysis of the U.S. National Centers for Environmental Prediction (NCEP) monthly SST fields (1982-1994), Chu et al. [1997b] found that during the spring-to-summer monsoon transition (March to May) a warm anomaly (greater than 1.8°C) is formed in the central SCS at 112°-119°30'E, 15°-19° 30'N. This warm eddy appears in the central SCS (west of Luzon Island) during the late spring season and strengthens until the onset of the summer monsoon (mid-May) and then weakens and disappears at the end of May. Although its size and

intensity varies, the SCS warm pool releases large moisture and heat fluxes into the atmosphere and in turn affects the monsoon circulation.

Most of the existing studies on the seasonal eddy variability were based on the surface data. What is the three-dimensional thermal structure and circulation pattern of the SCS eddies? In this thesis, we will use the minimum curvature spline method [Wessel and Smith, 1992] to establish a three-dimensional monthly varying gridded data from the MOODS, covering the area of 5°N - 25°N and 105°E - 125°E and from the surface to 400 m depth. For temperature, we binned the profiles into 204 monthly data sets from 1968 to 1984 (17 years). For salinity, a monthly climatological analysis was applied because of the paucity of data. After the gridded data set had been established, we utilized both composite analysis and the Empirical Orthogonal Function (EOF) analysis identifying the major thermal features of the mesoscale eddies. Furthermore, three-dimensional velocity fields were inverted from analysis of the temperature and salinity data.

The outline of this thesis is as follows: Chapter II depicts the South China Sea oceanography including the water masses, monsoon effect and mesoscale eddies. Chapter III describes the U.S. Navy's Master Oceanographic Observation Data Set (MOODS). Chapter IV describes the establishment of gridded data, and Chapter V depicts the composite analysis to obtain temperature and salinity seasonal variations. Chapter VI describes the EOF method to obtain nonseasonal variabilities. Chapter VII presents the SCS circulation using the P vector inverse method, major current systems and seasonal variation, and Chapter VIII includes our conclusions.

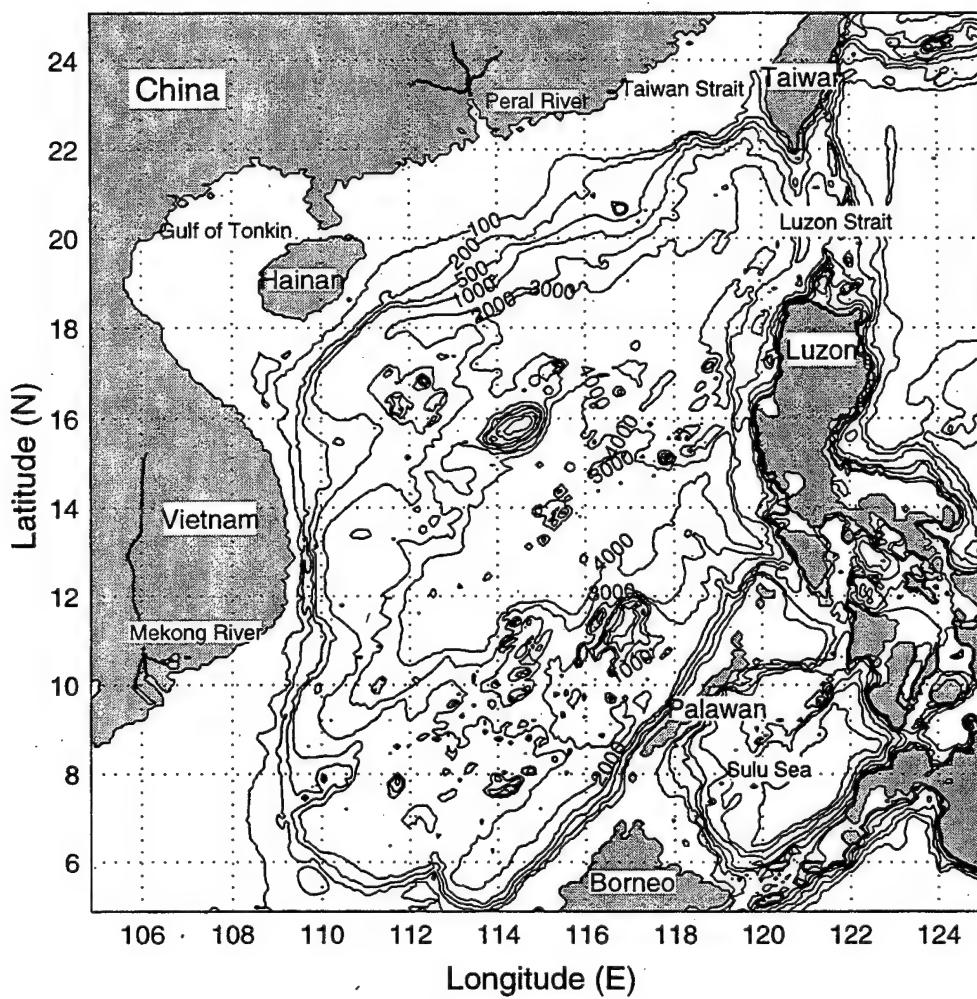


Figure 1.1 Bathymetry of the South China Sea

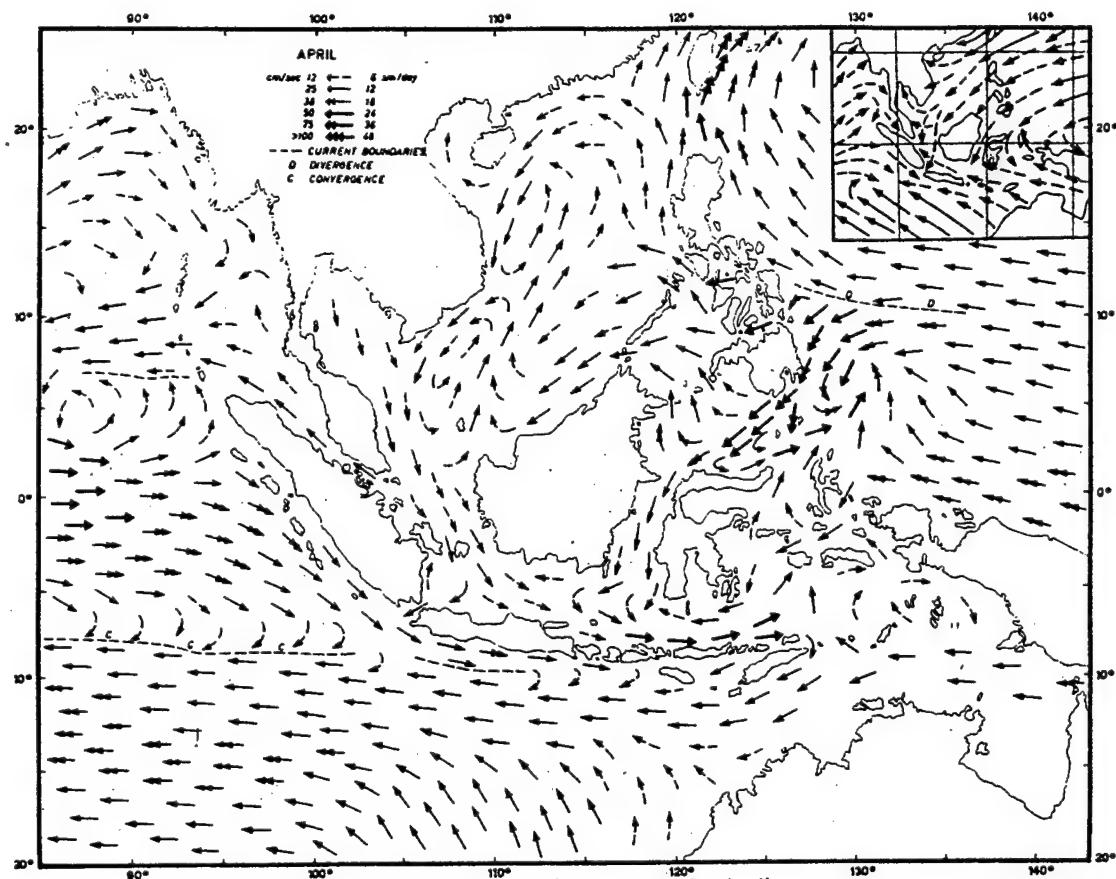


Figure 1.2 Observational Surface Currents of the Southeast Asia Waters in April
(From Wyrtki, 1961)

II. THE SOUTH CHINA SEA OCEANOGRAPHY

A. WATER MASSES

On the western side of the Luzon Strait, the SCS water masses can be divided into those four types [Wyrtki, 1961]: (1) the warm, less salinity Surface Layer Water, (2) the high salinity (34.8-35.2 psu) Subtropical Lower Water, (3) the low salinity (34.1-34.5 psu) Intermediate Water, and (4) the original Pacific Deep Water (34.65-34.7 psu). The salinity maximum of the Subtropical Lower Water is approximately 150 meters deep and the salinity minimum of the Intermediate Water is approximately 400 to 500 meters deep. At the Luzon Strait these two water masses move in opposite directions and the depth of the inversion is about 200 meter. The center of this inversion lies relatively uniformly at a temperature 16°C.

Wyrtki [1961] also found that during the winter monsoon season surface water masses from the Pacific Ocean are transported into the SCS through the Luzon Strait, chiefly along the western side of the SCS in depths between 400 and 900 meters. During the summer monsoon season these conditions are reversed.

Waters from the Western Pacific enter the northern SCS through the Luzon Strait and after mixing and modification form distinct water masses. Continental fresh water runoff is also very significant. Su and Weng [1994] classified eight water masses in the northern SCS. They grouped these water masses into three classes: (i) runoff diluted type of Near shore Diluted Water Mass (*F*); (ii) the shallow sea modified type composed of Coastal Mixed Water Mass (*M*), Warm Surface Water Mass (*WS*), Surface Water Mass (*S*) and Surface-Subsurface

Mixed Water Mass (*SU*); and (iii) the deep sea type, composed of Subsurface Water Mass (*U*), Subsurface-Intermediate Mixed Water Mass (*UI*) and Intermediate Water Mass (*I*).

Distribution of these water masses at the surface are nearly parallel to the coastline (Figure 2.1).

Both water masses *WS* and *S* originate from West Pacific Surface Water Mass. Various meteorological conditions modify this water mass and ultimately generate the high temperature and low salinity *WS* water mass and the low temperature, low salinity *S* water mass. Mixing modifies the West Pacific Subtropical Subsurface Water Mass to form the *SU* water mass, which is similar to the *S* water mass. The *U* water mass, distributed at approximately 150 m depth, retains the high salinity layer of the West Pacific water. The *UI* water mass is the interface between the deep high salinity layer and low salinity surface layer. The *I* water mass is an oceanic type water mass with the least modification from its source water mass and characterizes low salinity, distributed down to 700 m. The *F* water mass is a mixture of runoff and Near shore water mass. The *M* water mass undergoes the largest modification, mixing with *SU*, *WS* and *S* water masses, respectively, in varying seasons. Table 2.1 lists the characteristics of the water masses.

Water Mass	Feb.	May	Aug.	Nov.
F T(°C) Salinity		25.5-27.8 <30.0	29.0-30.5 <30.0	
M T(°C) Salinity	13.2-16.0 31.20-33.60	22.5-27.6 31.16-33.80	28.9-30.3 33.03-32.91	21.3-24.4 31.32-34.02
WS T(°C) Salinity	22.3-24.4 34.08-34.67	26.2-30.0 33.90-34.69	28.0-30.1 33.03-34.40	25.5-26.1 33.68-33.93
S T(°C) Salinity	20.4-22.3 34.43-34.80	22.2-26.2 33.85-34.62	23.5-28.0 33.65-34.62	22.5-25.5 33.97-34.60
SU T(°C) Salinity	17.5-20.4 34.18-34.75	19.8-22.2 34.16-34.71	21.0-23.5 34.32-34.70	19.0-22.5 34.42-34.76
U T(°C) Salinity	15.5-17.5 34.28-34.78	14.5-19.8 34.44-34.88	15.2-21.0 34.35-34.81	14.5-19.0 34.50-34.78
UI T(°C) Salinity	11.0-15.5 34.46-34.60	10.0-14.5 34.40-34.70	11.0-15.2 34.41-34.79	11.0-14.5 34.42-34.62
I T(°C) Salinity		5.3-10.0 34.33-34.64	5.6-11.0 34.34-34.52	6.4-11.0 34.30-34.50

Table 2.1. Ranges of Temperature and Salinity of Water Masses in the northern South China Sea (from Su and Weng, 1994)

B. MONSOON EFFECT ON THE CURRENT SYSTEM

The entire region of the South China Sea is under the influence of the monsoon system, and in the absence of major oceanic inflow, the currents undergo a seasonal reversal of direction.

1. Summer monsoon

During the summer monsoon season, a warm and weaker southwest wind blows over the SCS. The southwest-northeast oriented jet stream is positioned at the central SCS (Figure 2.2). Such a typical summer monsoon pattern lasts nearly four months (mid-May to

mid-September). The summer monsoon forces a wide, uniform northeasterly flowing surface current over most of the basin (Figure 2.3). Westward intensification generates a strong current along the western side of the basin, off the coasts of Thailand and Vietnam. The larger part of the surface flow passes south of Taiwan and merges with the northerly flowing Kuroshio; a smaller amount flows north through the Taiwan Strait. Wyrtki (1961) reported the existence of a counter current on the eastern side of the basin, with a southwesterly flow along the Borneo coast. This flow turns back northerly in the region of Natuna Island, in the southern SCS, forming an anticyclonic gyre. Wyrtki hypothesizes that an insufficient supply of water into the basin from the Java Sea produces this gyre. In September, these movements decrease and in October the northeast monsoon begins blowing with considerable strength, resulting in the complete reversal of the current fields.

2. Winter Monsoon

During the winter monsoon season, a cold northeast wind blows over the SCS, as a result of the Siberian high pressure system located over the east Asian continent. Radiative cooling and persistent cold air advection maintain cold air over the SCS. The northeast-southwest oriented jet stream is positioned at the central SCS (Figure 2.4). Such a typical winter monsoon pattern lasts nearly six months (November to April). The mean northeast wind stress over the Western Pacific deflects the water masses of the North Equatorial Current to the south, causing them to enter the SCS through the Luzon Strait. Water from the East China Sea moves southerly through the Taiwan Strait and enters the SCS. This southerly moving water turns southwesterly and flows along the coast of China and Vietnam,

with a remarkable westward intensification (Wyrtki, 1961). In the center of the SCS, a northerly flowing counter current develops over about 10 degrees of latitude (Figure 2.5).

During the early period of the northeast monsoon, not all of the southerly flowing water can flow into the Java Sea, since the southeast monsoon is still blowing weakly over this region. This situation produces a northward flowing counter current along the coast of Borneo. The water flows as far north as Luzon, where it turns southward and merges into the main current, forming a closed cyclonic gyre.

During December the northwest monsoon is fully developed and the currents are their strongest, exceeding 100 cm/s off the coast of Vietnam. The northward flowing counter current in the central SCS is located farther to the east, due to the strength of the main current. A weak southward flowing coastal counter current forms along the northwest coast of Borneo.

C. MESOSCALE EDDIES

Seasonal occurrence of the SCS eddies have been reported by several authors. Huang and Wang [1994] mentioned that eddies in the SCS are predominantly cyclonic in winter and anticyclonic in summer, with sizes from small (100 km) to medium scale (500 km). Dale [1956] and Uda and Nakao [1972] reported a cold eddy off the central Vietnam coast in summer. Nitani [1970] found a cold eddy located northwest of Luzon in summer. Reports from the South China Sea Institute of Oceanology (SCSIO) [1985] indicated that a warm-core eddy appeared in summer and winter in the central SCS, but in summer, it was closer to Vietnam at the surface. Recently, a cold-core eddy was detected in the central SCS

between December 29, 1993, and January 5, 1994, from the analysis of TOPEX/ POSEIDON data [Soong et al. 1995]. Chu et al. [1997a] and Chu and Chang [1997] identified the existence of a central SCS surface warm-core eddy in mid-May from a historical data set: the U.S. Navy's Master Observational Oceanographic Data Set (MOODS). From the composite analysis of the U.S. National Centers for Environmental Prediction (NCEP), monthly sea surface temperature (SST) fields (1982-1994), Chu et al. [1997b] found that during the spring-to-summer monsoon transition (March-May) a warm anomaly (greater than 1.8°C) was formed in the central SCS at 112°-119°30'E, 15°-19°30'N.

D. AN AIR-SEA FEEDBACK SCENARIO

The circulation at intermediate to upper layers of the SCS are mainly influenced by monsoons. The prevailing summer (winter) monsoon results in an cyclonic (anti-cyclonic) circulation of the surface layer. The reason may be that the SCS is large, semi-enclosed and only slightly affected by the Kuroshio [Huang et al.,1994]. Chu and Chang [1997] investigated the historical SST data from the MOODS, and proposed an air-sea feedback scenario for the central SCS warm-core eddy formation (Figure 2.6). The anticyclonic surface winds prevail in the central SCS from late winter to spring. This anticyclonic wind forcing generates downwelling in the central SCS and in turn prevents the cold deep water from being advected to the surface. This will promote the formation of the warm-core eddy in the central SCS. After the summer monsoon onset, an atmospheric surface cyclone occupies the central SCS, which entrains the deep cold water into the surface mixed layer. This upwelling effect finally destroys the central SCS warm-core eddy.

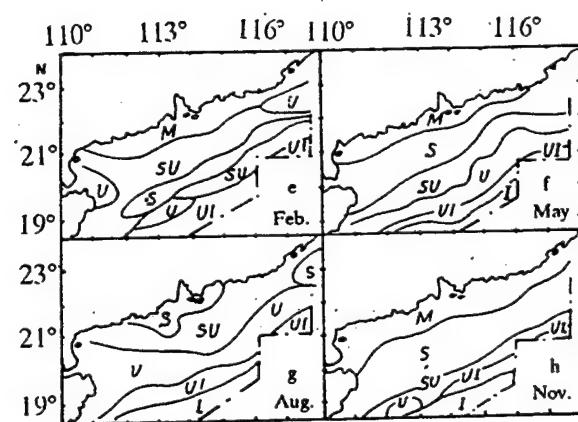
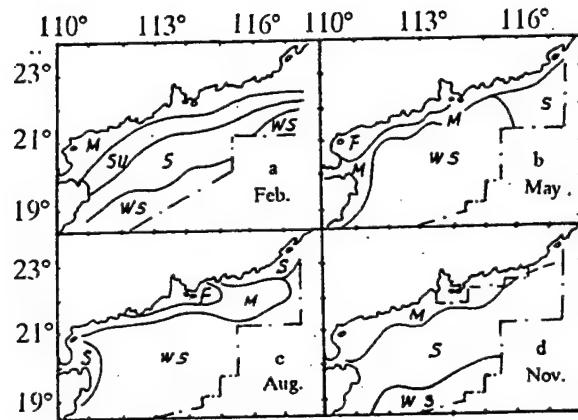


Figure 2.1 Distribution of water masses at the sea surface (a-d) and bottom layer (e-h) in the northern South China Sea. a, February; b, May; c, August; d, November; e, February; f, May; g, August; h, November; see text for acronyms (from Su and Weng, 1994)

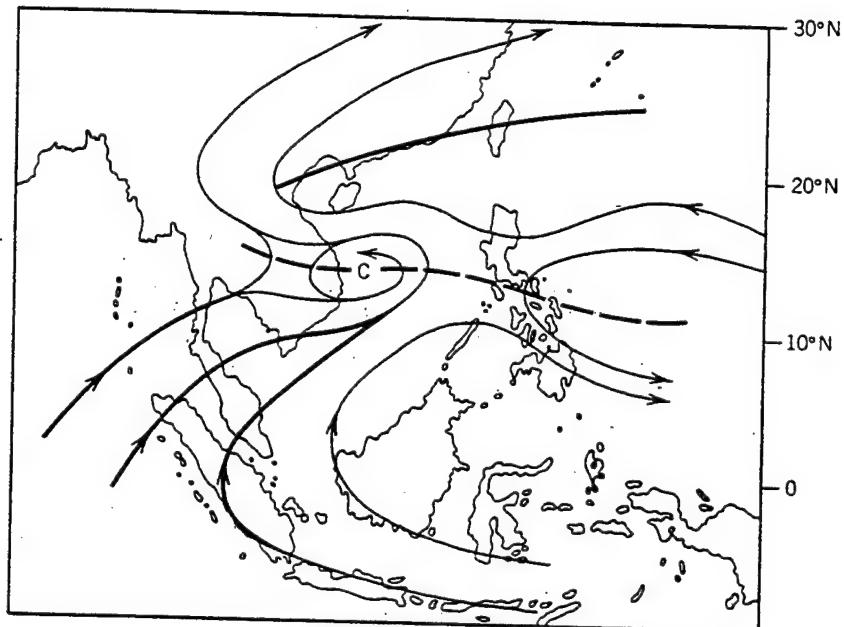


Figure 2.2 Mean Atmospheric Surface Streamline Analysis for summer monsoon (From Cheang, 1980)

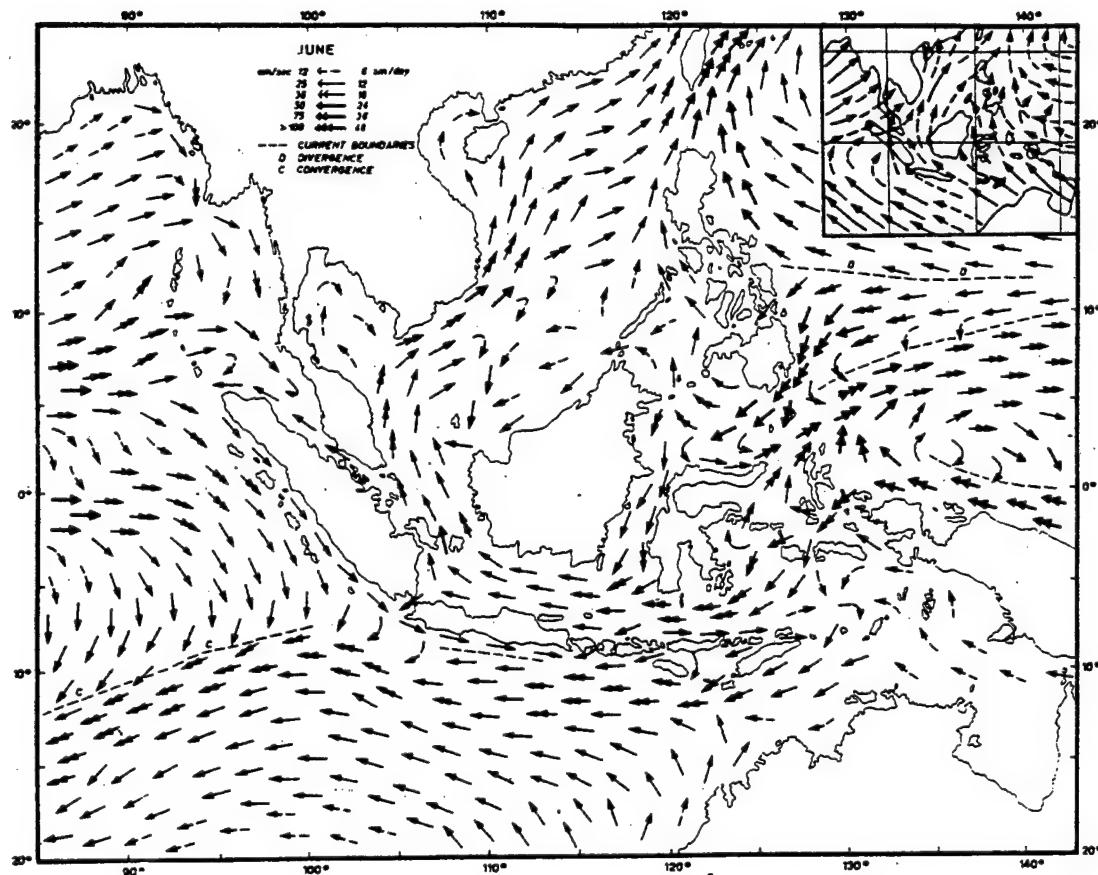


Figure 2.3 Observational Summer (June) surface Circulation of the Southeast Asia Waters (From Wyrtki, 1961)

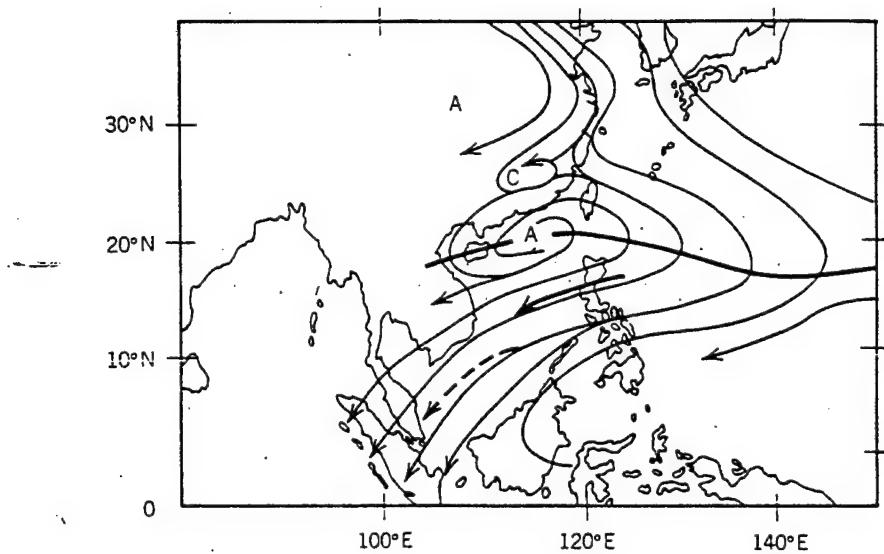


Figure 2.4 Mean Atmospheric Surface Streamline Analysis for winter monsoon (From Cheang, 1980)

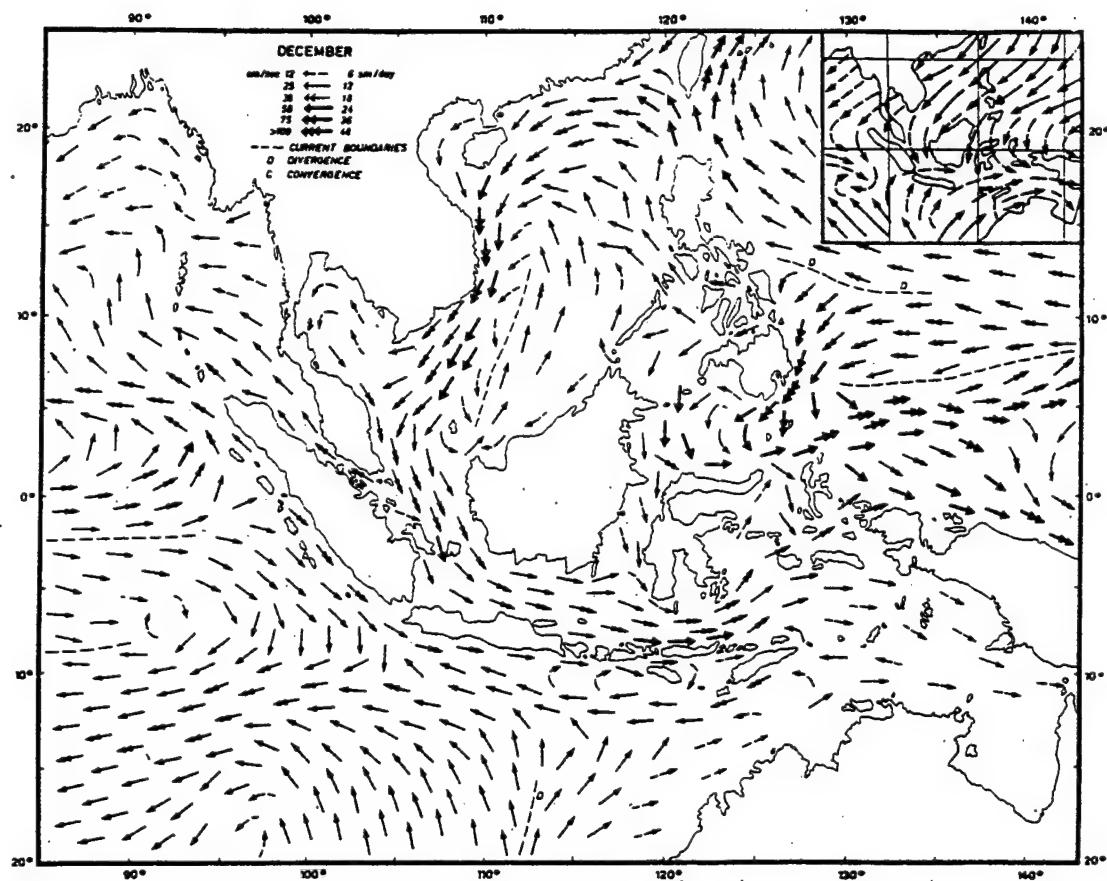


Figure 2.5 Observational Winter (December) Surface Circulation of the southeast Asian Waters (From Wyrtki, 1961)

Central SCS Surface Atmospheric Anti-cyclone

Central SCS Downwelling

Isolating Deep Cold Water

Promotes Surface Warm-Core Eddy

Atmospheric Low Pressure at the Central SCS

Atmospheric Monsoon Onset over SCS

Downwelling Effect Disappears

**Figure 2.6. An Air- Sea Feedback Scenario for the SCS Warm-Core Eddy Life Cycle
(From Chu and Chang 1997)**

III. MASTER OCEANOGRAPHIC OBSERVATION DATA SET (MOODS)

The MOODS is a compilation of observed ocean data worldwide consisting of (a) temperature-only profiles; (b) both temperature and salinity profiles; (c) sound-speed profiles; and (d) surface temperature (drifting buoy). These measurements are, in general, irregular in time and space. The data are from the early nineteen century to the present and include 189,059 temperature profiles (Figure 3.1) and 14,004 salinity profiles (Figure 3.2). In this study, we analyze the temperature profiles obtained during 1968-84 from a variety of instruments. Our study domain includes the area 5°N to 25°N and 105°E to 125°E. The primary editing procedures included removal of profiles with obviously erroneous location, profiles with large spikes, and profiles displaying features that do not match the characteristics of surrounding profiles. In shallow water, this procedure can be partially automated, but it also involves subjective interpretation because of the under sampling of MOODS, compared to the spatial and temporal variability of the ocean.

The temporal and spatial distribution of the MOODS data are irregular. The temporal distribution (Figure 3.3) indicates that most observations were obtained during the Vietnam War. There are nearly 14,800 profiles (maximum number of observations in a year) in 1968 (Figure 3.4). The minimum number of observations was in 1984 (near 3,00 profiles). These figures indicate that the number of observations within a given year exhibits a seasonal variation.

The main limitation of the MOODS data set is its irregular distribution in time and space. Certain periods and areas are over sampled while others lack enough observations to gain meaningful insight. Vertical resolution and data quality are also highly variable depending a great deal on instrument type and sampling expertise.

We binned seventeen years' temperature profiles (from 1968 to 1984) into monthly data for an individual year which produced 204 temperature data sets. For the salinity profiles, we binned into monthly climatology data bins which produced 12 mean monthly salinity data sets.

MOODS temperature profiles with 189,059 data

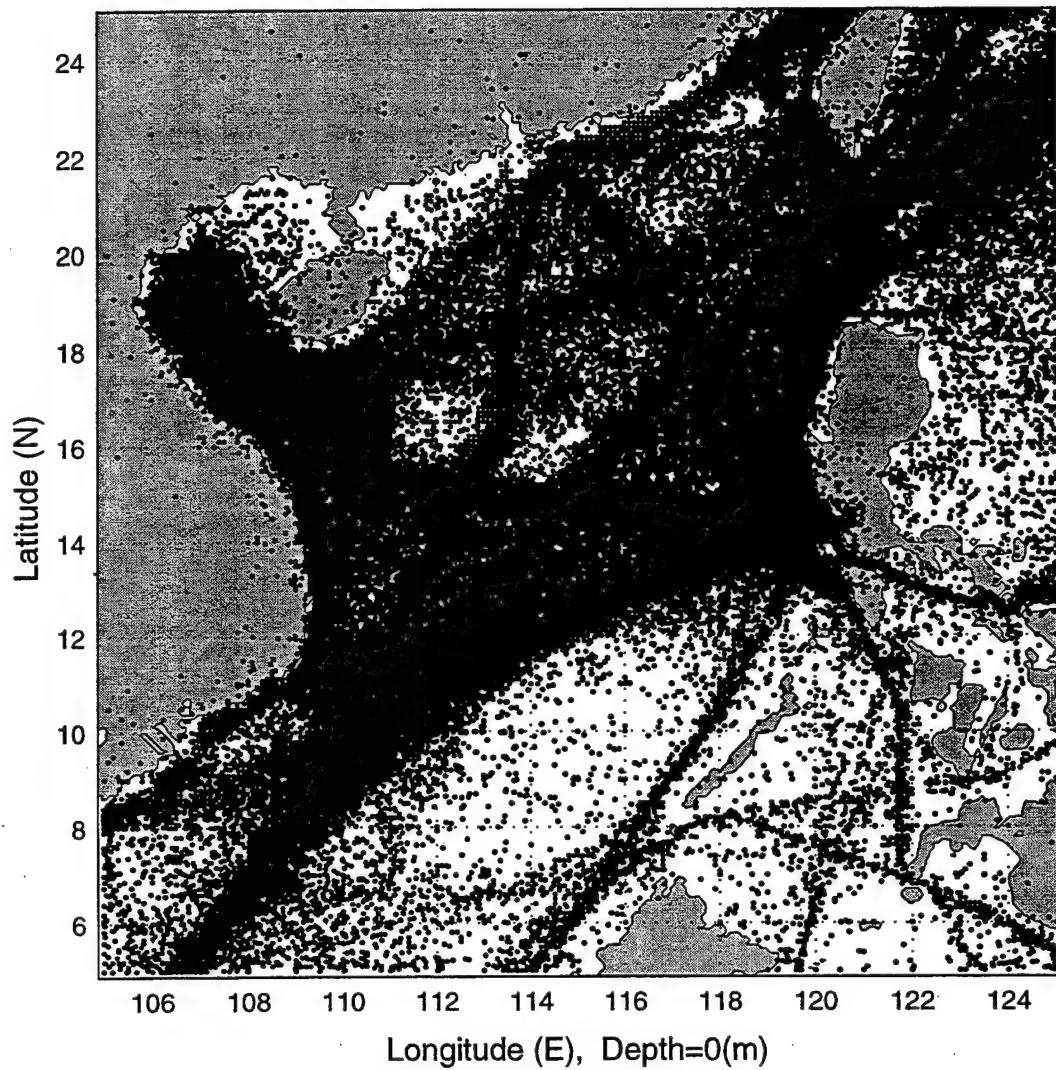


Figure 3.1: The Spatial distribution of MOODS temperature profiles

MOODS salinity profiles with 14,004 data

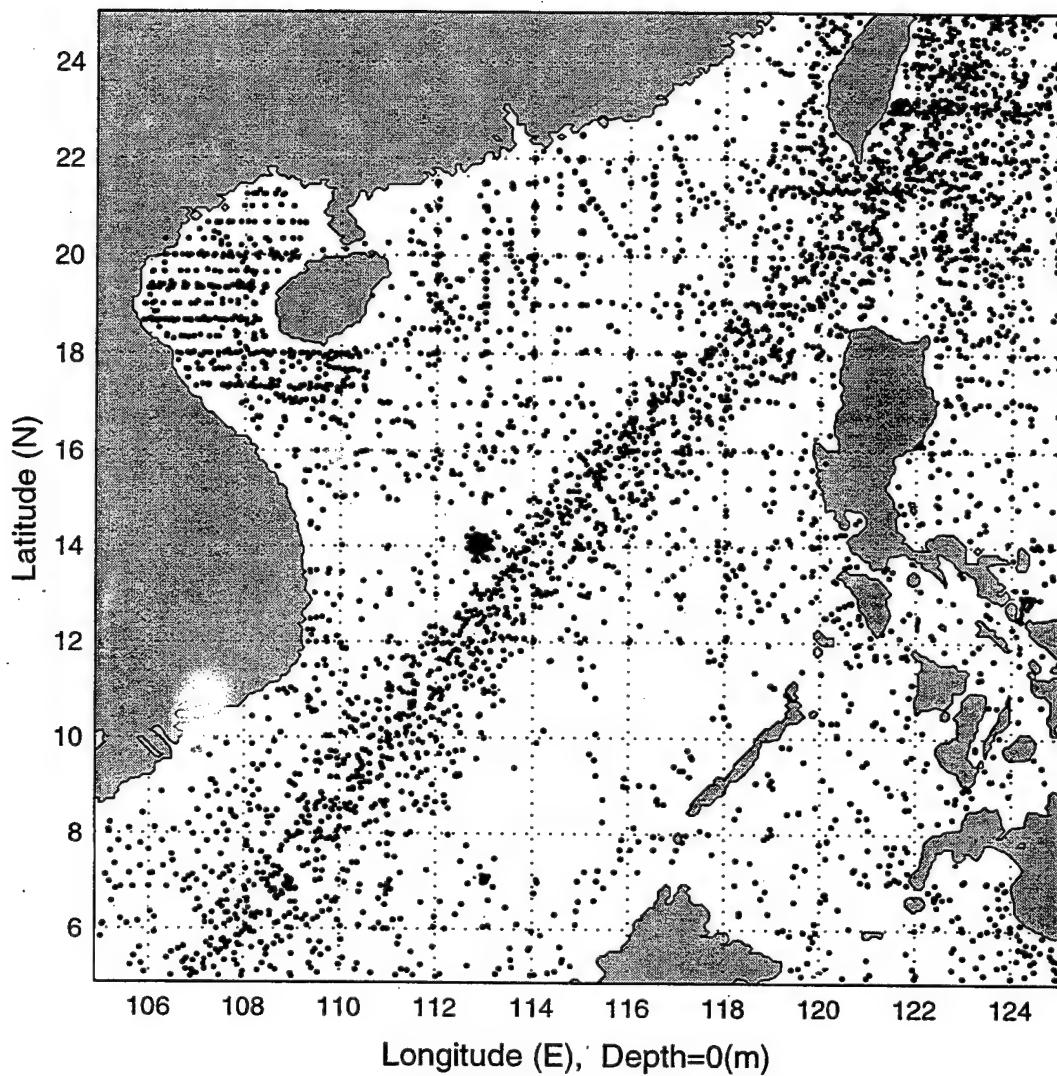


Figure 3.2 The Spatial distribution of MOODS salinity profiles

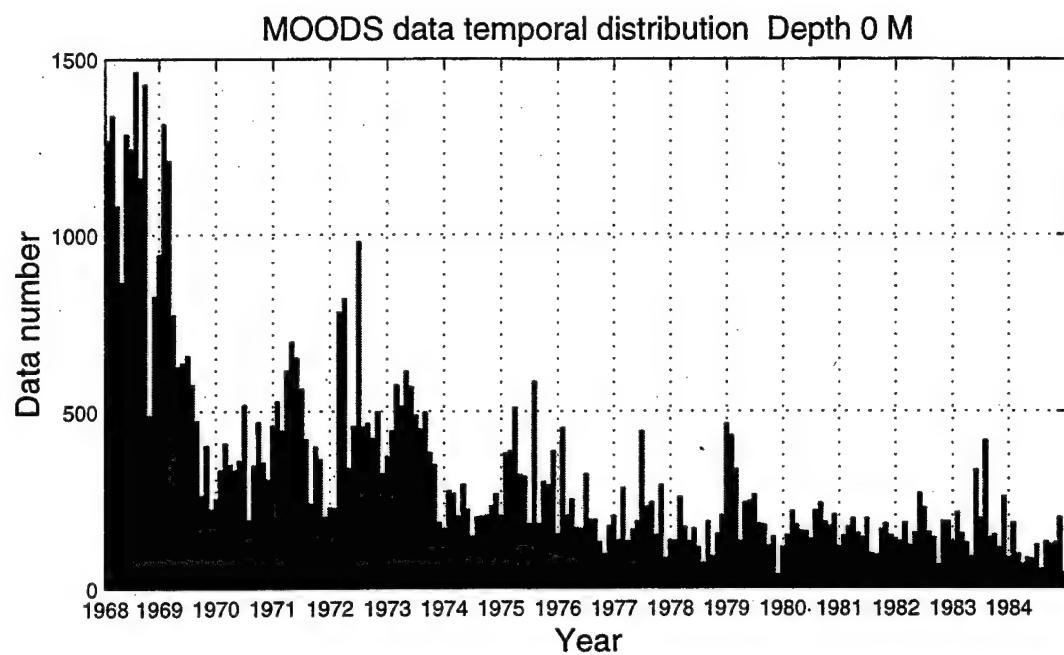


Figure 3.3 The temporal distribution of MOODS

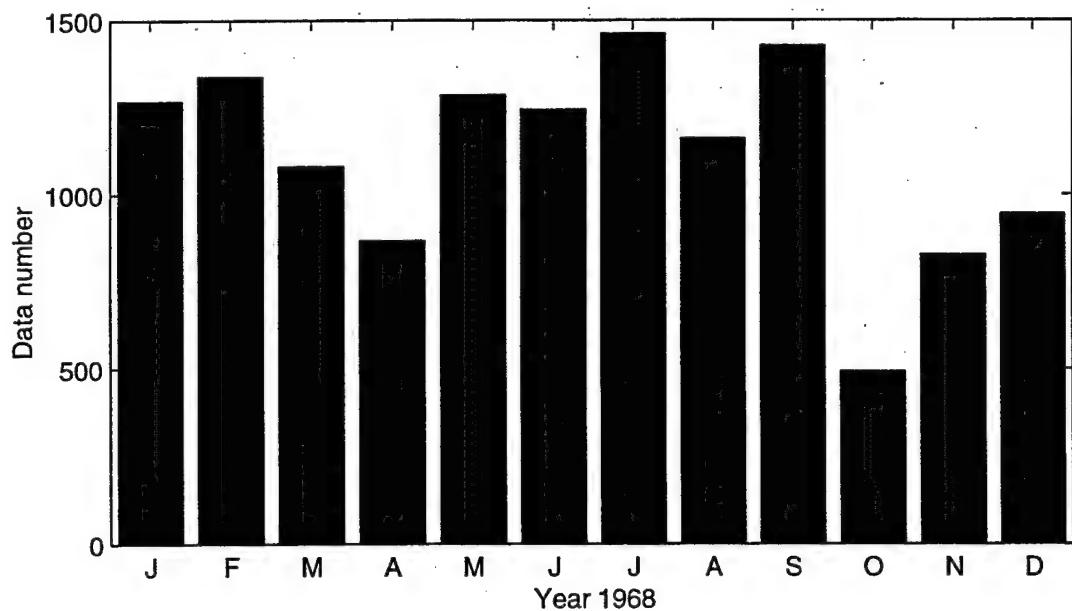


Figure 3.4 The temporal distribution of MOODS in 1968

IV. ESTABLISHMENT OF GRIDDED DATA

For each temperature (or salinity) profile, we linearly interpolated the data into thirteen standard depths (Table 4.1). After this process, we used the minimum curvature spline method [Smith and Wessel, 1990] from the Generic Mapping Tools (GMT) [Wessel and Smith, 1992] to create horizontal gridded data. This method interpolates the data ϕ_{ij} at observational points (x_i, y_j) onto the grid points with a spline function $\phi(x, y)$ such that at observational points;

$$\phi(x_i, y_j) = \phi_{ij}^{(0)} \quad (0)$$

The selection of the spline function is based on the minimum curvature principle, which requires continuous second derivatives and minimal total squared curvature,

$$C = \iint (\nabla^2 \phi)^2 dx dy \quad (1)$$

Briggs [1974] showed that minimizing C is equivalent to solving the differential equation,

$$\nabla^2(\nabla^2 \phi) = \sum_i f_{ij} \delta(x - x_i, y - y_j) \quad (2)$$

where f_{ij} must be chosen such that Equation (1) should be satisfied and where δ is the Kronecker delta function. To solve Equation (2) we need the following boundary conditions

$$\frac{\partial^2 \phi}{\partial n^2} = 0 \quad (3)$$

and

$$\frac{\partial}{\partial n} (\nabla^2 \phi) = 0 \quad (4)$$

along the edges, where $\partial/\partial n$ indicates a derivative normal to an edge, and

$$\frac{\partial^2 \phi}{\partial x \partial y} = 0 \quad (5)$$

at the corners. Equations (3),(4),(5) are called free edge conditions; and with these conditions, equation (2) has a unique solution with continuous second derivatives called the natural bi-cubic spline. The nomenclature comes from an analogy with elastic-plate flexure. Small displacements ϕ of a thin elastic plate of constant flexural rigidity D , subject to a vertical normal stress q and constant horizontal forces per unit vertical length of T_{xx} , T_{xy} , T_{yy} , approximately satisfy

$$D \nabla^2 (\nabla^2 \phi) - [T_{xx} \frac{\partial^2 \phi}{\partial x^2} + 2T_{xy} \frac{\partial^2 \phi}{\partial x \partial y} + T_{yy} \frac{\partial^2 \phi}{\partial y^2}] = q \quad (6)$$

[Love. 1927]. The minimum-curvature gridding equation (2) is a special case of equation (6) when horizontal forces are zero, and the boundary conditions represent zero bending moment on the edges (3), zero vertical shear stress on the edges (4), and zero twisting moment at the corners (5) [Timoshenko and Woinowsky-Krieger, 1968].

Suppose that $T_{xx} = T_{yy} = T$ and $T_{xy} = 0$, then Equation (6) becomes

$$D\nabla^2(\nabla^2\phi) - T\nabla^2\phi = q \quad (7)$$

When $T = 0$, Equation (7) is equivalent to Equation (2); but for an arbitrarily large T , the solution is dominated by the second term. Here, T has units of force per unit length and the T required to adjust the solution scales with D and q ; Smith and Wessel [1990] avoided this problem by writing

$$(1-T_I)\nabla^2(\nabla^2\phi) - T_I\nabla^2\phi = \sum_i f_{ij}\delta(x-x_i, y-y_j) \quad (8)$$

where T_I is a tension parameter and the I subscript indicates internal tension. When $T_I = 0$, equation (8) reduces to equation (2); and therefore, the minimum-curvature solution is one end-member case of equation (8). When $T_I = 1$, the first term in equation (8) vanishes; and the solution is harmonic between constraining points. One may prefer to think of this end member as representing the steady-state temperature field in a conducting plate with heat sources or sinks at the data points. For any T_I in $0 \leq T_I < 1$, equation (8) gives a solution with continuous curvature, although it does not minimize equation (1) except when $T_I = 0$ [Smith and Wessel, 1990].

For the boundary condition, they implemented conditions (4) and (5) but replace condition (3) by

$$(1 - T_B)\frac{\partial^2\phi}{\partial n^2} + T_B\frac{\partial\phi}{\partial n} = 0 \quad (9)$$

where T_B is a tension parameter for the boundary which also varies between 0 and 1. The free-edge condition corresponds to $T_B = 0$; $T_B = 1$ forces the solution to flatten at the edge (Figure 4.1a,b). This flattening is sometimes desirable, as when gridding potential anomalies which should decay toward a regional background field away from the source region. Gridding with tension is an improvement because it adds a degree of freedom and relaxes the minimum-curvature constraint.

Layer	Depth (m)	Layer	Depth (m)
1	0	8	125
2	10	9	150
3	20	10	200
4	30	11	250
5	50	12	300
6	75	13	400
7	100		

Table 4.1 The standard depth of 13 layers.

a)

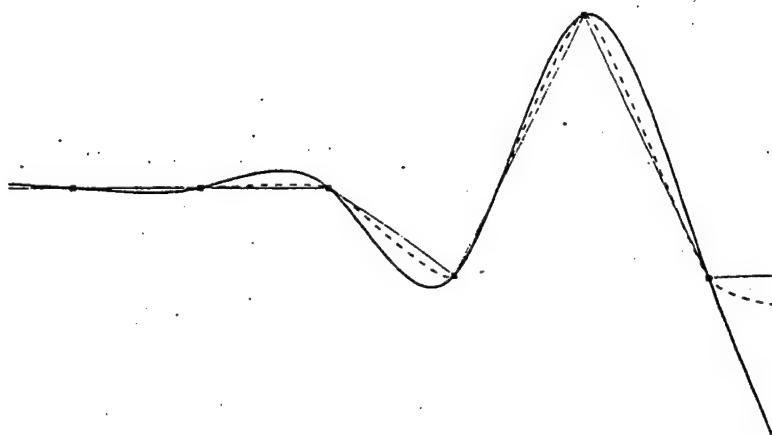


Figure 4.1a Cross-sections through surfaces produced with splines in tension. The black squares are data constraints. The heavy line is the minimum-curvature end member, the thin line is the harmonic end member, and the dashed line is an intermediate case using some tension (from Smith and Wessel, 1990)

b)

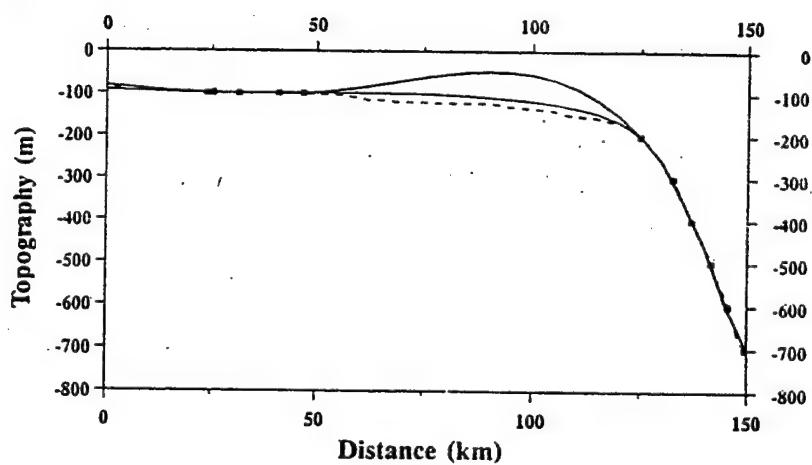


Figure 4.1b Cross-sections through continental shelf and slope. The black squares represent the intersection between the measured bathymetry (dashed line) and 100m isobath contours. These intersections (contour coordinates) were then gridded using minimum curvature (heavy solid line) and some tension (thin solid line). The minimum-curvature method introduces an extraneous inflection point and exceeds the -100m level (The bathymetry in this region is bounded by the -200m and -100m level). The surface produced with tension gives a much better approximation since it suppresses local maxima and minima between data constraints (from Smith and Wessel, 1990)

V. COMPOSITE ANALYSIS

Our goal is to investigate the temporal and spatial variabilities of the SCS thermohaline structure. We use $\psi(x_i, y_j, z_k, \tau_l, t_m)$ to represent temperature and salinity gridded data, where (x_i, y_j) are the horizontal grids, z_k ($= 1, 2, \dots, 13$), is the vertical level, τ_l ($= 1968, 1969, \dots, 1984$) is the time sequence in years, and t_m ($= 1, 2, \dots, 12$) is the time sequence in month. We define the following temporal average:

$$\bar{\Psi}(x_i, y_j, z_k, t_m) \equiv \frac{1}{\Delta\tau} \sum_l \Psi(x_i, y_j, z_k, \tau_l, t_m), \quad (10)$$

which is the long-term mean value for the month t_m , and

$$\bar{\bar{\Psi}}(x_i, y_j, z_k) \equiv \frac{1}{12} \sum_{m=1}^{12} \bar{\Psi}(x_i, y_j, z_k, t_m), \quad (11)$$

which is the ensemble (climatological annual) mean value. Here, $\Delta\tau \equiv 17$ years.

A. ANNUAL MEAN

The annual mean (1968-1984) temperature $\bar{\bar{T}}$ field over the SCS shows the pattern of northeast-southwest oriented isotherms at the upper layer from the surface to 75 m depth (Figure 5.1a). The annual surface mean has a rather weak horizontal temperature gradient, decreasing from 28.5°C near the Borneo coast to 25°C near the southeast China coast. A strong temperature front is found near the Luzon Strait in the sub-surface layer from 100 m to 400 m (Figure 5.1b). The SCS water temperature is quite uniform (e.g., near 15°C at 200

m) and much lower than the water east of the Luzon Strait, the West Pacific Ocean Water. This might imply that the annual mean Kuroshio intrusion is not significant in the subsurface layer.

In the central SCS region at 15°N zonal cross-section (Figure 5.2a), the isotherms of \bar{T} bend slightly downward from west to east and no frontal structure is found. However, in the northern SCS region at 20°N zonal cross-section, the isotherms of \bar{T} show a strong frontal structure near 120° to 125°E (Figure 5.2b), which may suggest two distinguished water masses, the SCS water mass (both surface and under-surface) and the West Pacific Ocean water mass. The front between the two water masses strengthens from surface to 400 m depth.

The annual mean salinity \bar{S} shows more complexity than temperature. In the upper layer (Figure 5.3a), a large amount of freshwater enters the SCS from the Zhujiang (Pearl) River in the northwest and from the Mekong River in the southwest. The Kuroshio brings the salty water through the Luzon Strait into the north SCS and forms a salty tongue (34 psu) stretching into the southeast China coast. As the depth increases, both the Kuroshio intrusion and the river run-off effects become less important. At 75 m depth, the Kuroshio intrusion effect is still evident, but not the river run-off effect. Below 200 m depth (Figure 5.3b), the salinity is more uniform (near 34.6 psu at 200 m) throughout the whole SCS.

In the central SCS region at 15°N zonal cross-section (Figure 5.4a), the isohalines of \bar{S} are almost parallel to the isobaths in the upper 100 m. Below 100 m depth, the salinity

is very uniform (34.4 psu). However, in the northern SCS region at 20°N zonal cross-section (Figure 5.4b), the 34.6 psu isohaline clearly shows the Kuroshio intrusion from the Luzon Strait into the northern SCS in the layer between 100 and 220 m reaching 115°E.

B. SEASONAL VARIATION

The long-term monthly mean values relative to the annual mean

$$\Psi(x_i, y_j, z_k, t_m) \equiv \bar{\Psi}(x_i, y_j, z_k, t_m) - \bar{\bar{\Psi}}(x_i, y_j, z_k) \quad (12)$$

represent the composite features of the monthly mean variations of temperature and salinity.

1. Temperature

a. Surface

We choose the SST to represent the thermal feature of the surface layer. The seasonal SST variation obtained from the MOODS data is quite consistent with earlier investigations based on the National Center for Environmental Predictions (NCEP) data [Chu et al., 1997b].

During winter (January), \tilde{T} is negative almost everywhere throughout the whole SCS (Figure 5.5a). The typical winter (January) pattern contains northeast-to-southwest oriented isotherms in the northern SCS (north of 12°N), a warm anomaly ($\tilde{T} > -1.2^{\circ}\text{C}$) in the west of Borneo- Palawan islands (WBP), and a cool anomaly ($\tilde{T} < -2.4^{\circ}\text{C}$) near the South Vietnam coast (SVC) in the southern SCS (south of 12°N). The spring-to-summer transition (March to May) pattern shows the northward expansion of the WBP warm anomaly and the formation of a central SCS (10°-15° N) warm anomaly with \tilde{T}

$> 0.6^{\circ}\text{C}$. The isoline 1°C encloses almost all the SCS in May.

The summer (July) pattern is characterized by northeast-to-southwest oriented isotherms in the northern SCS (north of 15°N) (Figure 5.5b), a WBP cool anomaly ($\tilde{T} < 0.4^{\circ}\text{C}$), and a SVC warm anomaly ($> 1.2^{\circ}\text{C}$) in the southern SCS. The summer pattern is opposite to the winter pattern. The fall-to-winter transition (October) pattern shows the northward expansion of a WBP cool anomaly and the formation of a central SCS (10° - 15°N) cool anomaly.

b. Sub-Surface Level (75 m)

We chose 75 m depth to represent the sub-surface (Figure 5.6). The seasonal variation of this layer is characterized by the west Luzon coast (WLC) and SVC cool (warm) anomalies and southeast China coast (SCC) warm (cool) anomaly in winter (summer). The WLC cool anomaly appears in December, reaching its maximum strength in January with $\tilde{T} < -3.4^{\circ}\text{C}$ (Figure 5.6a), lasting two months and disappears in April. The WLC warm anomaly forms in June with $\tilde{T} > 2^{\circ}\text{C}$, reaches $\tilde{T} > 2.4^{\circ}\text{C}$ in July (Figure 5.6b), and lasts for four months.

Figure 5.7 shows the zonal cross-section at 19°N of the \tilde{T} field, representing the vertical structure of the WLC cool eddy in winter (Figure 5.7a), and the vertical structure of the WLC warm eddy in summer (Figure 5.7b). Both WLC winter cool and summer warm eddies reach 250 m depth. The winter cool-core ($\tilde{T} < -3^{\circ}\text{C}$) and the summer warm-core ($\tilde{T} > 2.5^{\circ}\text{C}$) are located between 50 m to 100 m depth.

c. *Intermediate Level (200 m)*

At 200 m depth, the seasonal variation of temperature is featured by a basin-wide cool pool ($\tilde{T} < -0.8^{\circ}\text{C}$), a strong SCC warm pool ($\tilde{T} > 0.8^{\circ}\text{C}$), and a weak WBP warm pool ($\tilde{T} > 0.2^{\circ}\text{C}$) during the winter (Figure 5.8a) and a basin-wide warm pool ($\tilde{T} > 0.4^{\circ}\text{C}$), and a weak SVC cool pool ($\tilde{T} < 0^{\circ}\text{C}$) during the summer (Figure 5.8b). The WLC winter cool eddy ($\tilde{T} < -1.0^{\circ}\text{C}$) and summer warm eddy ($\tilde{T} > 0.8^{\circ}\text{C}$) are still quite evident at that depth. The weak WBP warm pool strengthens, expands toward the northeast in spring (Figure 5.8a), gradually occupies the whole SCS basin, and turns to the summer pattern in July (Figure 5.8b). In autumn, the weak SVC cool pool strengthens and expands toward northeast, gradually occupies the whole SCS basin and turns to the winter pattern in January. Below 300 m depth, there is no significant seasonal variability.

2. **Salinity**

The seasonal salinity variation \tilde{S} is evident only in the layer above 200 m depth. Below this depth, the seasonal variability is very weak.

a. *Surface*

During winter (January), \tilde{S} is positive almost everywhere throughout the whole SCS except the SVC and the Gulf of Tonkin (Figure 5.9a). A salty tongue with $\tilde{S} > 0.4$ psu stretches from the Luzon Strait to the continental shelf along the southeast China coast, representing a strong Kuroshio intrusion. Another weak fresh pool with $\tilde{S} < -0.2$ psu is found to the west of Luzon Island. During summer (July), a salty tongue with \tilde{S} around 0.4 psu

stretches from the Vietnam coast to 118°E between 10°-17°N, occupying the central SCS (Figure 5.9b). Everywhere else is occupied by negative \tilde{S} . A strong fresh tongue occupies the continental shelf along the southeast China coast and the Gulf of Tonkin. The negative values in the vicinity of the Luzon Strait indicate the cease of the Kuroshio intrusion into the SCS. On the other hand, the negative \tilde{S} in the southern SCS shows the influx of fresh water from the southern boundary.

b. Sub-Surface Level (75 m)

The seasonal \tilde{S} variation is featured by a wide salty tongue stretching southwestward from the Luzon Strait to the SCS basin in the winter (Figure 5.10a) and a fresh tongue stretching northward from the southwest boundary near the Mekong River mouth to the SCS basin in the summer (Figure 5.10b). The former represents the intrusion of the salty Kuroshio water (with maximum $\tilde{S} > 0.6$ psu) through the Luzon Strait, and the latter indicates the low salinity water (with minimum $\tilde{S} < -0.4$ psu) extending to the SCS.

Figure 5.11 shows the zonal cross-section at 19°N of the \tilde{S} field, representing the vertical structure of the WLC high salinity anomaly ($\tilde{S} > 0.4$ psu) in winter (Figure 5.11a) and low salinity anomaly ($\tilde{S} < -0.2$ psu) in summer (Figure 5.11b). Both WLC high /low salinity anomalies are located between 50 m to 100 m depth.

c. Intermediate Level (200 m)

At 200 m depth, the seasonal variation of \tilde{S} shows a similar pattern (Figure 5.12) to that at 75 m depth. In the winter (Figure 5.12a), positive \tilde{S} with a maximum value of 0.3 psu occupies the most area of the SCS, except the southwest corner near the Mekong

River, where \tilde{S} is negative (-0.4 psu). In the summer (Figure 5.12b), a narrow fresh tongue with a minimum value of -0.4 psu stretches northeastward from the southwest corner near the Mekong River to 20°N (Figure 5.12b).

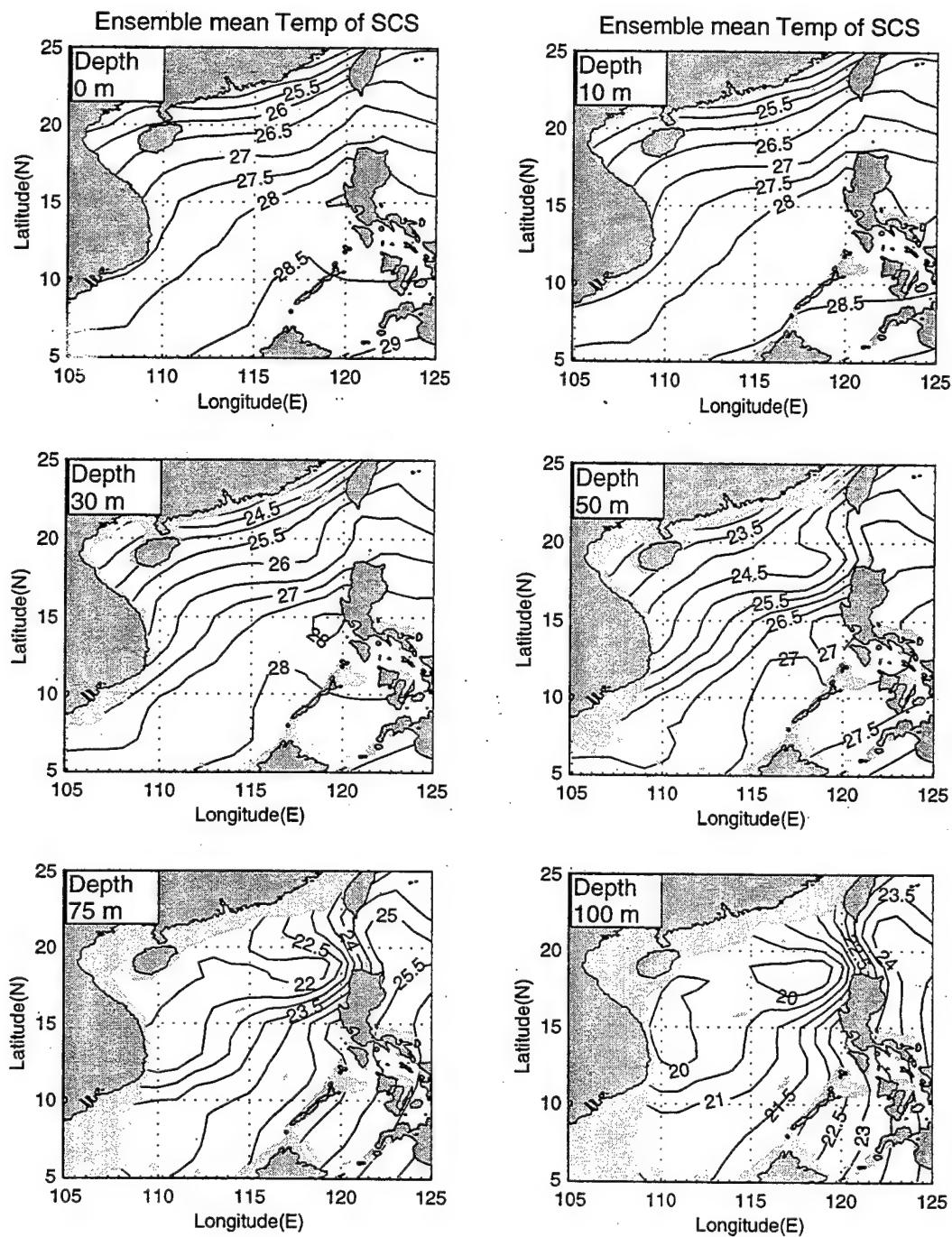


Figure 5.1a The annual mean temperature field (\bar{T}) from surface to 100 meters

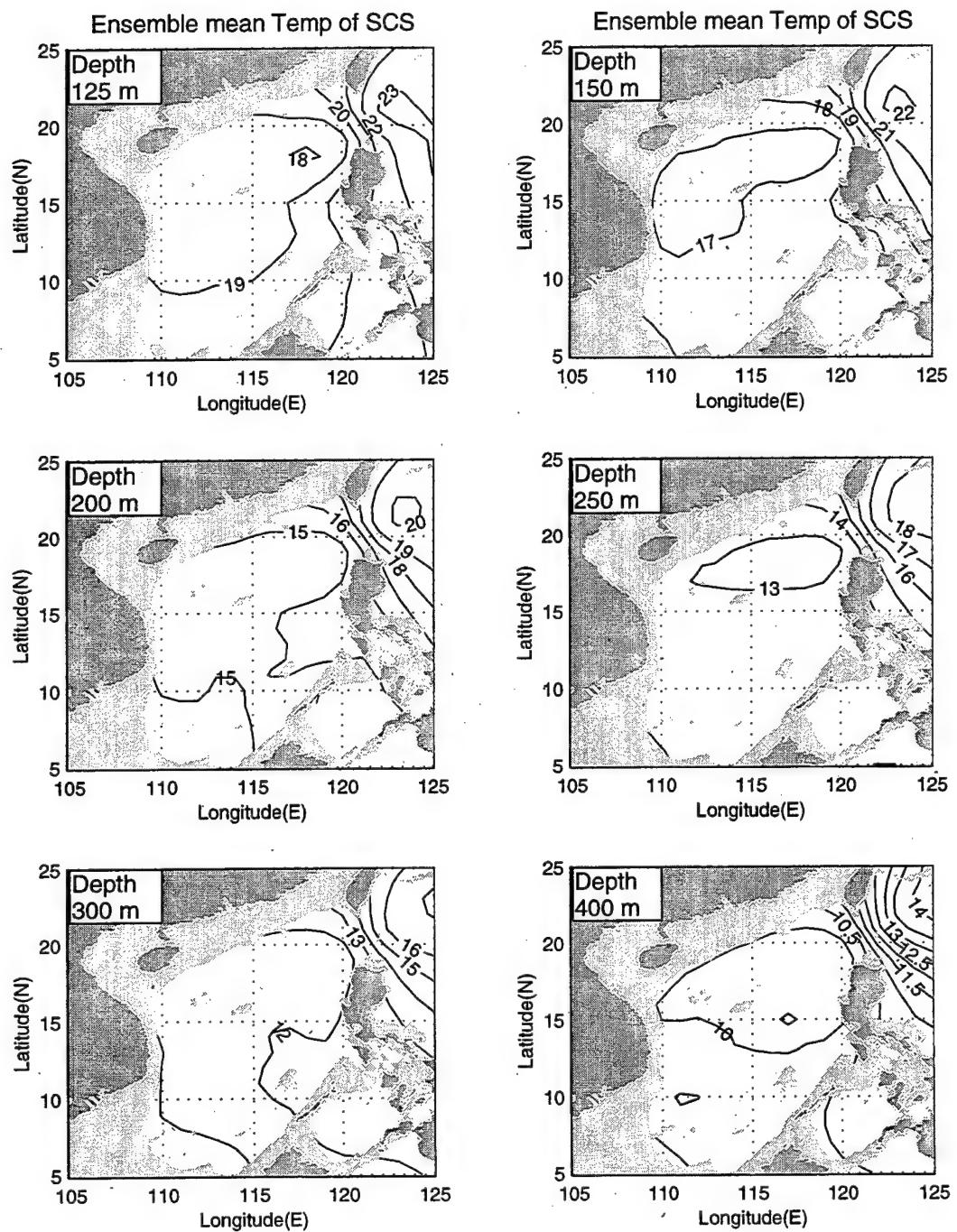


Figure 5.1b The annual mean temperature field (\bar{T})
from 125 to 400 meters

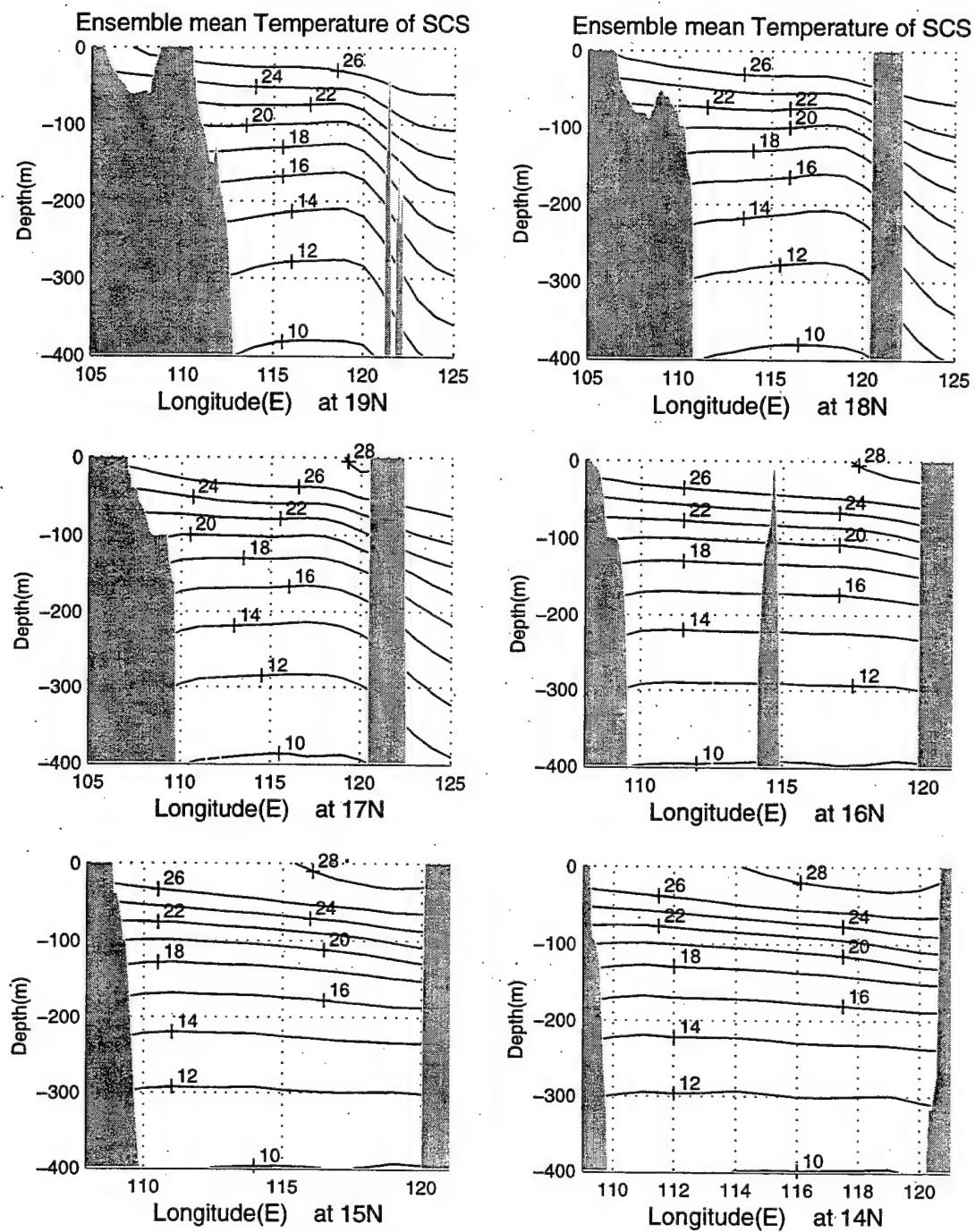


Figure 5.2a The zonal cross-section view of annual mean temperature \bar{T} from Latitude 14°N to Latitude 19°N

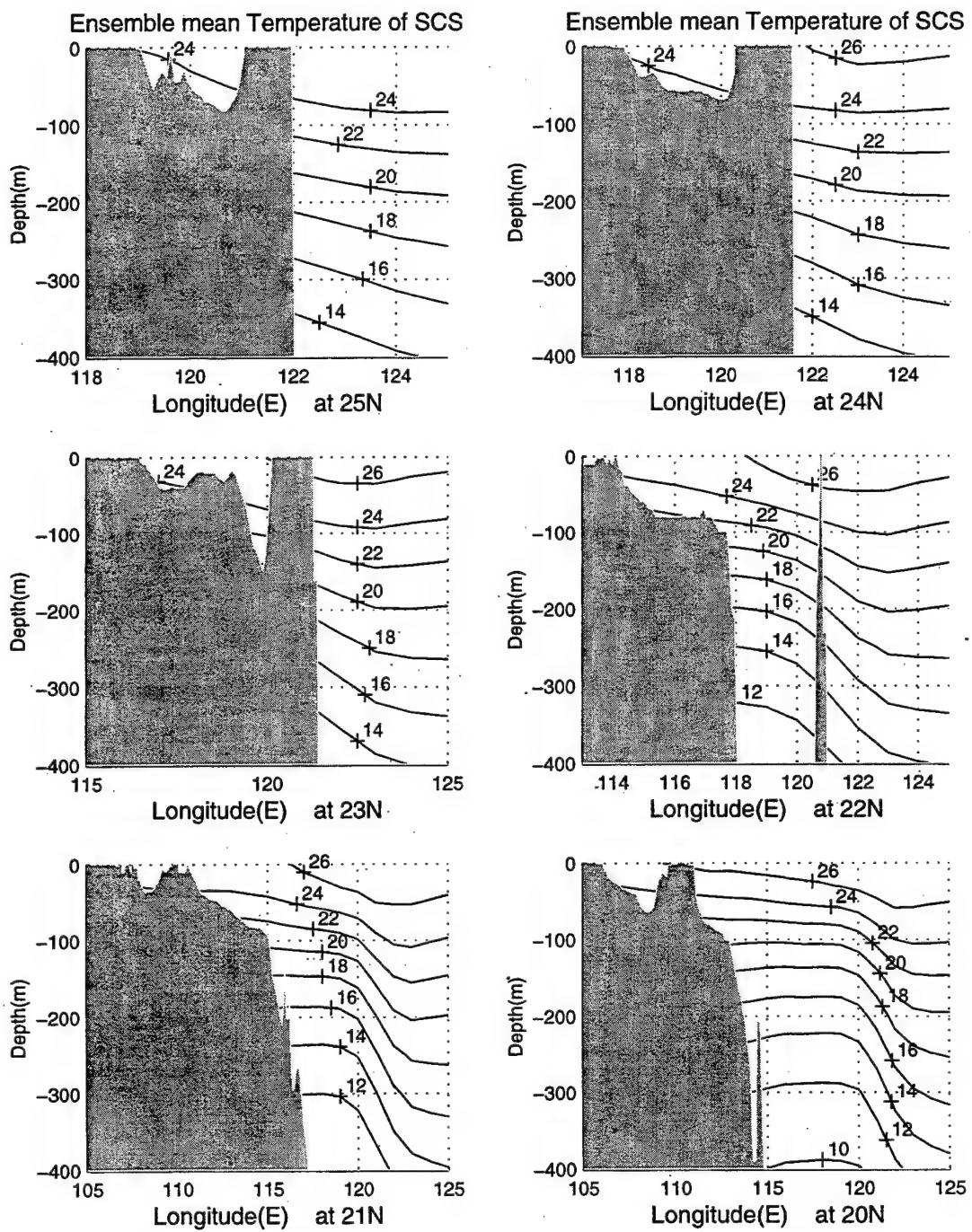


Figure 5.2b The zonal cross-section view of annual mean temperature \bar{T} from Latitude 20°N to Latitude 25°N

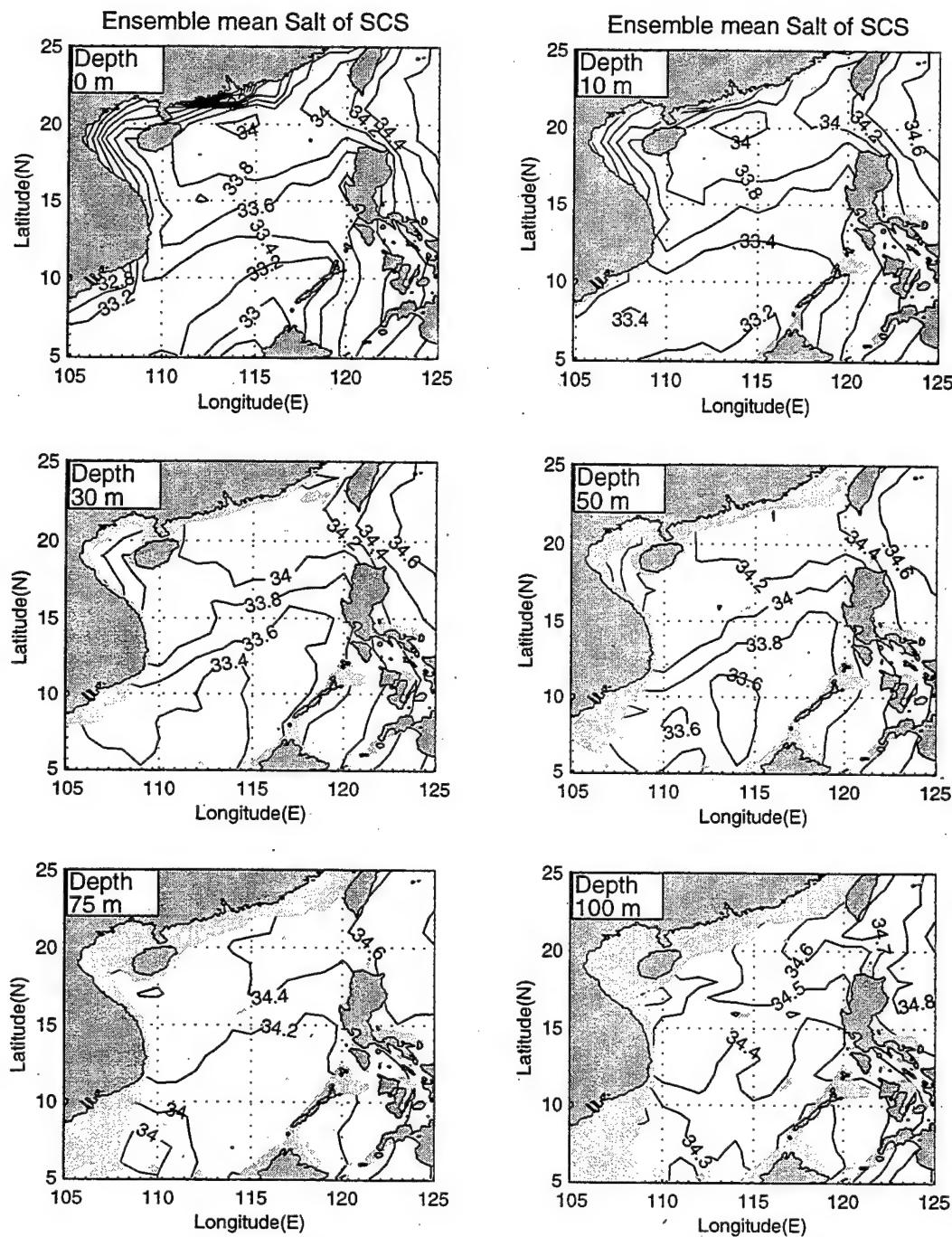


Figure 5.3a The annual mean salinity field (\bar{S})
from surface to 100 meters

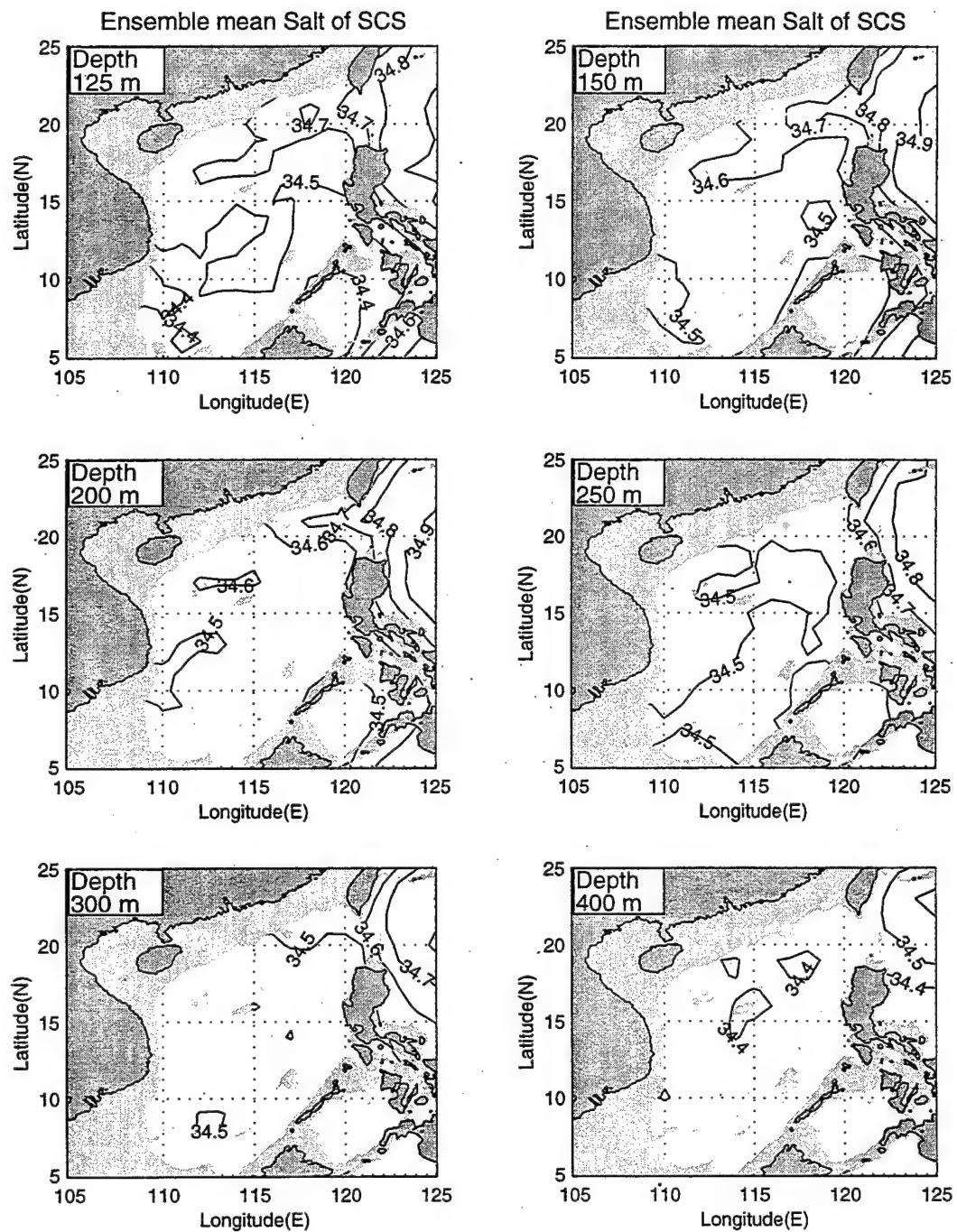


Figure 5.3b The annual mean salinity field (\bar{S}) from 125 to 400 meters

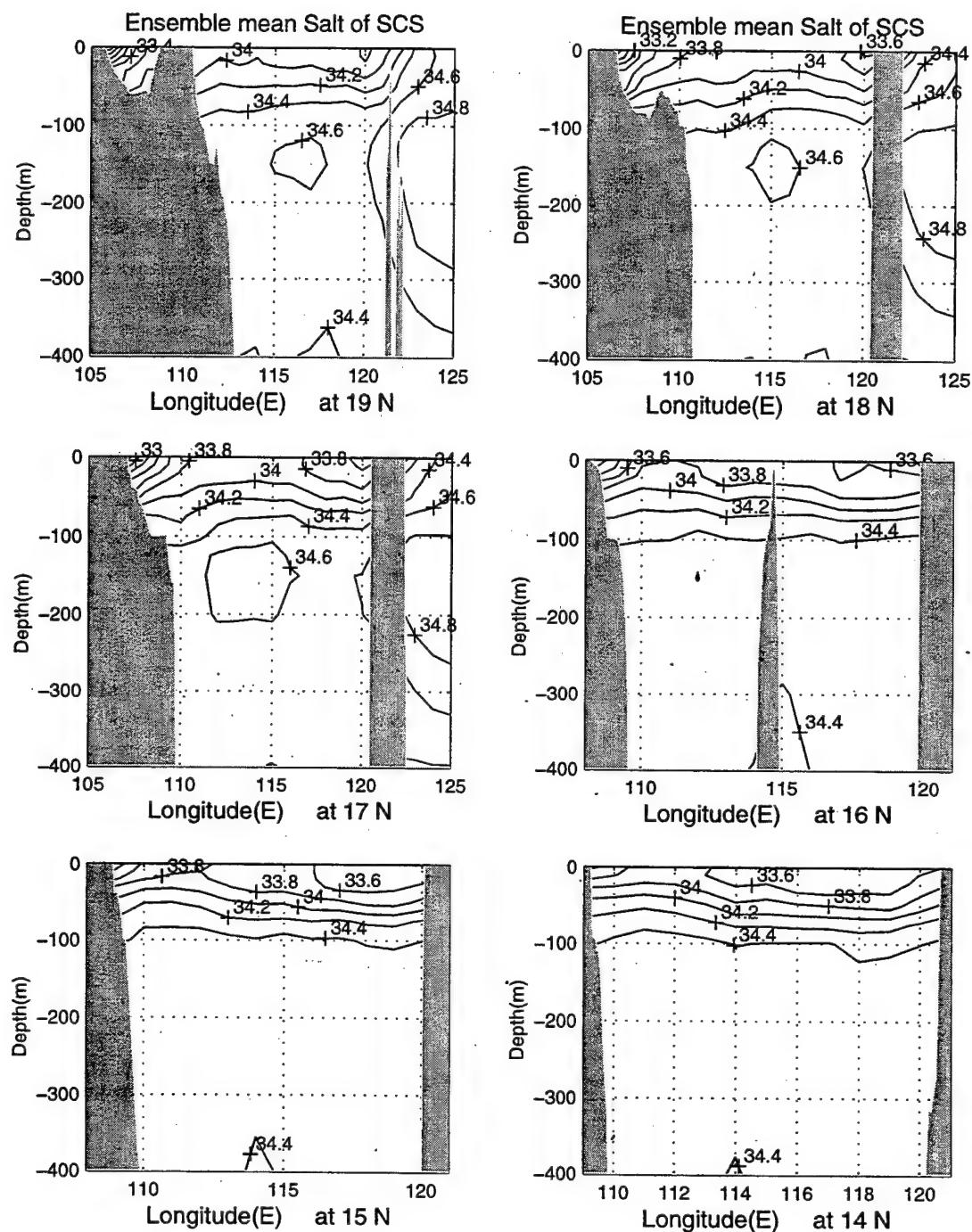


Figure 5.4a The zonal cross-section view of annual mean salinity (\bar{S}) from Latitude 14°N to Latitude 19°N

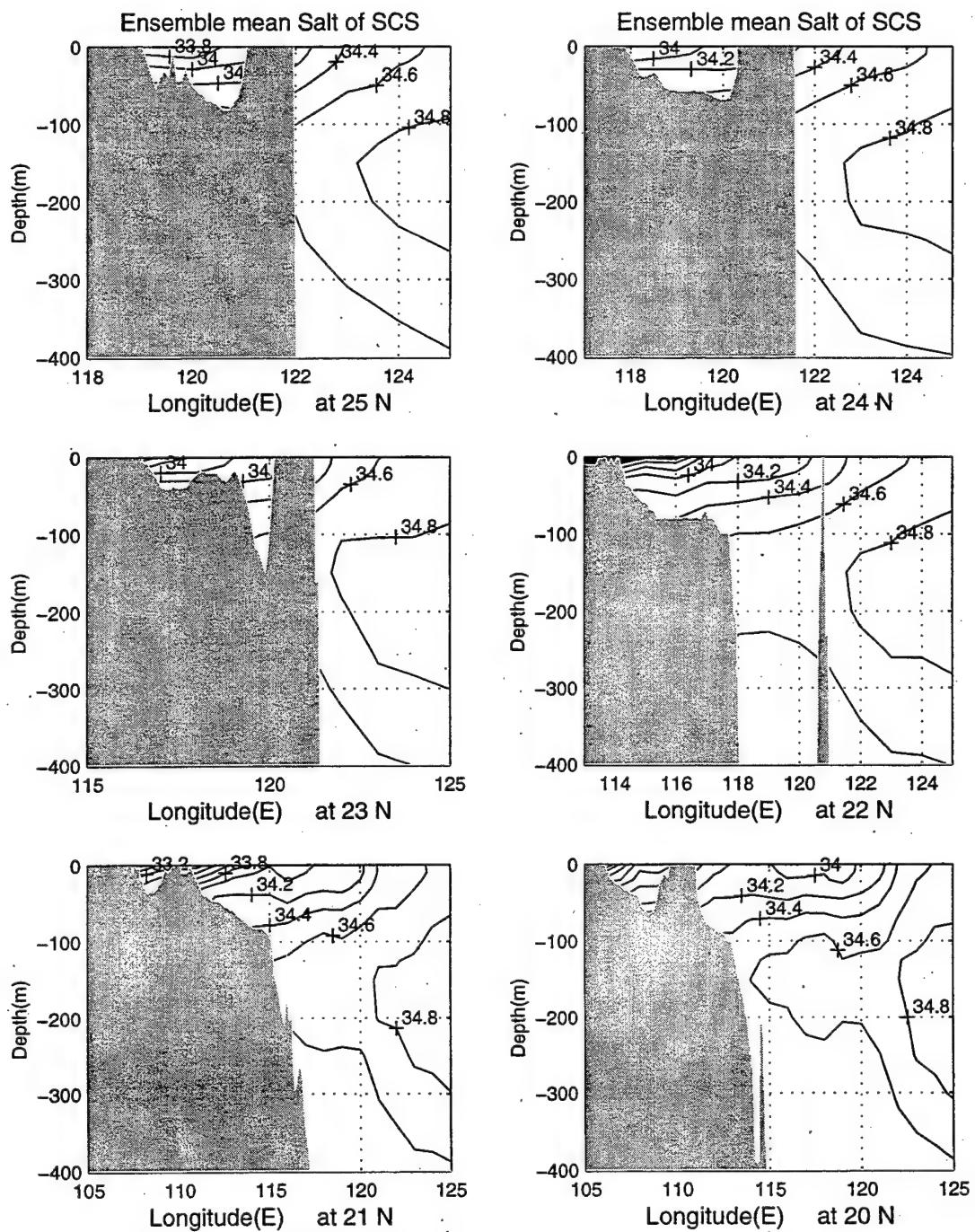


Figure 5.4b The zonal cross-section view of annual mean salinity (\bar{S}) from Latitude 20°N to Latitude 25°N

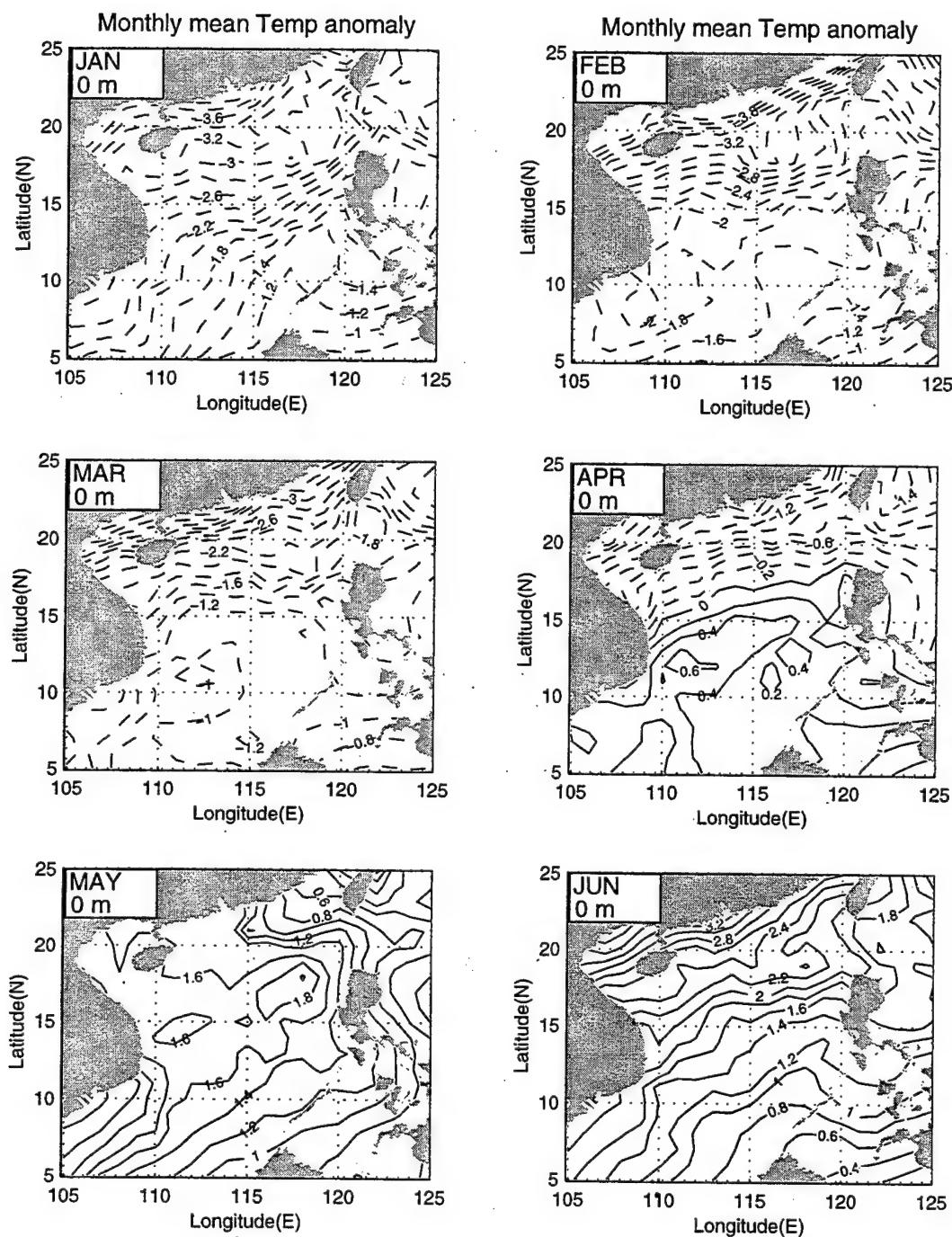


Figure 5.5a Monthly mean temperature anomalies (\tilde{T}) at surface from January to June

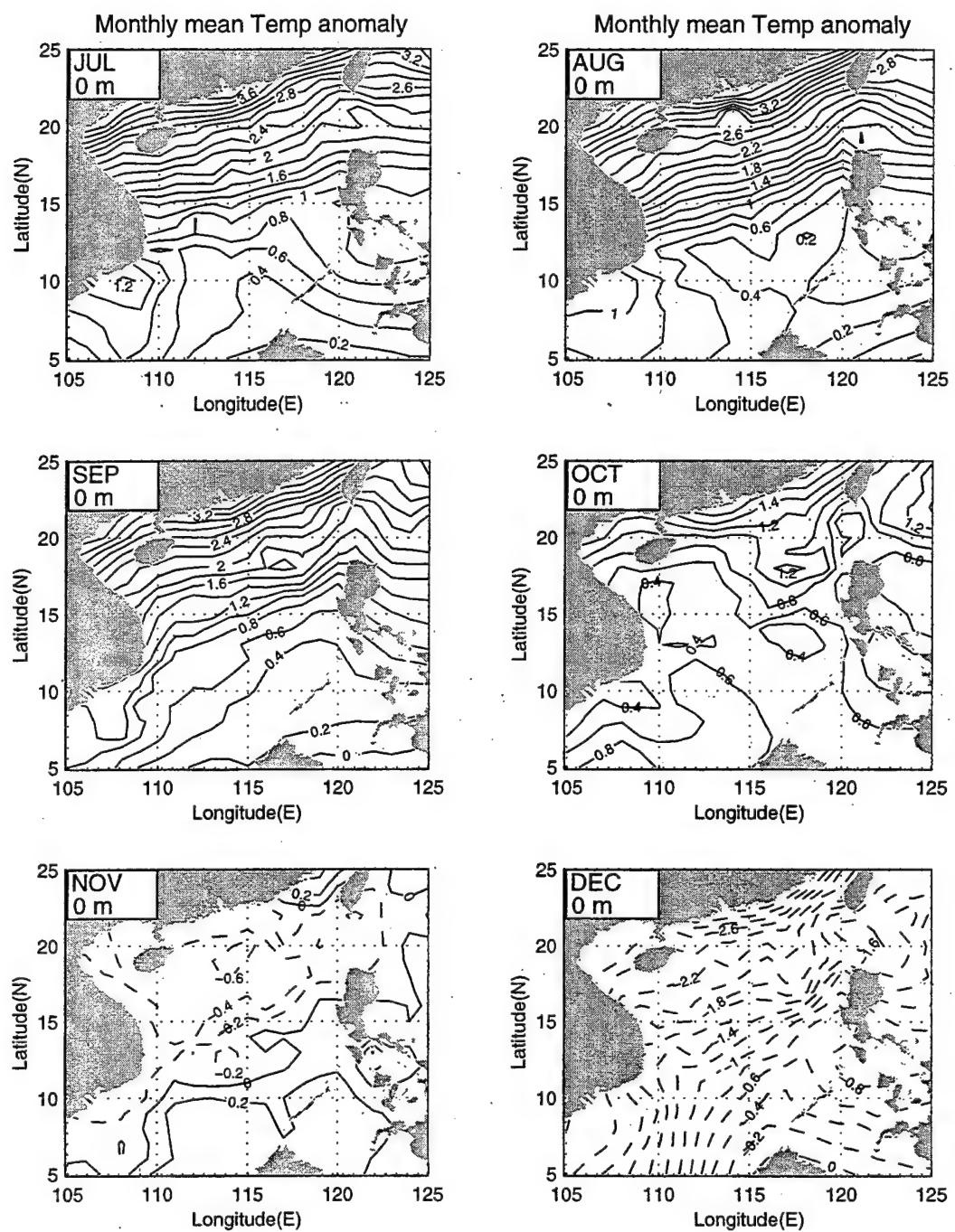


Figure 5.5b Monthly mean temperature anomalies (\tilde{T}) at surface from July to December

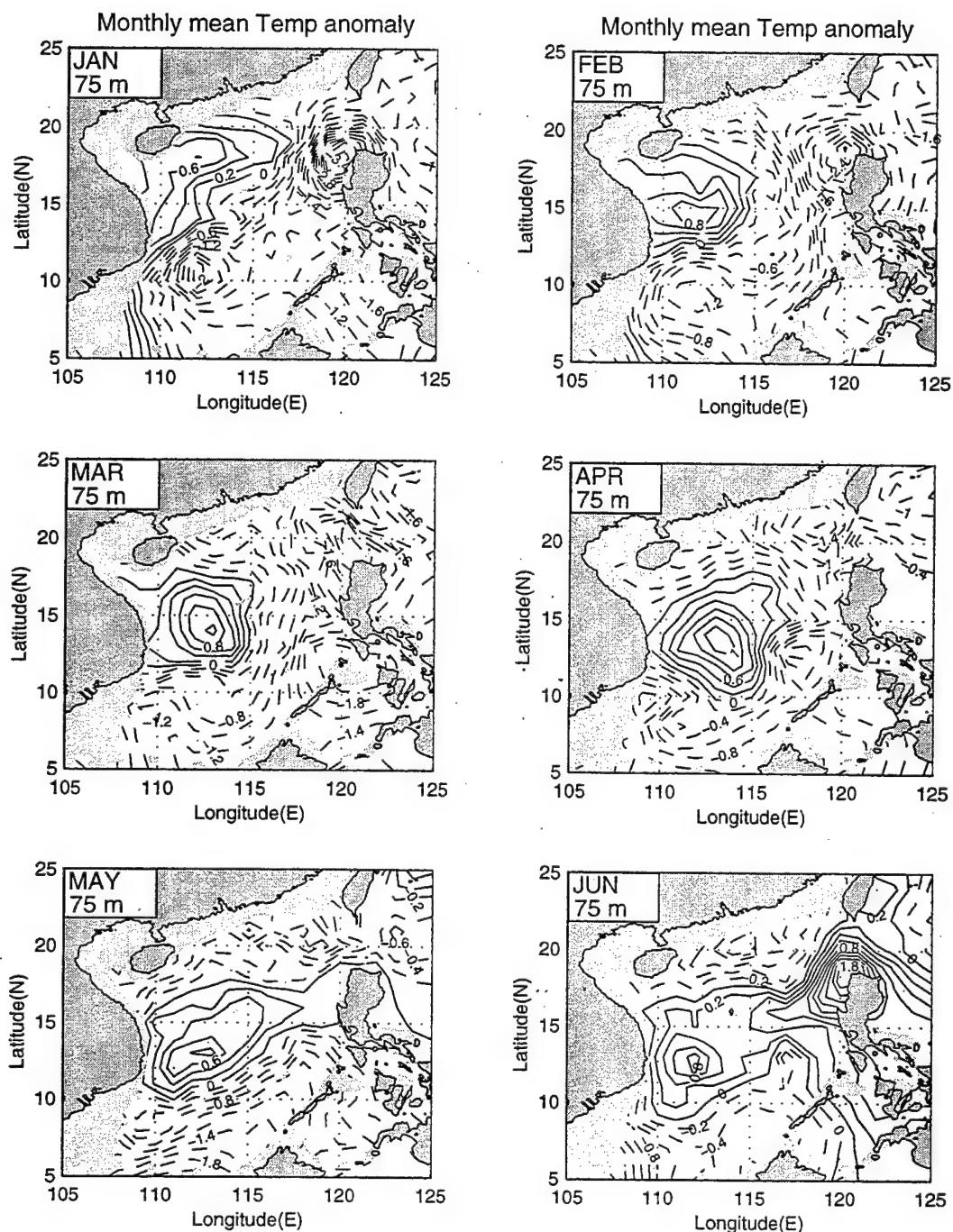


Figure 5.6a Monthly mean temperature anomalies (\tilde{T}) at 75 meters from January to June

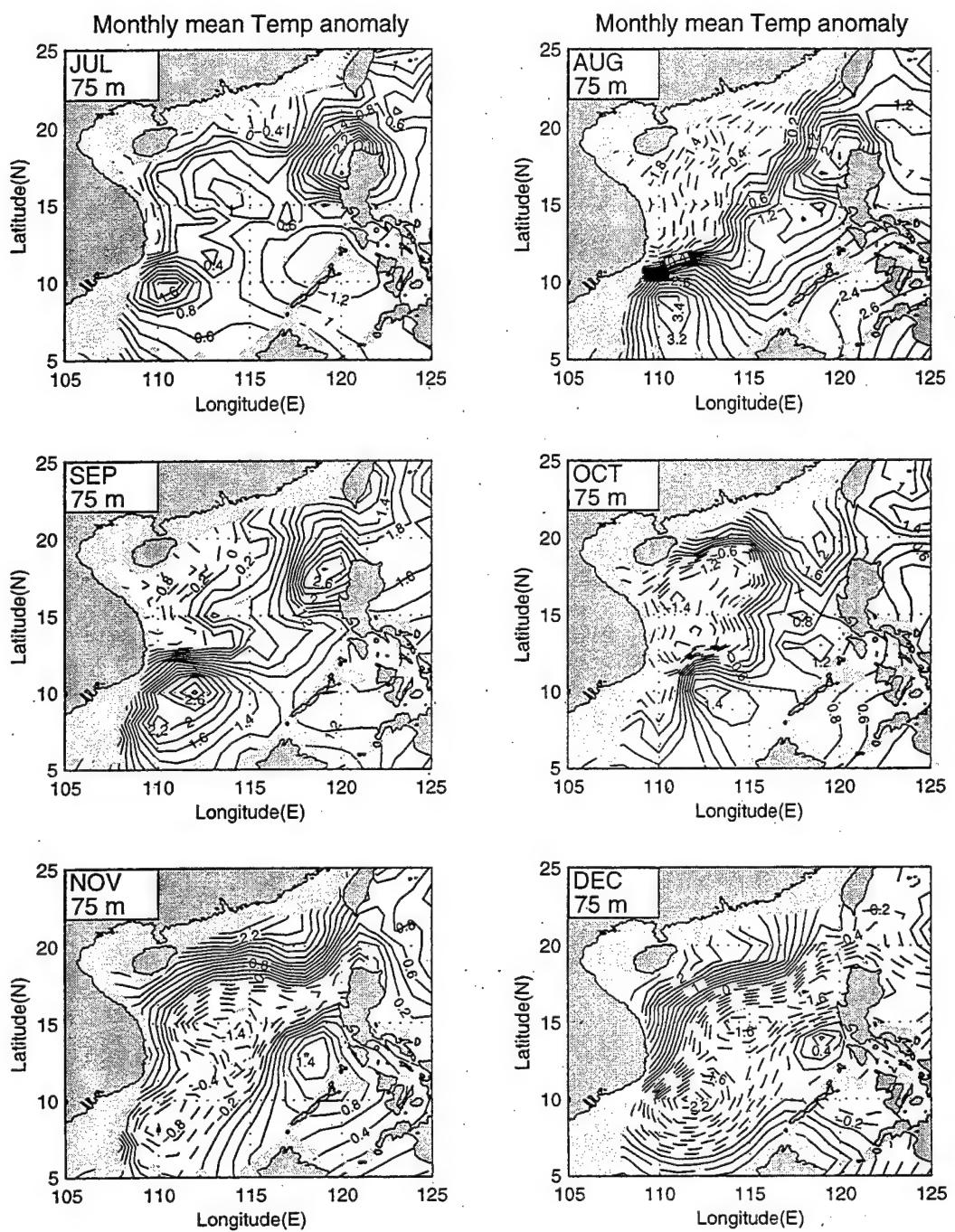


Figure 5.6b Monthly mean temperature anomalies (\tilde{T}) at 75 meters from July to December

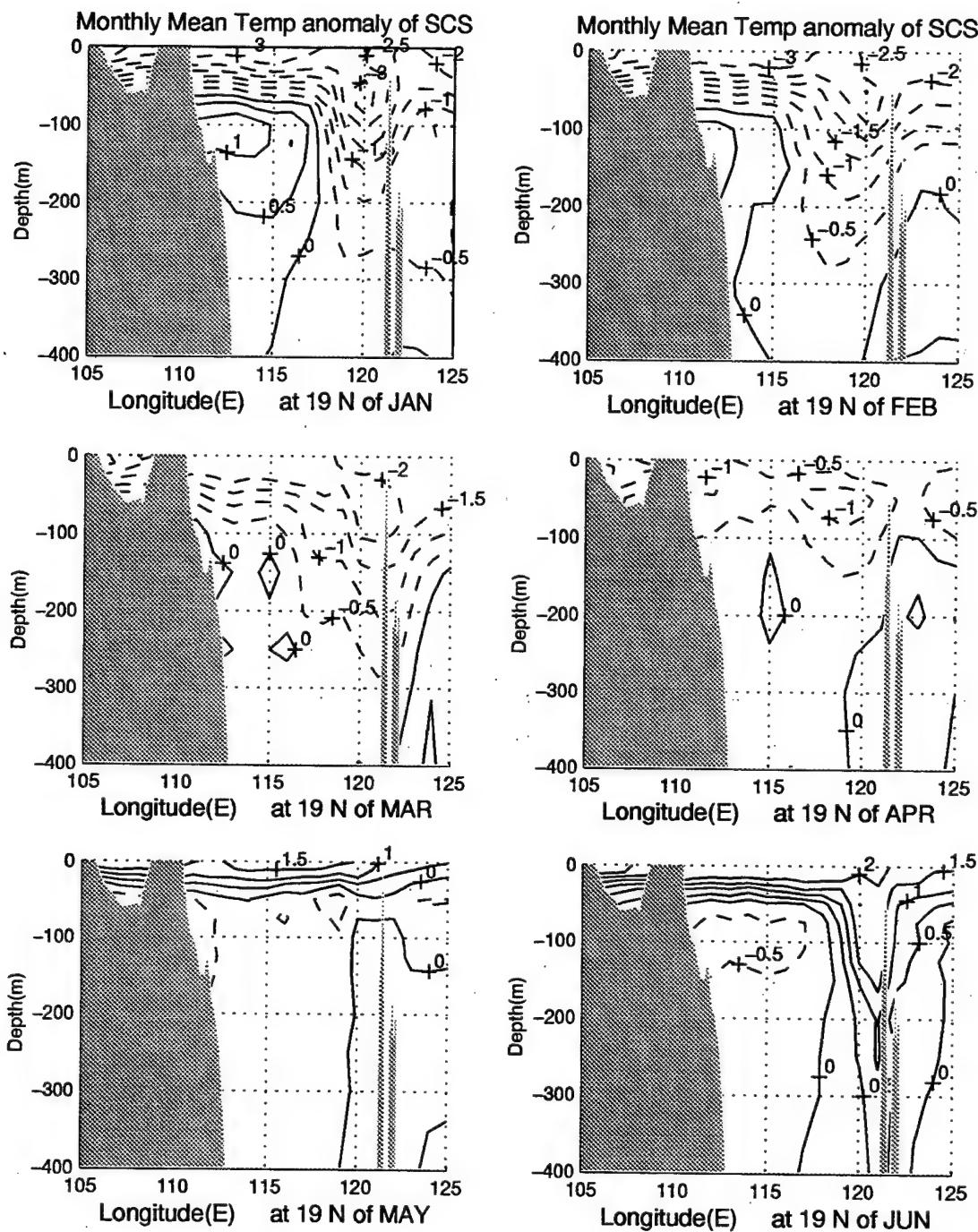


Figure 5.7a Zonal cross-section view of monthly mean temperature anomalies (\tilde{T}) at 19°N from January to June

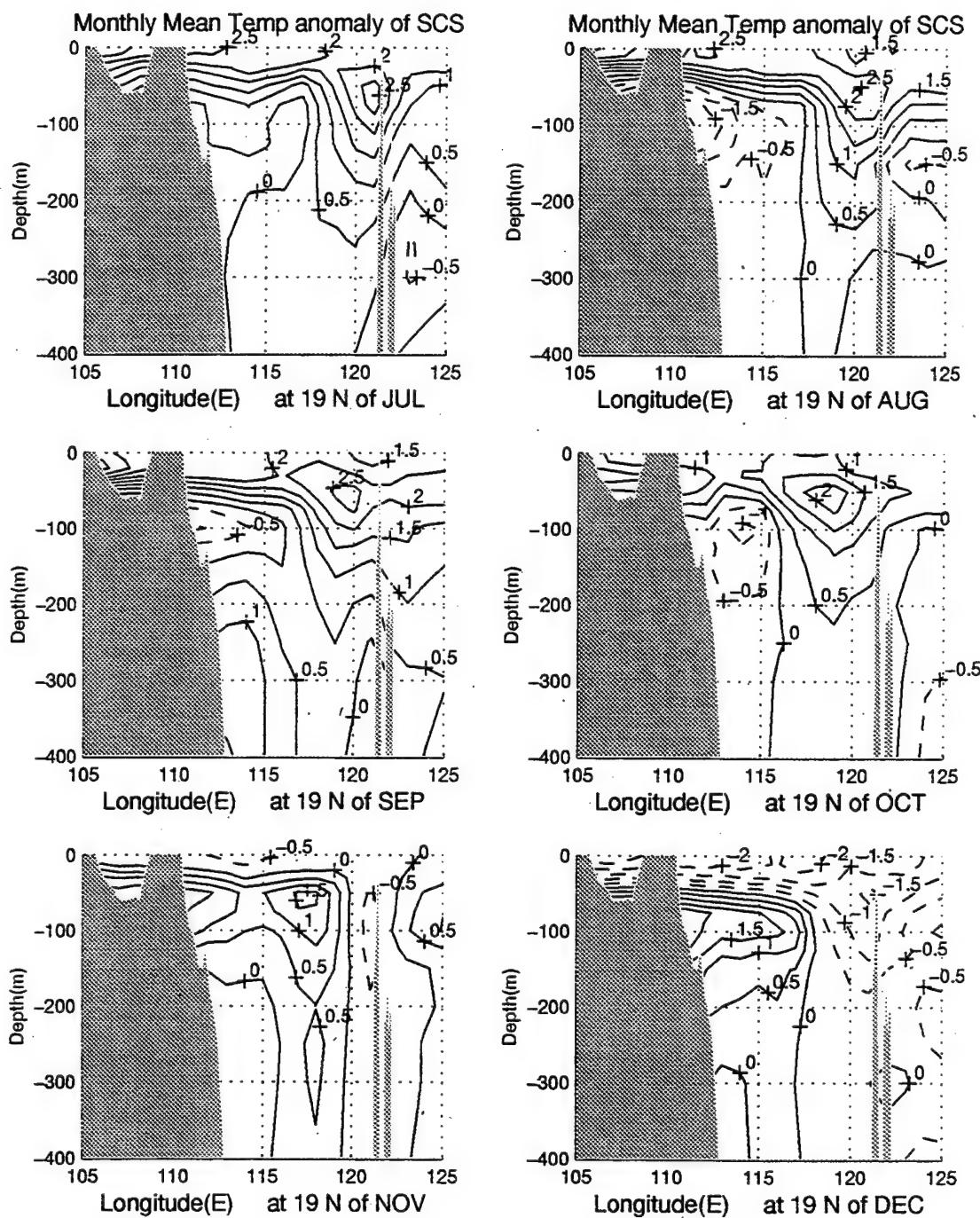


Figure 5.7b Zonal cross-section view of monthly mean temperature anomalies (\tilde{T}) at 19°N from July to December

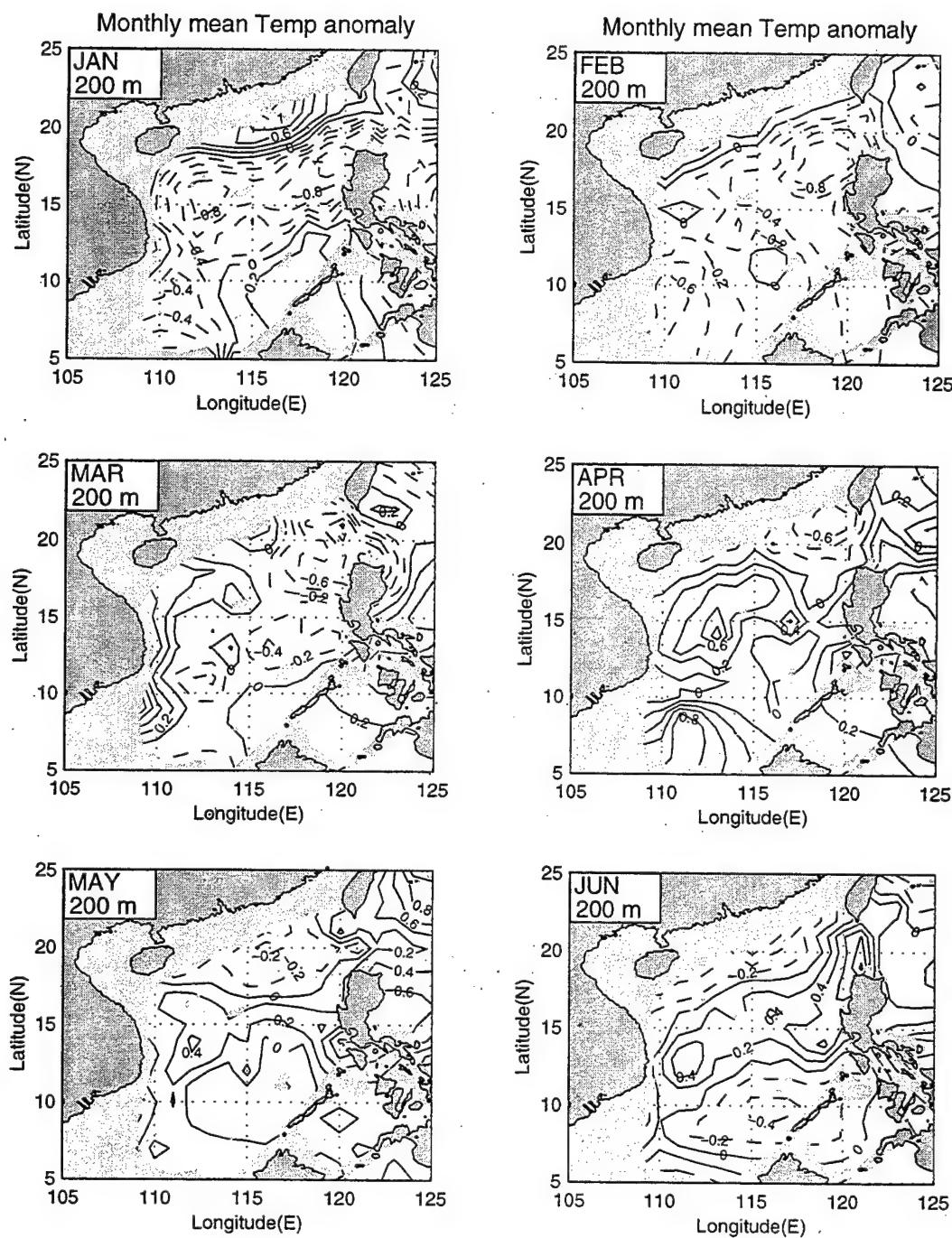


Figure 5.8a Monthly mean temperature anomalies (\tilde{T}) at 200 meters from January to June

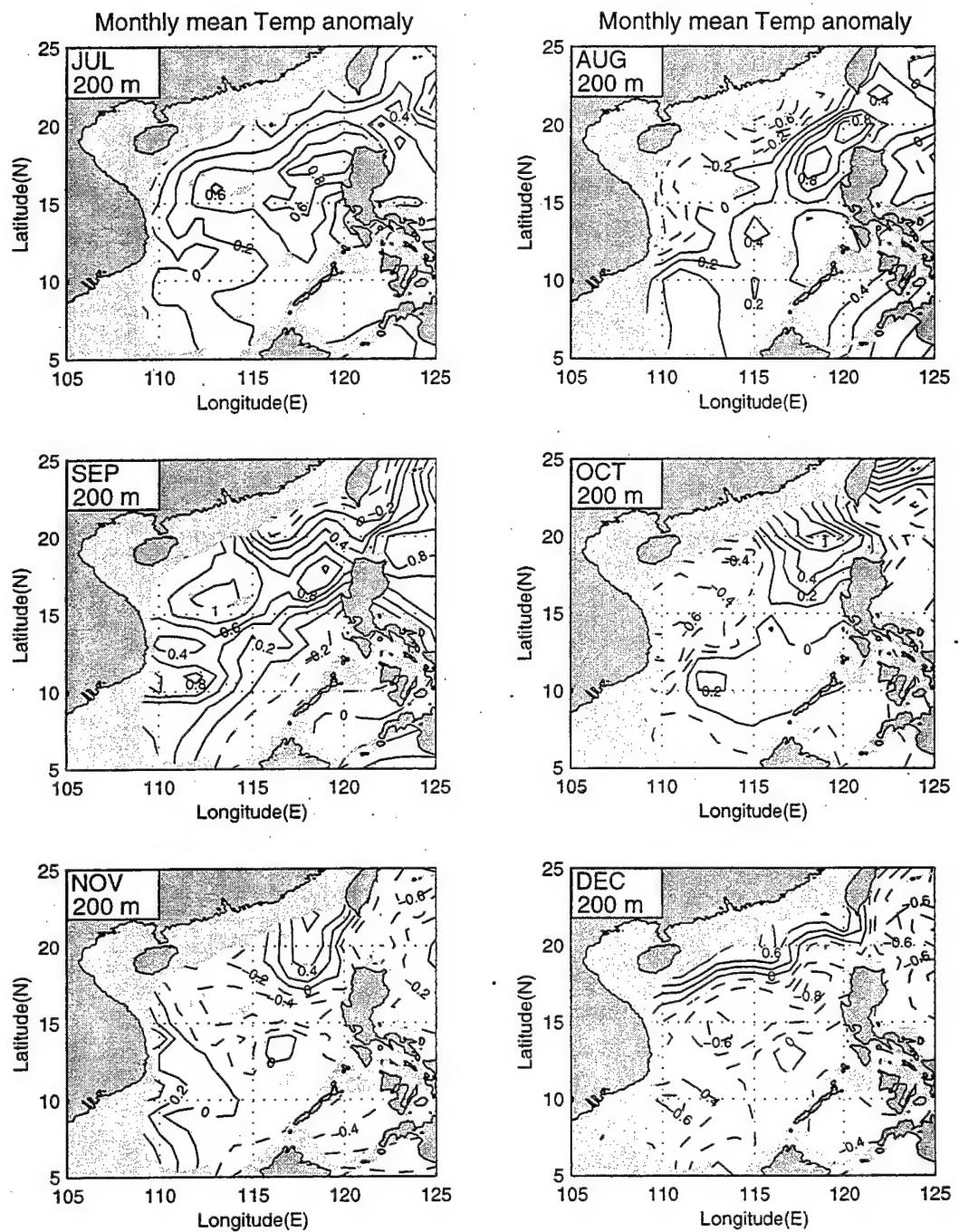
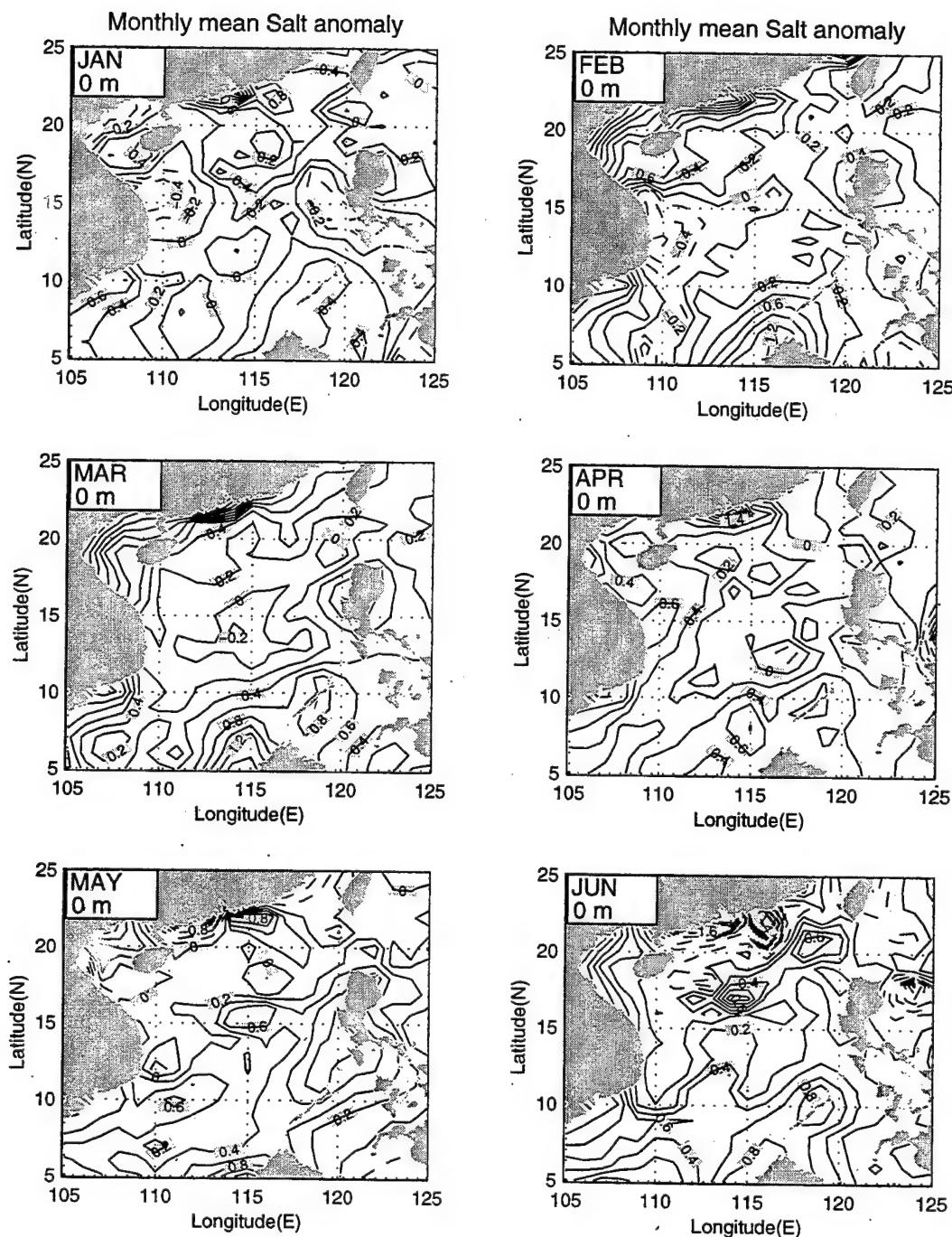


Figure 5.8b Monthly mean temperature anomalies (\tilde{T}) at 200 meters from July to December



**Figure 5.9a Monthly mean salinity anomalies (\tilde{S}) at surface
from January to June**

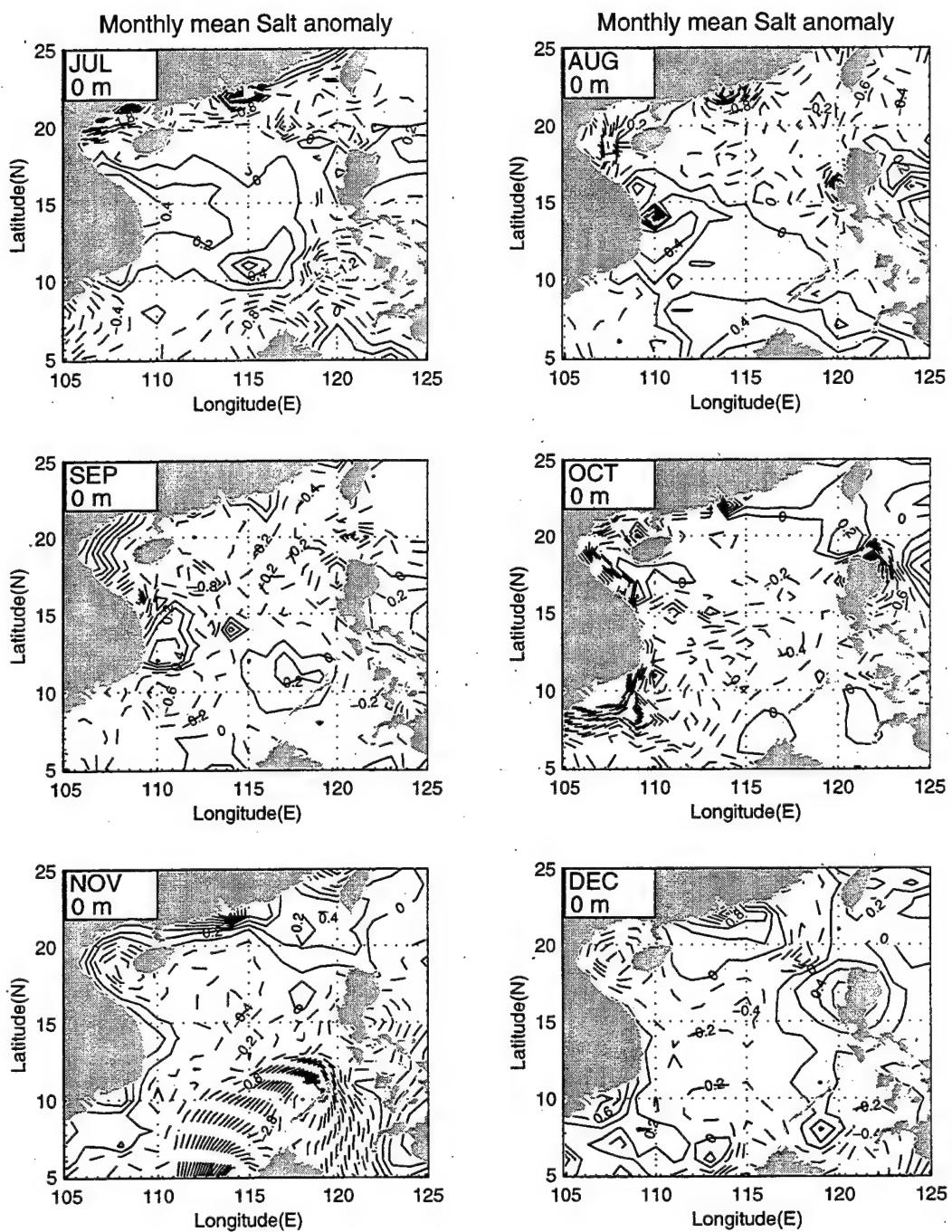


Figure 5.9b Monthly mean salinity anomalies (\bar{S}) at surface from July to December

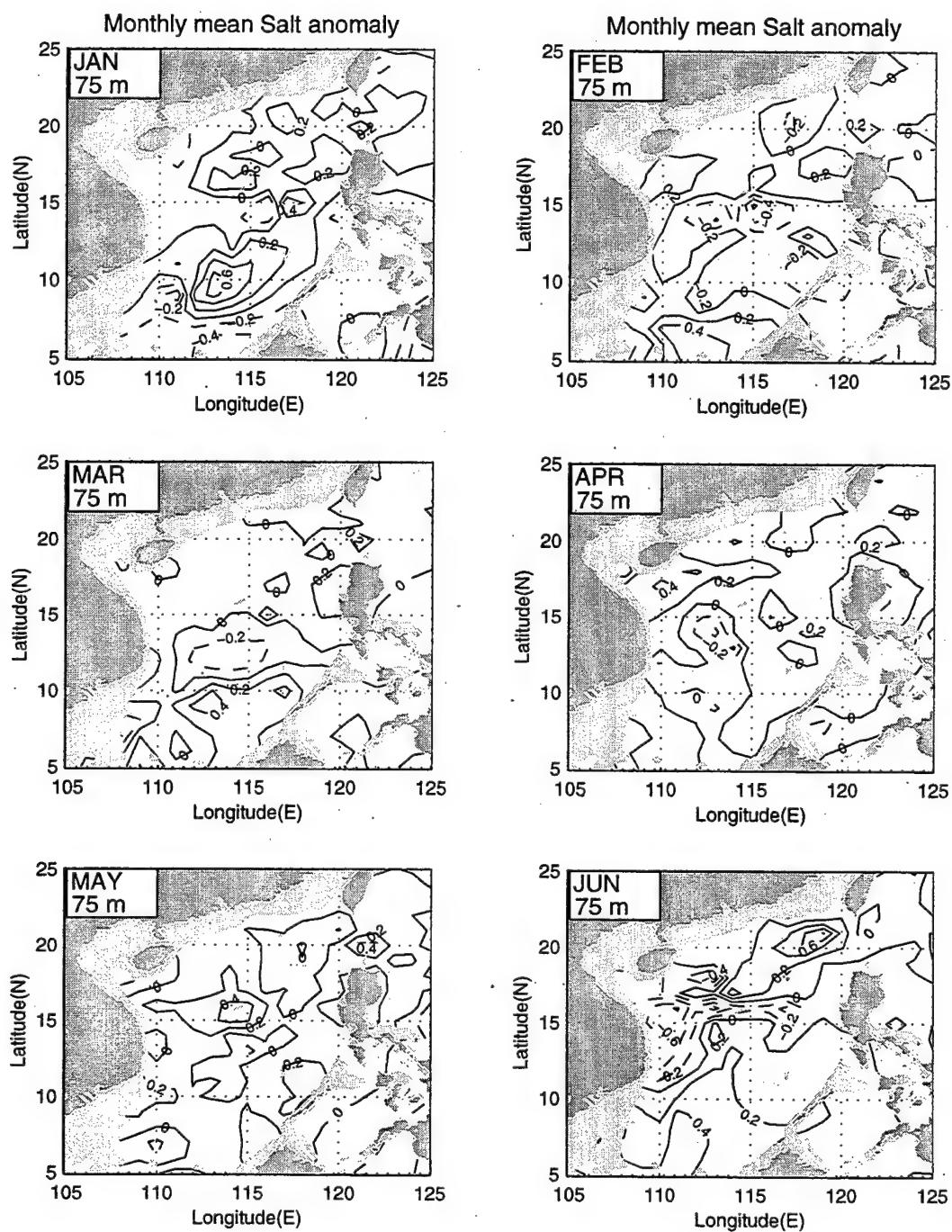


Figure 5.10a Monthly mean salinity anomalies (\tilde{S}) at 75 meters from January to June

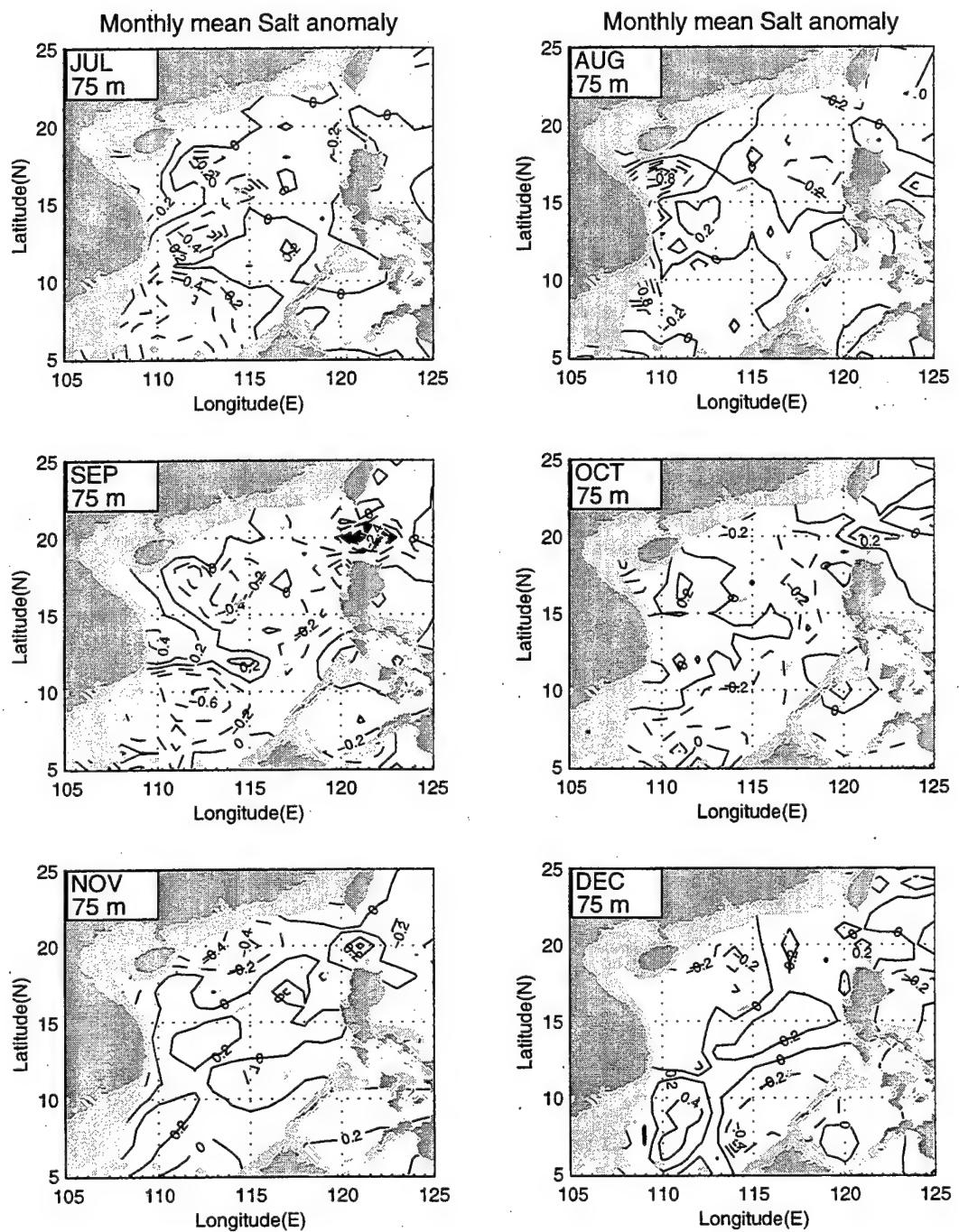


Figure 5.10b Monthly mean salinity anomalies (\bar{S}) at 75 meters from July to December

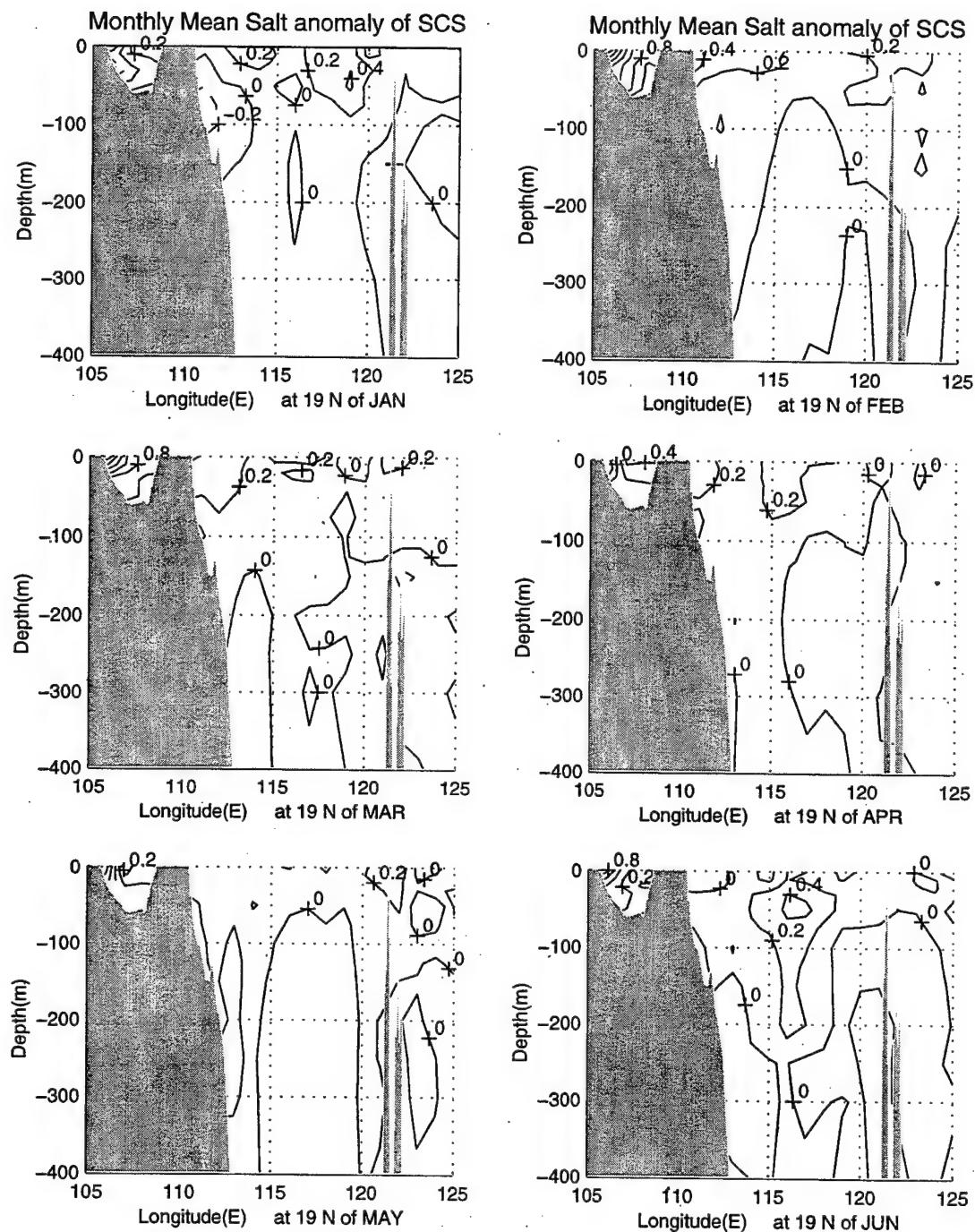


Figure 5.11a Zonal cross-section view of monthly mean salinity anomalies (\tilde{S}) at 19°N from January to June

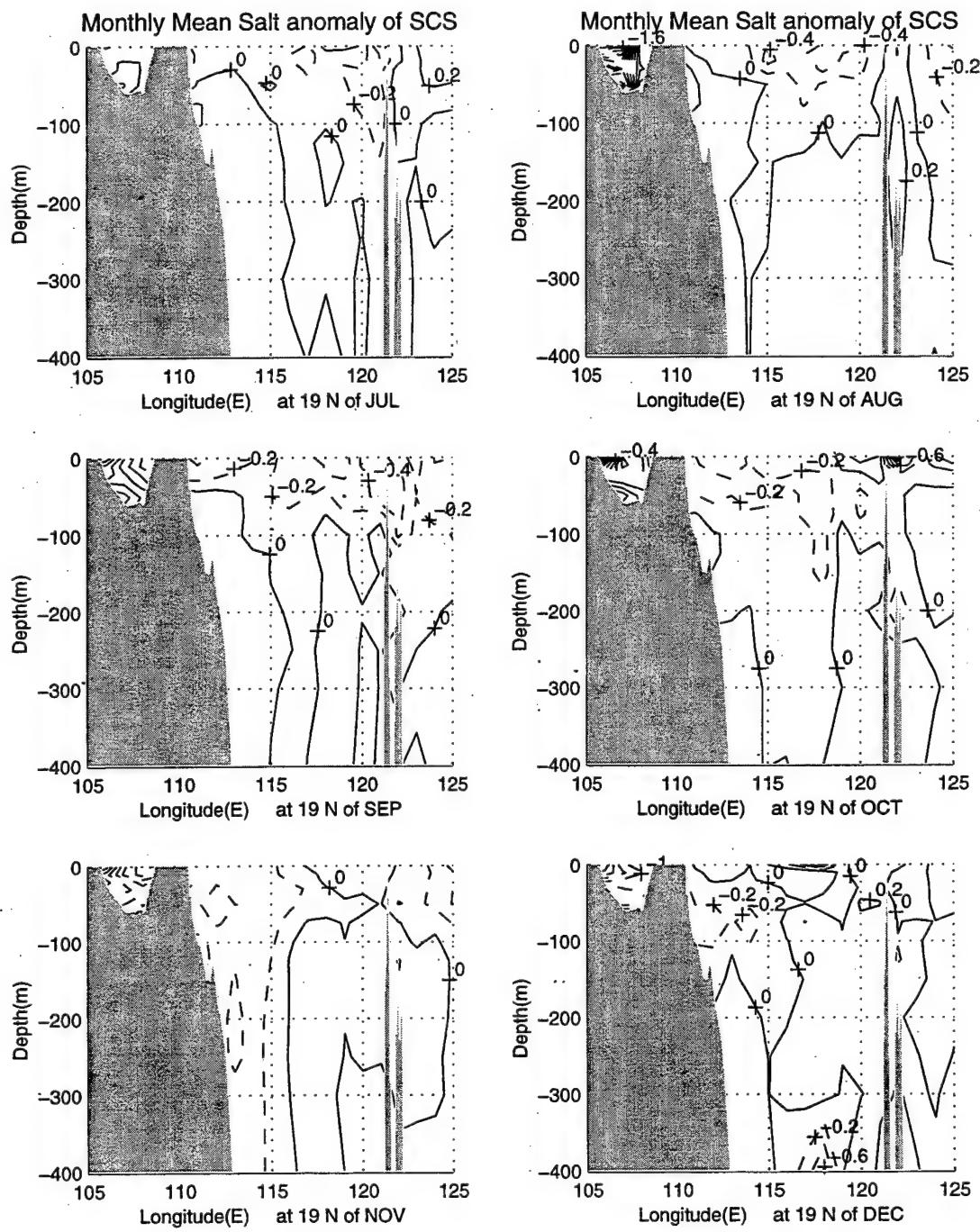


Figure 5.11b Zonal cross-section view of monthly mean salinity anomalies (\bar{S}) at 19°N from July to December

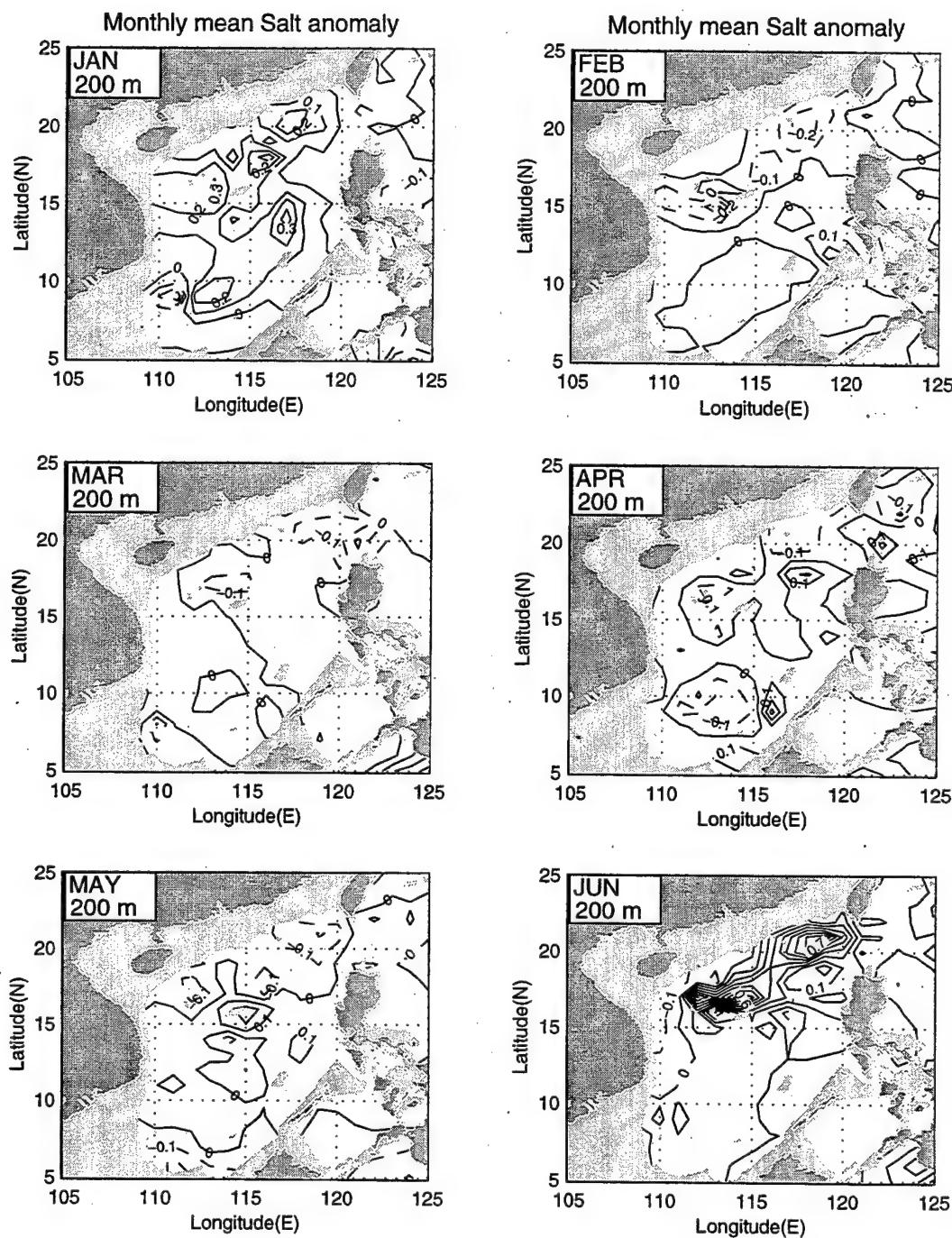


Figure 5.12a Monthly mean salinity anomalies (\tilde{S}) at 200 meters from January to June

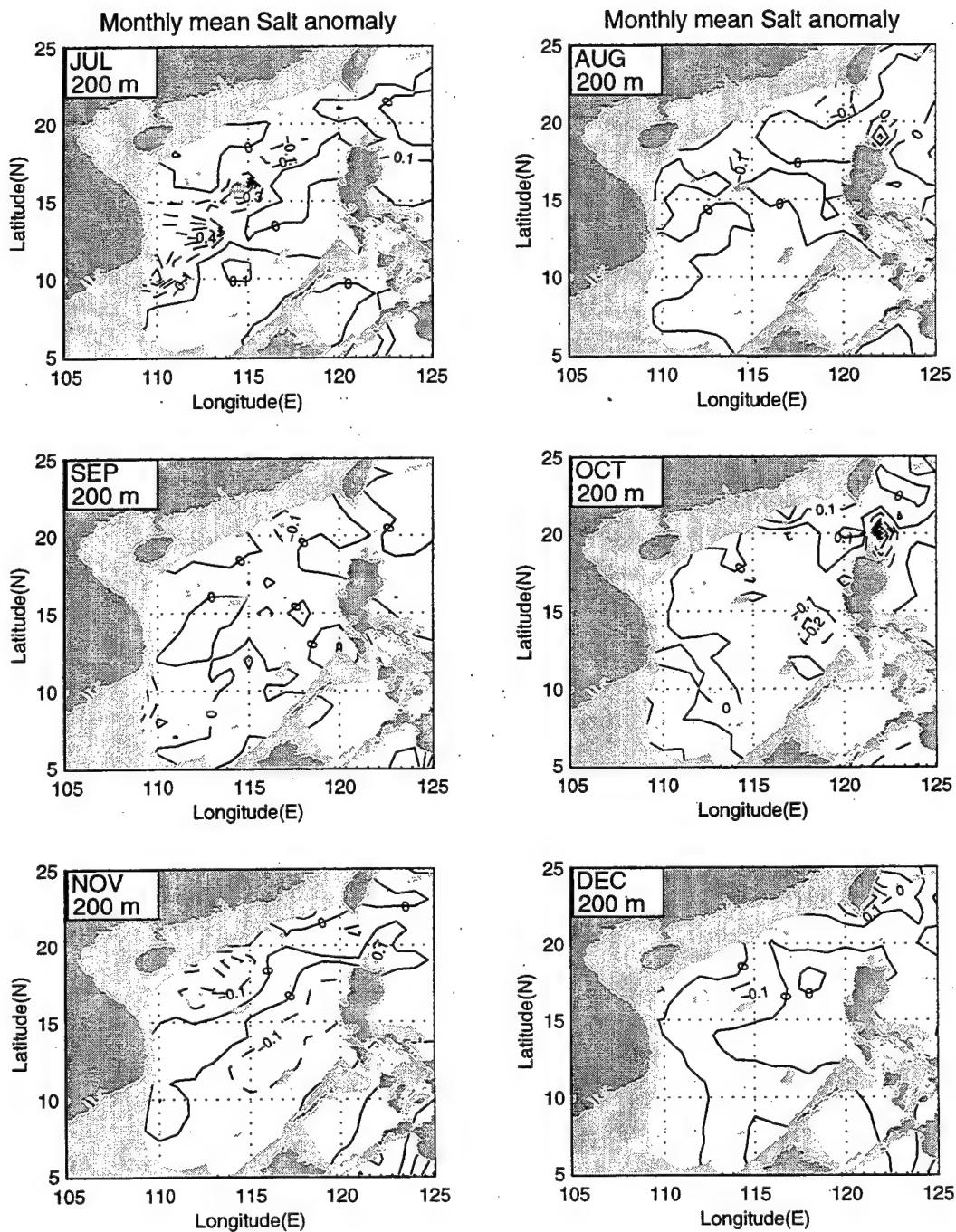


Figure 5.12b Monthly mean salinity anomalies (\tilde{S}) at 200 meters from July to December

VI. EMPIRICAL ORTHOGONAL FUNCTION (EOF) ANALYSIS

The empirical orthogonal function (EOF) analysis is a useful tool to describe the main mode of temporal and spatial variabilities. It is usually applied to the anomaly data relative to the climatological mean.

A. THERMAL VARIABILITY

The temperature anomaly field relative to the climatological annual mean field

$$\hat{T}(x_i, y_j, z_k, \tau_l, t_m) \equiv T(x_i, y_j, z_k, \tau_l, t_m) - \bar{\bar{T}}(x_i, y_j, z_k) \quad (13)$$

is re-arranged into a $N \times P$ matrix $\hat{T}(r_n, \tilde{t}_p)$, $n = 1, 2, \dots, N$; and $p = 1, 2, \dots, P$. Here $P = 204$ is the total number of time points used for computing the covariance matrix, that is, 17 years of monthly data sets; $N = 5733$, corresponds to the number of grids ($i = 1, 2, \dots, 21; j = 1, 2, \dots, 21; k = 1, 2, \dots, 13$). The non-seasonal thermal variability is investigated using the Empirical Orthogonal Function (EOF) analysis. This method separates the data sets into eigenmodes. Generally speaking, each mode has an associated variance, a dimensional spatial pattern, and a non-dimensional time series. For example, Lorenz (1965) used the eigenvectors of the covariance matrix associated with a sample data field to calculate the time series of coefficients or predictors for the statistical weather prediction. Chu et al. (1997a, b) used this method to investigate the non-seasonal variabilities of SST and surface wind stress. From our data $\hat{T}(r_n, \tilde{t}_p)$, a 5733×5733 spatial covariance matrix is calculated by

$$R = \begin{vmatrix} R_{11} & R_{12} & \dots & R_{1N} \\ R_{21} & R_{22} & \dots & R_{2N} \\ \dots & \dots & \dots & \dots \\ R_{N1} & R_{N2} & \dots & R_{NN} \end{vmatrix}, R_{nm} = \sqrt{\frac{1}{P} \sum_p \hat{T}(r_n, \tilde{t}_p) \hat{T}(r_m, \tilde{t}_p)}, N=5733, P=204 \quad (14)$$

where n and m ($1, 2, \dots, 5733$) denote the grid locations. The diagonal elements of the covariance matrix R_{mm} ($n=1, 2, \dots, N$) are the variance at location r_n . The off-diagonal elements are the covariance with spatial lag equal to the difference between the row and column indices. This symmetric matrix has its 5733 real eigenvalues λ_α , and eigenvectors $\Phi_\alpha(r_i)$ such that

$$\sum_{j=1}^N R_{ij} \Phi_\alpha(r_i) = \lambda_\alpha \Phi_\alpha(r_i), \quad i = 1, 2, \dots, N \quad (15)$$

The eigenvectors $\Phi_1, \Phi_2, \dots, \Phi_N$ are called Empirical Orthogonal Functions with the unit of $^{\circ}\text{C}$. Each Φ_α is a 5733-point ($21 \times 21 \times 13$) distribution of non-seasonal variation temperature anomaly pattern. The eigenvalues, λ_α ($\alpha=1, 2, \dots, N$), are all positive and the summation of them, $\sum \lambda_\alpha$, equal the total variance. Therefore, λ_α is considered as portion of total variance "explained" by the EOF Φ_α . It is convenient to label the eigenfunctions, Φ_α , so that the eigenvalues are in descending order, i.e., $\lambda_1 > \lambda_2 > \lambda_3 > \dots$

The data matrix $\hat{T}(r_n, \tilde{t}_p)$ is thus written approximately by

$$\hat{T}(x_i, y_j, z_k, \tau_l, t_m) \approx \sum_\alpha PC_\alpha(\tau_l, t_m) \Phi_\alpha(x_i, y_j, z_k) \quad (16)$$

where $PC_a(\tau, t_m)$ is the principal component representing the temporal variation of the associated spatial pattern described by the EOF mode, $\phi_a(x_i, y_j, z_k)$.

B. PRINCIPAL EOF MODES

The first six leading EOF modes are able to account for 64.1% of the total variance (Table 6.1). The first two leading modes, EOF1 and EOF2, explain 44.4% of the total variance. Each EOF mode is three-dimensional and normalized so that its total spatial variance is equal to unity. We may easily see the vertically coherent structure of each mode.

1. The EOF1 Mode

The EOF1 mode (Φ_1) shows frontal and multi-eddy structures. The frontal structure is evident in the northern SCS. Only positive values occur in the upper layer (above 75 m depth) and both positive and negative values appear at the other depths (Figure 6.1a,b). However, we cannot use these positive/negative values of Φ_1 to identify the warm or cool anomaly of the individual eddy. This is because the temperature anomaly, due to the EOF1 pattern, is the product of PC_1 and Φ_1 .

a. *Western Boundary Current and Frontal Structures*

From the surface to 30 m depth, a bi-frontal structure (northeast-to-southwest oriented isolines) is the major thermal feature in the northern SCS (north of 12° N): a strong coastal front along the China coast, and a relatively weak and wide front across the SCS basin from the Vietnam coast to the Luzon island between 12°-17°N. The two fronts change their strengths synchronously, since the values of Φ_1 are positive for the two fronts. The bi-frontal structure weakens with the depth and disappears at 50 m depth. The front

reoccurs from 75 m depth and continues to be seen down to 300 m depth. Below 75 m depth in the northern SCS, Φ_1 shows a northeast-to-southwest oriented single front structure aligning to the China coast. The values of Φ_1 across the front change signs from negative near the China coast to positive in the middle of the northern SCS, indicating the out-of-phase variability of the front near the China coast and the deep basin.

Furthermore, we may notice that the values of Φ_1 change signs from the top layer (0-30 m) to the lower layer (100-300 m) near the western boundary. This implies a strong baroclinicity of the western boundary currents with the opposite directions at the top layer and the lower layer.

b. Southern SCS Multi-Eddy Structure

In the southern SCS (south of 12° N) from the surface to 30 m depth, the EOF1 shows a dipole structure (dual eddies) with a high center (0.3°C) near the mouth of the Mekong River, and a low center (< 0.14°C) in the west of the Borneo-Palawan islands (WBP). This dipole structure is still quite evident from 30 m to 75 m depths. Below 75 m depth, the western eddy, near the Mekong River mouth, is much stronger than the eastern eddy.

At 30 m depth, an eddy (>0.4°C) appears in the northern SCS. This eddy slants towards the east (the Luzon Strait) with depth and becomes very strong in the layers between 75 m and 150 m. Below 150 m depth, this eddy reduces its strength.

c. Kuroshio Intrusion

In the northern SCS, the isolines of Φ_1 intersect the cross-section of the Luzon Strait with the patterns showing Kuroshio intrusion/SCS outflow through the Luzon Strait. This pattern indicates a weak Kuroshio intrusion/SCS outflow in the upper layer above 50 m depth, becoming stronger below 50 m depth and reaching maximum strength in the layer between 100m and 150 m depths.

2. The Second EOF Mode

Similar to the first EOF mode, the second EOF mode (Φ_2) has only positive values in the upper layer from the surface to 50 m depth and has both positive and negative values appearing on the other depths. The negative Φ_2 area is limited in the southeast corner of the SCS with small absolute values (Figure 6.2a,b). This means that the overall SCS basin thermal variability is either warming or cooling. We may call this mode the warming/cooling mode. In addition, the isolines of Φ_2 at all the depths near the Luzon Strait are almost parallel to the cross-section of the strait. This indicates that the second EOF (warming/cooling) mode is not caused by the Kuroshio intrusion/SCS outflow. It might be related to the atmospheric forcing. Furthermore, the second EOF mode also shows coastal front and multi-eddy structures.

a. Coastal Front Structure

In the north SCS, a coastal front structure can be identified on the continental shelf near the China coast (Figure 6.2a). As the depth increases, this front structure extends to the southern SCS and occupies the western part of the SCS from 100m to 300 m depths

(Figure 6.2b). This strong gradient of Φ_2 may be caused by the western boundary current.

b. Northern SCS Multi-Eddy Structure

The EOF2 clearly shows a multi-eddy structure in the northern SCS sub-surface layer between 50 m and 125 m. At 50 m depth, a strong north-south dipole structure (dual eddies) with a high center (0.2°C) in the west of the Luzon Strait (18°-22°N, 115°-119° E), and a low center (< 0.04°C) in the central SCS (12°-15°N, 110°-116° E). This dipole structure strengthens at 75 m depth and weakens as depth increases from 75 m. Below 125 m depth, the northern SCS multi-eddy structure disappears.

EOF	Variance(%)	Accumulative Variance(%)
1	26.7	26.7
2	17.7	44.4
3	7.1	51.5
4	5.9	57.4
5	3.7	61.1
6	3.0	64.1

Table 6.1 Variances of the First Six Leading EOFs

C. TEMPORAL VARIABILITIES

Each principal component can be treated as the projection of the temperature anomaly through a 'filter' of corresponding EOF mode (Chu et al., 1997).

1. First Principal Component

The first principal component, $PC_1(\tau_l, t_m)$, is the time series (1968-1984) of the EOF1 amplitudes and shows basically a seasonal variation. During the winter (summer) monsoon season, $PC_1(\tilde{t}_p)$ has negative (positive) values (Figure 6.3), which indicate that the temperature anomaly, due to this mode, has the opposite (same) sign with respect to EOF1. Since the first EOF mode Φ_1 is always positive throughout the upper layer (0 - 50 m) of the whole SCS (Figure 6.1), positive (negative) values of $PC_1(\tilde{t}_p)$ during summer (winter) monsoon season correspond to warm (cool) anomalies. This shows the regular seasonal variation.

An interesting feature of the first EOF mode Φ_1 is its negative value near the western boundary in the sub-surface layer (75 - 300 m). Since $PC_1(\tilde{t}_p)$ has negative (positive) values during winter (summer) monsoon season, the thermal variability of the western boundary is out-of-phase with respect to the seasonal variability, that is, warm (cool) anomaly in the winter (summer) monsoon season. The warm anomaly in the winter could be related to the Kuroshio intrusion.

Accordingly, the seasonal variation represented by $PC_1(\tilde{t}_p)$ is not a pure sinusoidal. The summer had a larger variability in the 1980's than in the early 1970's. However, the winter had a larger variability during 1968-1972 than the rest of the periods.

2. Second Principal Component

The second principal component, $PC_2(\tilde{t}_p)$, is the time series (1968-1984) of the second EOF (warming/cooling) mode amplitudes and shows interannual variabilities with periods of two to five years (Figure 6.3). The positive (negative) values of $PC_2(\tilde{t}_p)$ indicate the SCS warming (cooling). The maximum value of \tilde{t}_p is 0.3°C near the China coast at the surface and a high center with isoline of 0.2°C in the west of Luzon Strait at depths between 50 m and 125 m (Figure 6.2).

The values of $PC_2(\tilde{t}_p)$ vary between 10 and -10. Its maximum value (10) appeared in August 1969 and September 1976, which indicates the strong SCS warm anomaly with the maximum warming of 3°C [$0.3^{\circ}\text{C} \times 10$] at the surface near the China coast, and the occurrence of a sub-surface (50-125 m) warm eddy with the anomaly of 2°C [$0.2^{\circ}\text{C} \times 10$] in the west of the Luzon Strait. Its minimum value (-10) appeared in October 1974, which indicates the strong SCS cool anomaly with the maximum cooling of -3°C [$0.3^{\circ}\text{C} \times (-10)$] at the surface near the China coast, and the occurrence of a sub-surface (50-125 m) cool eddy with the anomaly of -2°C [$0.2^{\circ}\text{C} \times (-10)$] in the west of the Luzon Strait.

We found the following criterions in evident warm/cool anomaly occurrence with the maximum temperature anomaly exceeding 1.5°C . When $PC_2(\tilde{t}_p) > 5$, the SCS has an evident warming (maximum 1.5°C) and a warm eddy occurs at the west of the Luzon Strait in the sub-surface with the warm anomaly of 1°C . On the other hand, $PC_2(\tilde{t}_p) < 5$, the

SCS has an evident cooling (maximum above 1.5°C) and a cool eddy occurs at the west of Luzon Strait in the sub-surface with the cool anomaly of -1°C.

The strong anomaly periods (maximum above 3°C) and evident periods (maximum above 1.5°C) are listed in Table 6.2. We may find that the SCS warm anomaly generally appeared during the period of 1968-1972. After 1972, the cool anomaly occurred more often, except in September of 1976.

Anomaly Period	Maximum Anomaly Above 3°C	Maximum Anomaly Above 1.5°C
SCS Warming	Aug. 1969 Sep. 1976	Sep. 1968, Jan. Feb. May Jul. Aug. 1969 Nov. 1969 Jun. 1970 Oct. Dec. 1971 May Jul. Sep. Nov. 1972 Sep. 1976 Jul. 1977
SCS Cooling	Oct. 1974,	Oct. 1974 Jan. 1976 Feb.- Mar. 1977 Feb. 1980 Apr. 1983

Table 6.2 SCS warm/cool anomaly periods

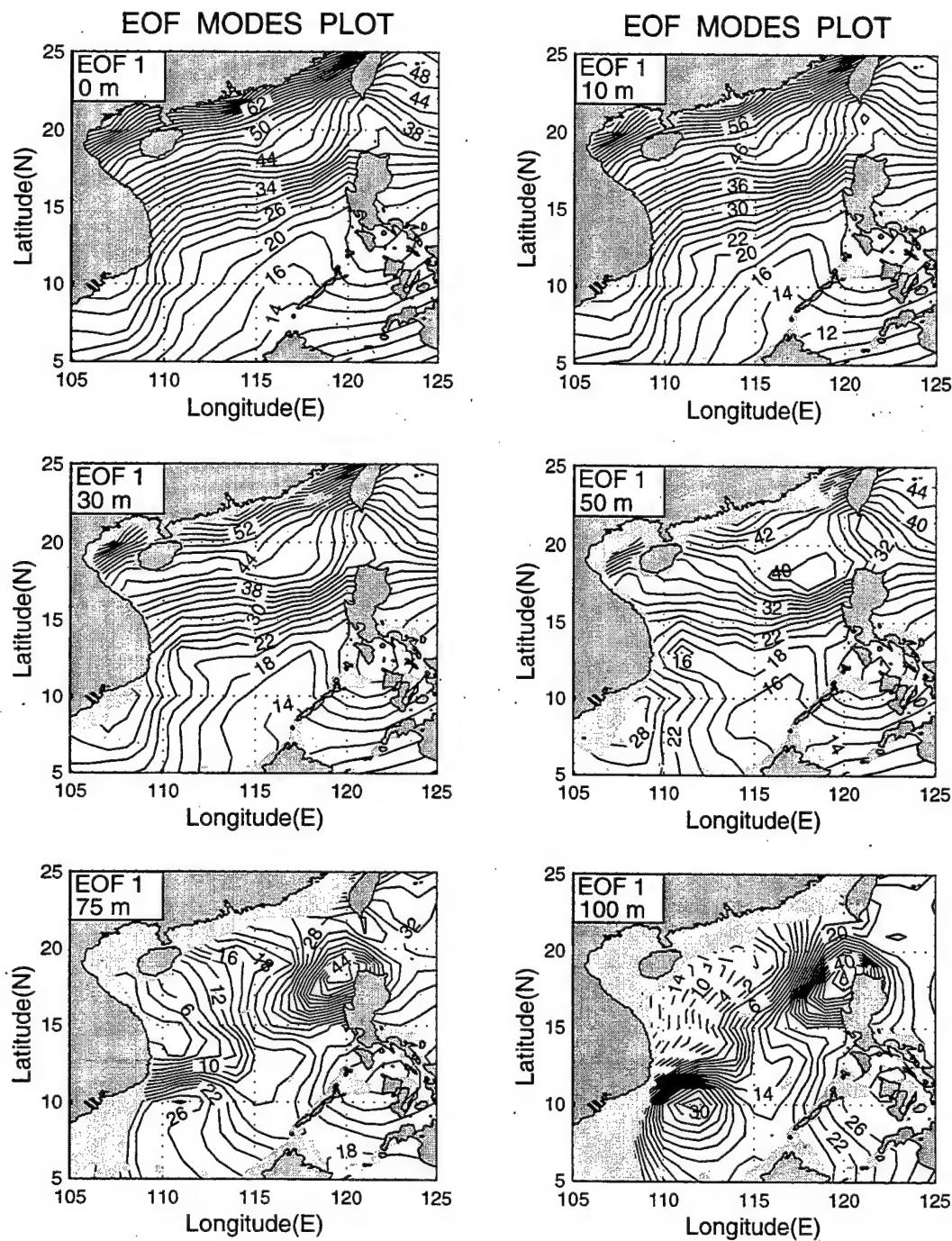


Figure 6.1a EOF 1 Temperature anomalies (Unit 0.01°C)

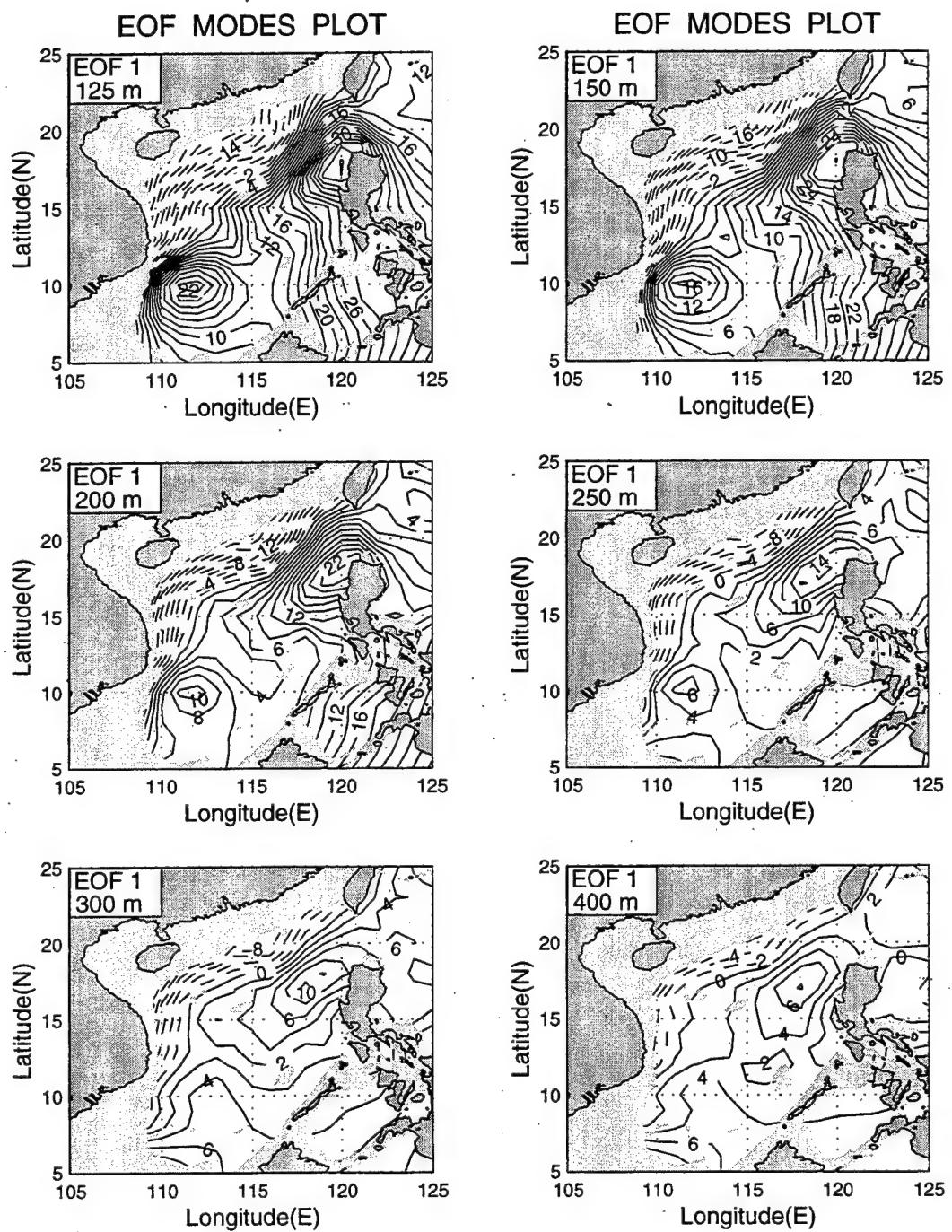


Figure 6.1b EOF 1 Temperature anomalies (Unit 0.01°C)

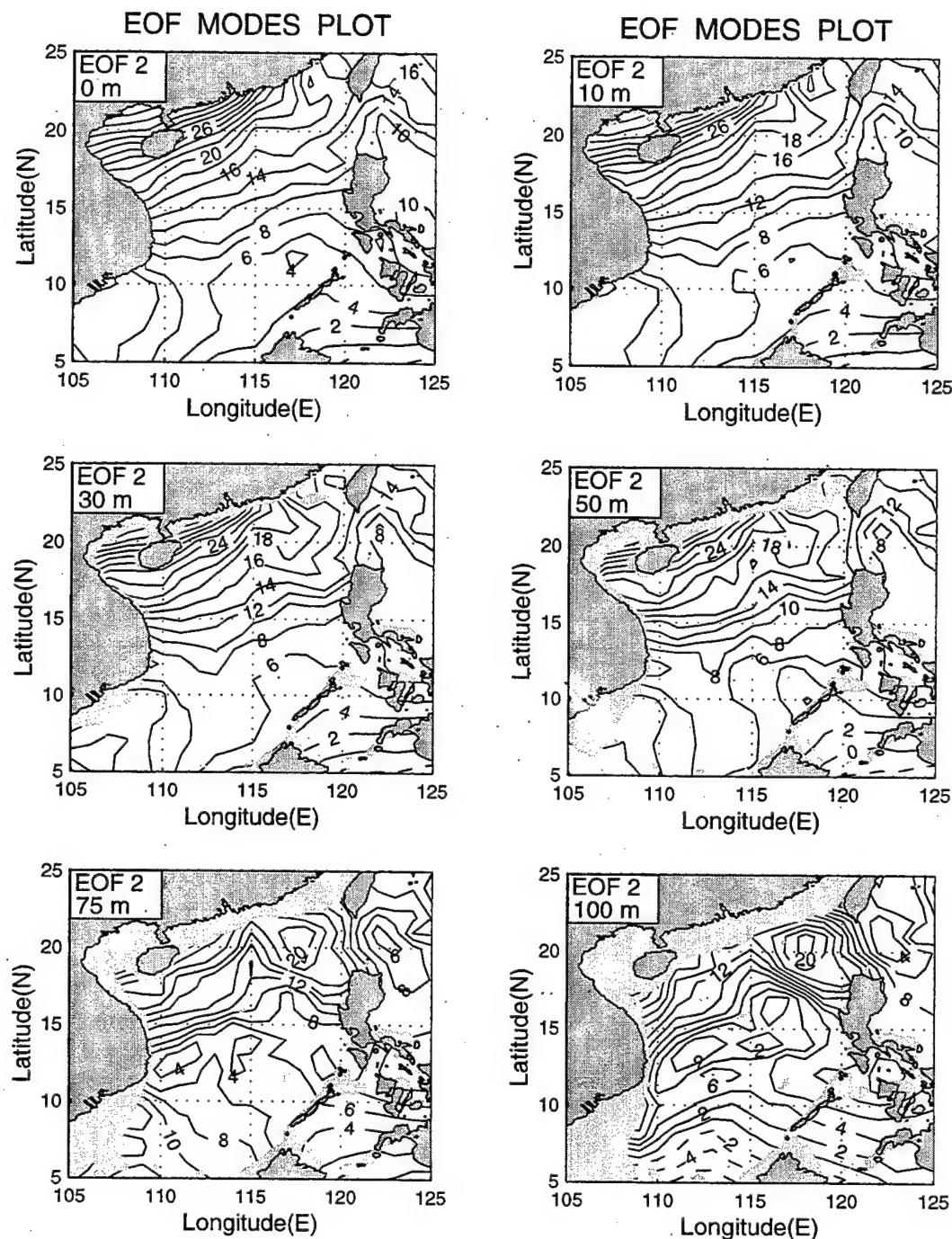


Figure 6.2a EOF 2 Temperature anomalies (Unit 0.01°C)

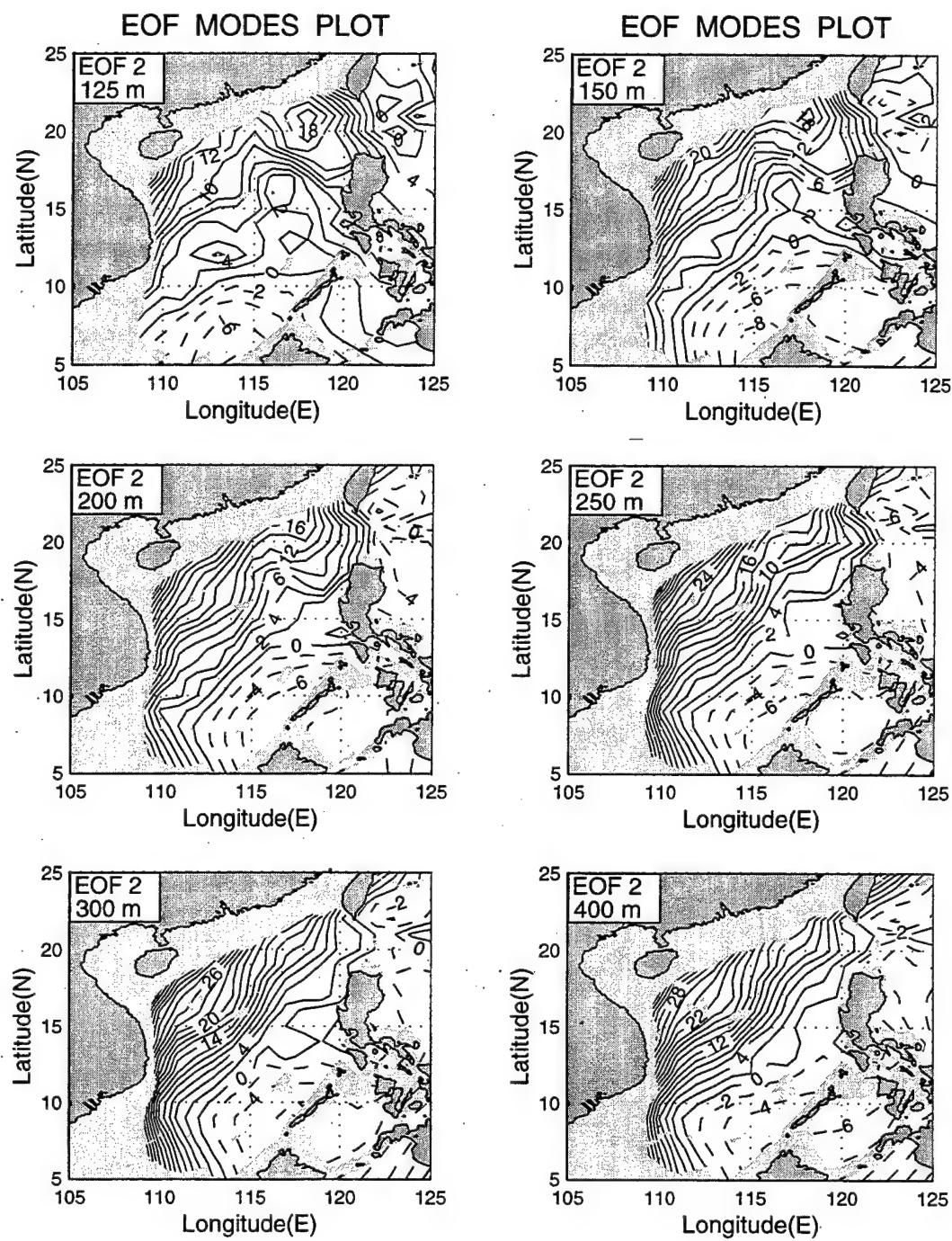


Figure 6.2b EOF 2 Temperature anomalies (Unit 0.01°C)

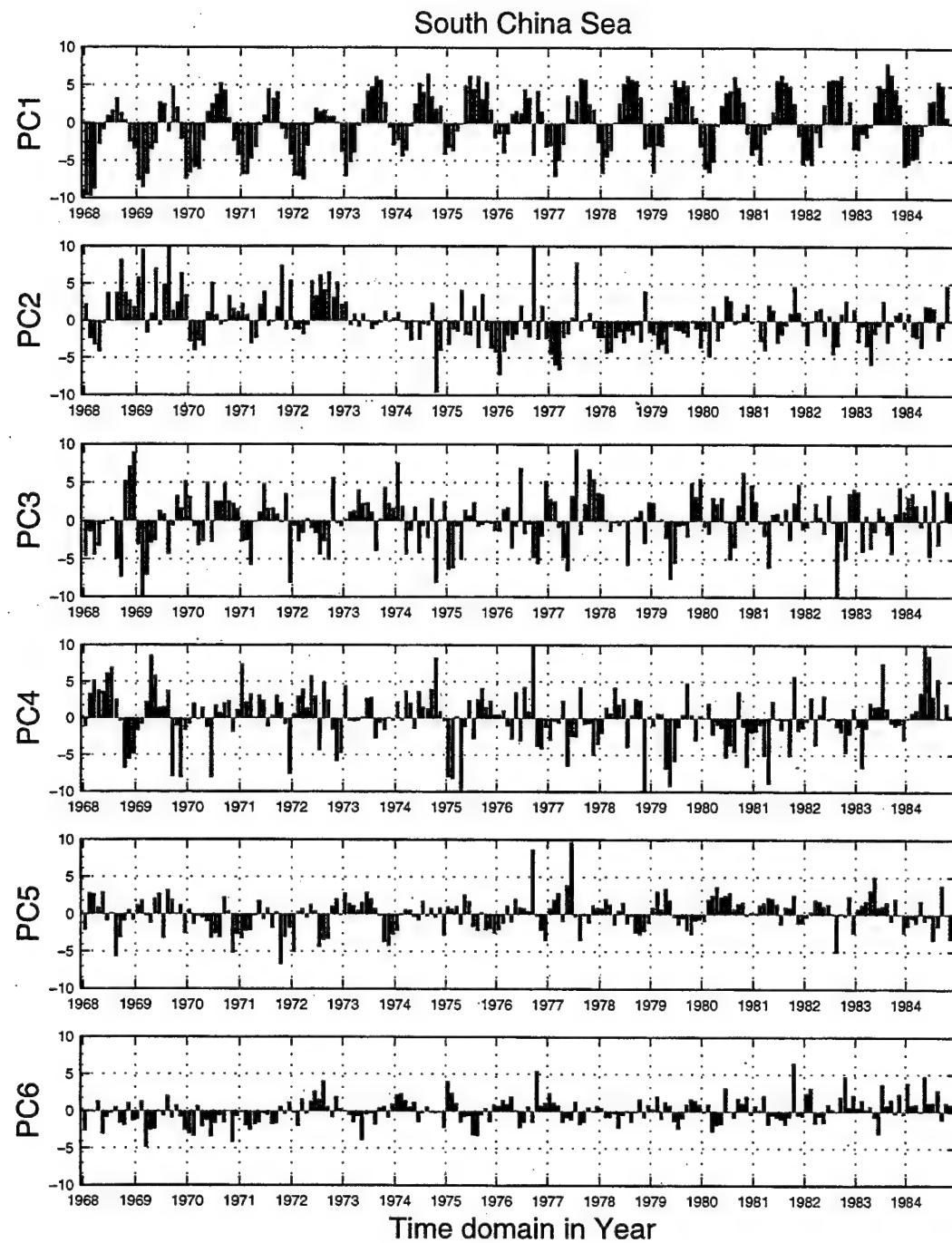


Figure 6.3 The first six principal components (PC) for 1968-1984

VII. THE SOUTH CHINA SEA CIRCULATION

A. GEOSTROPHIC VELOCITY INVERTED FROM DENSITY FIELD

The thermal wind relation is often employed to calculate geostrophic velocity from hydrographic data

$$u = u_o + \frac{g}{f\rho_0} \int_{z_o}^z \frac{\partial \hat{\rho}}{\partial y} dz' \quad (17)$$

$$v = v_o - \frac{g}{f\rho_0} \int_{z_o}^z \frac{\partial \hat{\rho}}{\partial x} dz' \quad (18)$$

where (u, v) and (u_o, v_o) are the geostrophic velocity at any depth z and at a reference depth z_o , $\hat{\rho}$ is the in-situ water density, ρ_o is the characteristic value of the density, $f=2\Omega\sin\lambda$ is the Coriolis parameter, where Ω is the earth's rotation rate and λ is the latitude. The hydrographic data determine the geostrophic vertical shear. The reference velocity (u_o, v_o) can be determined by several inverse techniques, such as the β -spiral method [Stommel and Schott, 1977; Schott and Stommel, 1978], the box inverse method [Wunsch, 1978], and the Bernoulli method [Killworth, 1986]. Wunsch [1994] proposed a generalized β -spiral and geostrophic balance inverse method based on a nonlinear optimization on Needler's P equation [Needler, 1967]. Davis [1978] pointed out that the β -spiral method and the box inverse method, regardless of appearances, are based on the same dynamical assumptions, and the existence of the β -spiral thus becomes a required condition for these inverse

methods.

Non-geostrophic inverse methods were also developed. Bogden et al. [1993] estimated the time-averaged velocity field in the North Atlantic from observations of density, wind stress and bottom topography based on the assumption of minimum mixing of potential density at mid-depth. Tziperman et al. [1992] applied the adjoint method to investigate the steady-state oceanic general circulation using a realistic numerical oceanic general circulation model and hydrographic data.

Recently, Chu [1995] and Chu et al. [1998a] proposed a simple P-vector inverse method to obtain the absolute velocity from hydrographic data. A velocity vector is represented into the product of a unit vector (P-vector) and a scalar,

$$\mathbf{V} = \mathbf{r}(x, y, z) \mathbf{P}. \quad (19)$$

The inversion of \mathbf{V} is fulfilled by two steps: (1) determination of the unit vector \mathbf{P} , and (2) determination of the scalar $r(x, y, z)$. Since the geostrophic flow is along both the isopycnal and the iso-potential vorticity surfaces, the velocity \mathbf{V} is parallel to $\nabla q \times \nabla \rho$. Here, ρ is the potential density, and

$$q = f \partial \rho / \partial z \quad (20)$$

is the potential vorticity. If the ρ surface is not parallel to the q surface, the unit vector \mathbf{P} can be defined by [Chu, 1995]

$$\mathbf{P} = \frac{\nabla \rho \times \nabla q}{|\nabla \rho \times \nabla q|} \quad (21)$$

Applying the thermal wind relation at two different depths z_k and z_m , as shown in Figure 7.1, a set of algebraic equations for determining the parameter r is obtained

$$\begin{aligned} r^{(k)} P_x^{(k)} - r^{(m)} P_x^{(m)} &= \Delta u_{km} \\ r^{(k)} P_y^{(k)} - r^{(m)} P_y^{(m)} &= \Delta v_{km} \end{aligned} \quad (22)$$

which are two linear algebraic equations for $r^{(k)}$ and $r^{(m)}$ [$r^{(i)} = r(x, y, z_i)$]. Here

$$(\Delta u_{km}, \Delta v_{km}) = \frac{g}{f \rho_o} \int_{z_m}^{z_k} \left(\frac{\partial \hat{\rho}}{\partial y}, -\frac{\partial \hat{\rho}}{\partial x} \right) dz' \quad (23)$$

where $\hat{\rho}$ is the in-situ density.

Chu et al. [1998b] shows the advantages of using the P-vector method, namely, the easy identification of the two necessary conditions for the β -spiral inverse method: (1) intersection between the ρ - and q -surfaces (existence of the vector P), and (2) the β turning (turning of the vector P).

For water columns satisfying the two necessary conditions, equation (22) may be used to compute $r^{(k)}$ for the level z_k . There are $(N-1)$ sets ($m = 1, 2, k-1, k+1, \dots, N$) of equations (22) for calculating $r^{(k)}$. Here, N is the total number of vertical levels of the water column. All of the $(N-1)$ sets of equations are compatible under the thermal wind constraint and should provide the same solution. However, due to errors in measurements (instrumentation errors) and computations (truncation errors), the parameters $r^{(k)}$ may vary with m . A least square error algorithm [Chu et al., 1998b] is used to minimize the error. For further details and validation of the algorithm presented, see Chu et al. [1998a].

B. SEASONAL VARIATION OF SCS CIRCULATION

1. General Description

The most obvious features of the inverted summer and winter SCS circulation are flow separation, basin gyres, and mesoscale eddies. Hinted in Wyrtki's (1961) depiction but more explicit in our computation, are the upper level (10 m depth) west-to-east cross-basin currents, which are almost parallel to 16°N latitude from February to July. The inverted monthly SCS circulation agrees quite well with earlier observational study (Wyrtki, 1961). As the commonly used inverse methods, the P-vector inverted western boundary currents are somewhat small. This could be caused by the neglect of relative vorticity in the potential vorticity calculation [see (21)].

2. Surface Circulation

During the winter monsoon period (November to March), the winter Asian high pressure system brings strong winds from the northeast (Figure 2.4) and the SCS surface circulation pattern is cyclonic (Figure 2.5). At the surface inflow from the Luzon Strait (the Kuroshio intrusion) turns southwest along the Asian continental shelf, then south along the coast of Vietnam (Figure 7.2). In November, this current splits into two currents at 12°N: a southward alongshore current and an eastward off-shore current. The southward branch turns east at 6°N, then turns northeast and joins the eastern branch at 115°E. An evident multi-eddy structure is obtained with two cyclonic eddies in the north SCS (north of 12°N) and cyclonic and anticyclonic eddies in the southern SCS (south of 12°N). The flow pattern does not change vary much from November to December, except the cyclonic eddy near the

Luzon Strait strengthens. In January, the west cyclonic eddy in the northern SCS expands toward the south. In February, the west cyclonic eddy in the northern SCS disappears and instead a cross-basin flow appears along 16°N latitude and joins the cyclonic eddy near the Luzon Strait. The southern SCS is occupied by an anticyclonic eddy. This anticyclonic eddy expands to north and forms the only evident eddy in the central SCS in March (Figure 7.2a). This eddy is associated with the central SCS warm pool in spring (Appendix A) and expands toward the south in April. May is the month of the summer monsoon transition. The anticyclonic eddy reduces its strength and becomes unidentifiable.

During the summer monsoon period (Mid-May to August), winds blow from the southwest (Figure 2.2) and the SCS surface circulation generally follows suit with anticyclonicity in the southern basin (Figure 2.3). Inflow is through the southern boundary and outflow is through the northern Taiwan Strait and eastern Luzon Strait. The inverted July means the general circulation pattern has the following features. Velocities reach 20 cm/s near the Vietnam Coast and splits into two currents at 12°N: the coastal current and off-shore current. The off-shore current further bifurcates and partially leaves the coast; the bifurcation point is at 110°E. The northern branch moves northeast to 113°E and then turns zonally between 15°-18°N. The southern branch moves zonally until reaching the Palawan Island, then turns north and joins with the north branch at 16°N. A cyclonic eddy appears in July near the south Vietnam coast and strengthens in August.

3. Sub-Surface (75 m)

The sub-surface (75 m) shows a strong seasonal variation (Figure 7.3). Warm and salty Kuroshio water enters the SCS through the Luzon Strait in October-March, the transition to and during the winter monsoon season. The winter circulation pattern is the basin-wide cyclonic gyre (November - January). A cyclonic mesoscale eddy splits from the gyre near the Luzon Strait in January and keeps its strength in February. On the other hand, the basin-wide cyclonic gyre weakens and shrinks toward the southwest in February and disappears in March.

During the summer monsoon period (June-September), the Kuroshio intrusion through the Luzon Strait ceases. A weak anticyclonic eddy occurs in June near the South Vietnam coast and strengthens in July. A cross-basin current establishes in August from the north branch of that eddy to the Luzon Strait and forms a weak cyclonic gyre in the northwest and an anticyclonic gyre in the southeast. During the winter monsoon transition period (October), the southeast anticyclonic gyre weakens and the northeast cyclonic gyre gains strength and eventually the cyclonic gyre occupies the whole SCS basin, the beginning of the winter circulation pattern.

4. Intermediate Level (400 m)

As the water depth increases, the inverted velocity generally reduces with depth to 200 m. The velocity at 200 m depth is quite small (see Appendix D). However, the velocity increases with depth below 200 m. Figure 7.4 shows the monthly variation of the SCS circulation at 400 m. At that depth, the inverted flow flows out of the SCS through the

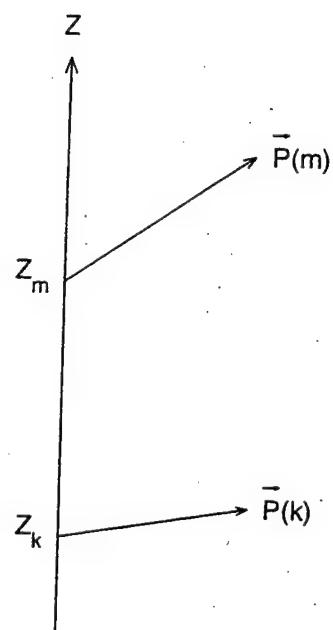
Luzon Strait. The winter pattern is characterized by three anticyclonic eddies (December–February), with two eddies in the northern SCS, and one in the southern SCS. The anticyclonic eddy near the Luzon Strait is evident from December to February. An east-to-west cross-basin current establishes along 16°N in February from the southern branch of the Luzon eddy. This cross-basin current sustains from February to April and separates the SCS basin into two parts. The northern part is occupied by an anticyclonic eddy and the southern part by a cyclonic eddy. The summer circulation pattern is featured by double anticyclonic gyres. The southern gyre is quite evident in June and July. The tangential velocity is around 4 cm/s.

5. Kuroshio Intrusion Through the Luzon Strait

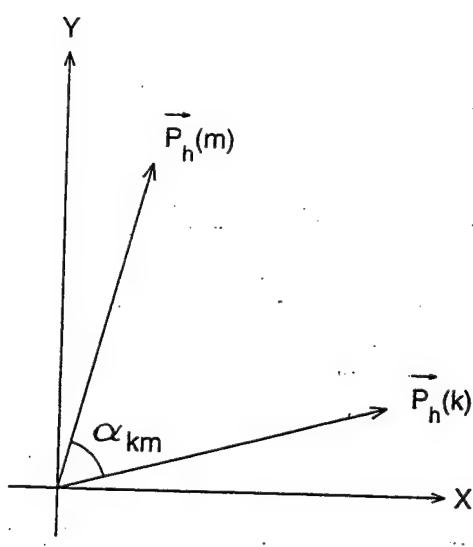
The SCS joins the Pacific Ocean through the Luzon Strait. The seasonal variations of the intrusion of the Kuroshio Water into the SCS through the Luzon Strait have been investigated in earlier studies [Fan and Yu, 1981; Shaw, 1989; Shaw, 1991]. As pointed out by Shaw [1991], the intrusion process is important not only to the transport of water masses into the SCS, but also to the shelf circulation off the southeast coast of China. Shaw [1989, 1991] used the discriminant analysis method to classify the water mass T, S characteristics at 150, 200, and 250 meters, and found that water characteristics of the Philippine Sea (Kuroshio) was identified along the continental margin south of China from October to January. The presence of this water indicated an intrusion current from the Philippine Sea into the SCS.

To verify Shaw's result, we computed the east-west geostrophic velocity along

120.5°E longitude using the P-vector method. The temperature and salinity used for the computation are the gridded data from the surface to 400 m depth along 120° and 121°E (Figure 7.5). The monthly zonal velocity in 120.5°E cross-section is given in Figure 7.6. The negative values indicate westward flow through the Luzon Strait (Kuroshio intrusion). The positive values show the outflow from the SCS to the Philippine Sea. Flow through the Luzon Strait has a strong seasonal variation, as well as a vertical shear. Evident Kuroshio intrusion (negative values) occurs during the winter monsoon season (November - March) in the upper 200 m. Below 200 m, the velocity is quite small, and most values are positive. We also computed the upper layer (0-400 m) volume transport through the Luzon Strait (Figure 7.7). The evident Kuroshio intrusion appears from November to March.



(a)



(b)

Figure 7.1 (a) Thermal wind relation at two different depths z_k and z_m .
 (b) β spiral turning angle (α_{km}) between the two levels z_k and z_m .

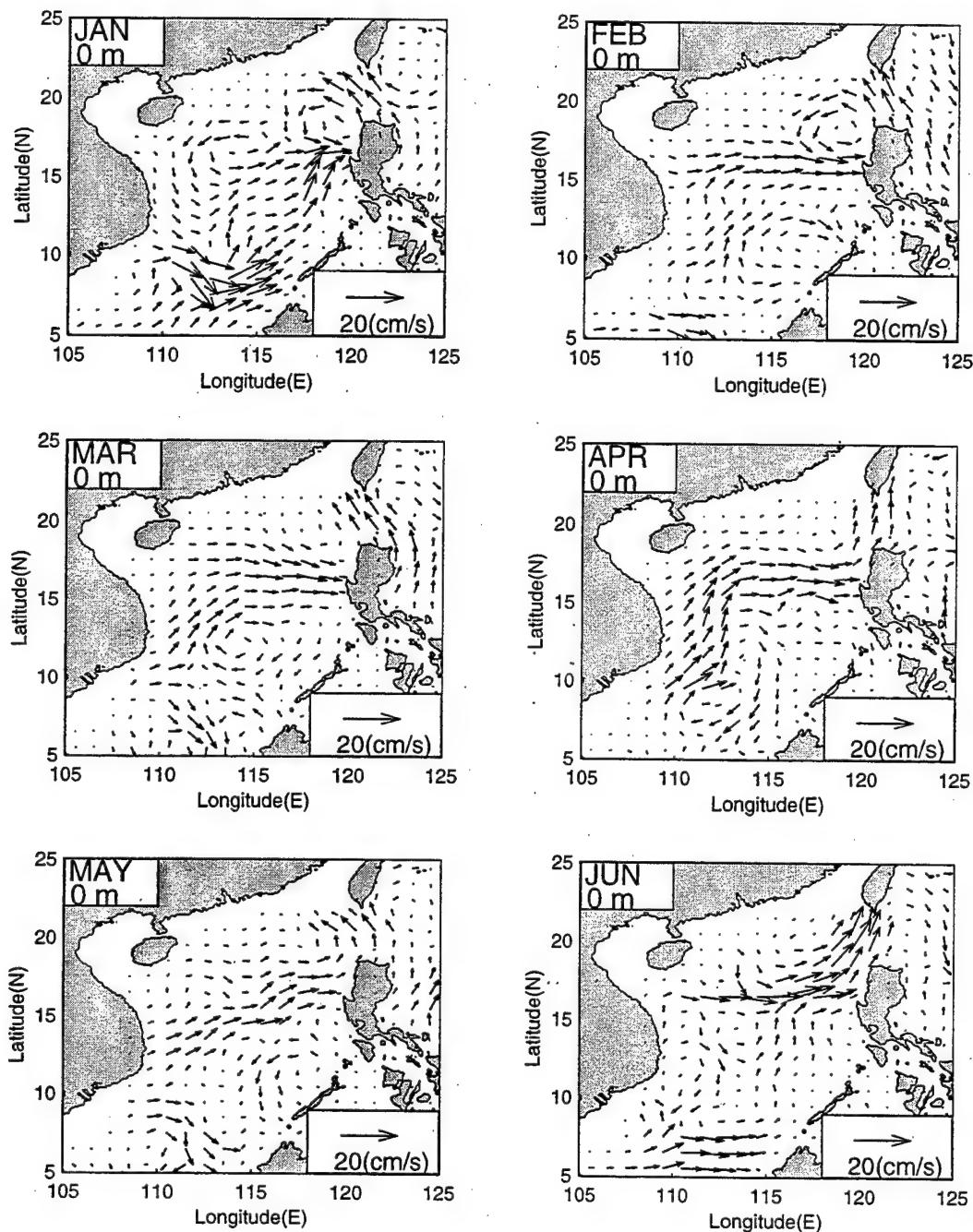


Figure 7.2a Surface Circulation from January to June

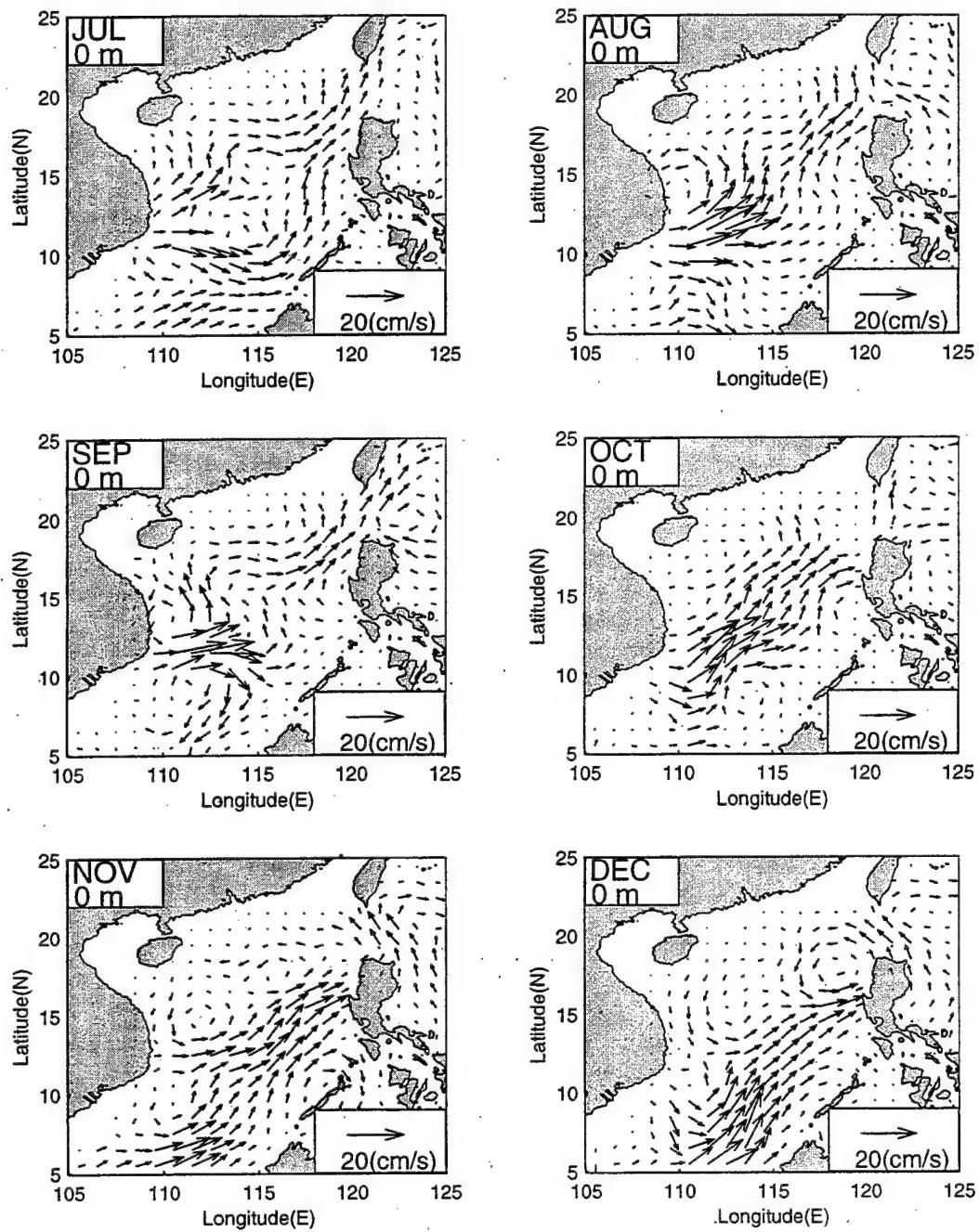


Figure 7.2b Surface Circulation from July to December

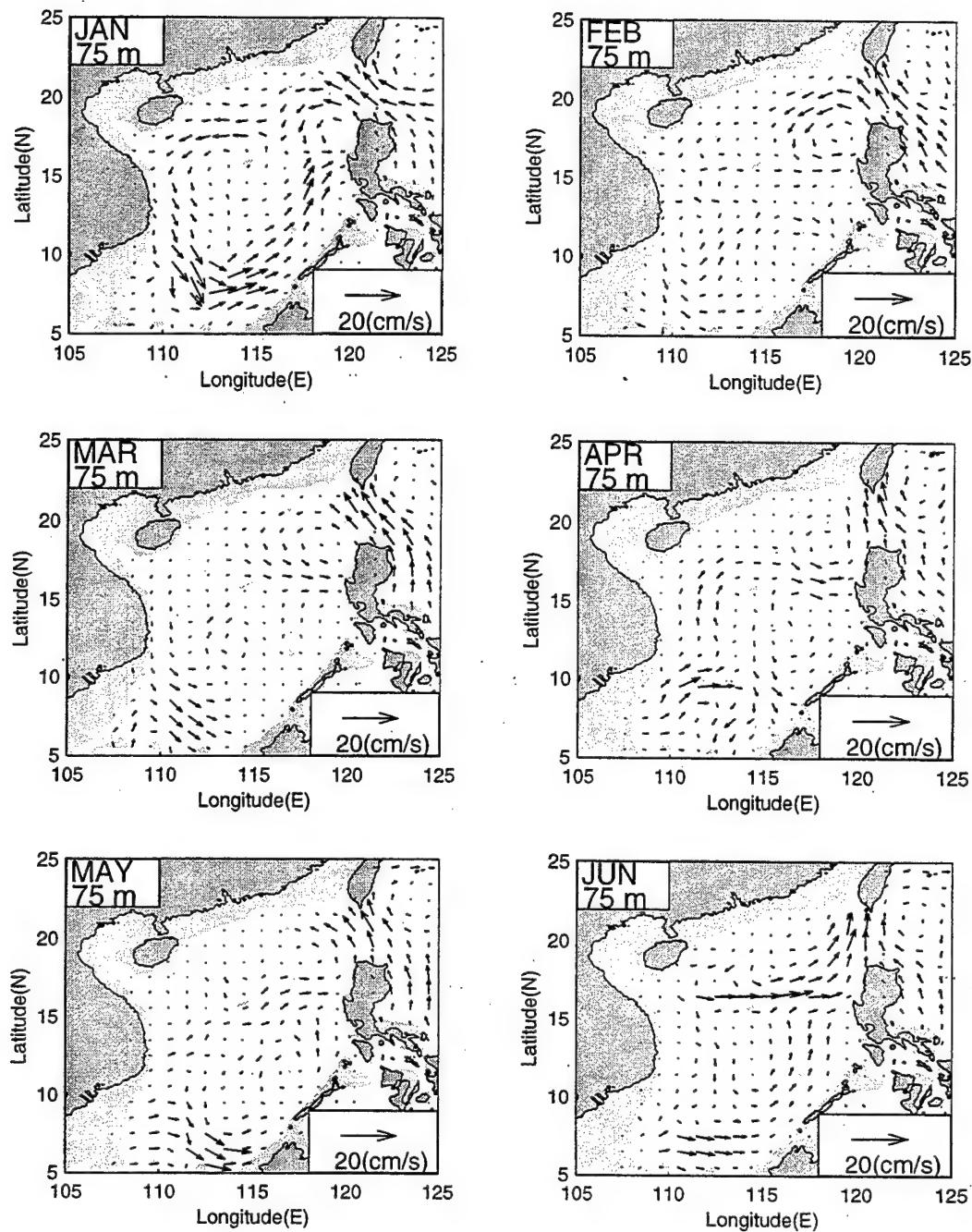


Figure 7.3a Sub-Surface (75 m) Circulation from January to June

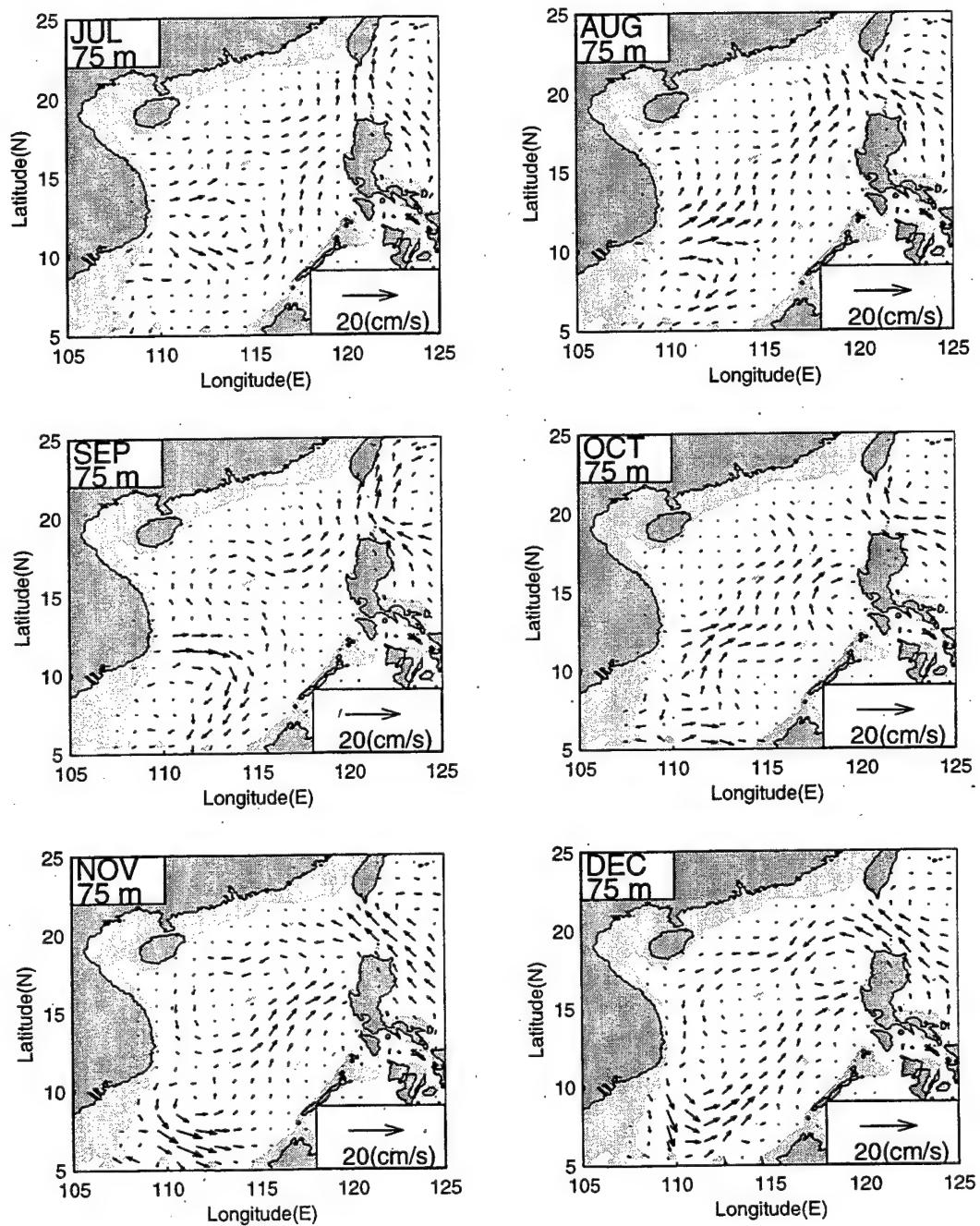


Figure 7.3b Sub-Surface (75 m) Circulation from July to December

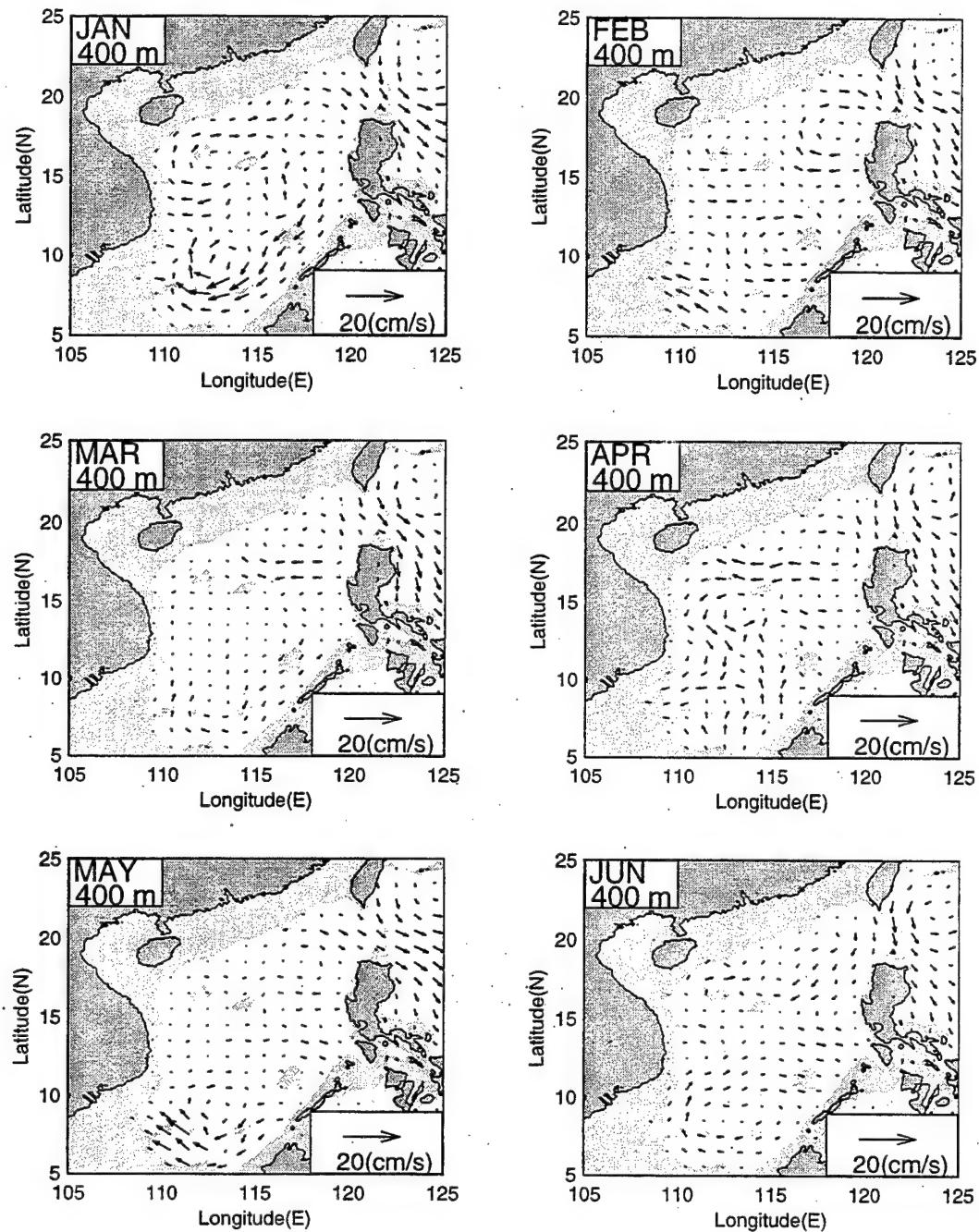


Figure 7.4a Intermediate Level (400m) Circulation from January to June

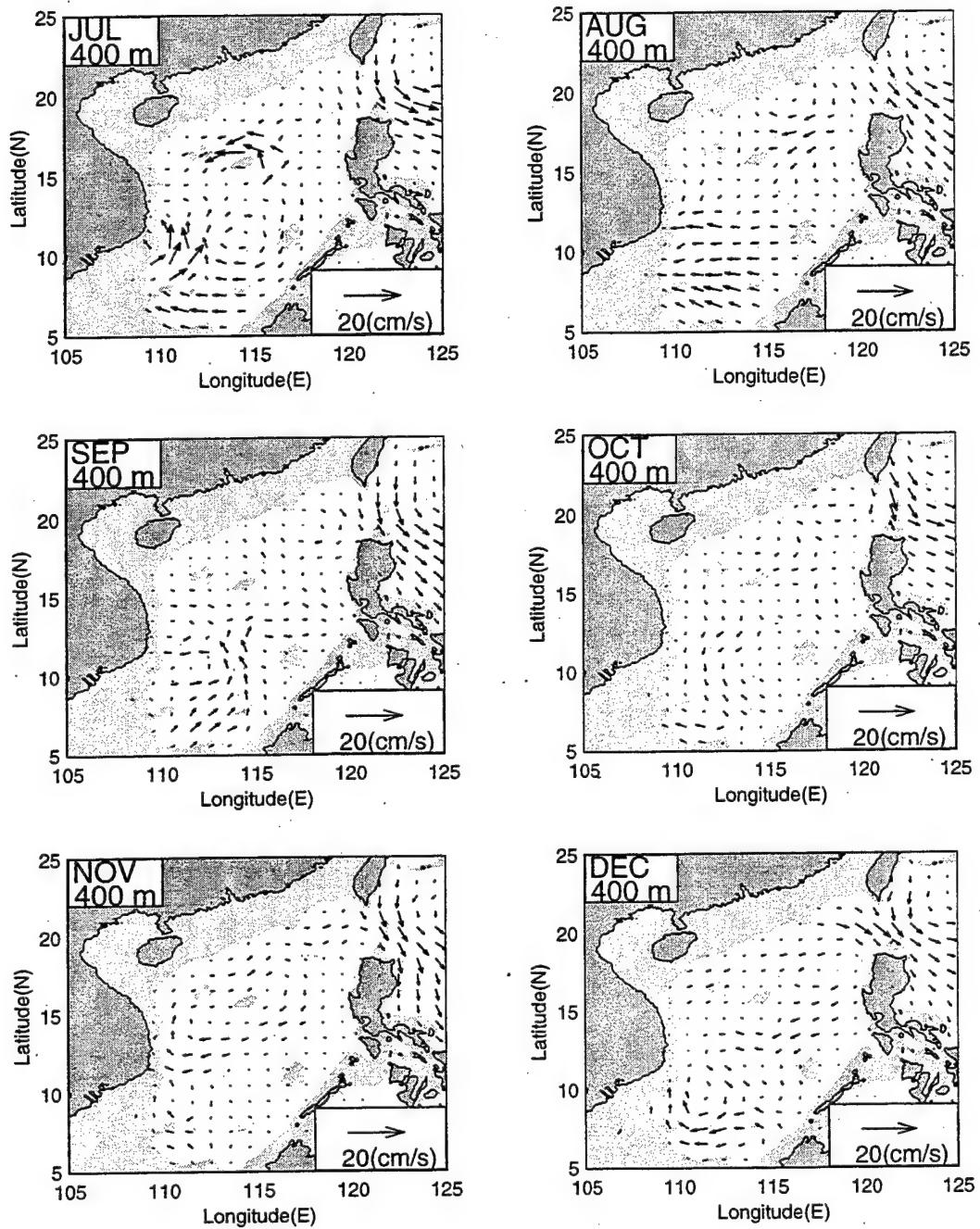


Figure 7.4b Intermediate Level (400 m) Circulation from July to December

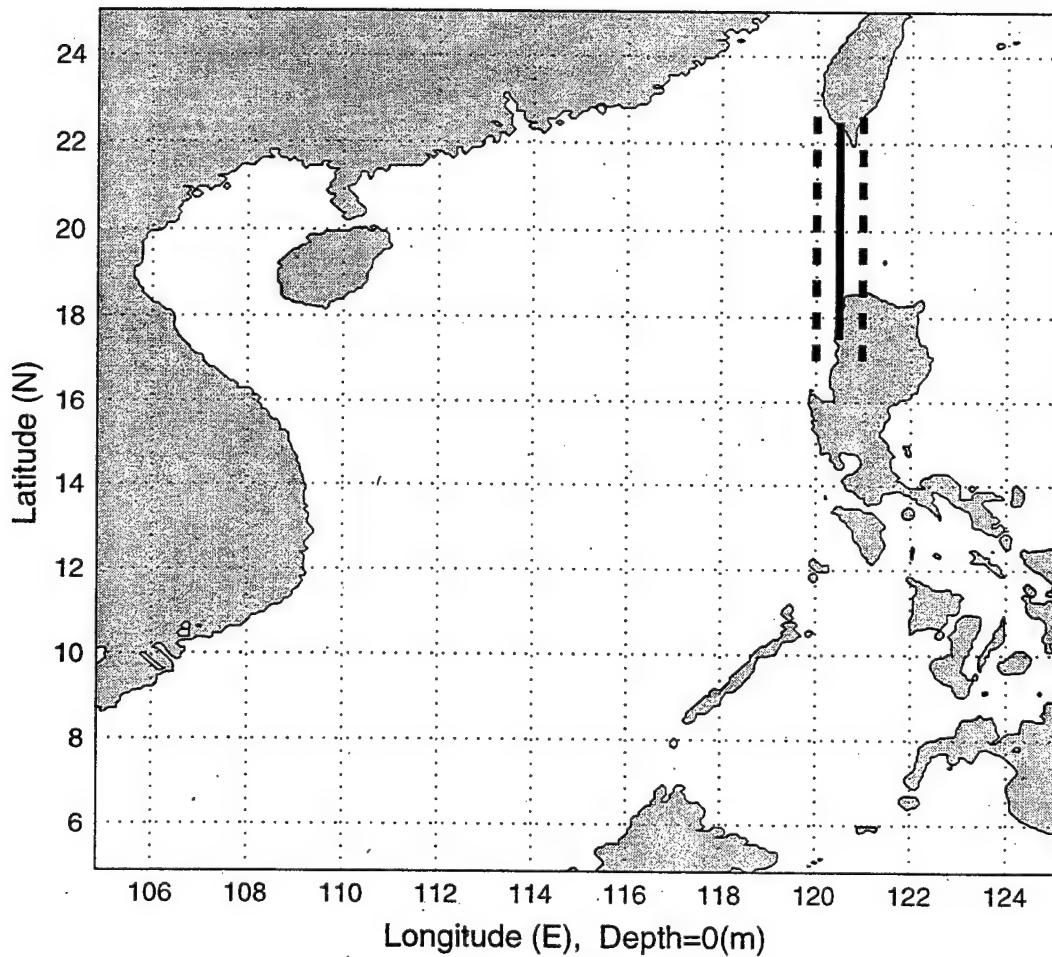
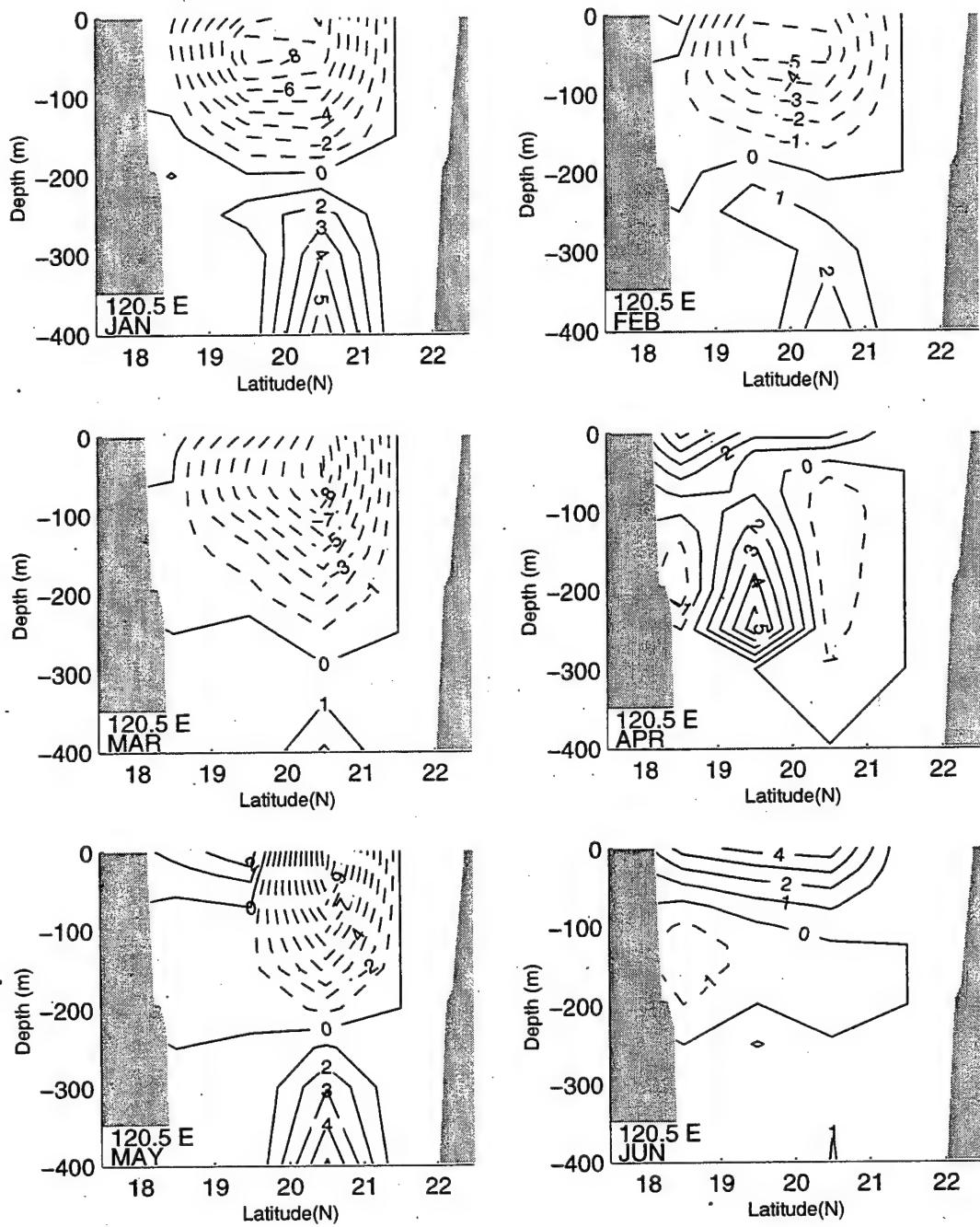


Figure 7.5 Temperature and Salinity data from surface to 400 meter used for the computation of east-west geostrophic velocity along 120.5°E (dash lines: T and S; solid line: geostrophic velocity)



**Figure 7.6a The monthly zonal velocity in 120.5E from January to June
(negative value indicate westward flow; Kuroshio intrusion)**

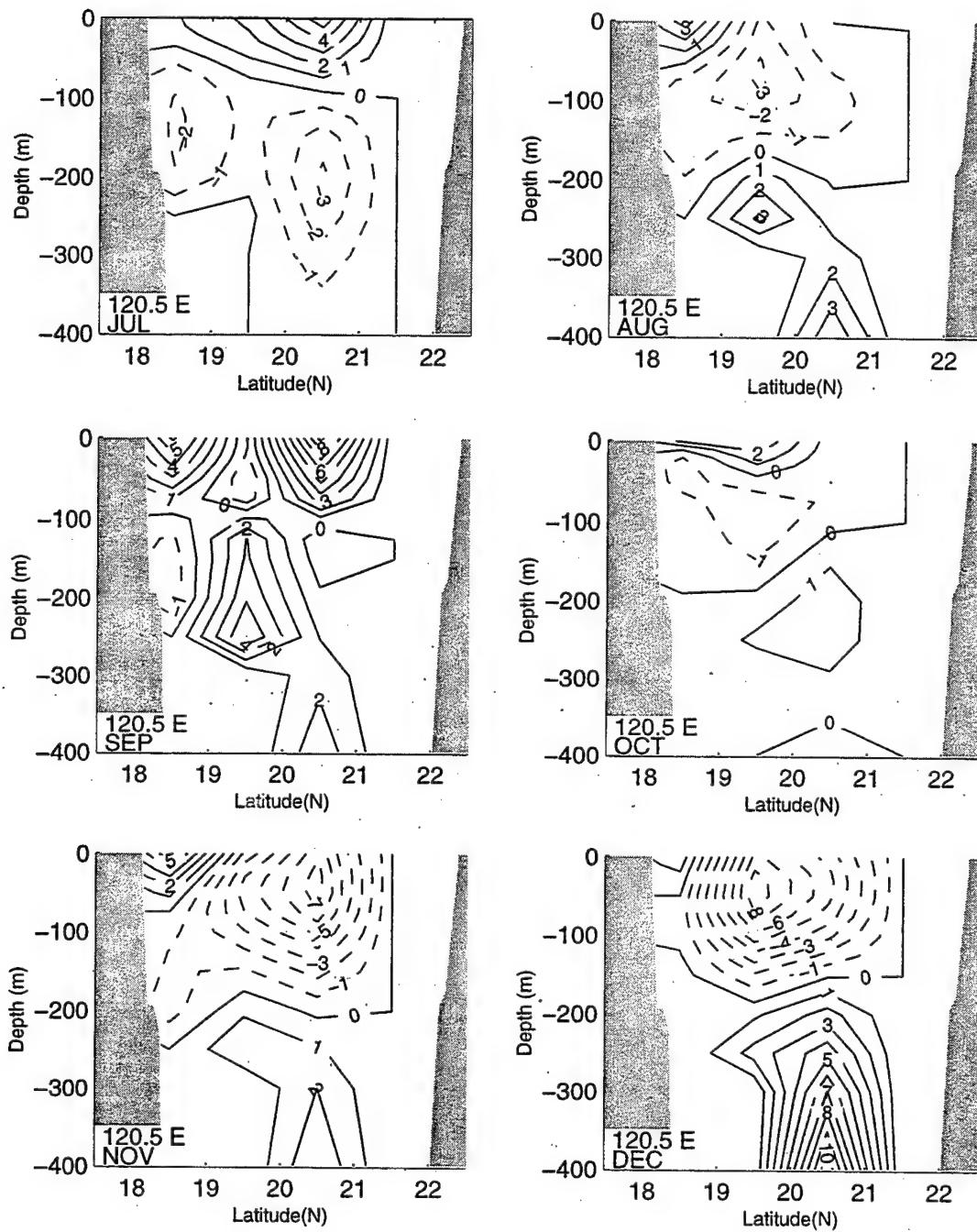


Figure 7.6b The monthly zonal velocity in 120.5°E from July to December
(negative value indicate westward flow; Kuroshio intrusion)

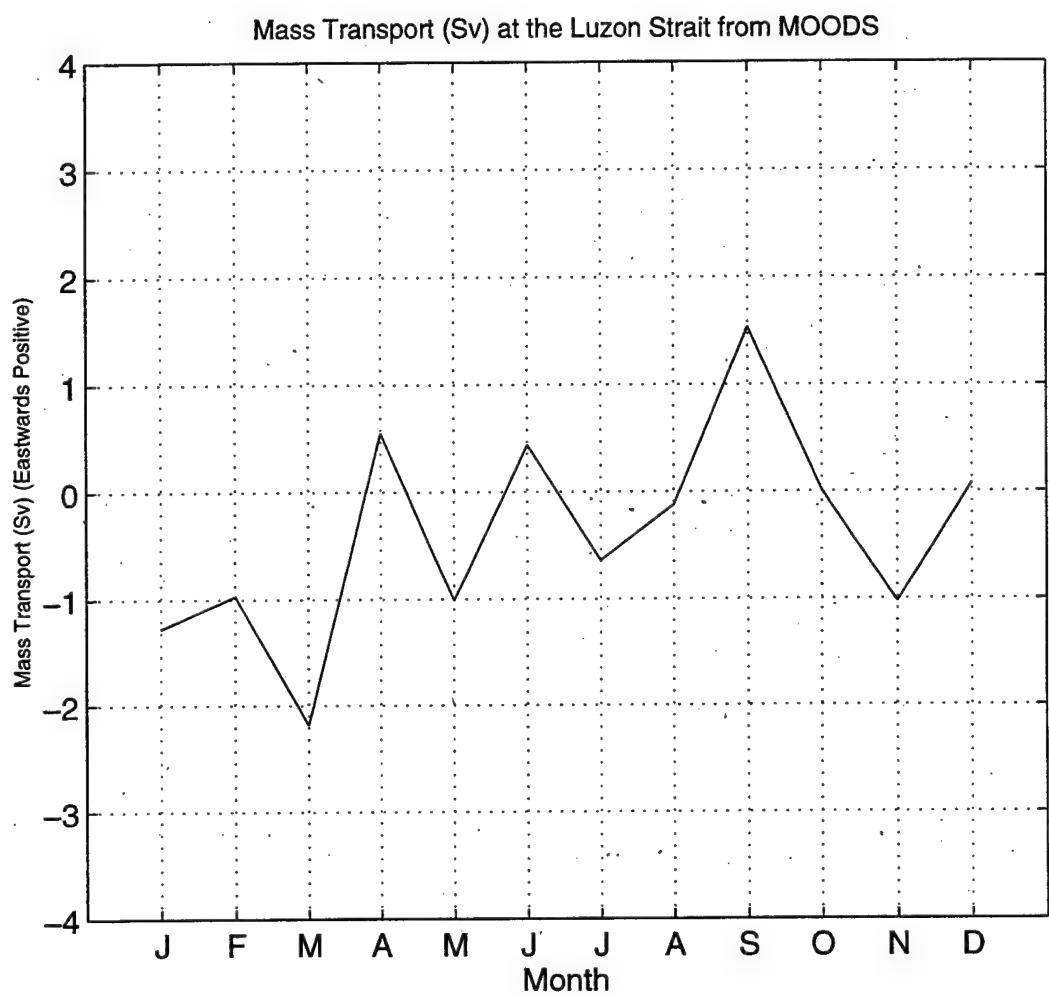


Figure 7.7 The Mass Transport (Sv) at the Luzon strait

VIII. CONCLUSIONS

The goals of this study were to investigate the thermohaline structure and the circulation patterns of the South China Sea using the historical MOODS hydrographic data. We applied the minimum curvature with spine method to produce thirteen level gridded data from the MOODS. Although the MOODS contain more than 180,000 temperature profiles, the deeper layer (below 400 m depth) is poorly sampled. Furthermore, the MOODS contain only 14,000 salinity profiles, so we were only able to establish climatological annual and monthly mean salinity fields at thirteen levels above 400 m depth. After the establishment of the gridded temperature and salinity data, we used the composite and EOF analysis to get the seasonal and interannual variabilities of the SCS thermohaline structure, and the P-vector inverse method to obtain the three-dimensional absolute geostrophic velocity fields. The major results from this research are summarized as follows.

A. CLIMATOLOGICAL MEAN THERMOHALINE FEATURES

The annual mean (1968-1984) temperature \bar{T} field over the SCS shows the pattern of northeast-southwest oriented isotherms at the upper layer from the surface to 20 m depth with a weak gradient from 28.5°C near the Borneo coast to 25°C near the southeast China coast. A strong temperature front is found near the Luzon Strait in the sub-surface layer from 100 m to 400 m. The SCS water temperature is quite uniform (e.g., near 13°C at 250 m) and much lower than the water east of the Luzon Strait, the West Pacific Ocean Water. The annual mean salinity \bar{S} shows that in the upper layer, a large amounts of freshwater

enter the SCS from the Zhujiang (Pearl) River in the northwest and from the Mekong River in the southwest. The Kuroshio brings the high salinity water through the Luzon Strait into the north SCS and forms a salty tongue (34 psu) stretching into the southeast China coast.

B. SEASONAL THERMOHALINE VARIABILITY

Seasonal thermohaline variability is associated with fronts and multi-eddies. The bi-frontal structure is the major thermal feature in the northern SCS (north of 12°N): a strong coastal front along the China coast, and a relatively weak and wide front across the SCS basin from the Vietnam coast to the Luzon island between 12°-17°N. The two fronts change their strengths synchronously; they weaken with the depth and disappear at 50 m depth. The front reoccurs from 75 m depth and is evident as deep as 300 m depth. At 30 m depth, an eddy ($>0.4^{\circ}\text{C}$) appears in the northern SCS and slants toward the east (the Luzon Strait) with depth and becomes very strong in the layer between 75 m and 150 m. Below 150 m depth, this eddy reduces its strength. In the southern SCS (south of 12°N) from the surface to 30 m depth, a dipole structure (dual eddies) was found with a warm (cool) eddy near the Mekong River mouth, and a cool (warm) eddy in the west of the Borneo- Palawan islands during the summer (winter) monsoon season. Below 75 m depth, the western eddy near the Mekong River mouth is much stronger than the eastern eddy.

The seasonal salinity variability was also identified. During winter (January), a salty tongue 1.2 psu anomaly stretches from the Luzon Strait to the continental shelf along the southeast China coast, representing a strong Kuroshio intrusion. A weak fresh anomaly (-

0.2 psu) is found in the west of the Luzon island. During the summer (July), a salty tongue with 0.4 psu stretches from the Vietnam coast to 118°E between 10°-17°N, occupying the central SCS while the rest is occupied by negative anomaly. A strong fresh tongue occupies the continental shelf along the southeast China coast and the Gulf of Tonkin.

C. KUROSHIO INTRUSION

Both water mass analysis and the inverted geostrophic velocity at the Luzon Strait confirm the Kuroshio intrusion during the winter monsoon season. Such an intrusion has a vertical shear. Evident Kuroshio intrusion (negative values) occurs during the winter monsoon season (November - March) in the upper 200 m while below 200 m the velocity is quite small and outflows from the SCS into the Philippine Sea. The computed upper layer (0-400 m) volume transport through the Luzon Strait has a strong seasonal variation: the maximum Kuroshio intrusion into the SCS with a value of -2.2 Sv occurring in March, and the maximum SCS outflow with a value of 1.5 Sv in September.

D. INTERANNUAL SCS WARMING/COOLING PHASES

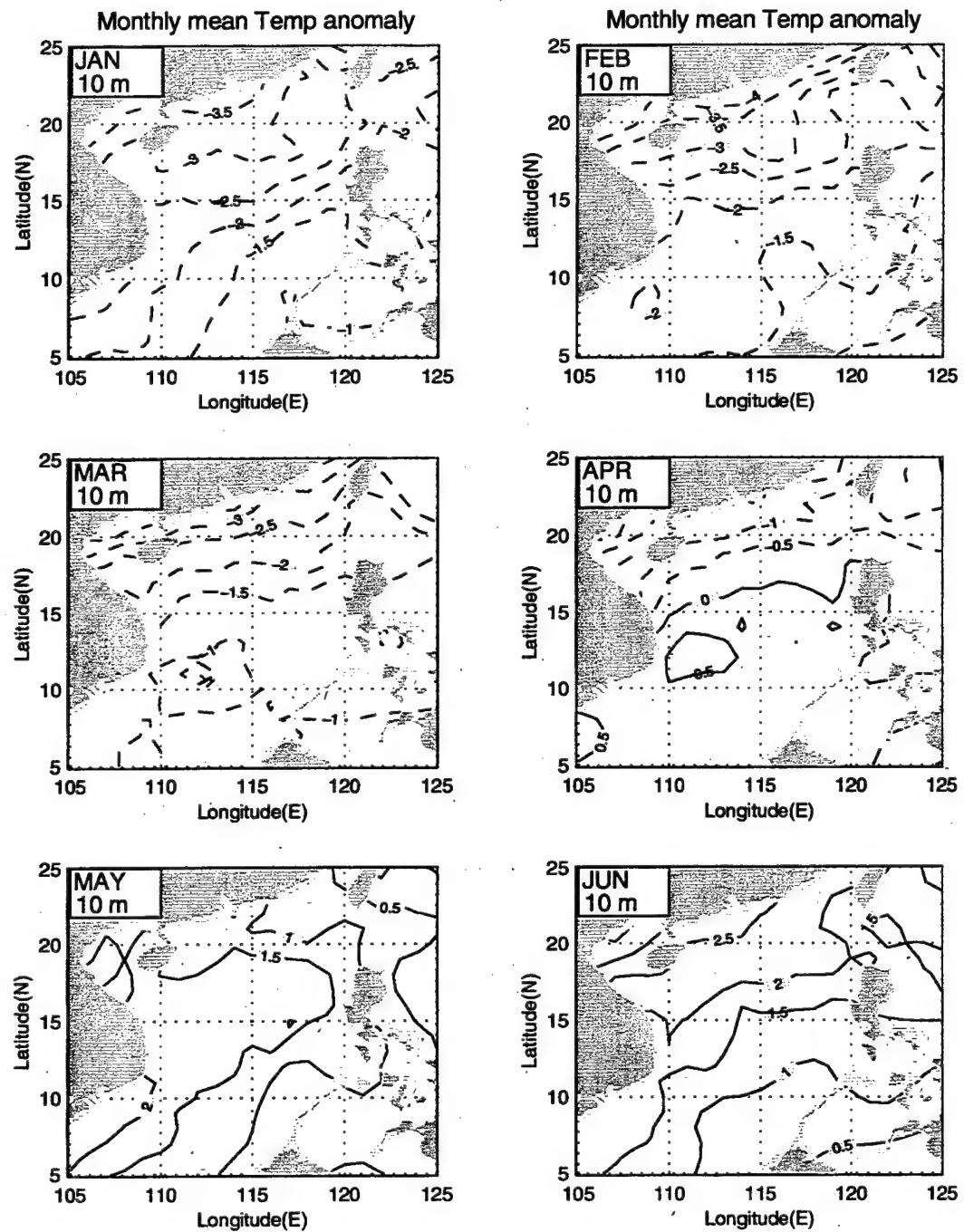
The interannual SCS warming/cooling phases were identified by the second EOF mode with periods of two to five years. The strongest SCS warming occurred in August 1969 and September 1976, with a warming of 3°C at the surface near the China coast and an occurrence of a sub-surface (50-125 m) warm eddy (2°C) in the west of Luzon Strait. The strongest SCS cooling appeared in October 1974 with a cooling of 3°C at the surface near the China coast, and an occurrence of a sub-surface (50-125 m) cool eddy (-2°C) in the west of the Luzon Strait.

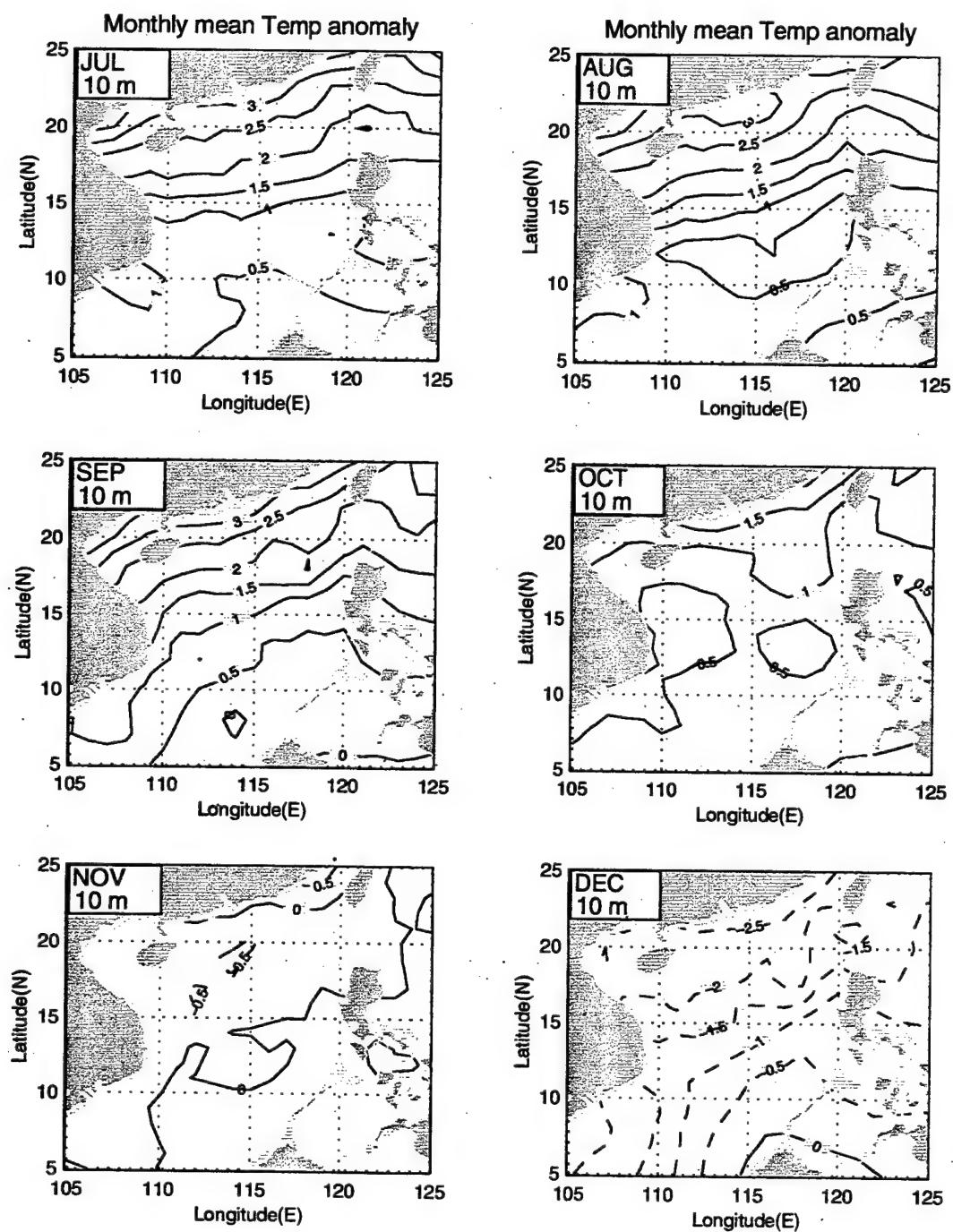
The warming events appeared between the late 1960's and first half of the 1970's, and the cooling events occurred in the second half of the 1970's and early 1980's.

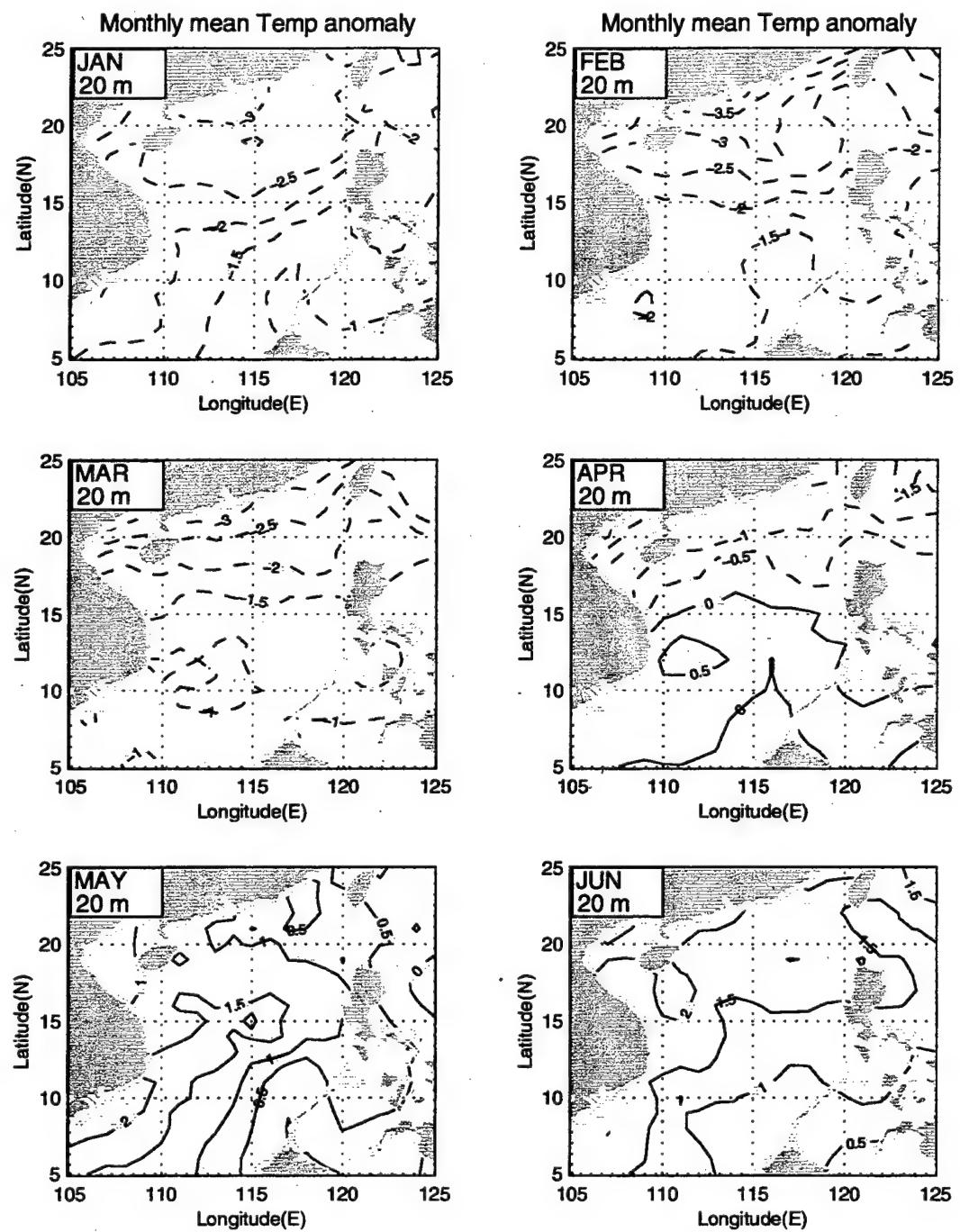
E. MULTI-EDDY STRUCTURE

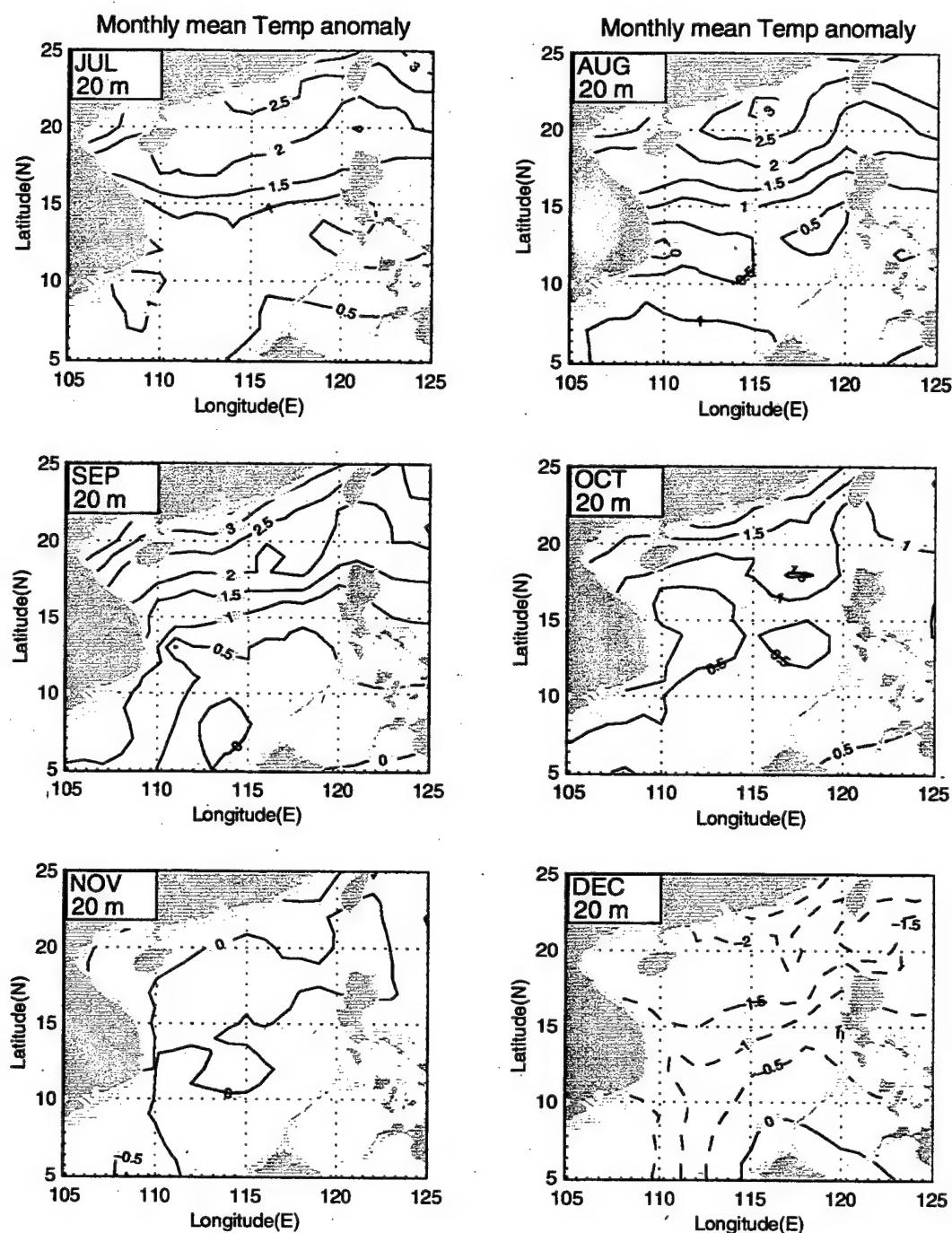
The T, S and the inverted velocity fields show the multi-eddy structure: two cyclonic eddies in the north SCS (north of 12°N) and cyclonic and anticyclonic eddies in the southern SCS (south of 12°N). The anticyclonic warm-core eddy expands to the north and forms the only evident eddy in the central SCS in March, and expands toward the south in April. May is the month of the summer monsoon transition. The anticyclonic warm-core eddy reduces its strength and becomes unidentifiable. During the summer monsoon period (mid-May to August), winds blow from the southwest and the SCS surface circulation generally follows suit with anticyclonicity in the southern basin. Inflow is through the southern boundary and outflow is through the northern Taiwan Strait and eastern Luzon Strait. The inverted July mean general circulation pattern has the following features. Velocities reach 20 cm/s near the Vietnam Coast and splits into two currents at 12°N: the coastal current and off-shore current.

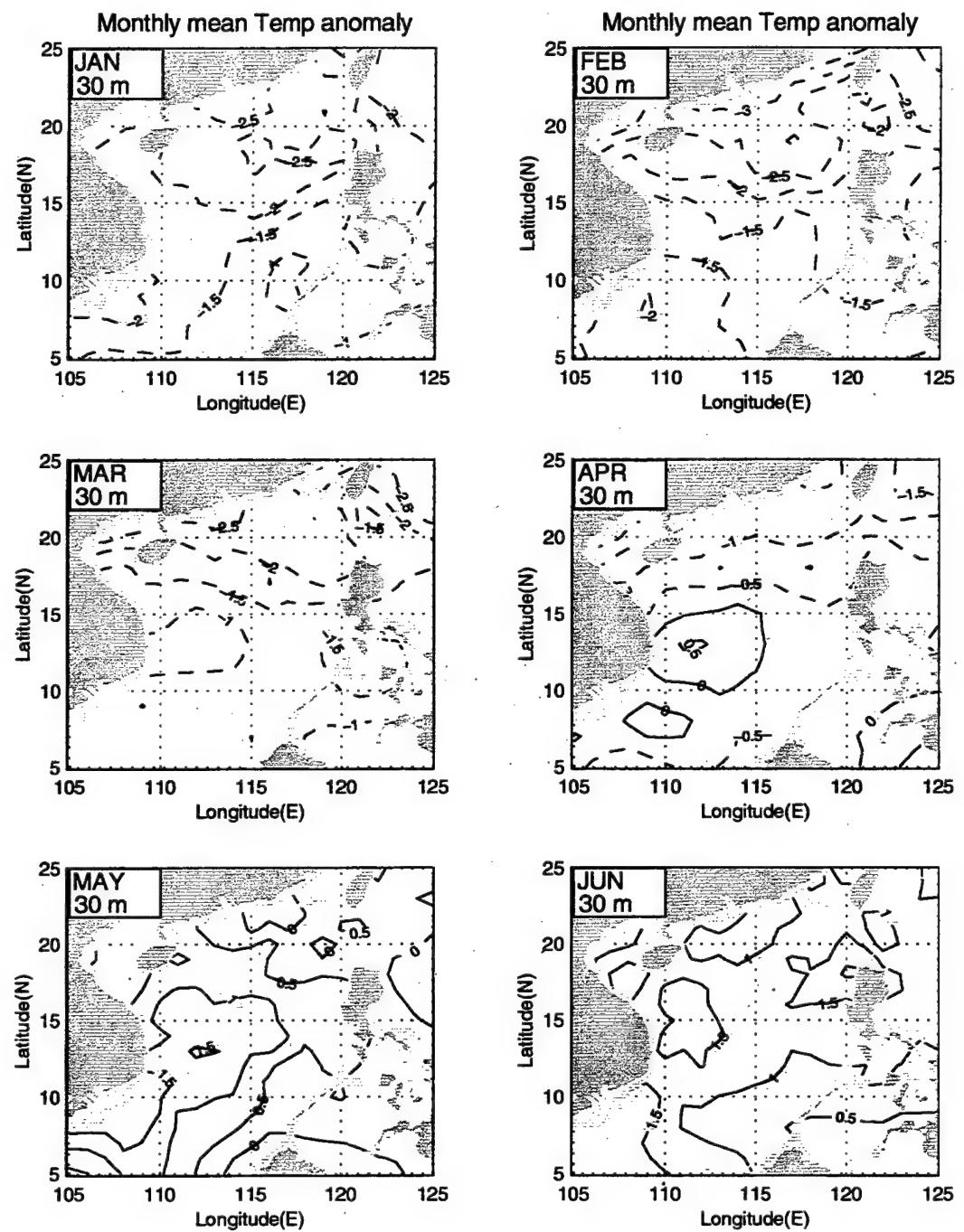
APPENDIX A. MONTHLY TEMPERATURE ANOMALY

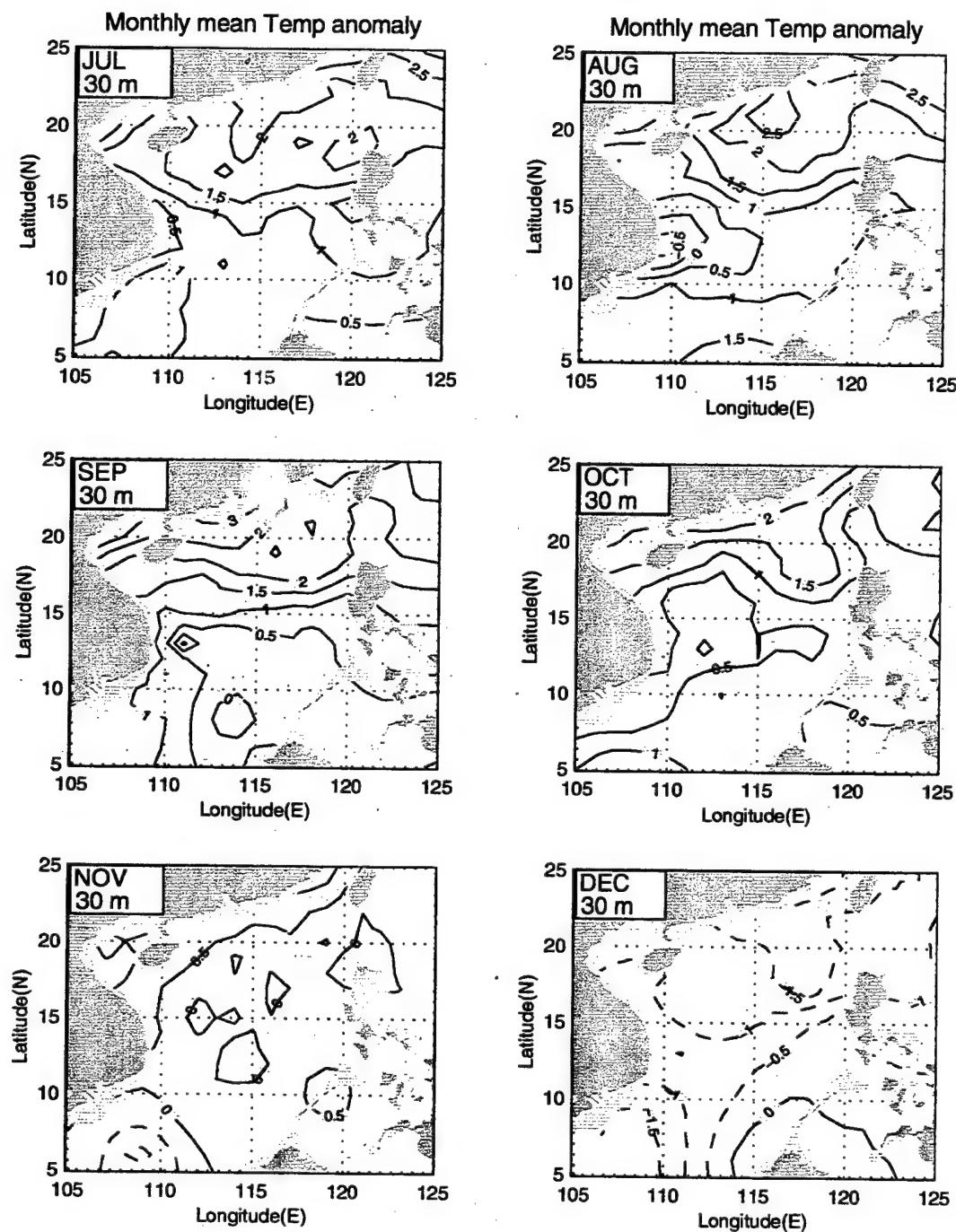


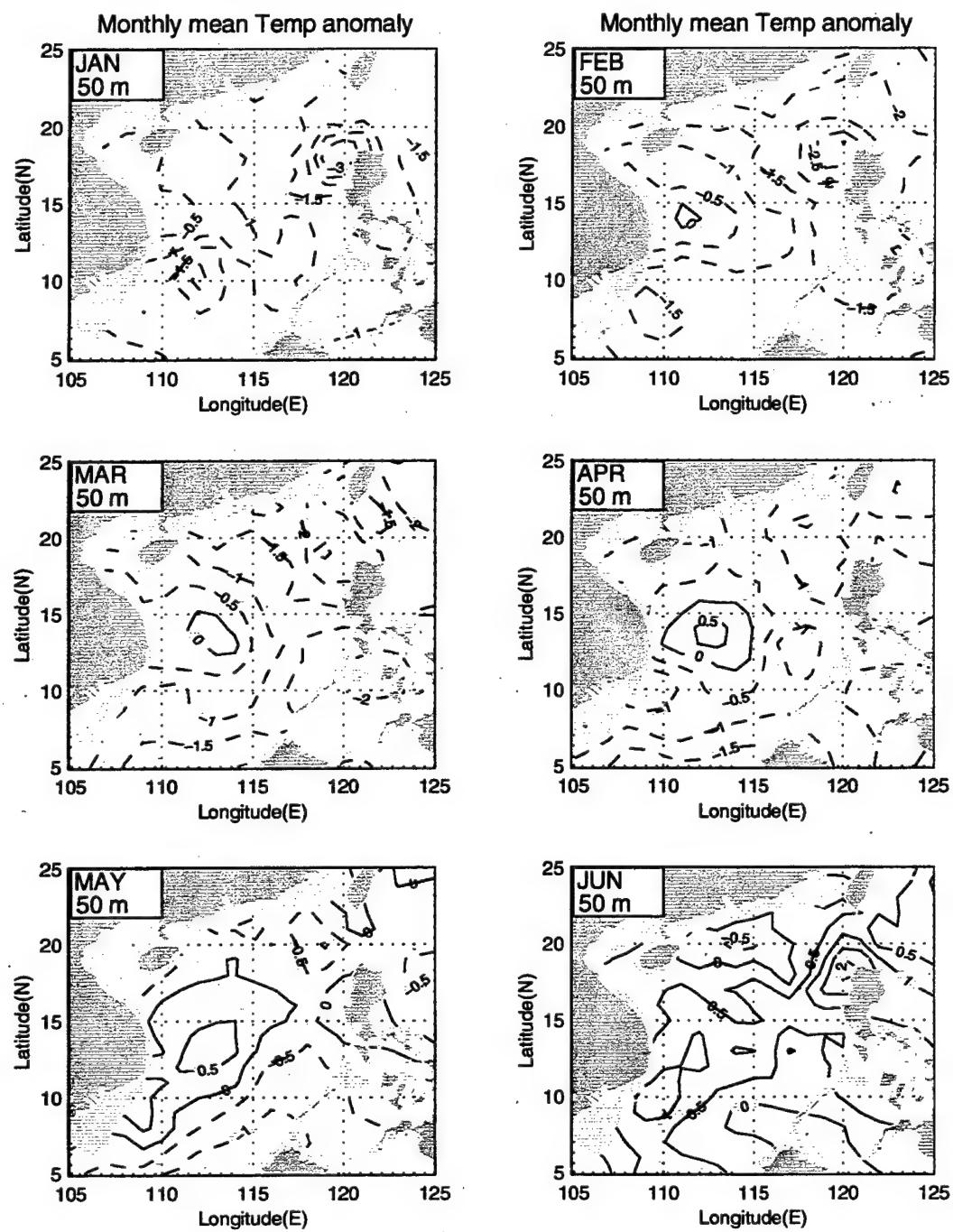


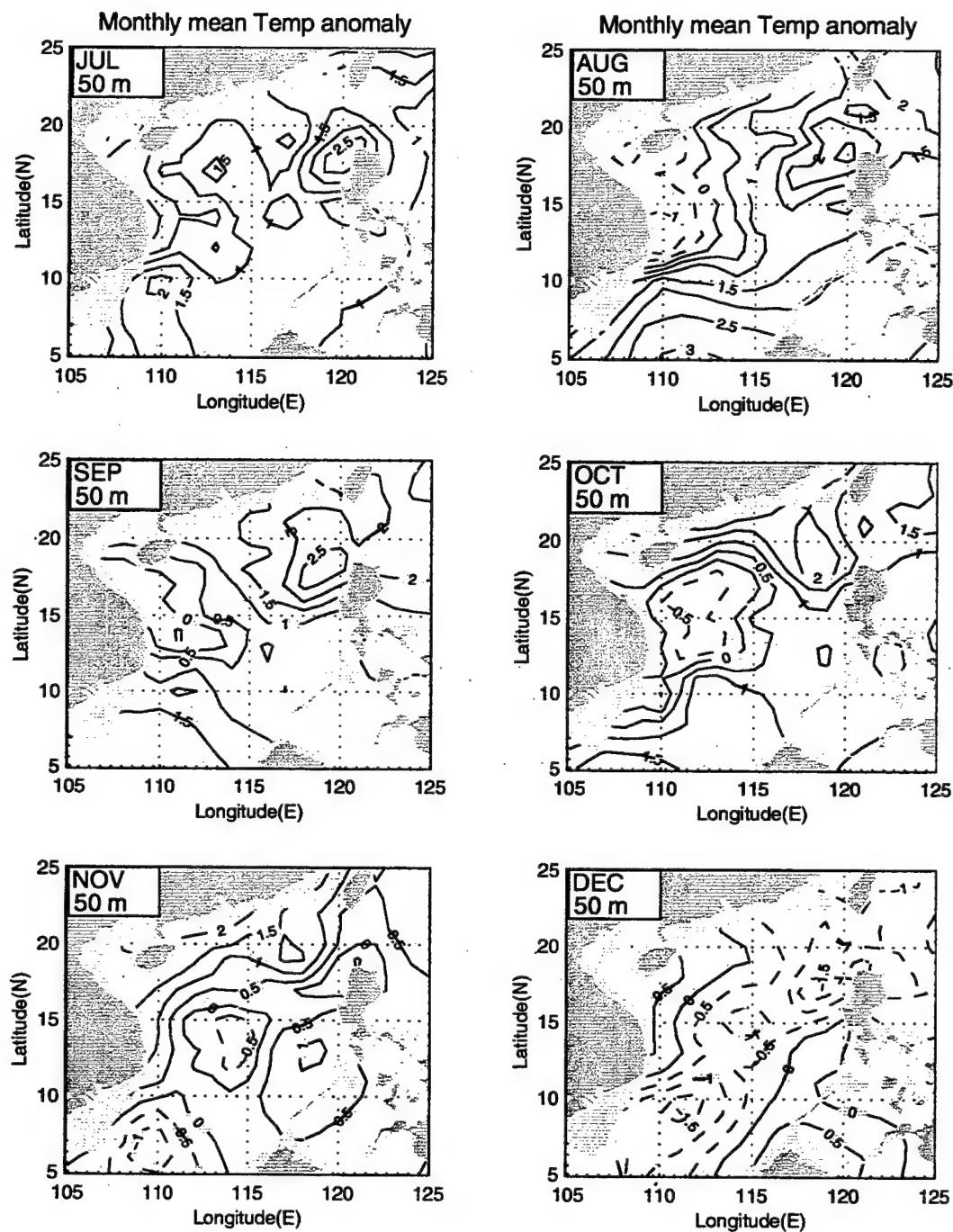


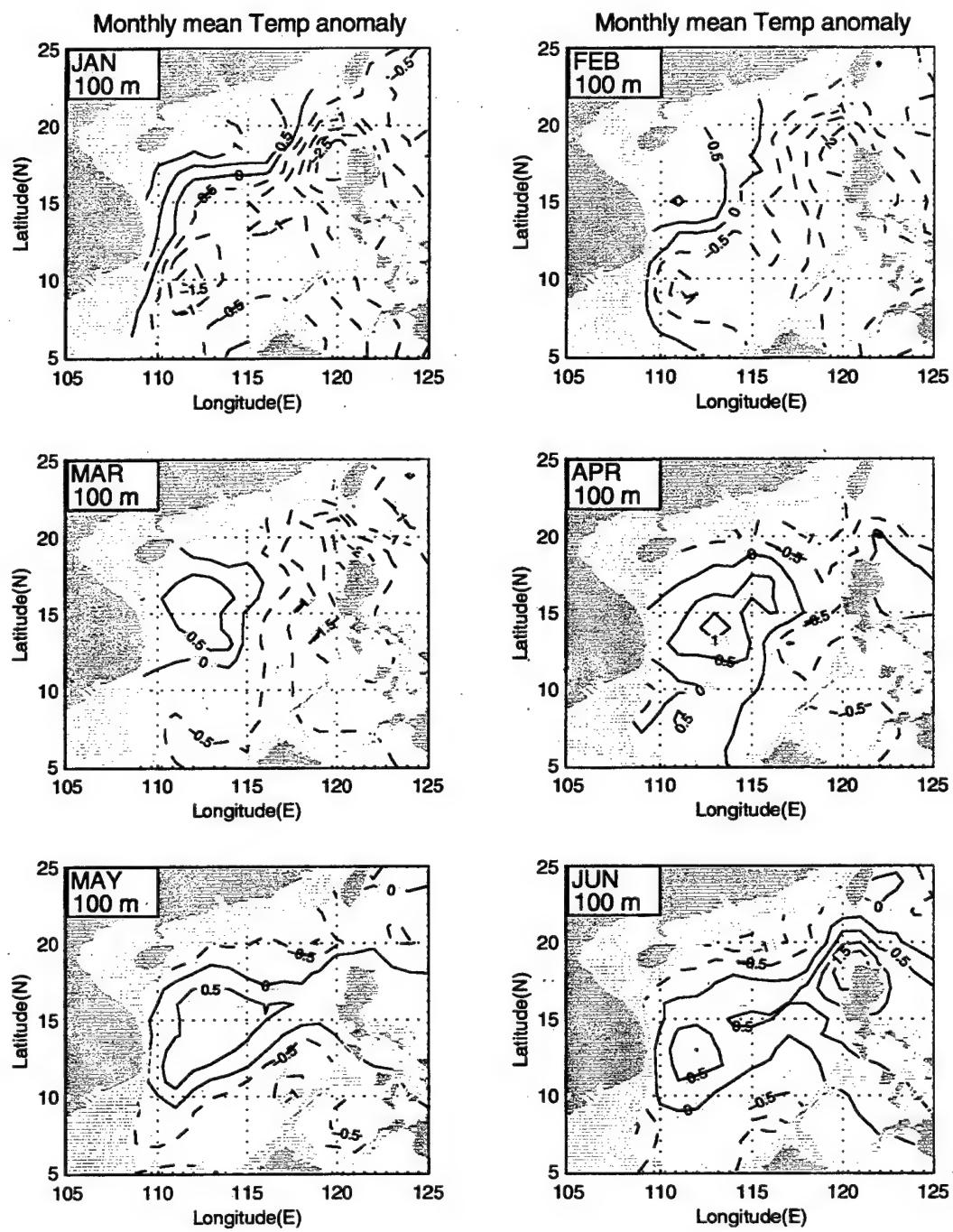


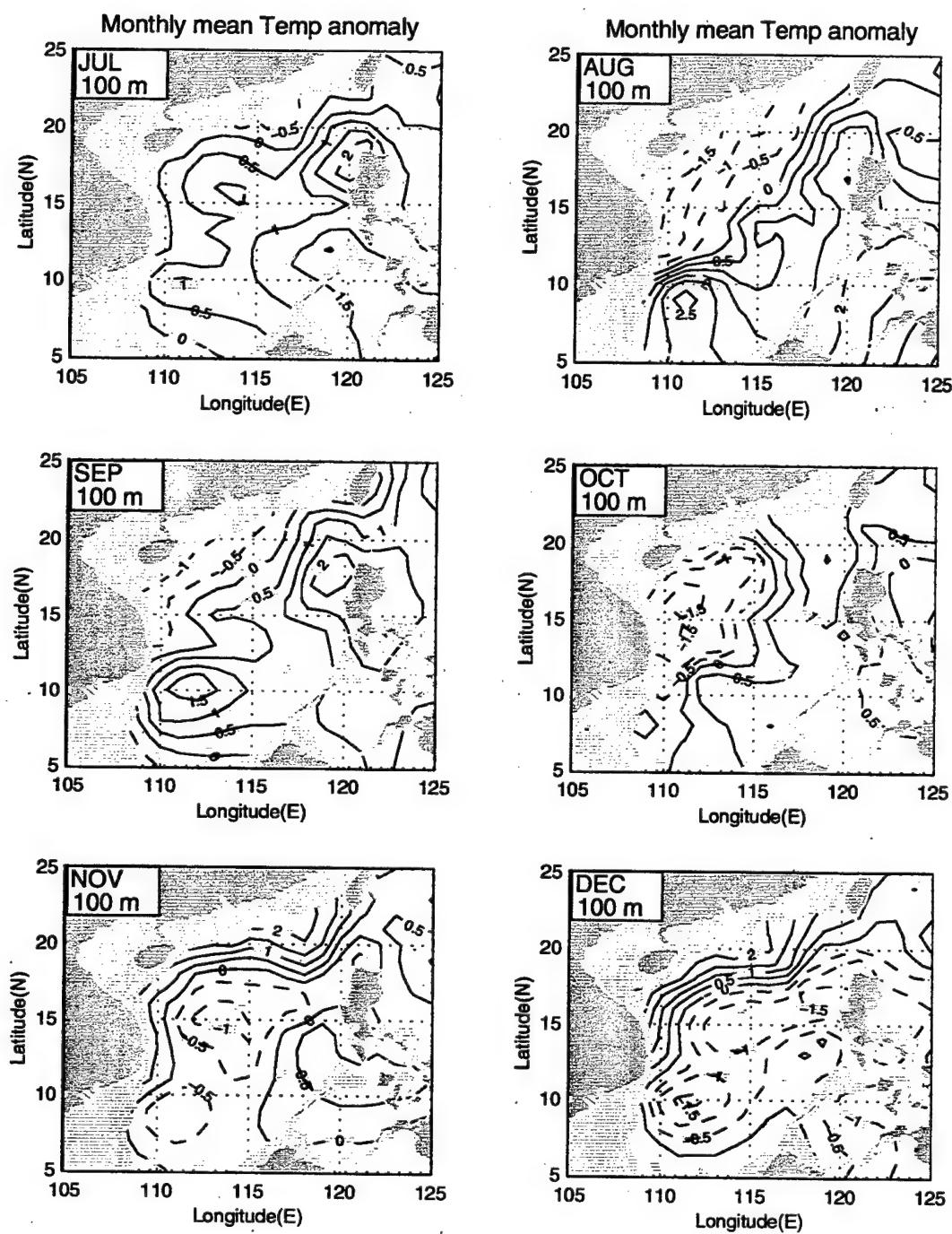


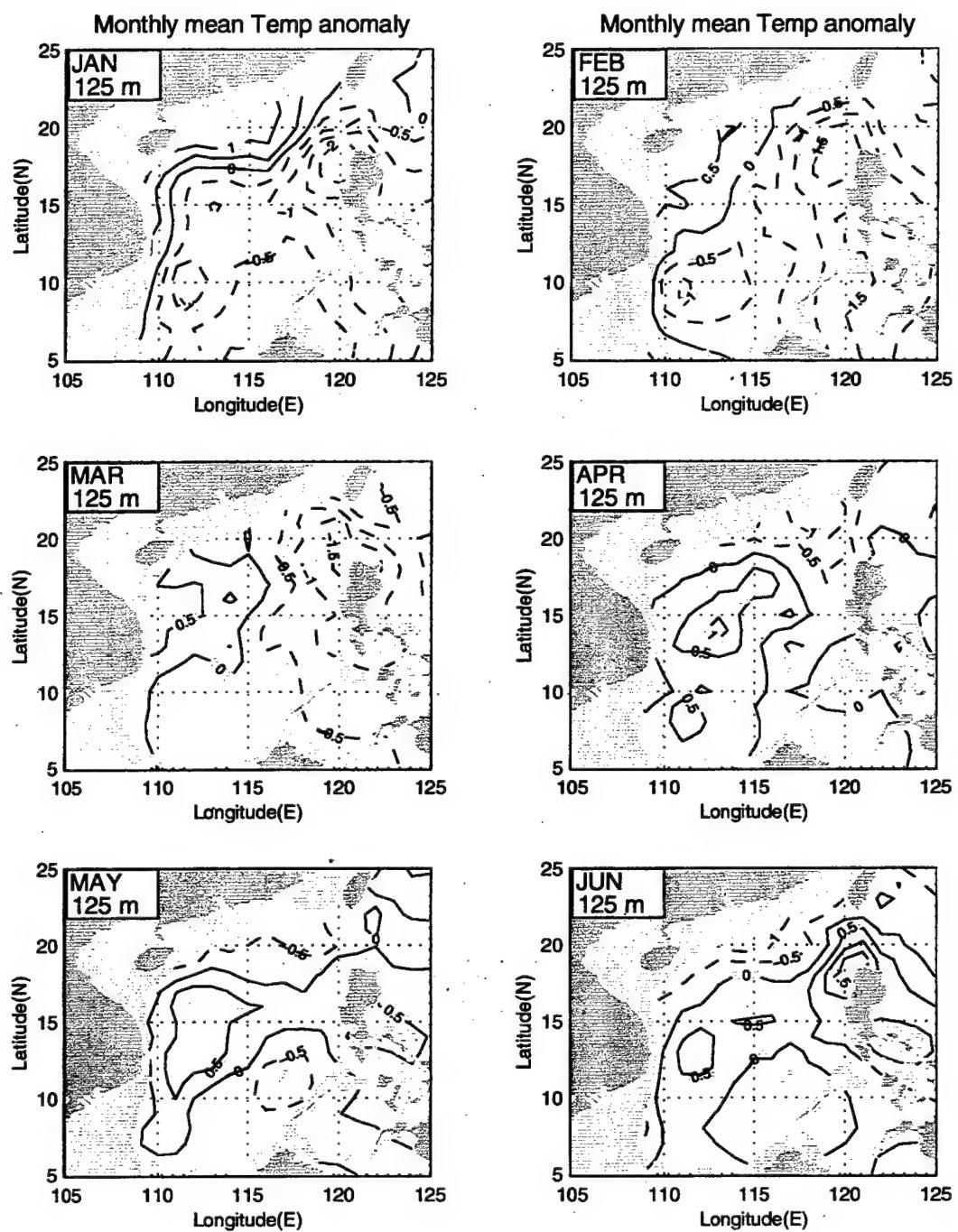


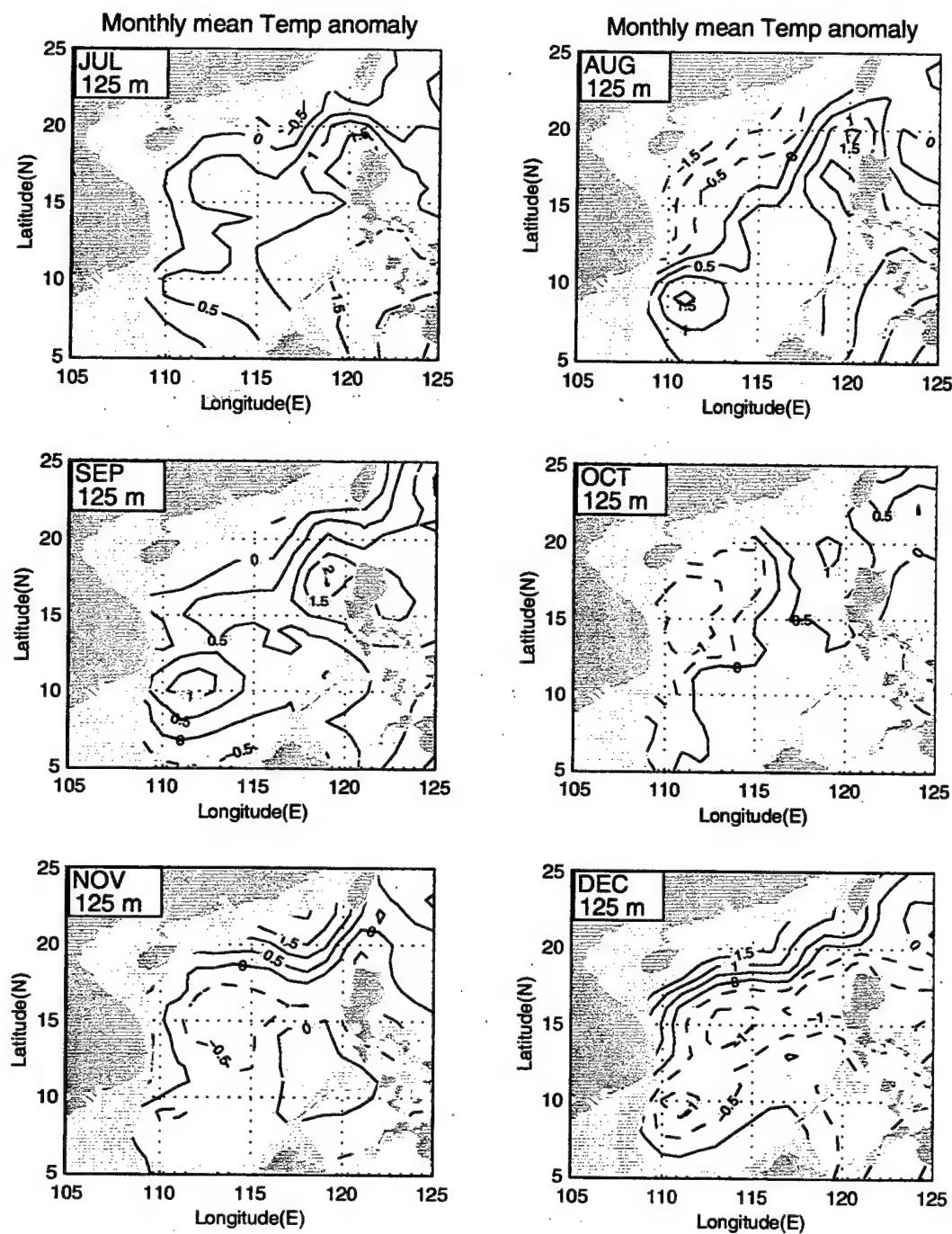


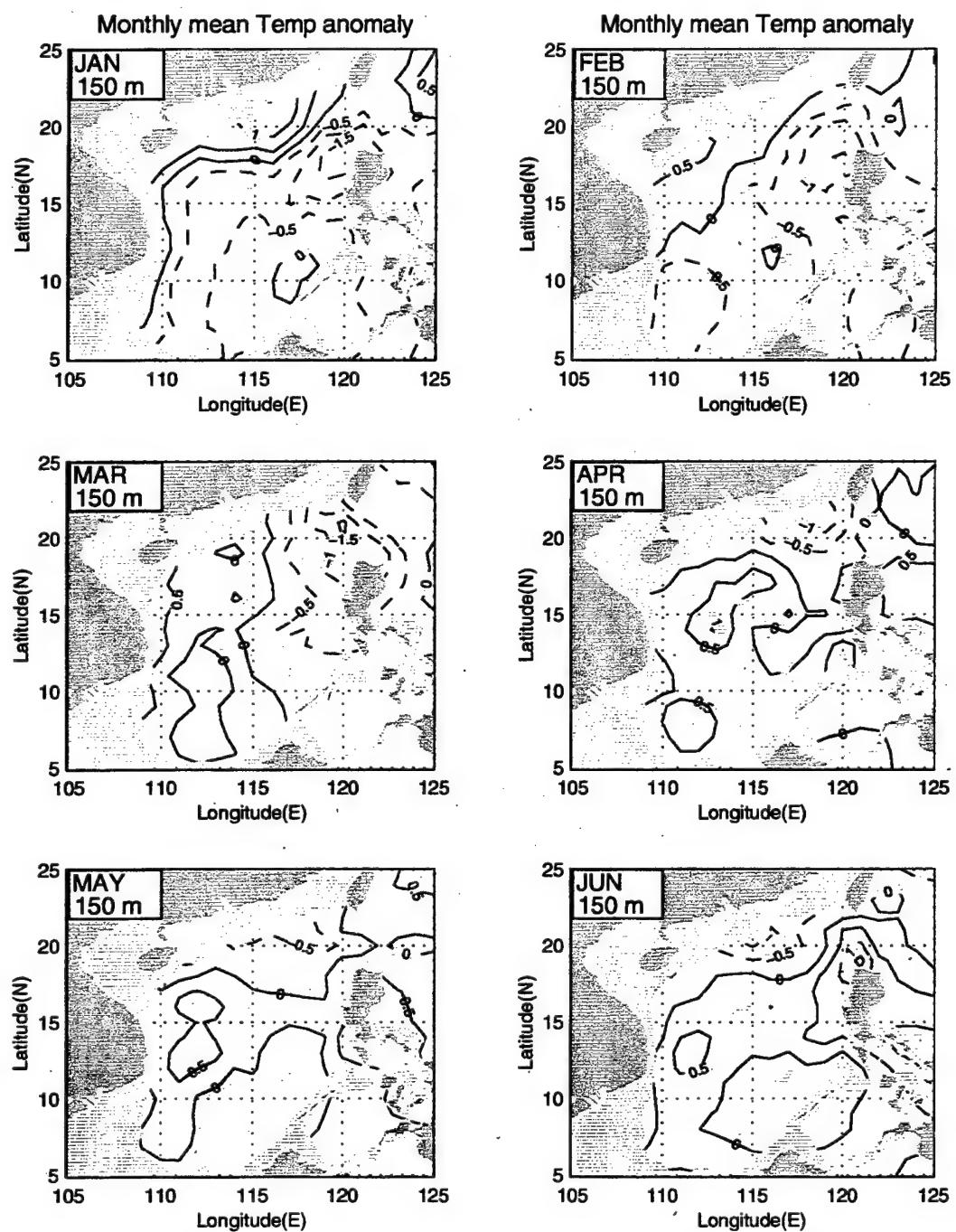


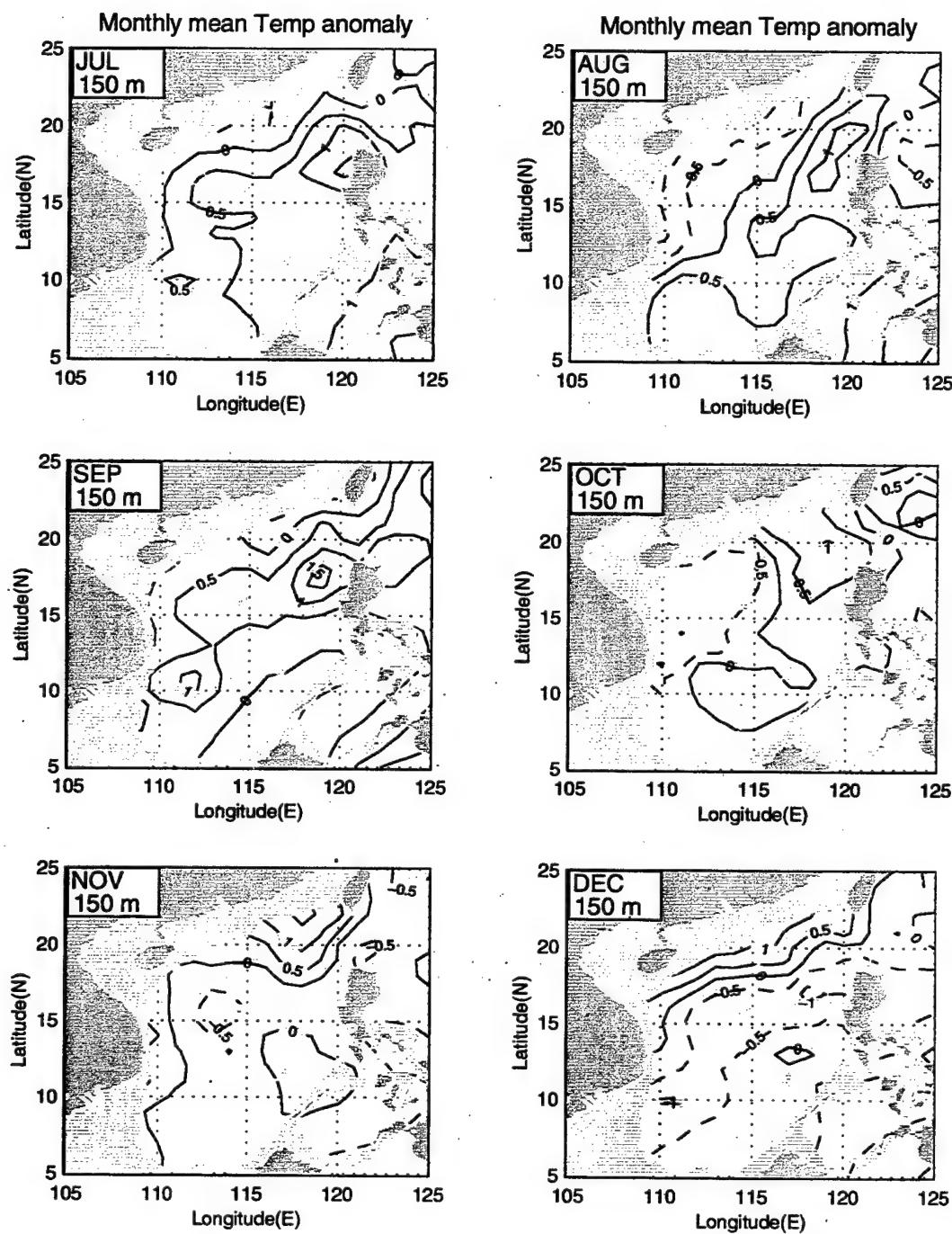


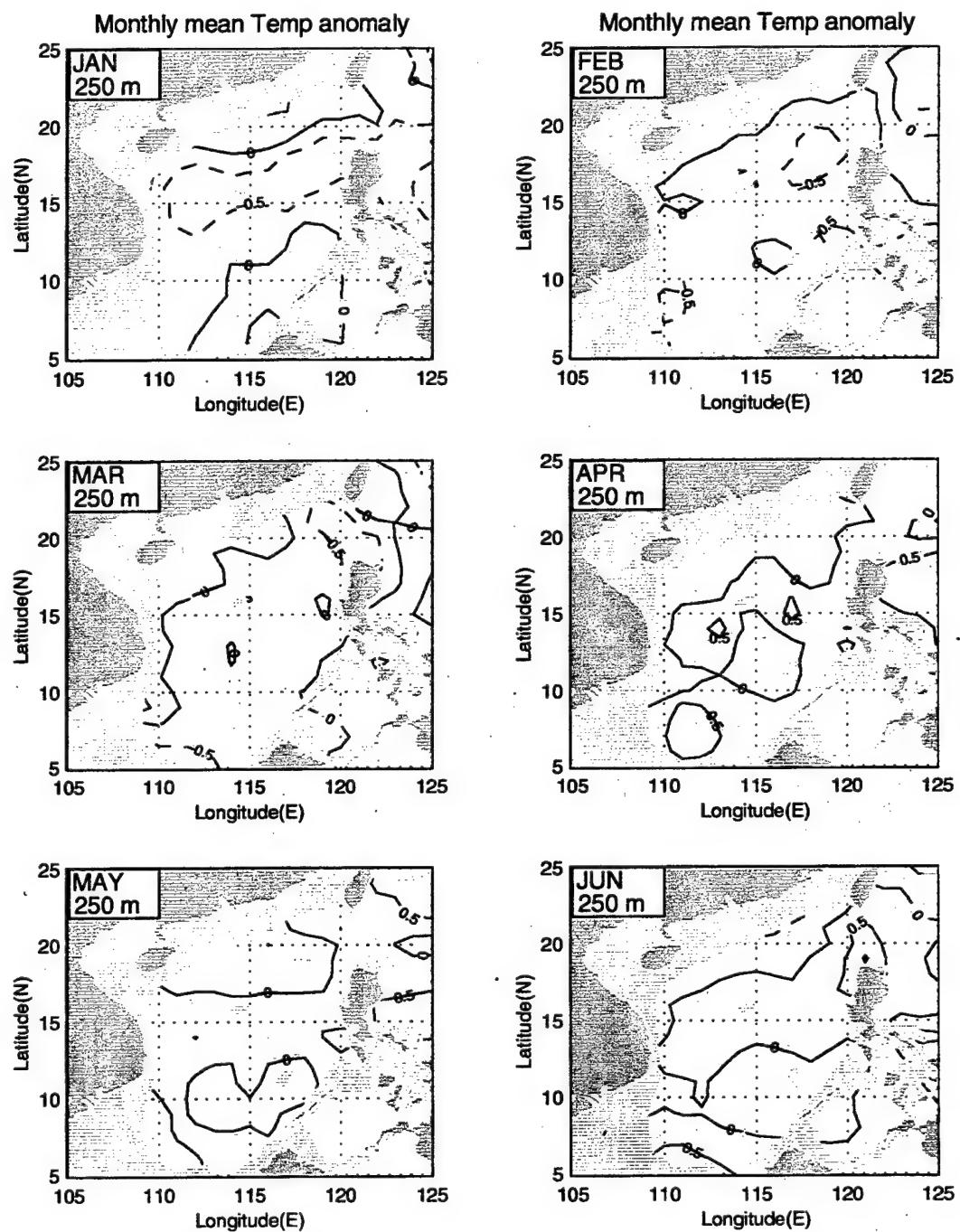


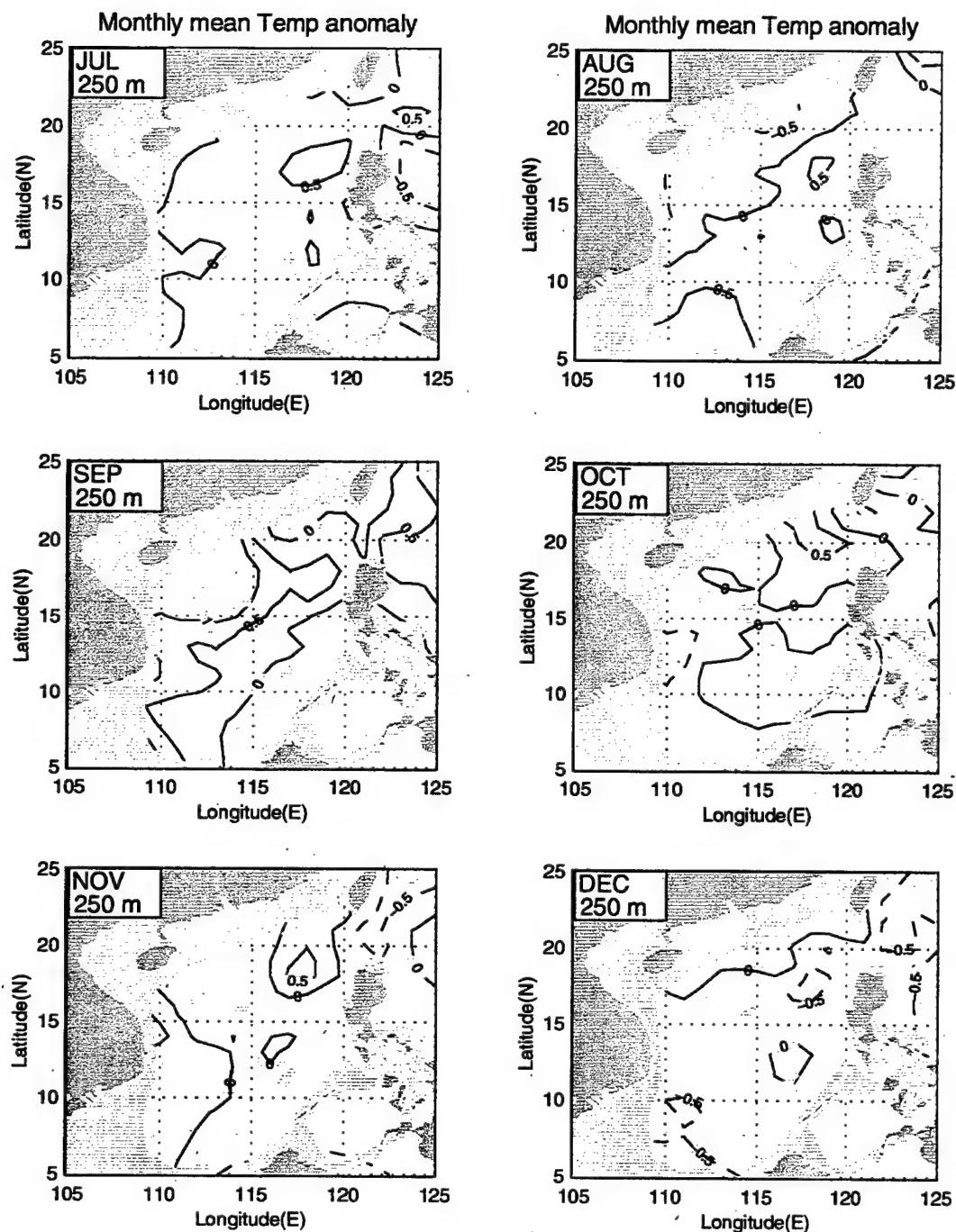


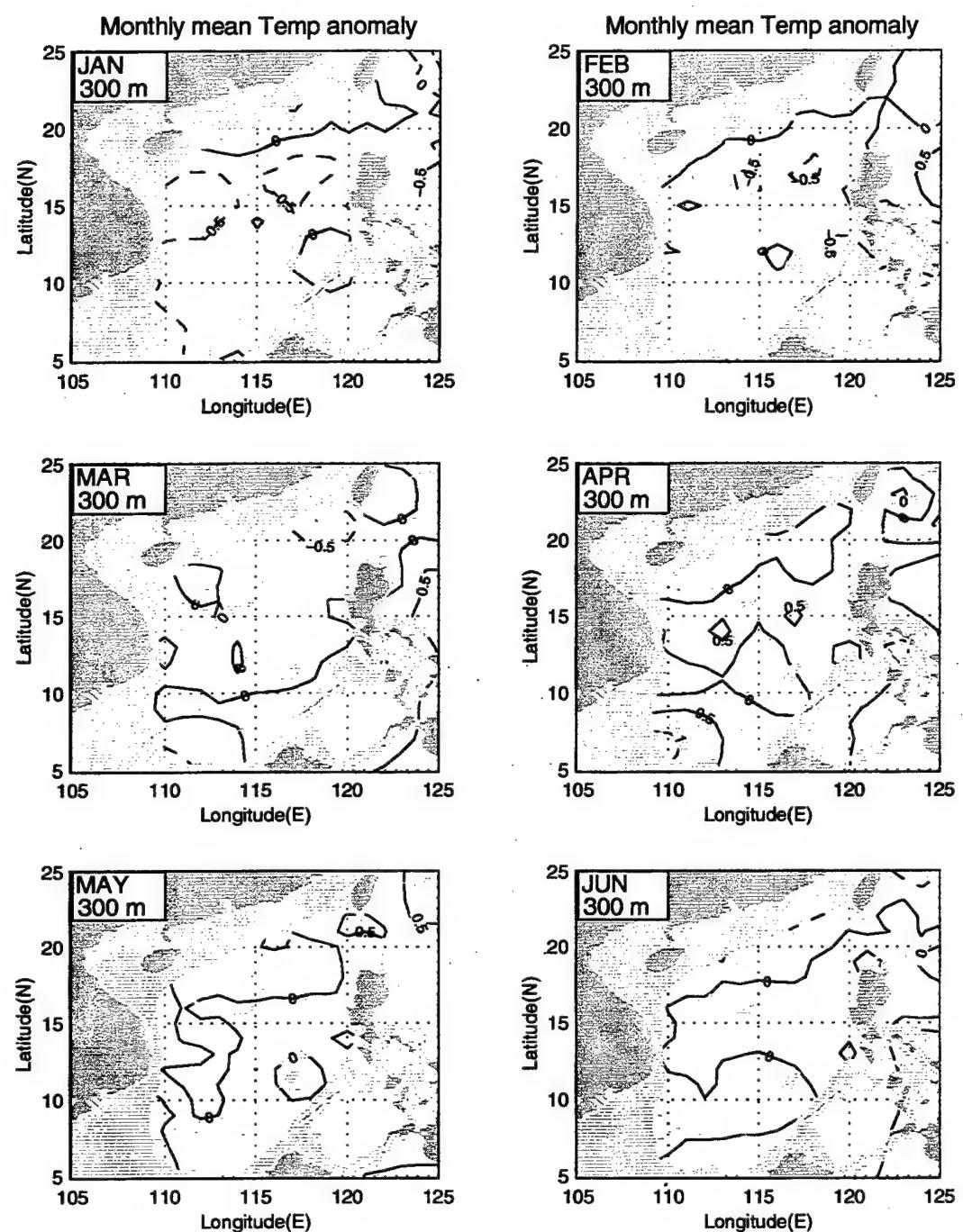


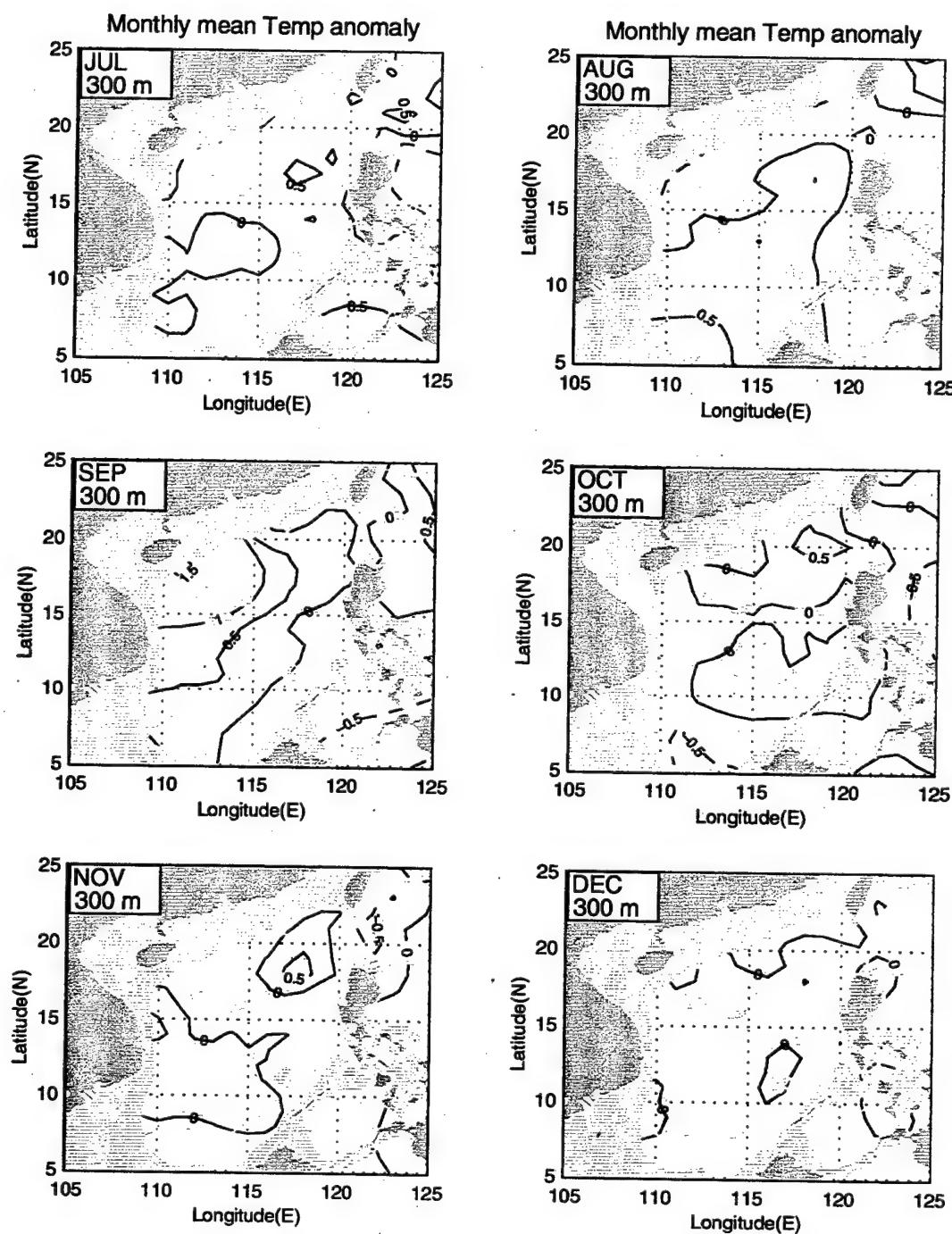


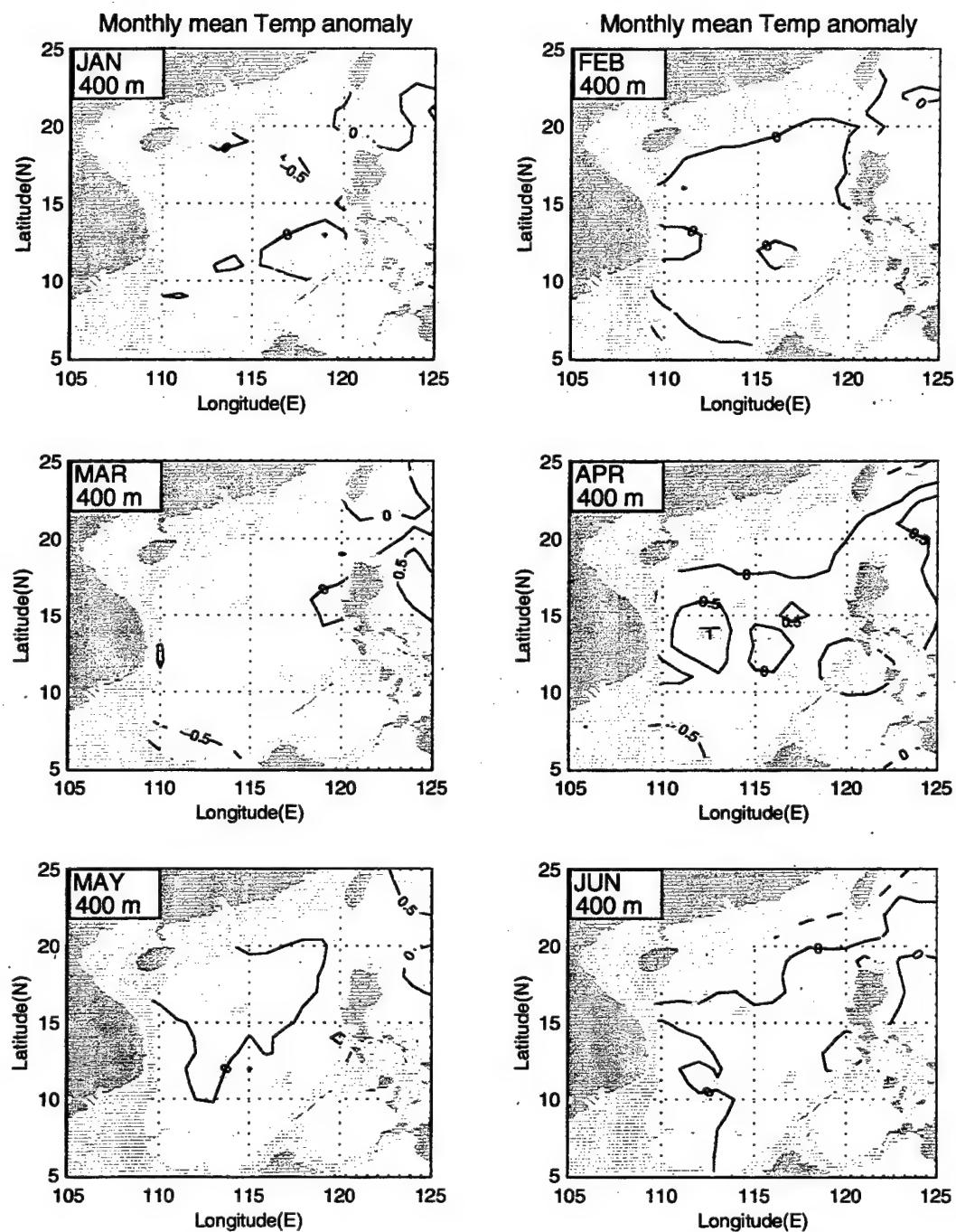


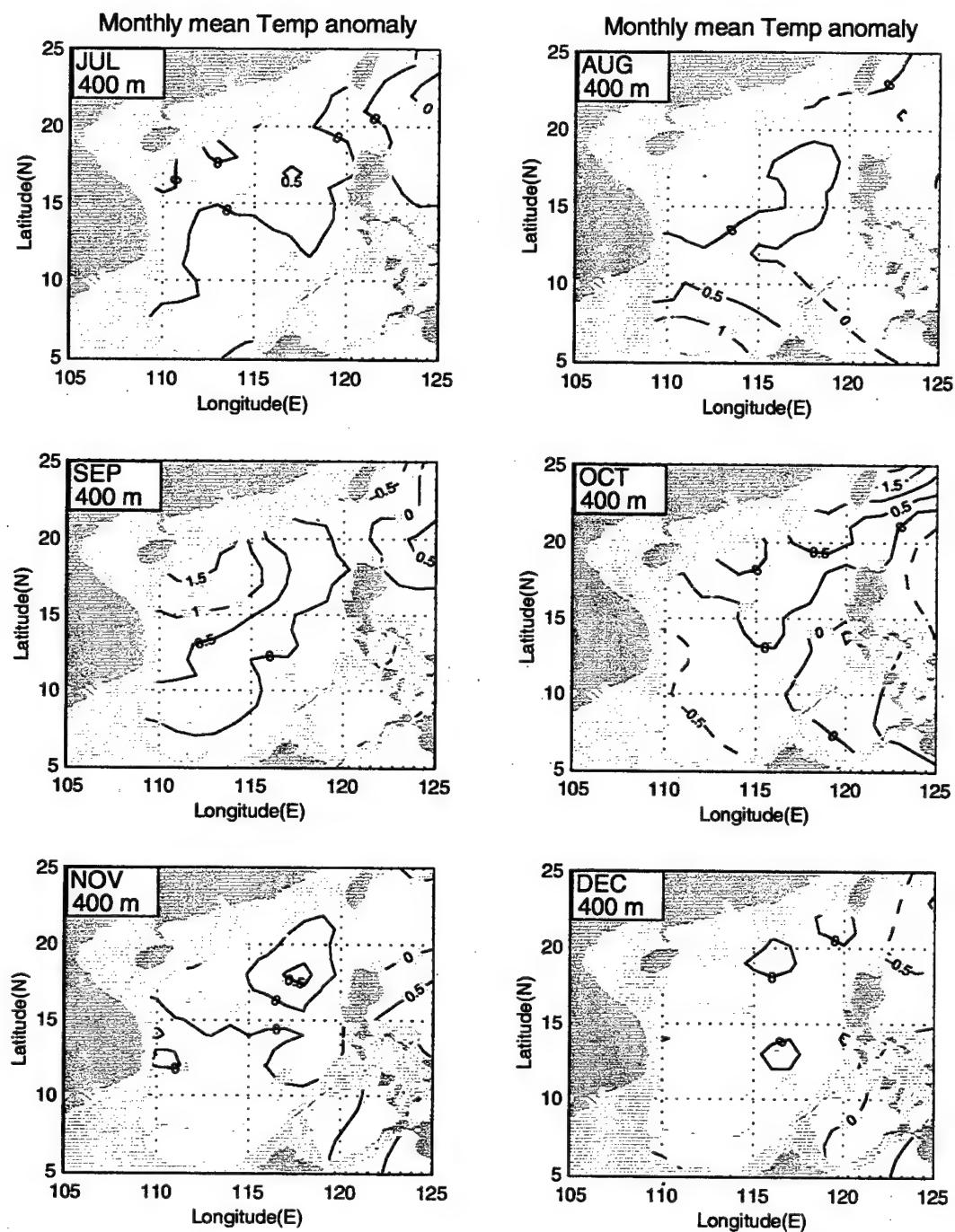


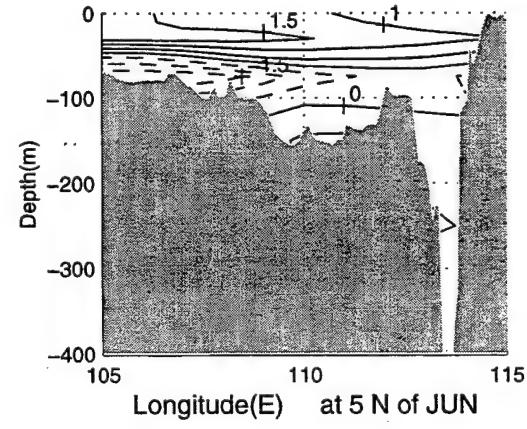
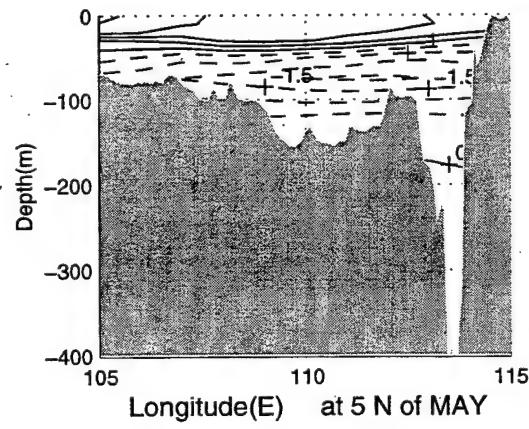
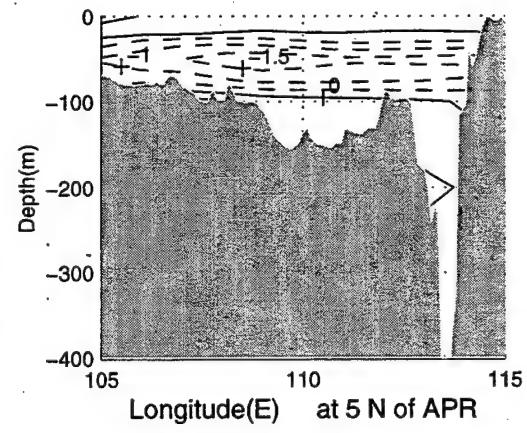
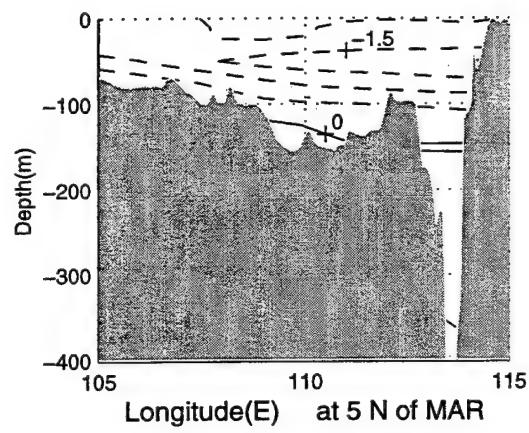
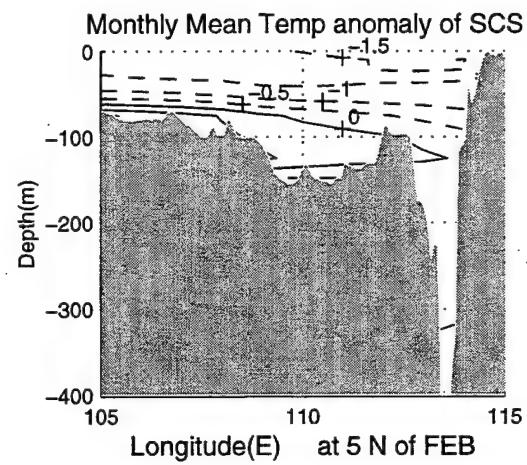
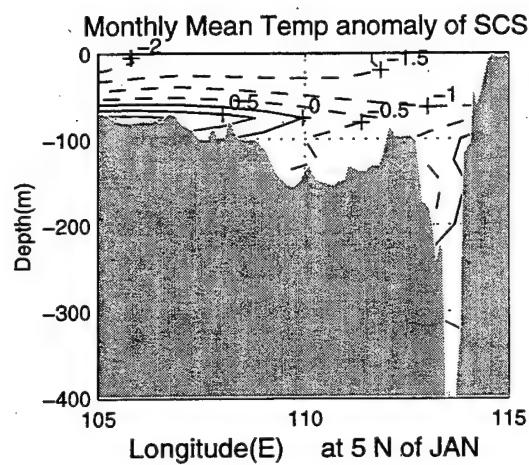


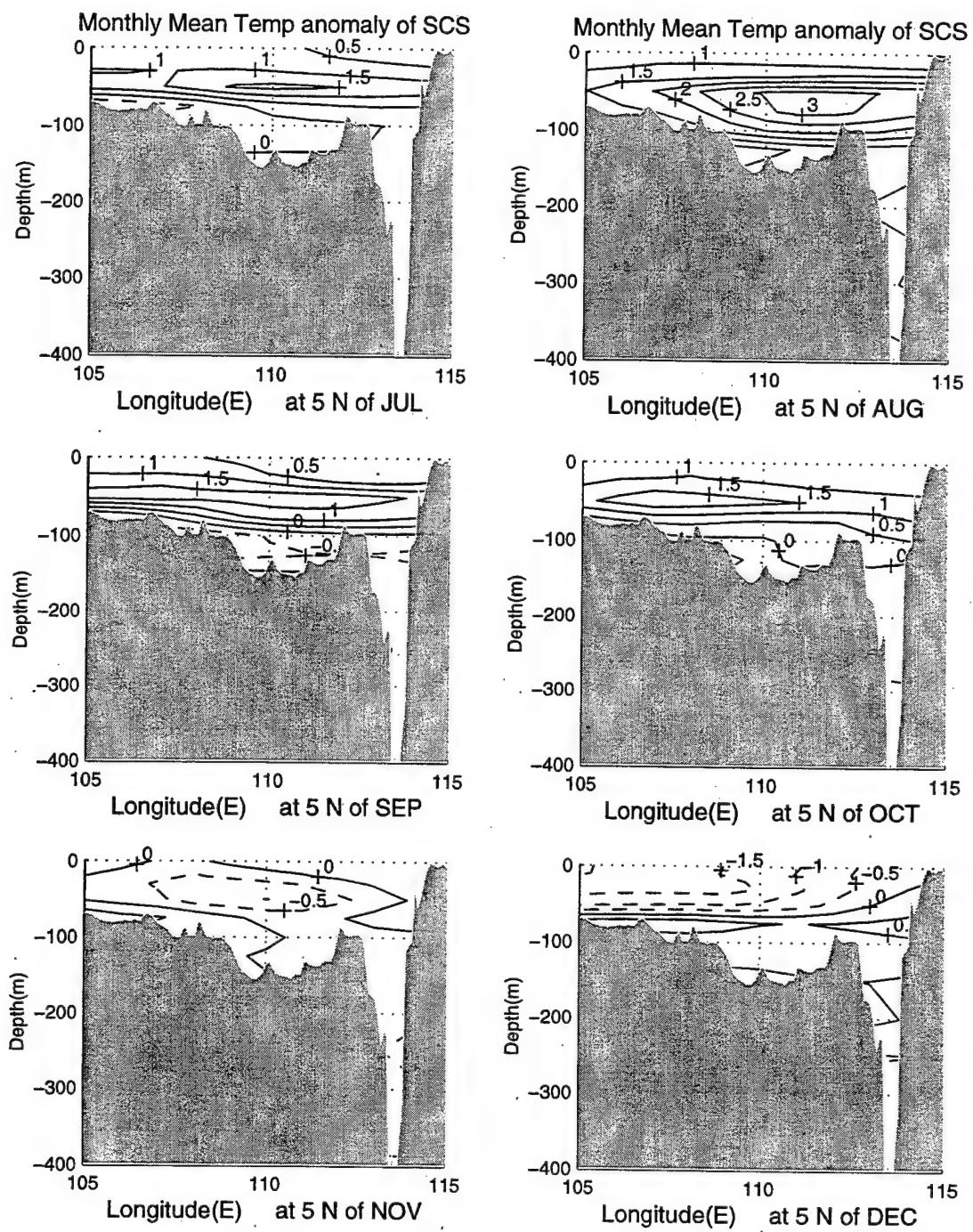


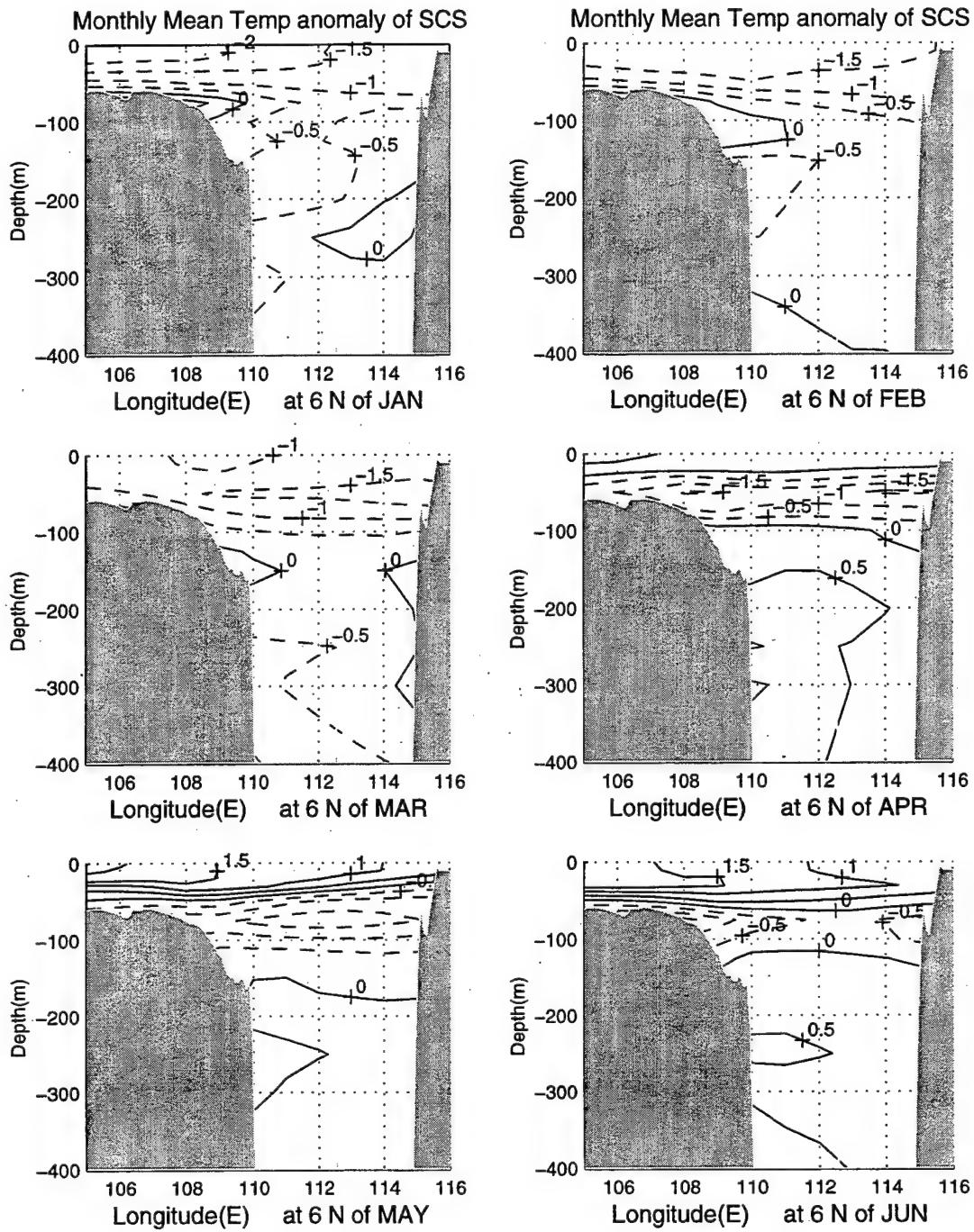


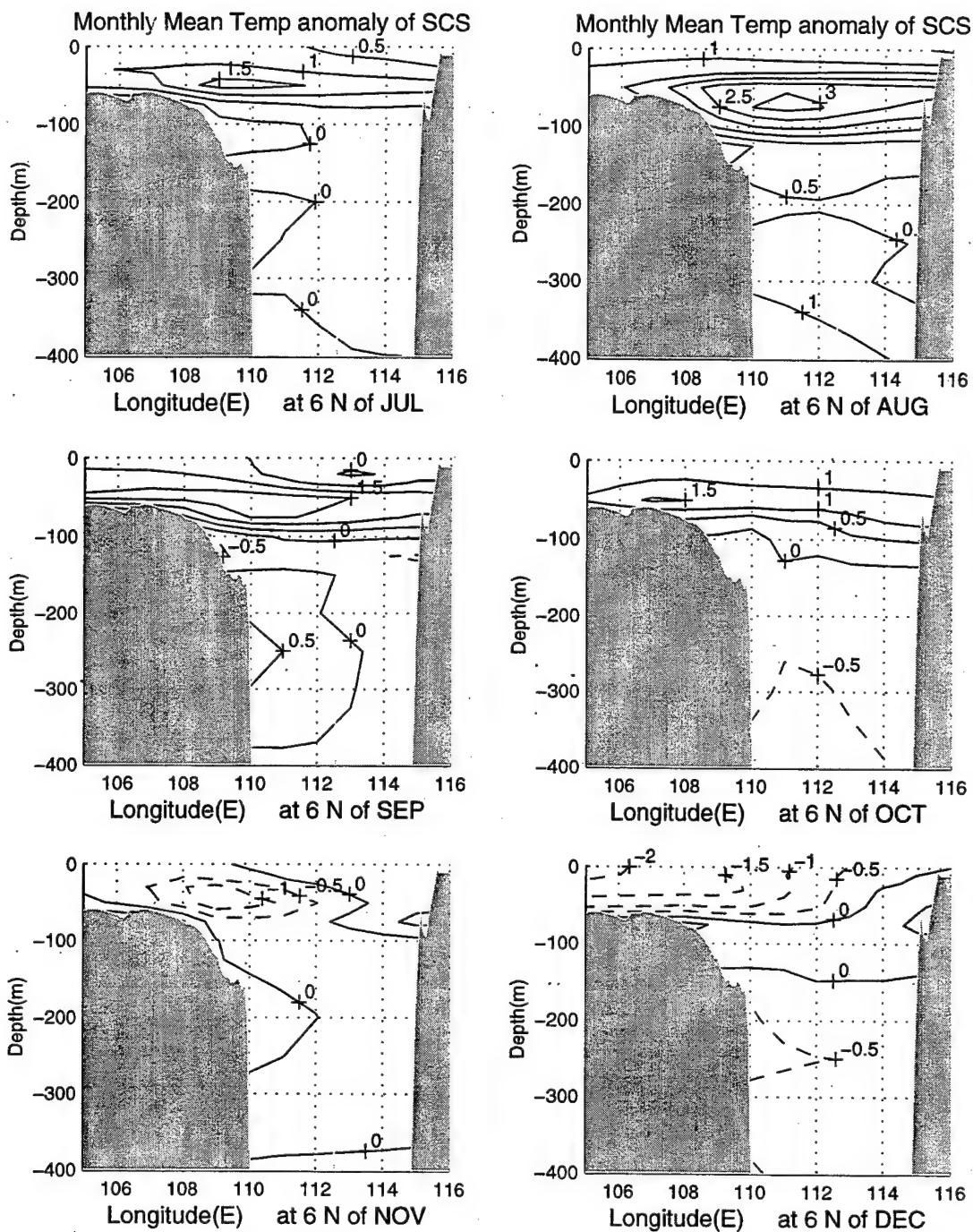


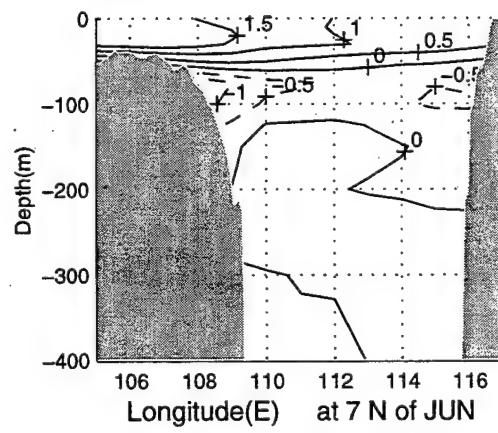
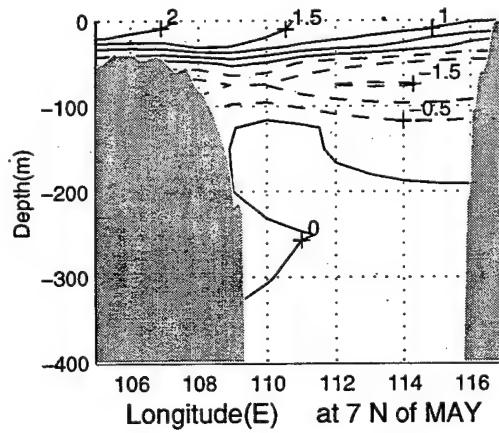
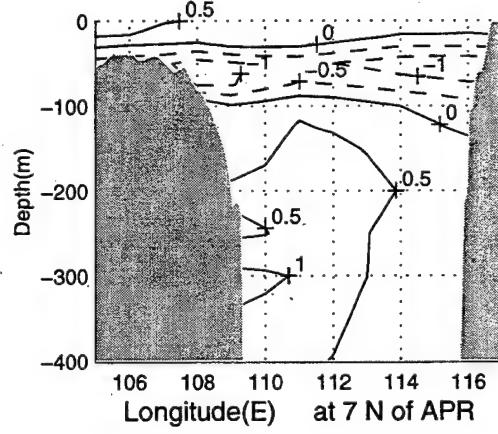
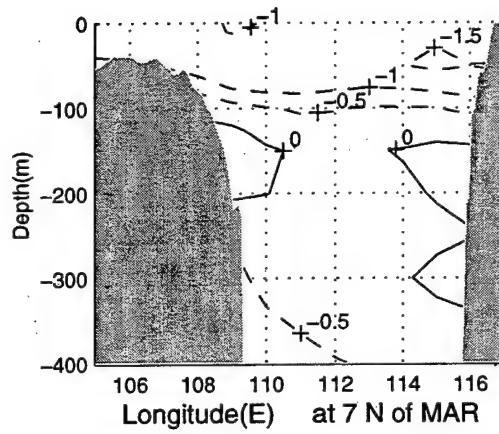
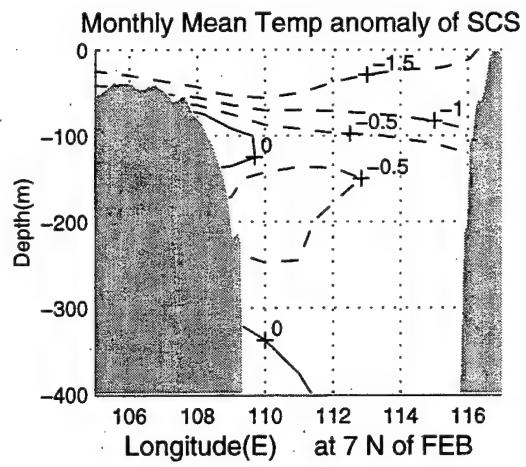
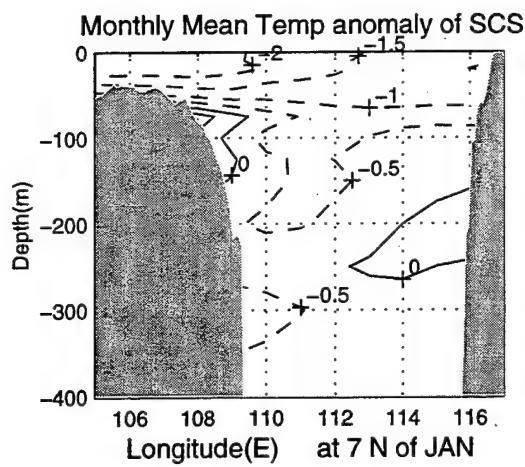


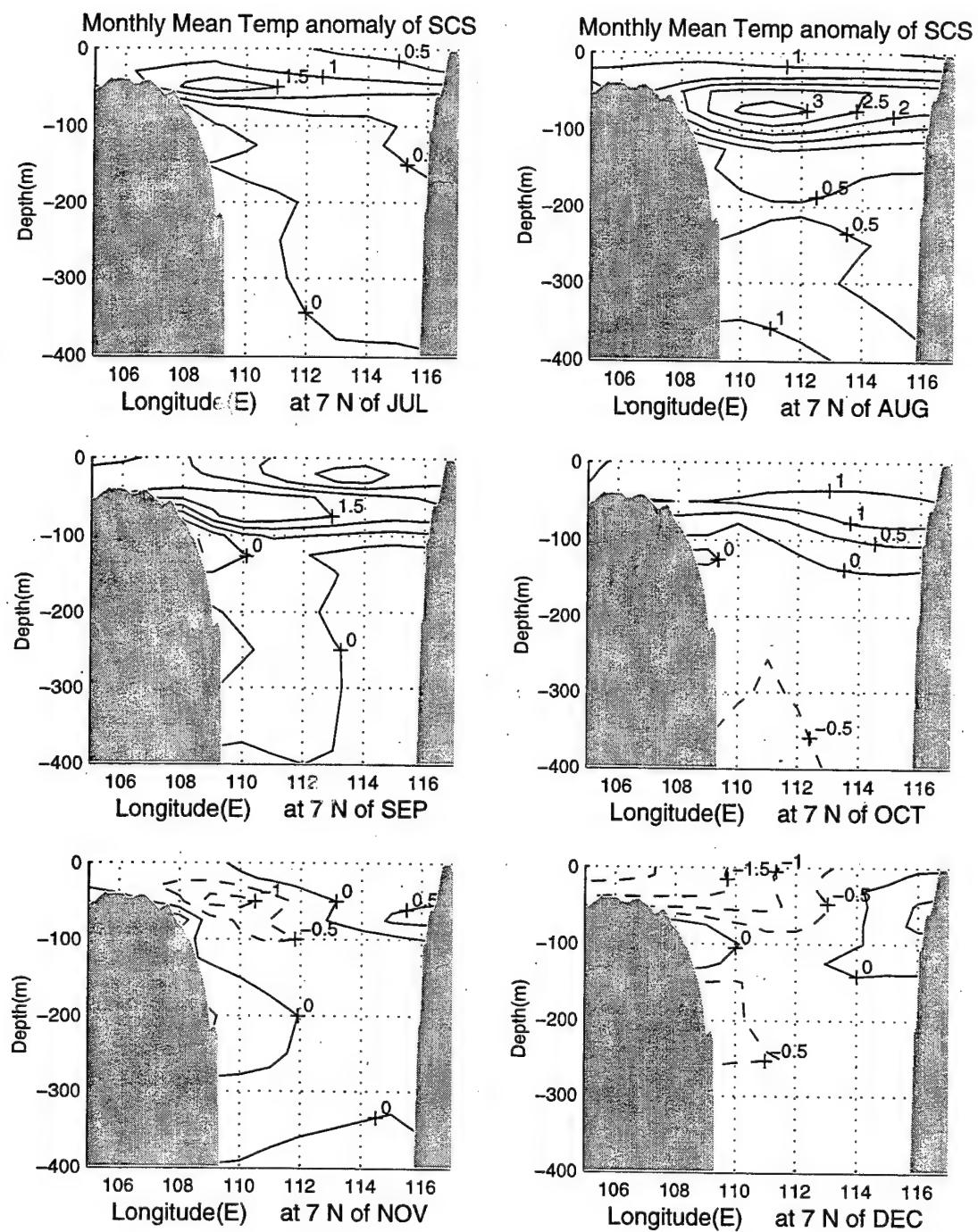


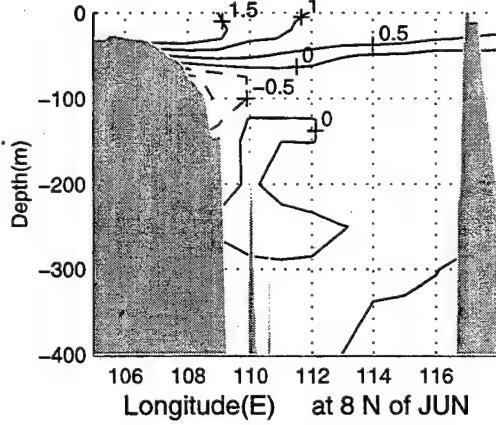
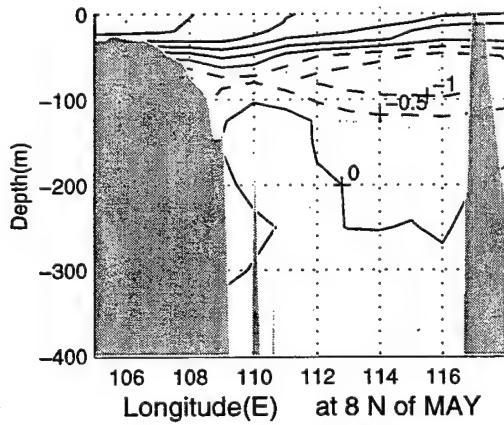
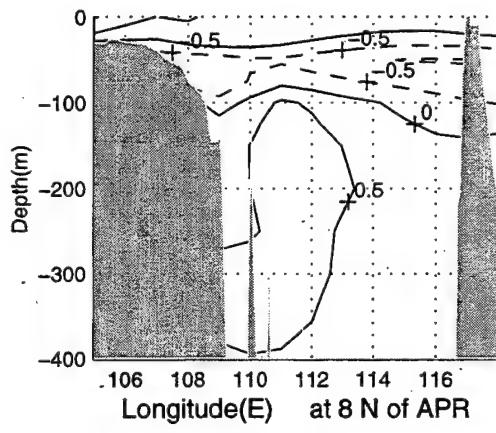
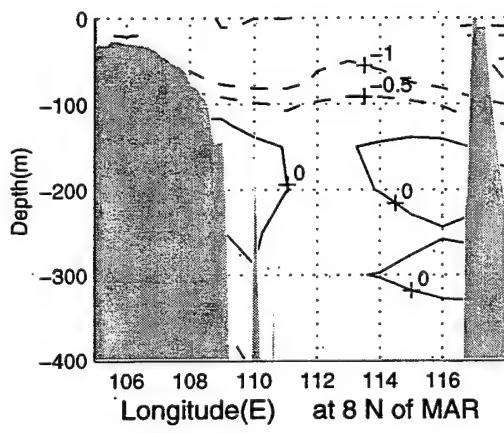
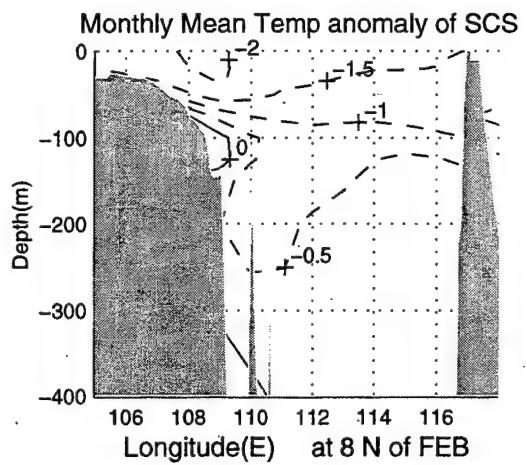
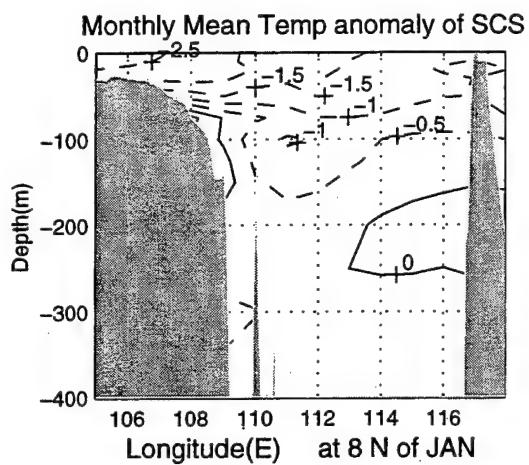


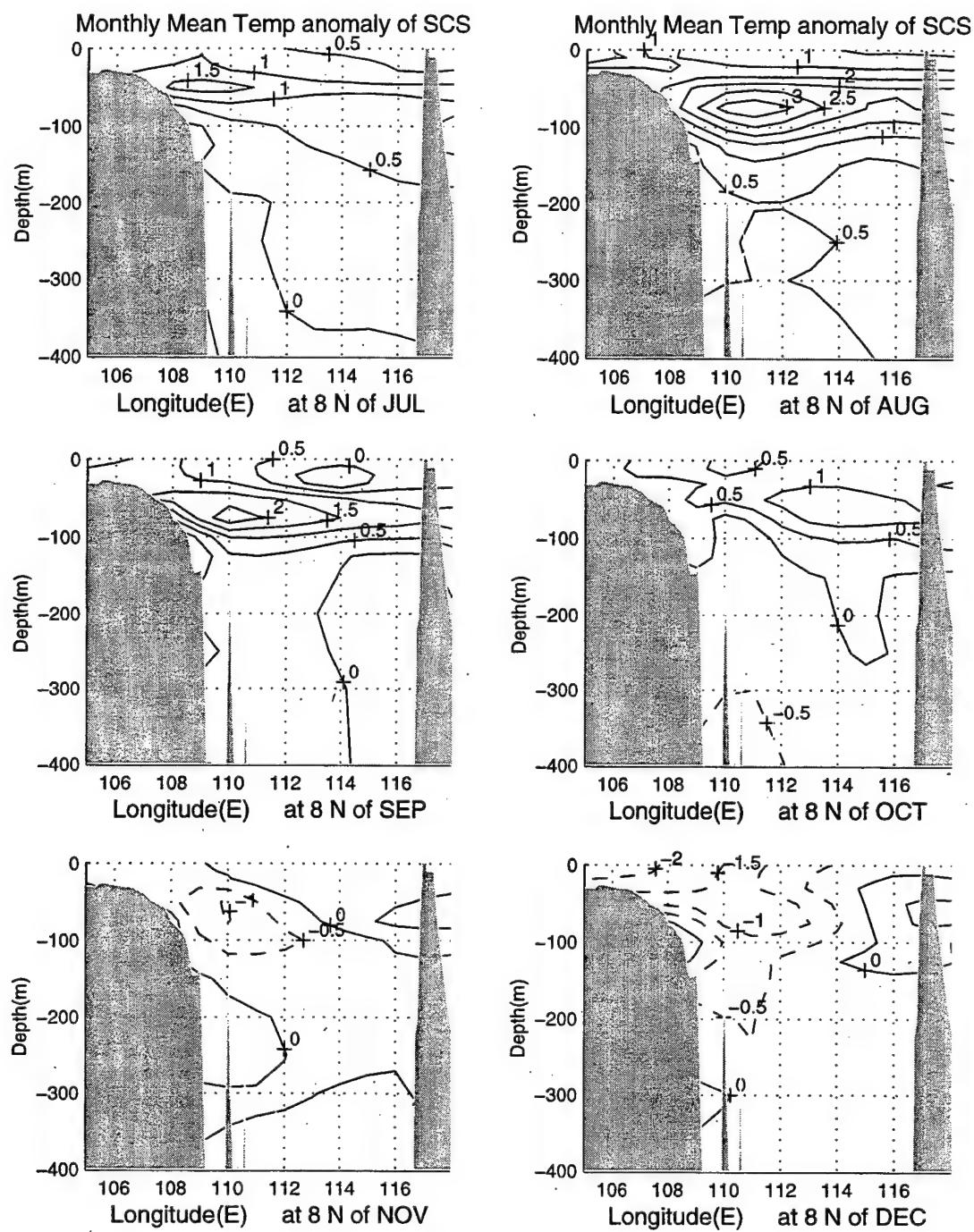


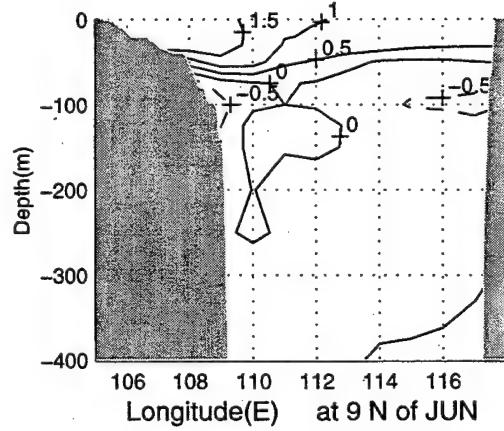
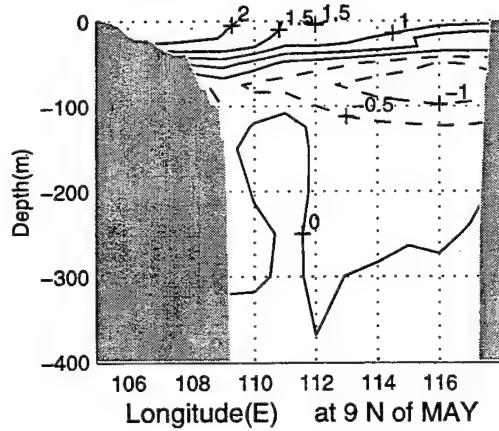
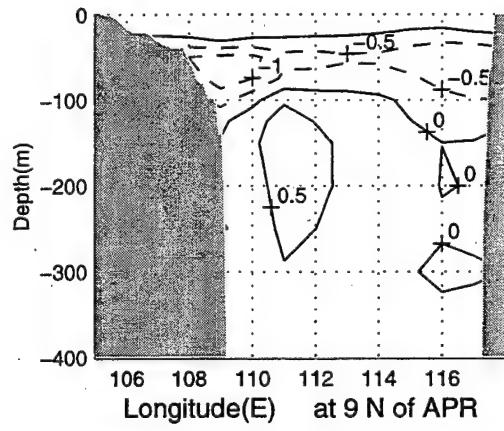
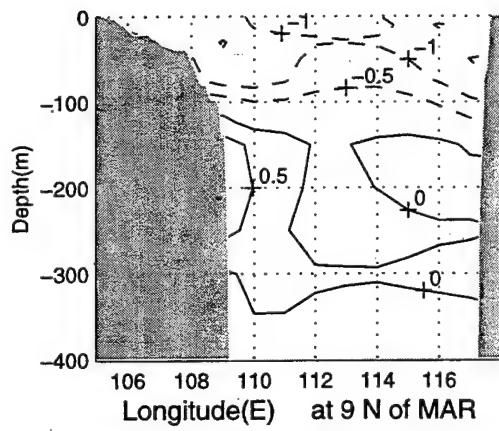
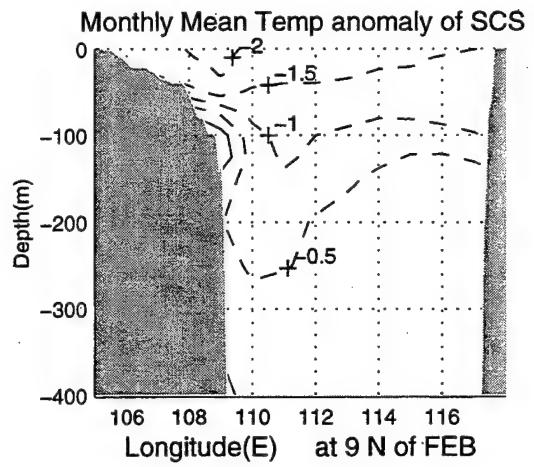
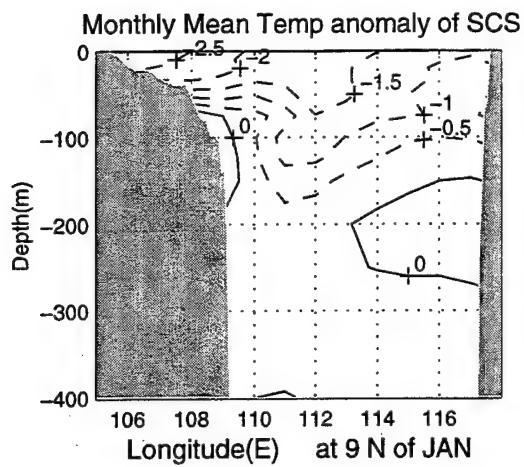


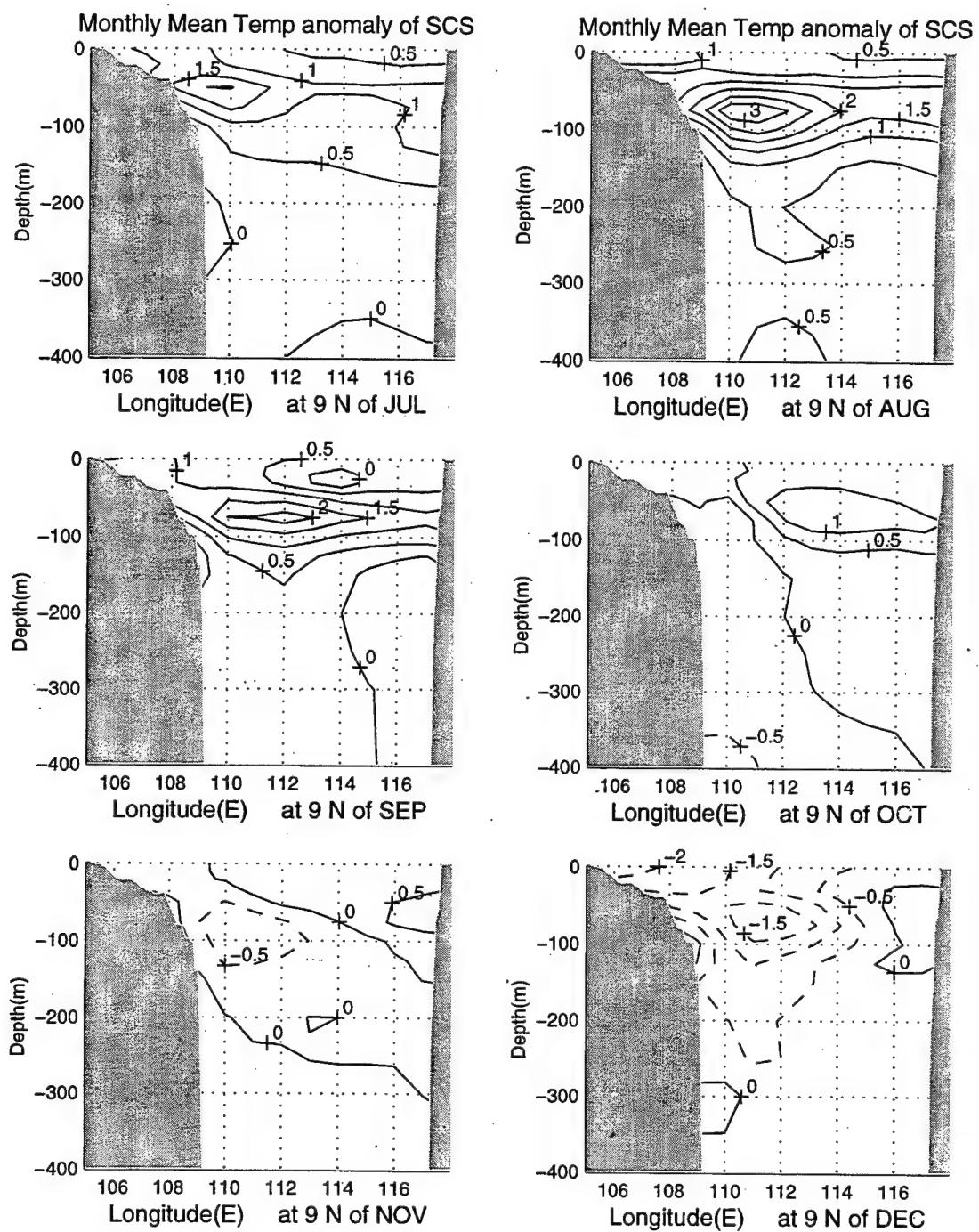


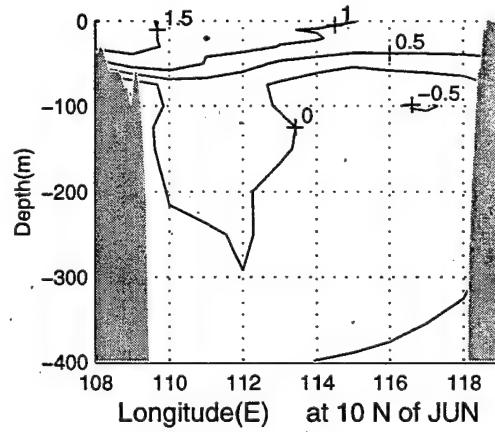
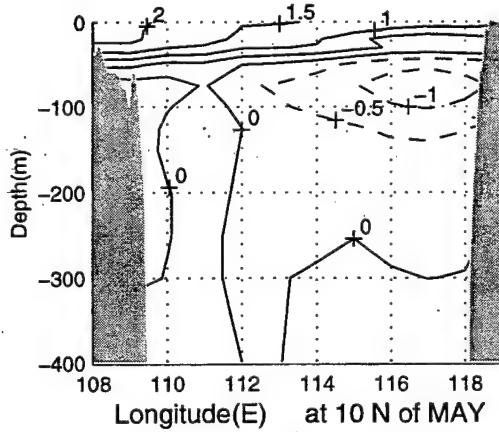
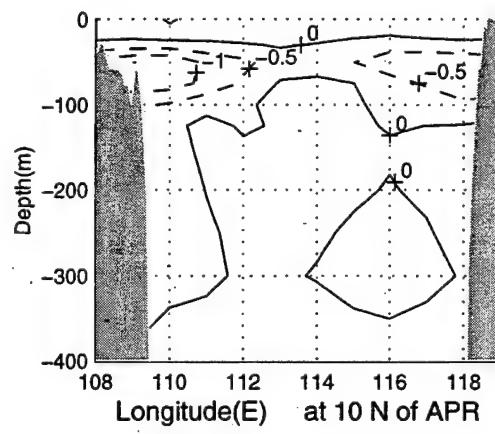
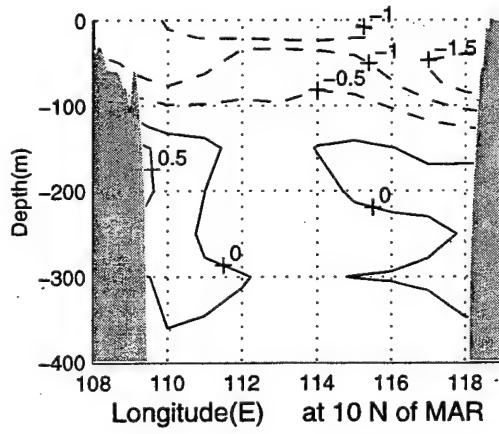
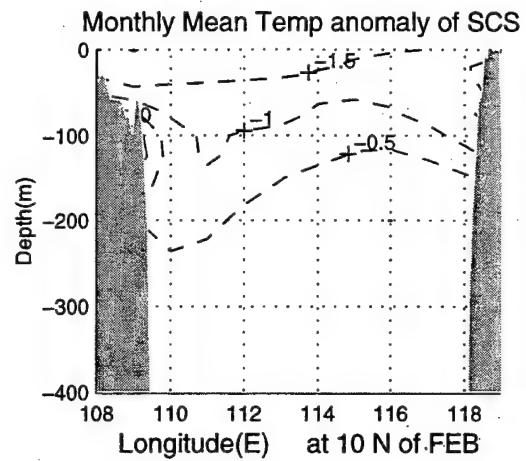
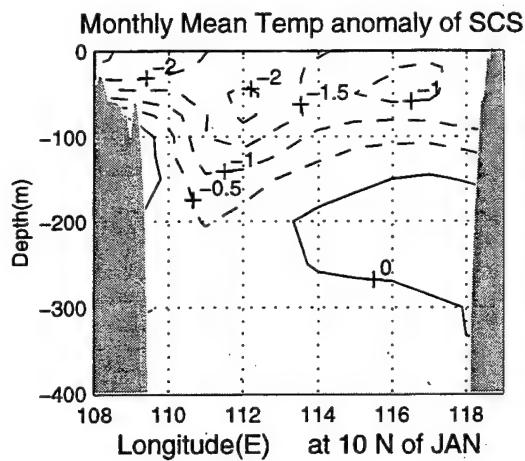


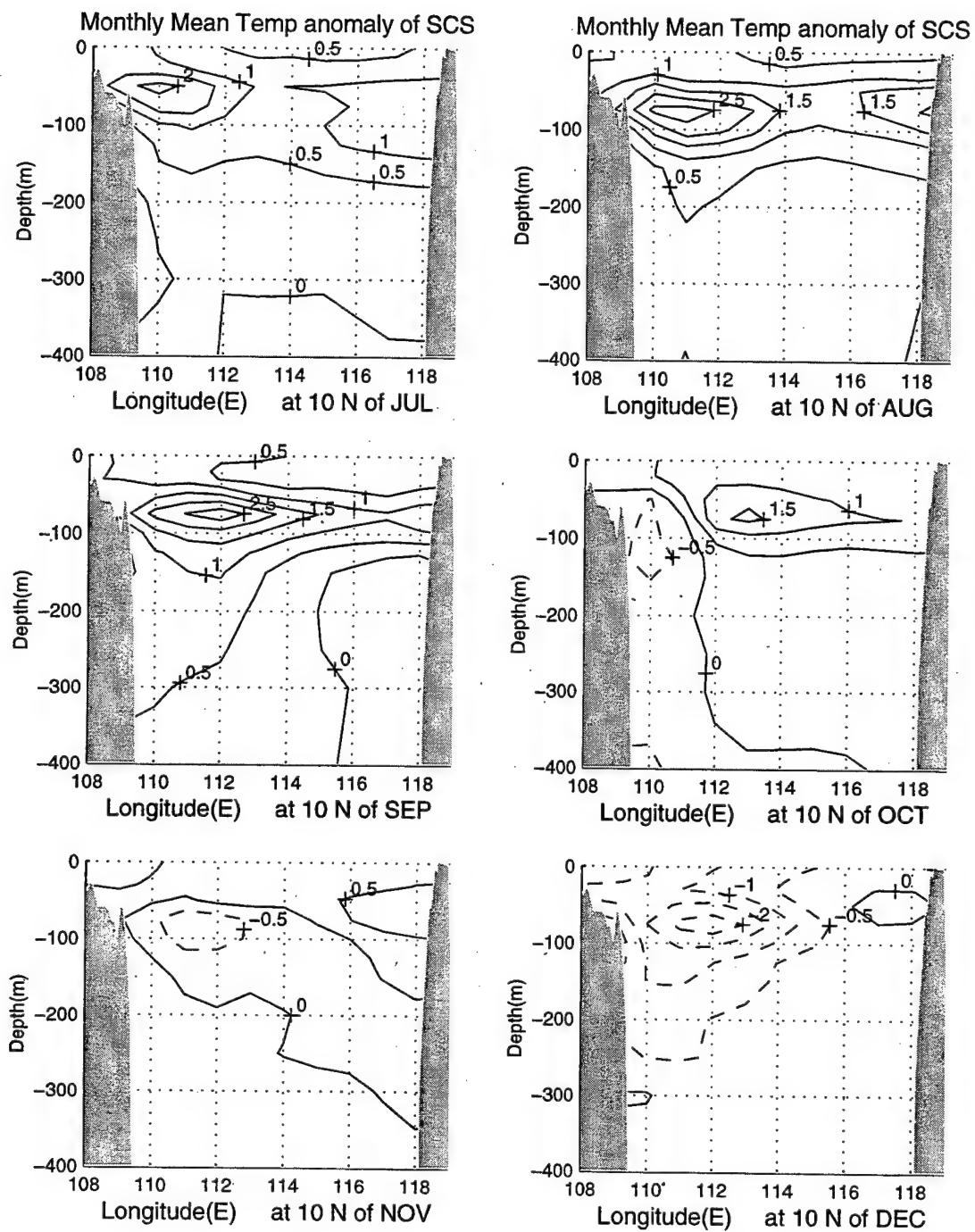


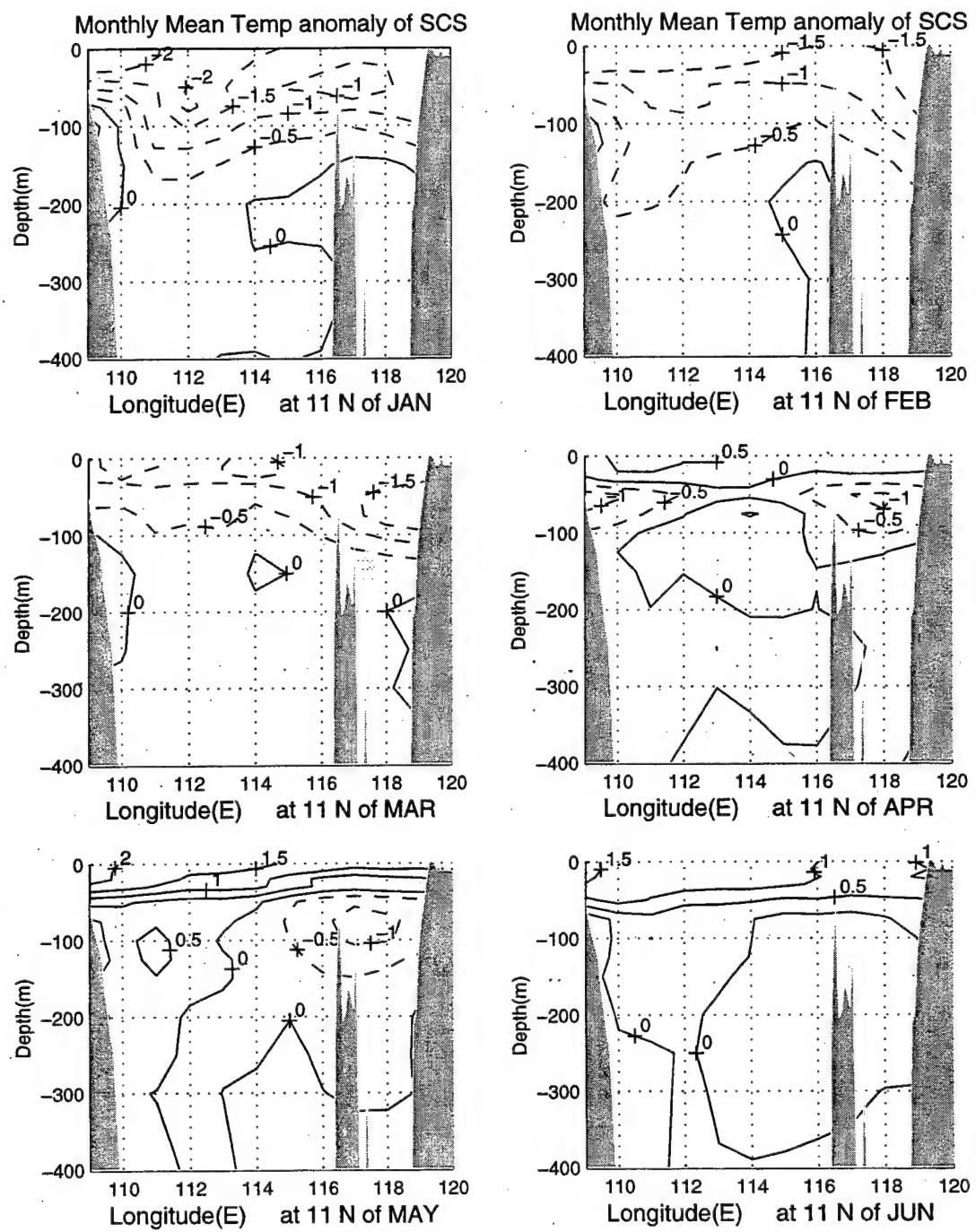


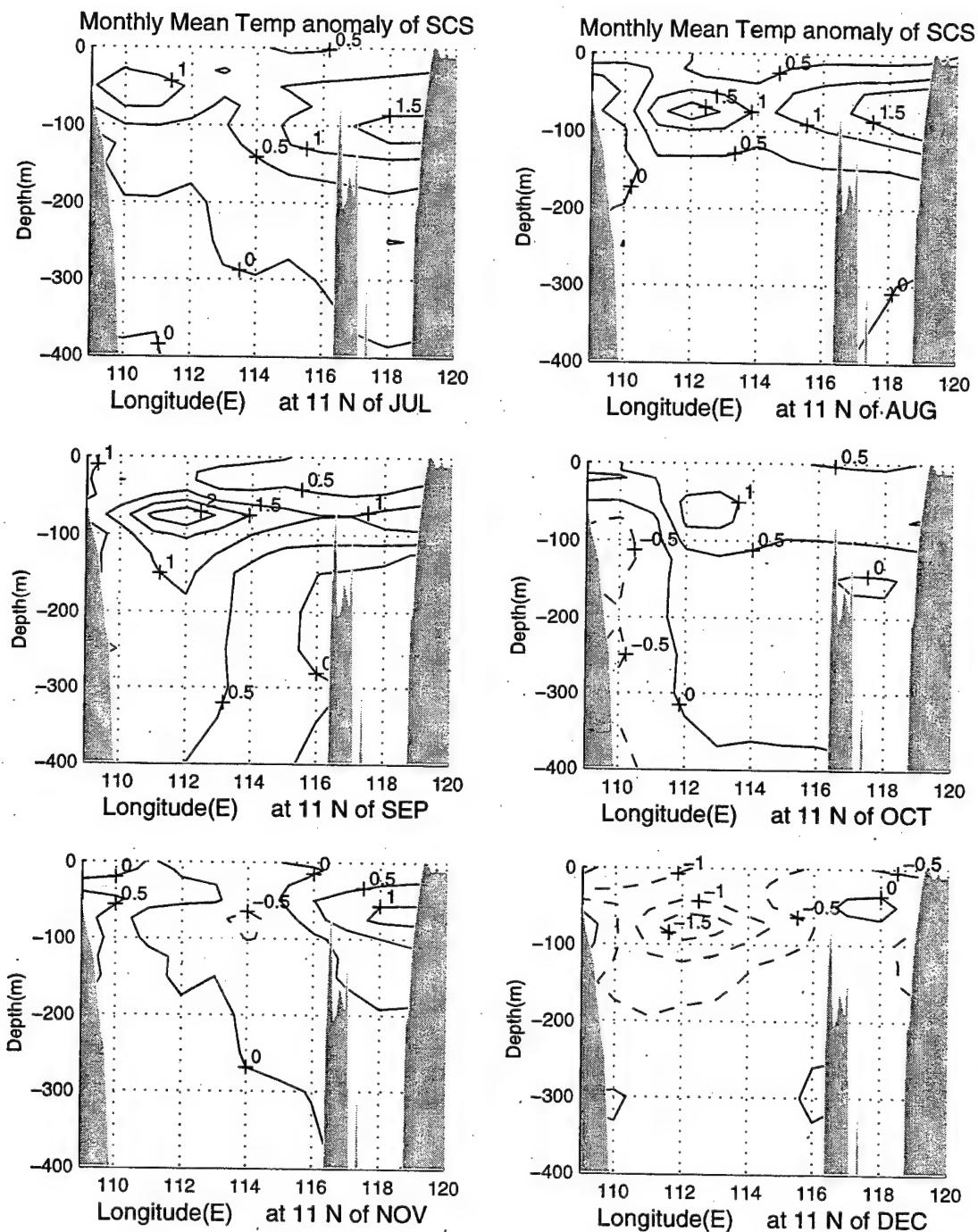


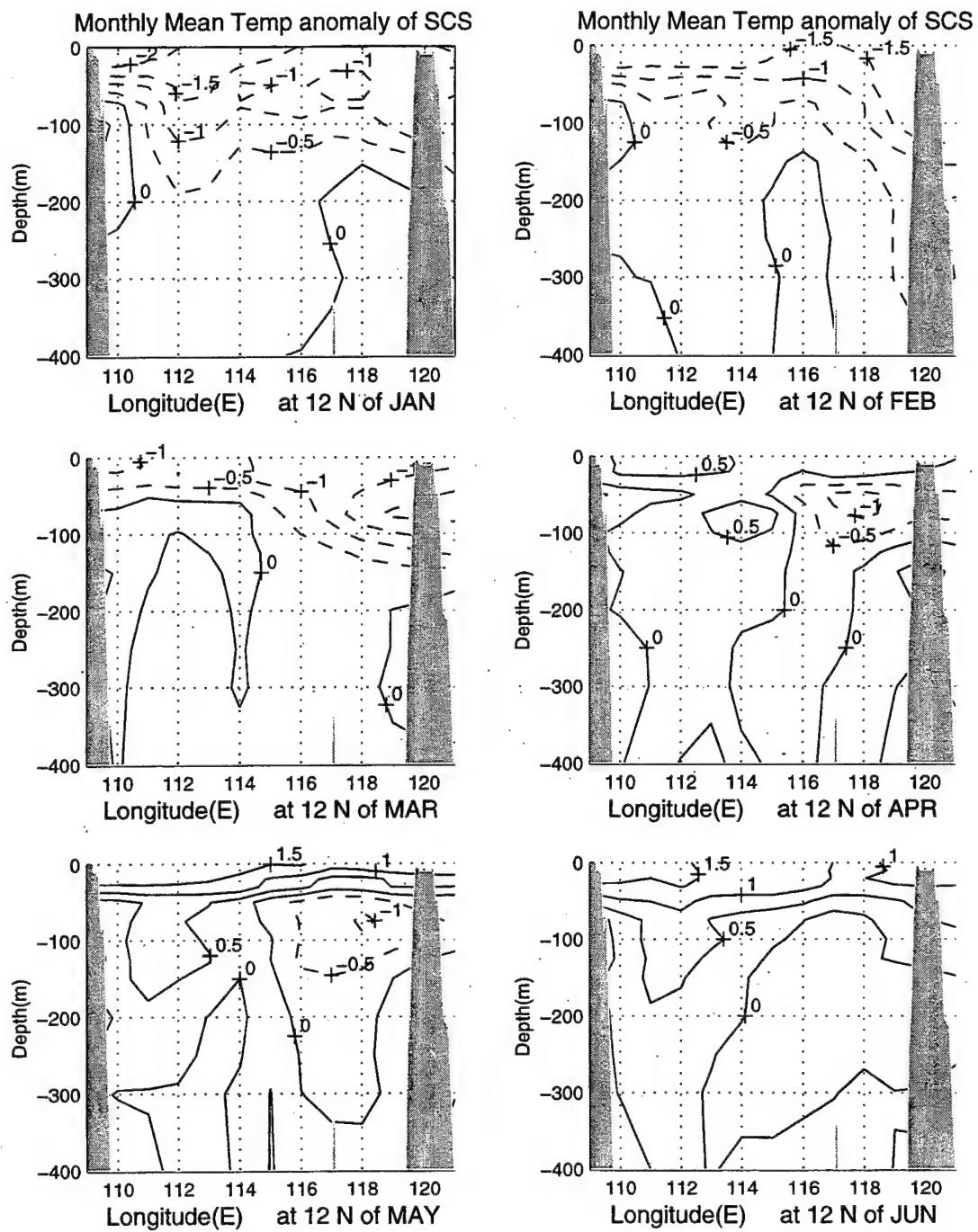


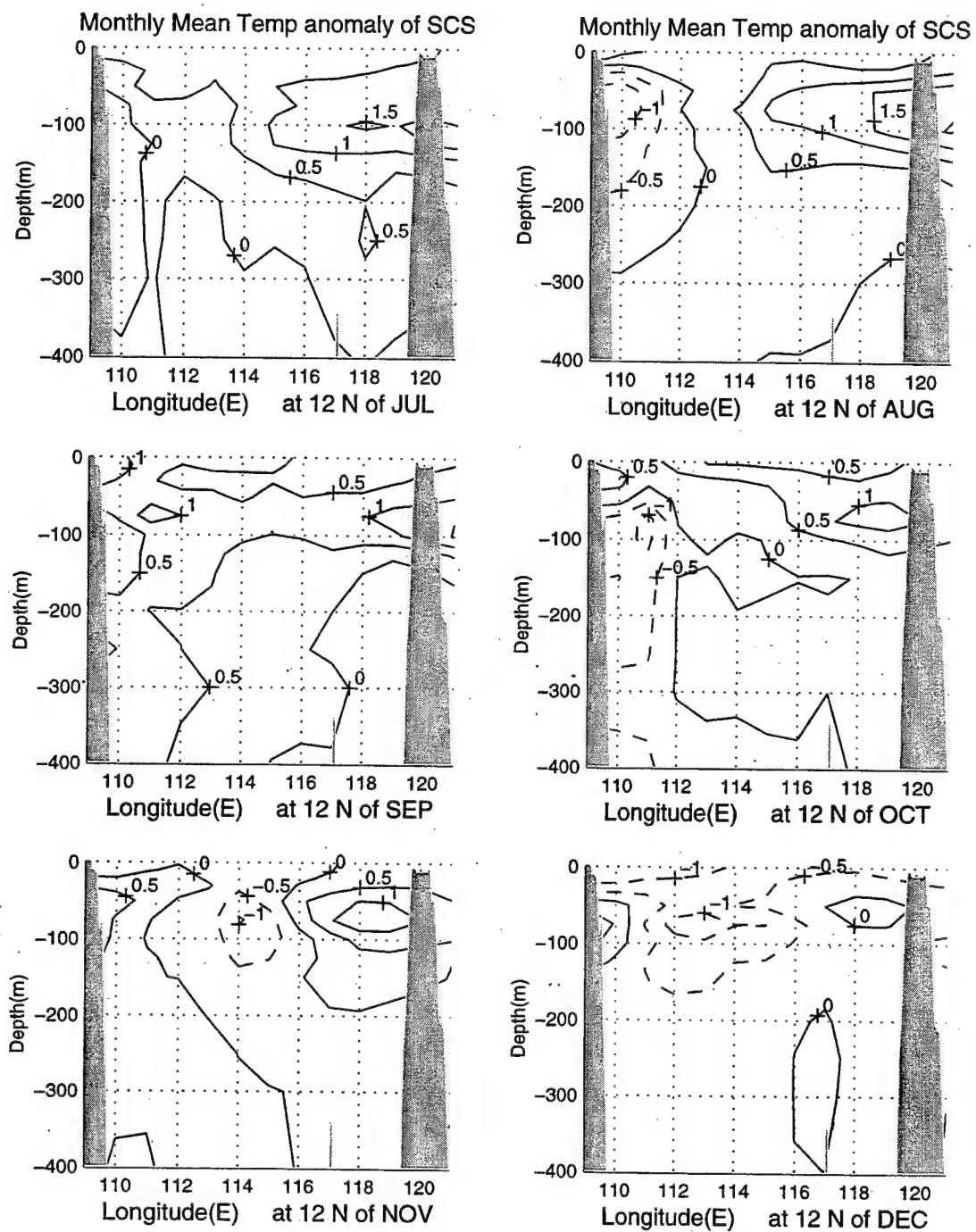


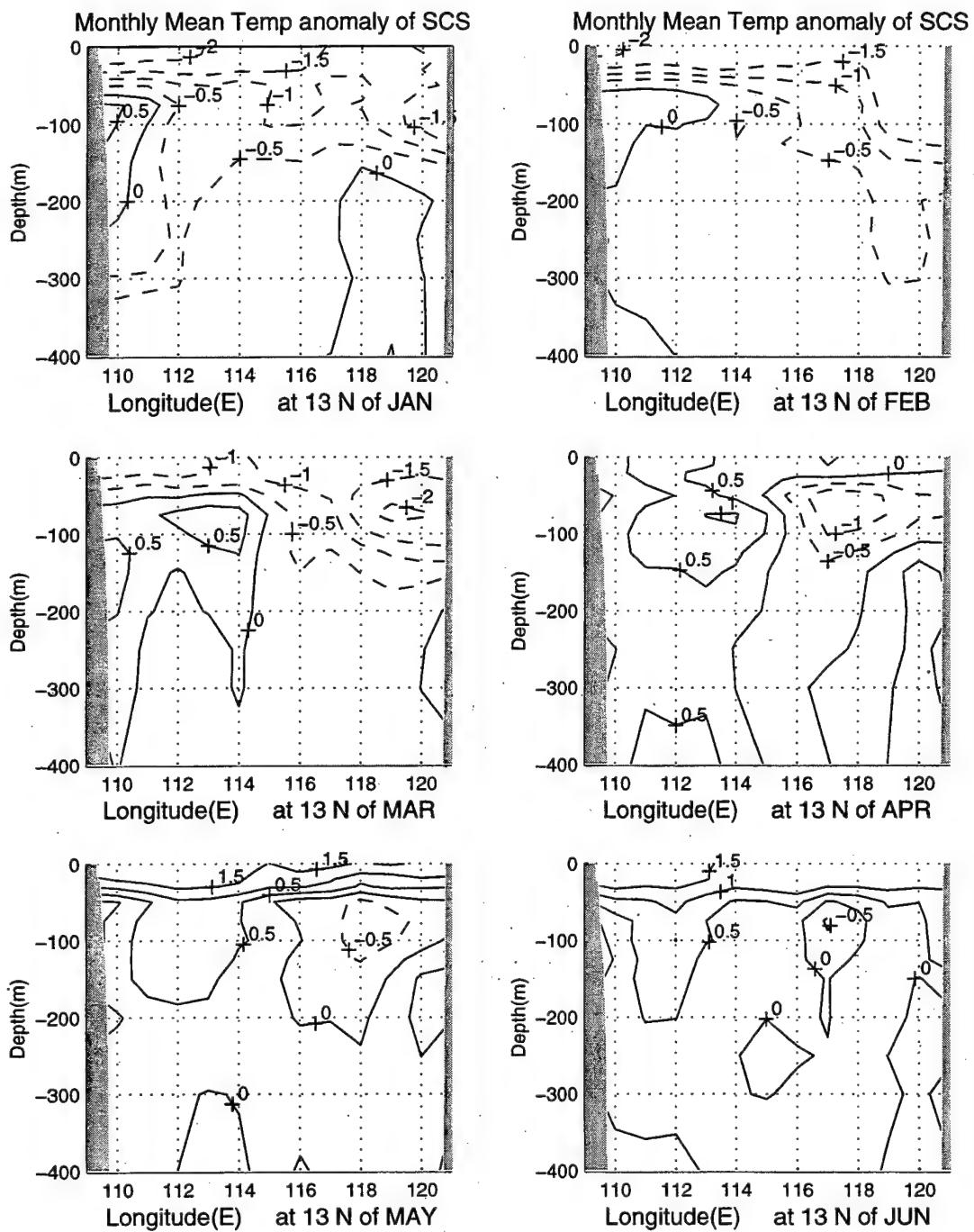


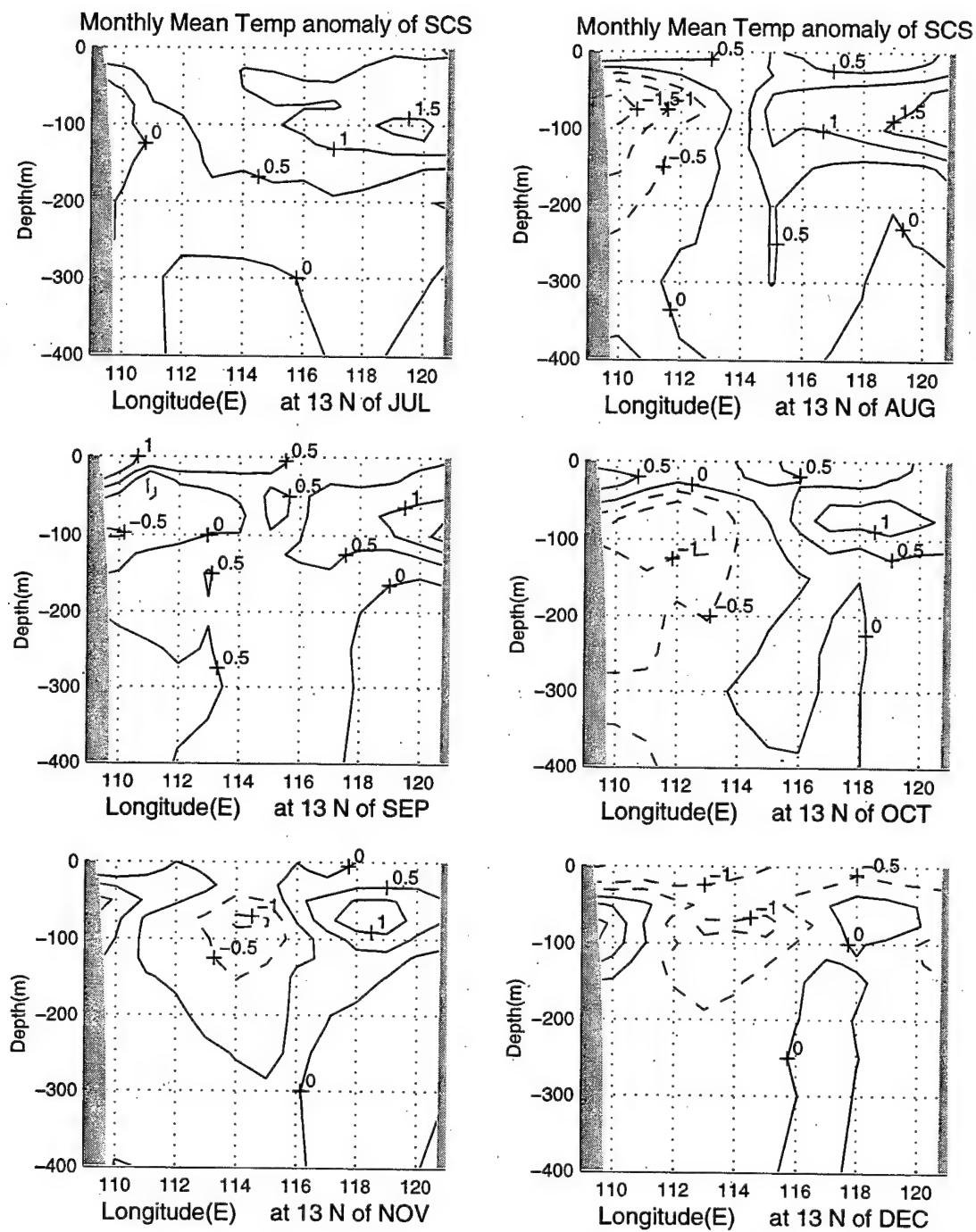


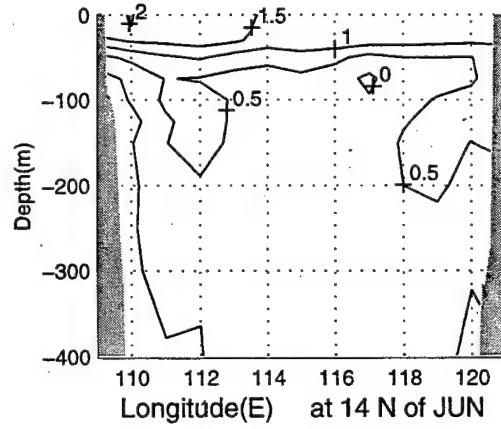
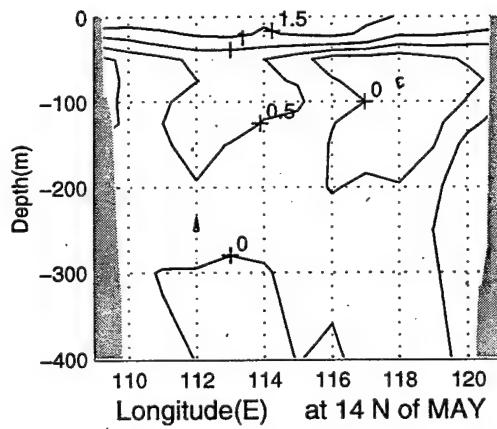
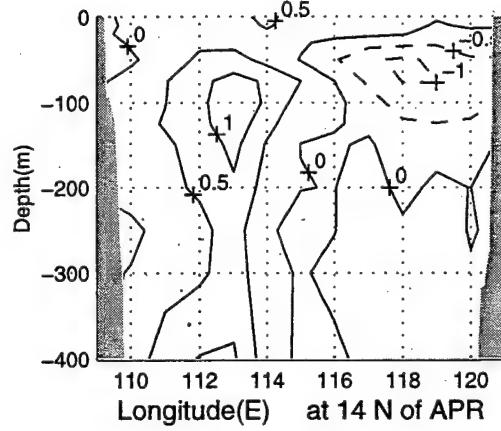
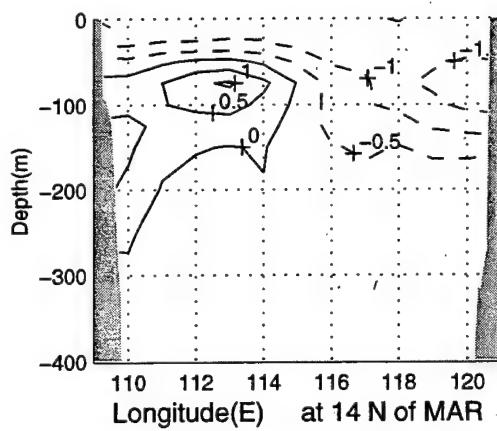
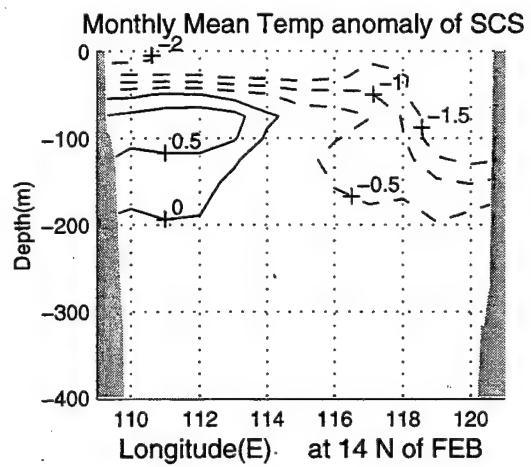
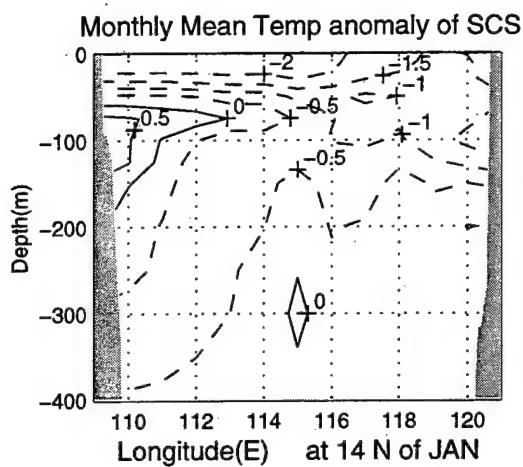


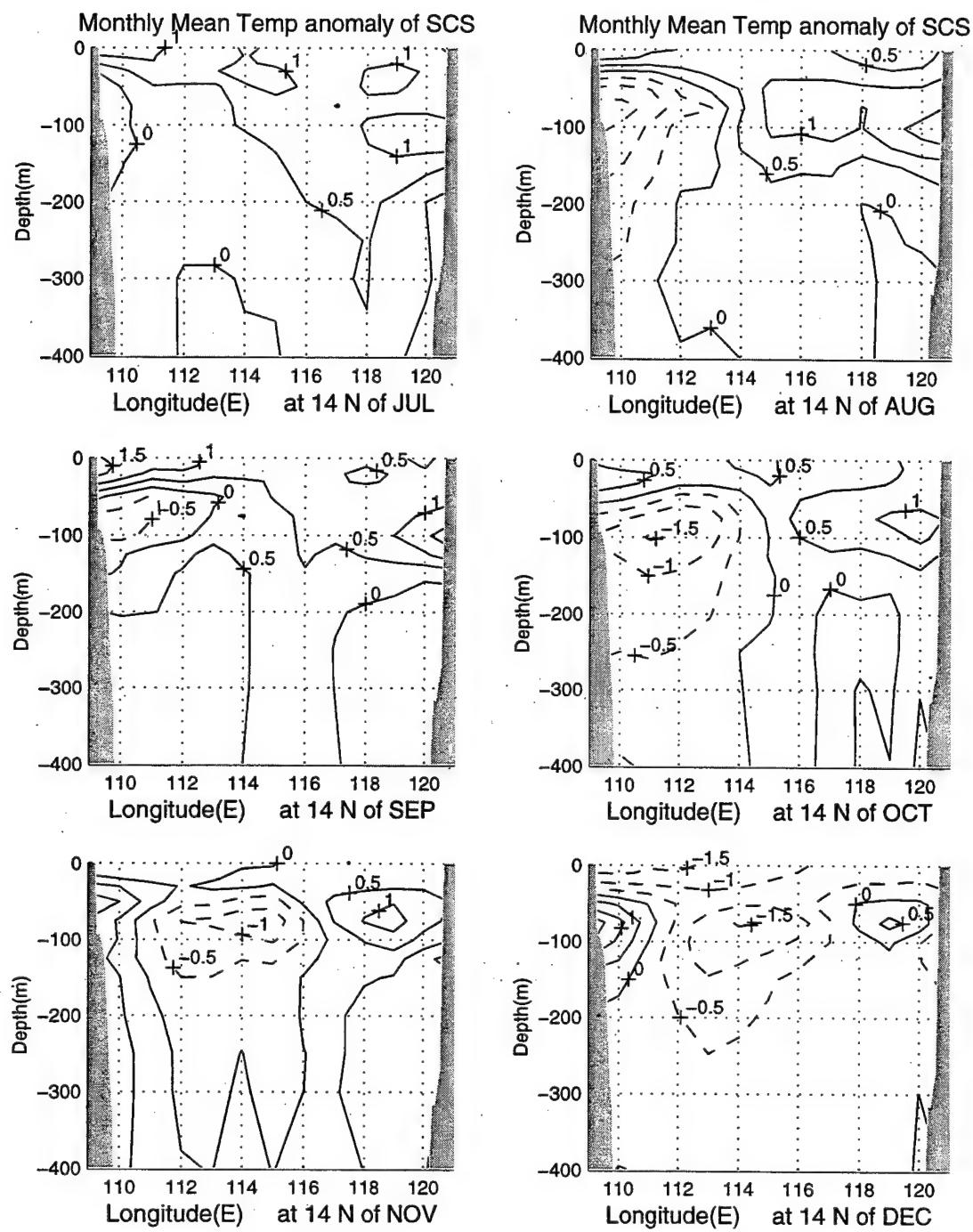


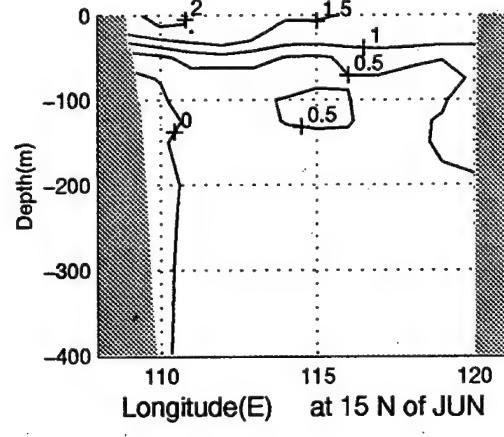
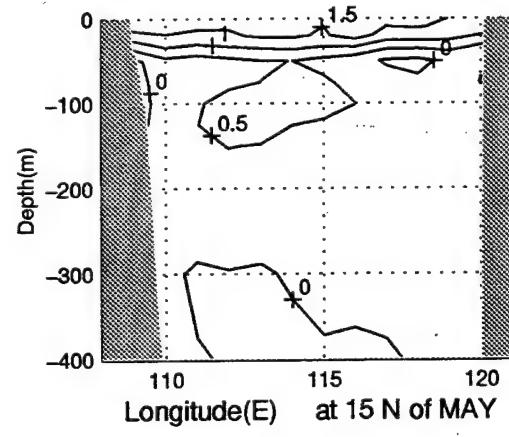
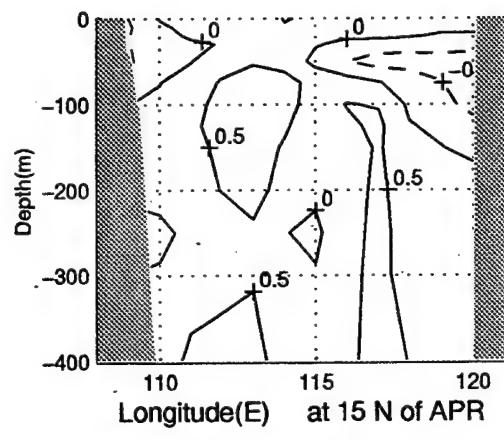
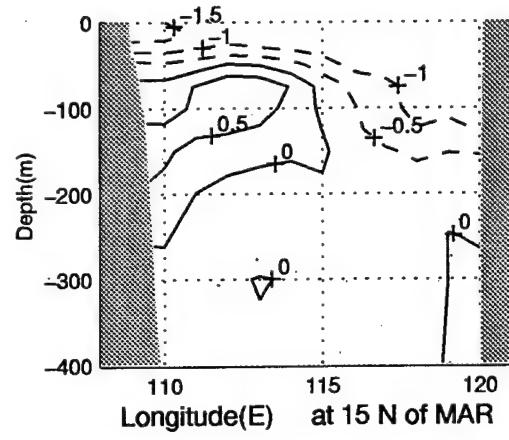
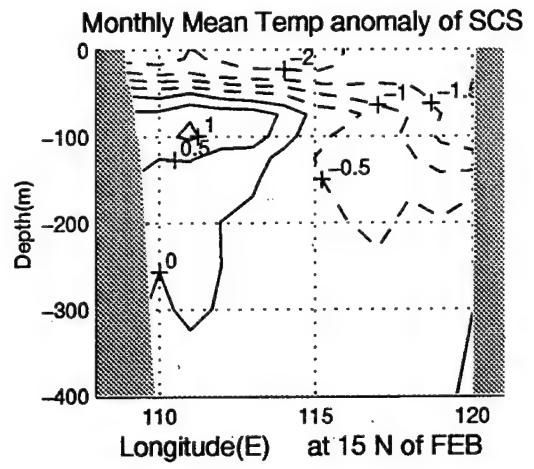
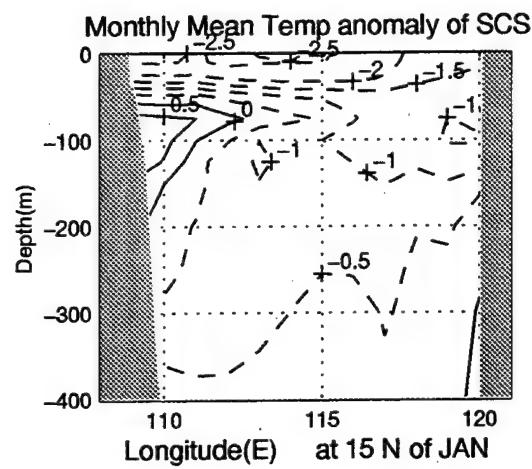


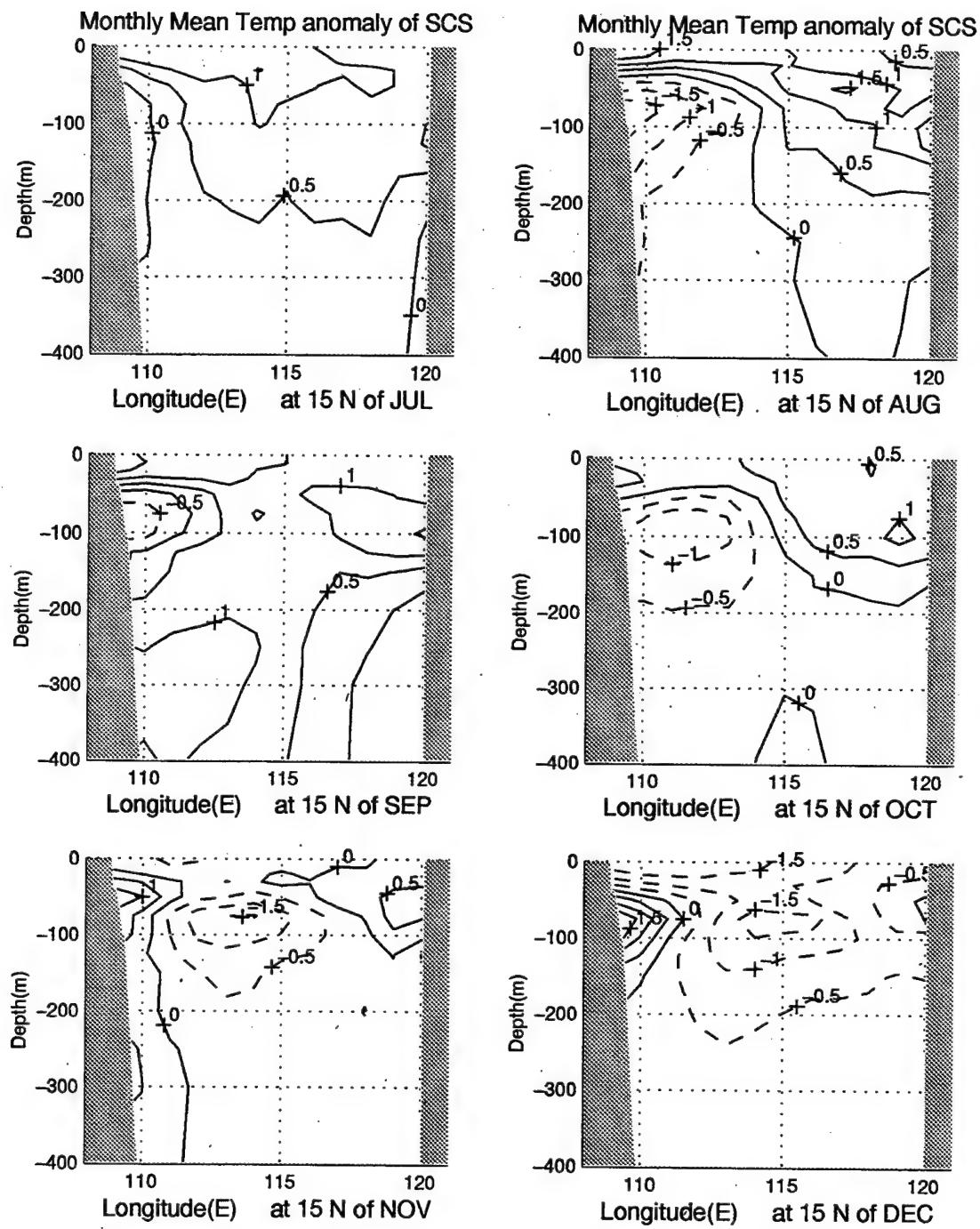


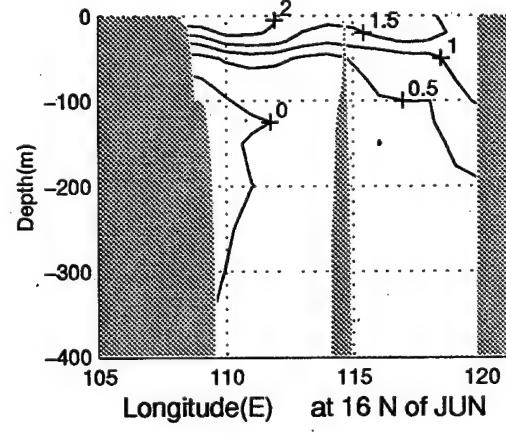
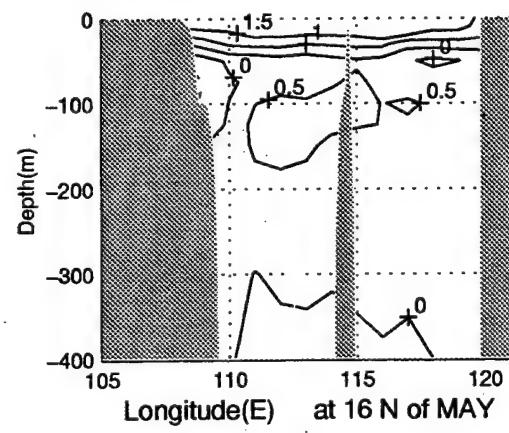
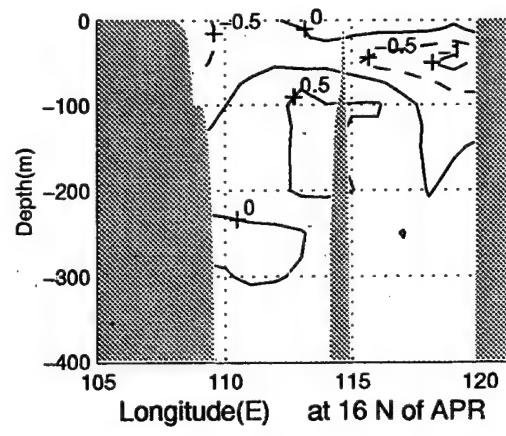
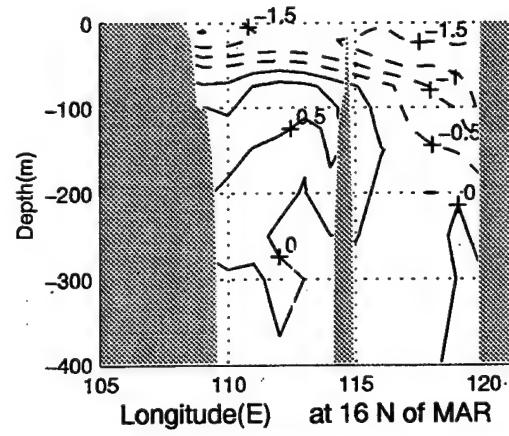
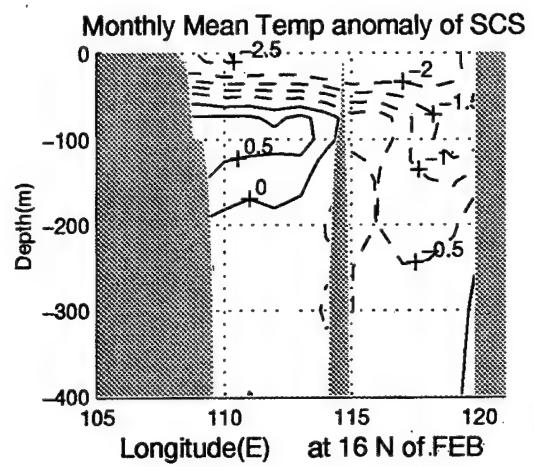
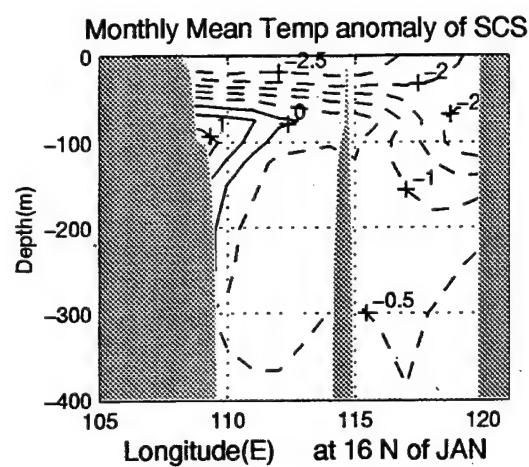


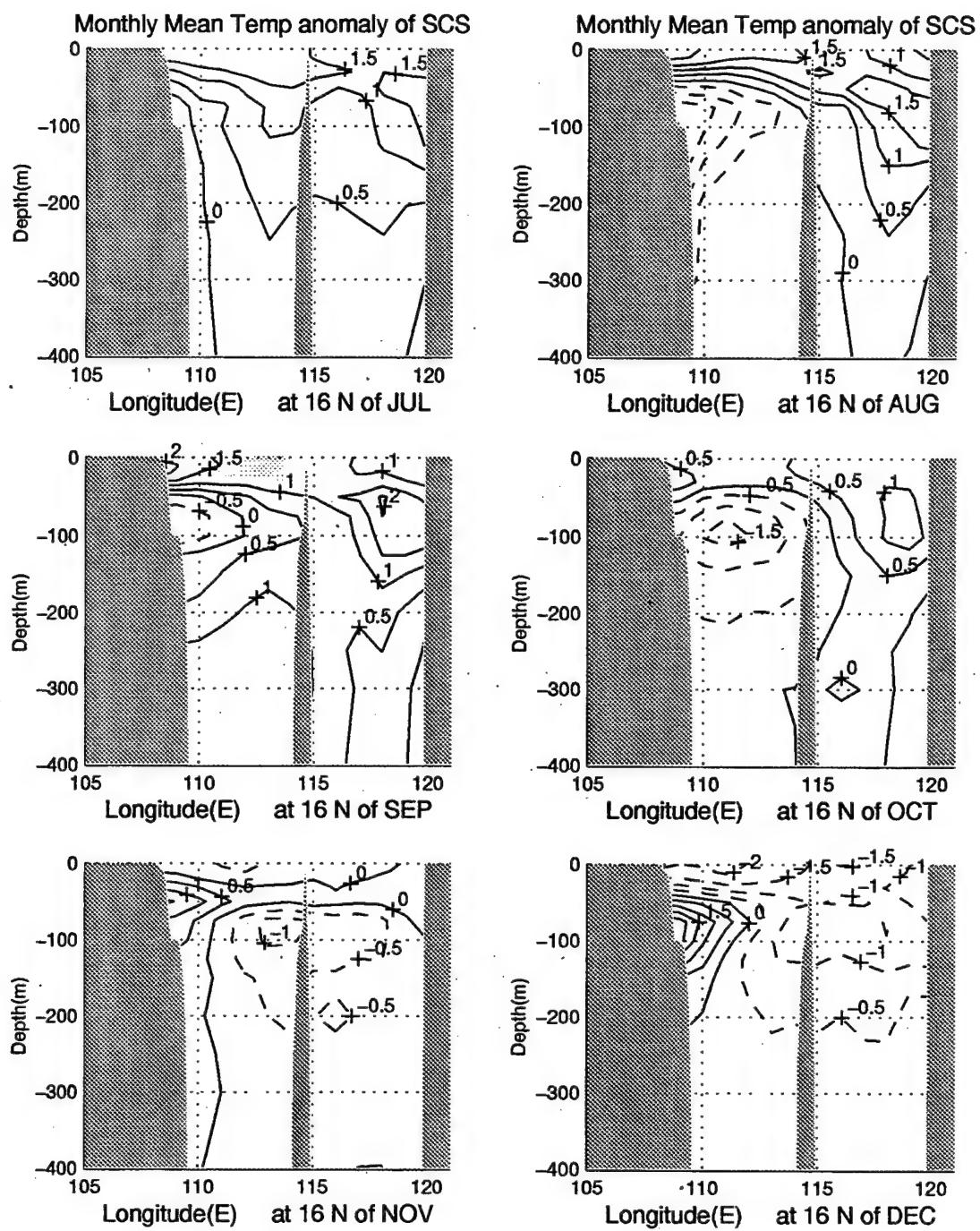


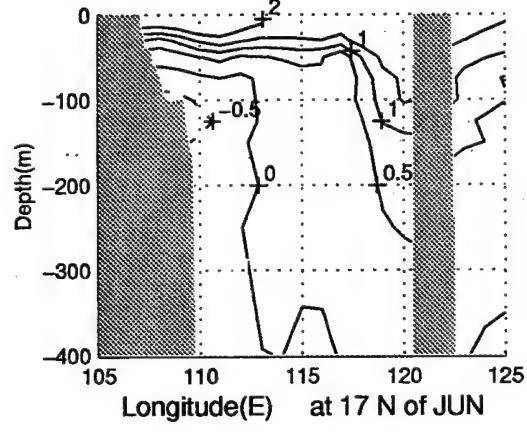
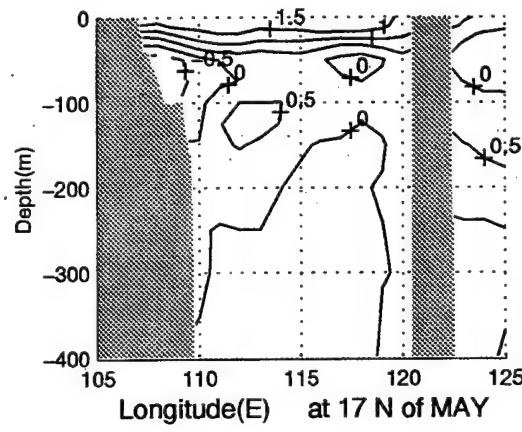
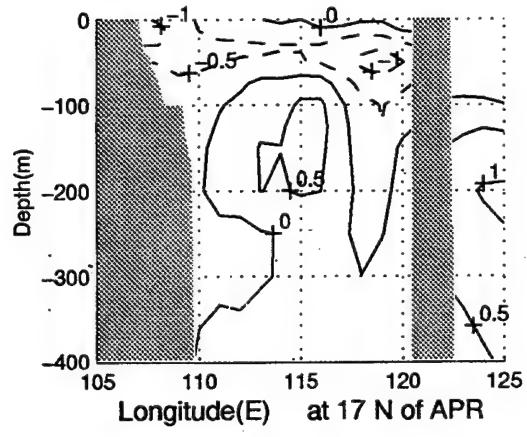
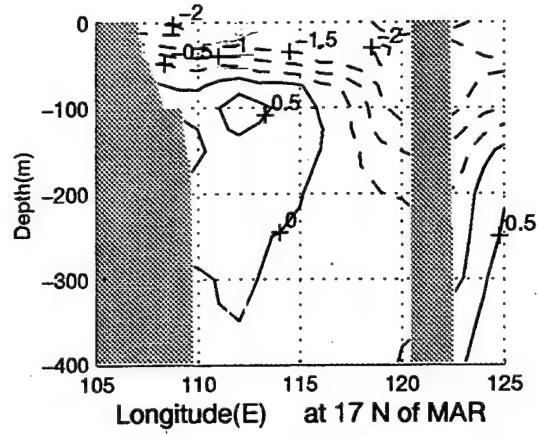
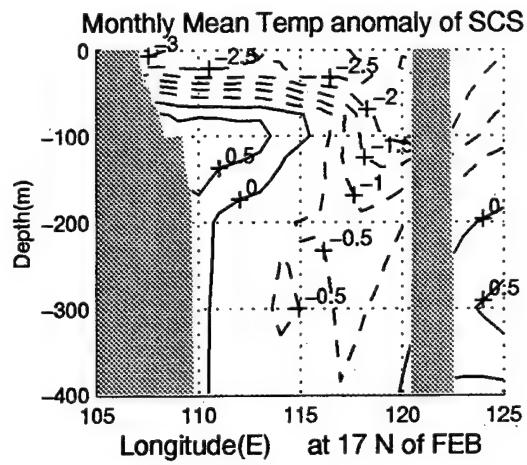
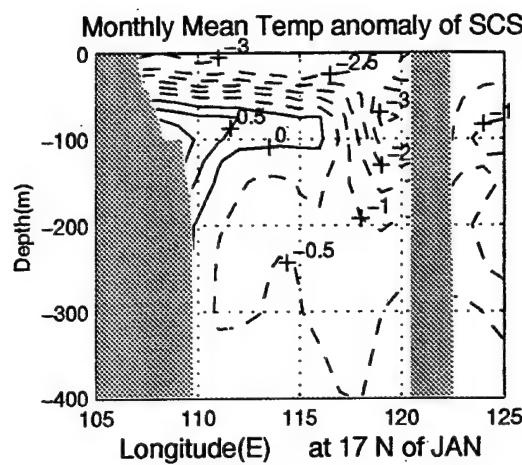


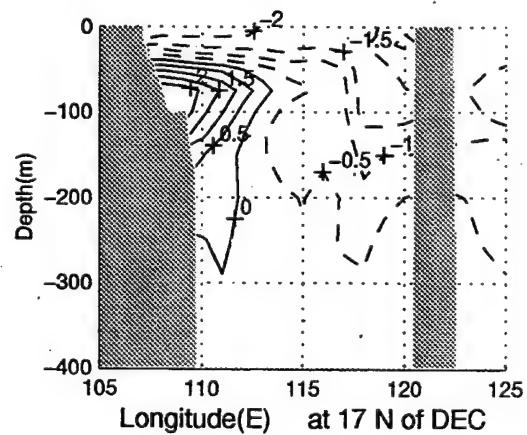
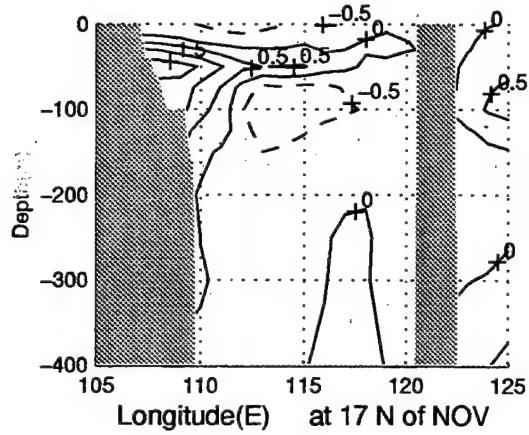
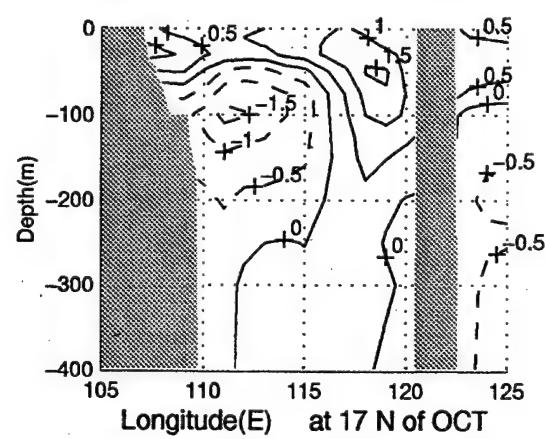
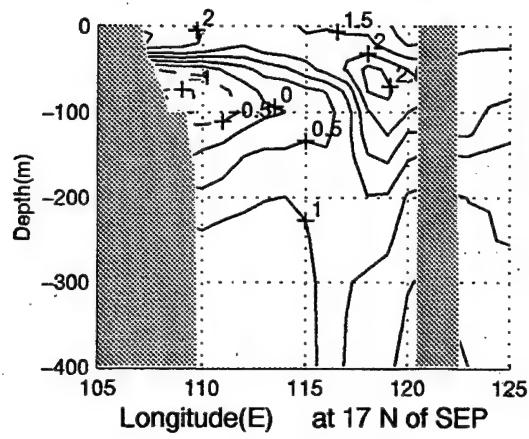
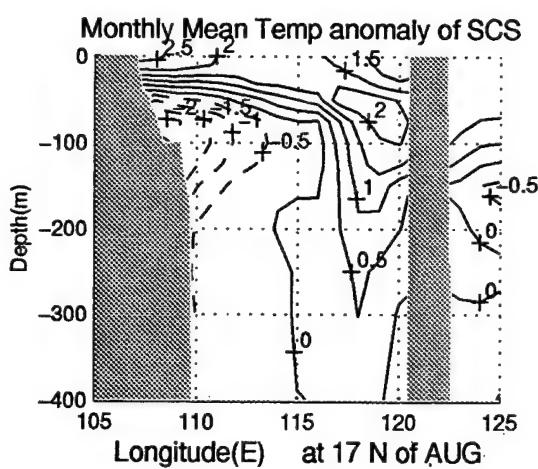
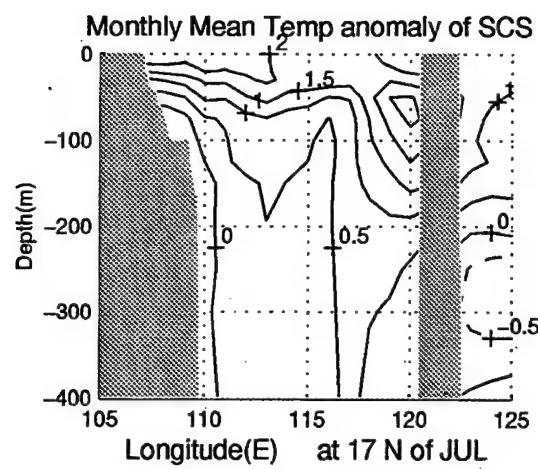


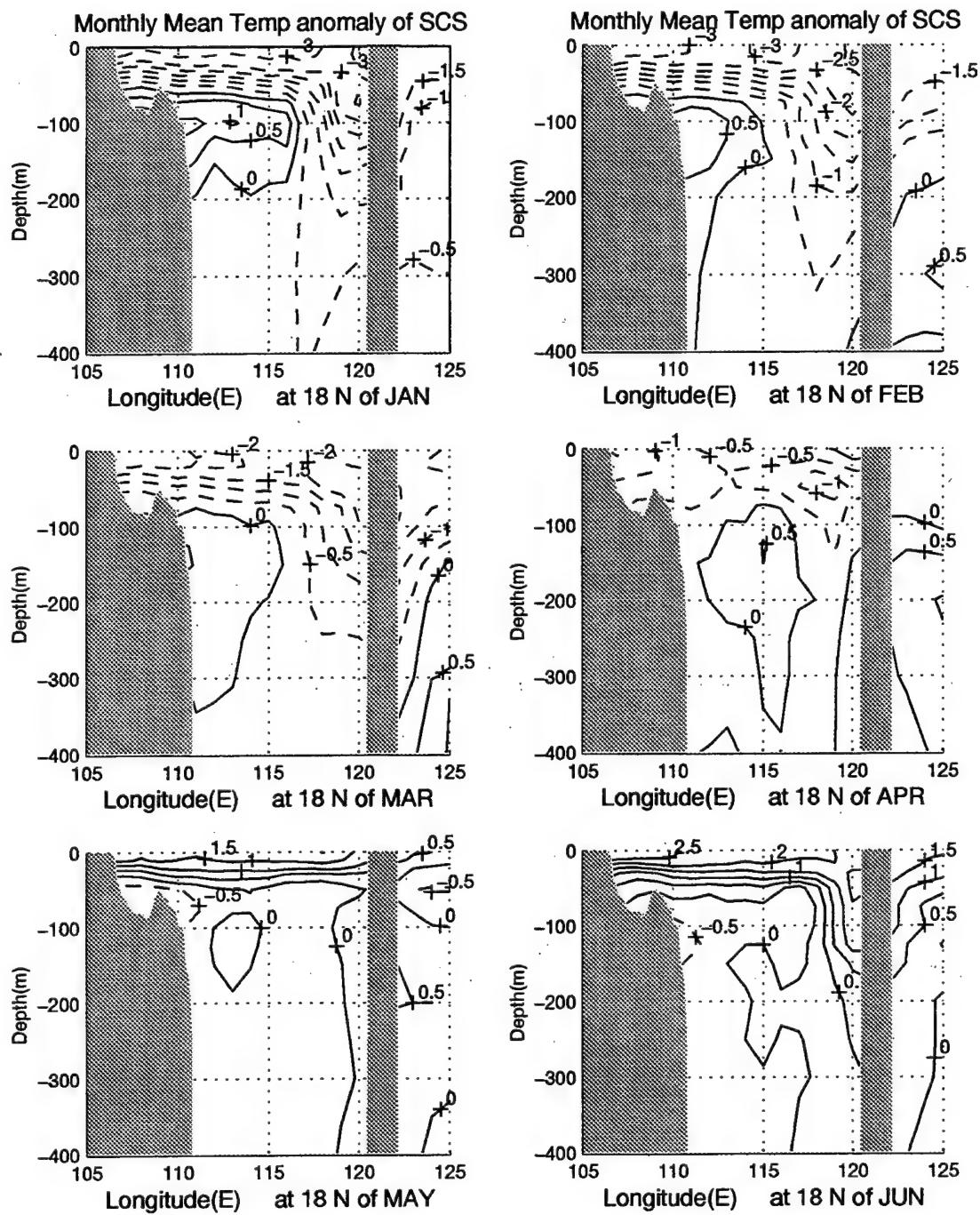


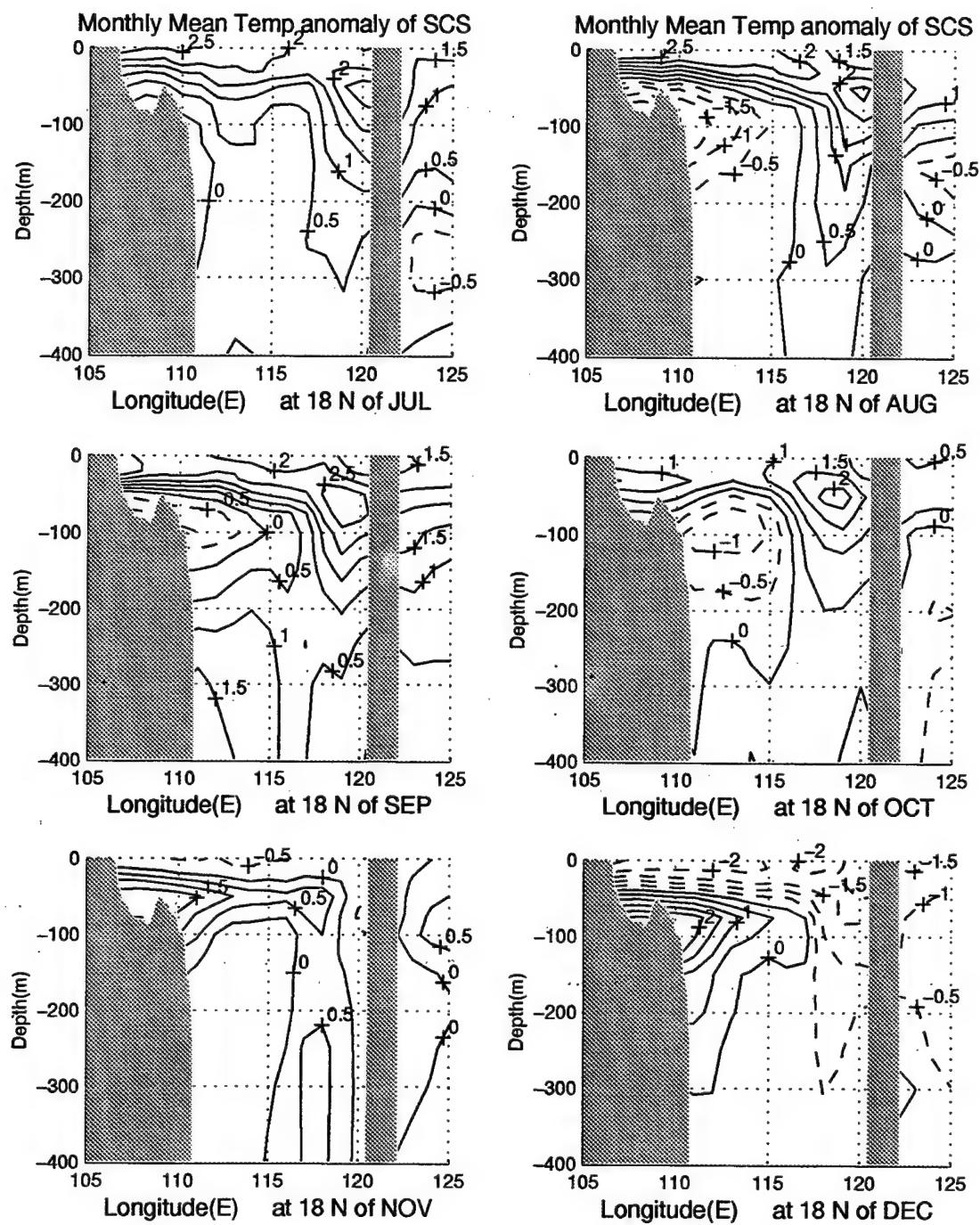


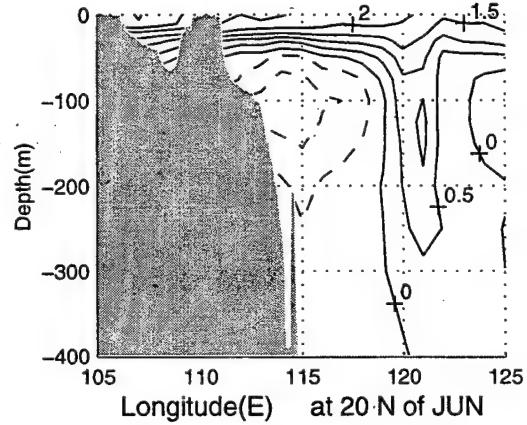
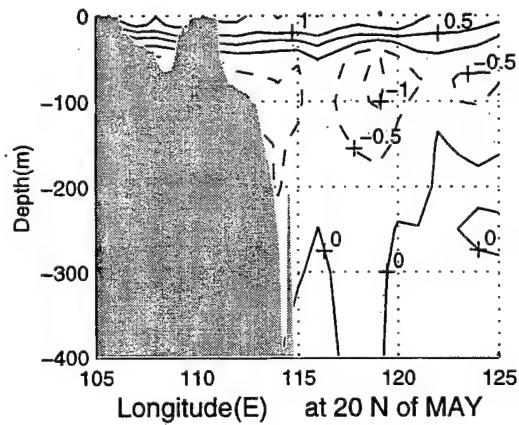
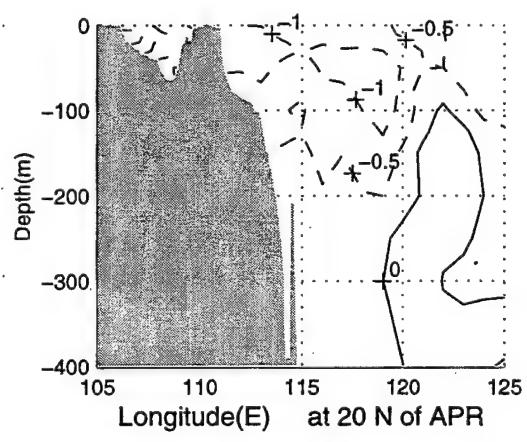
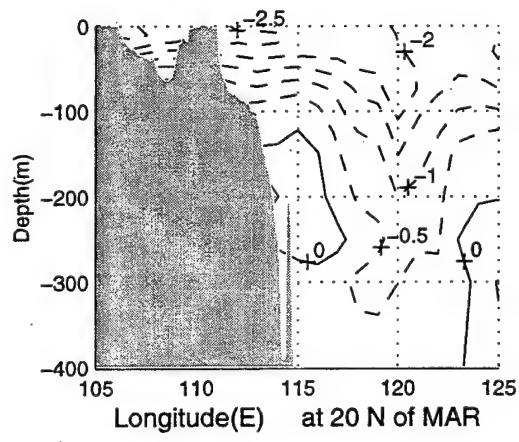
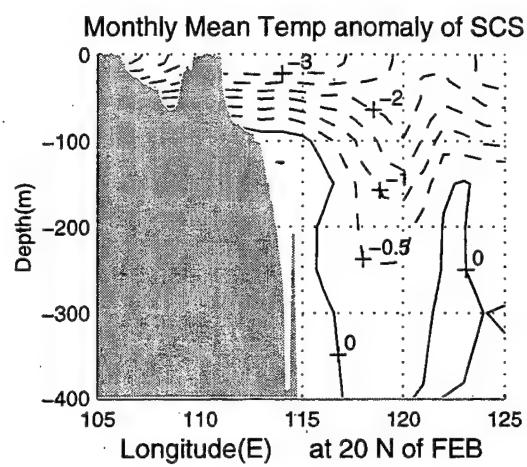
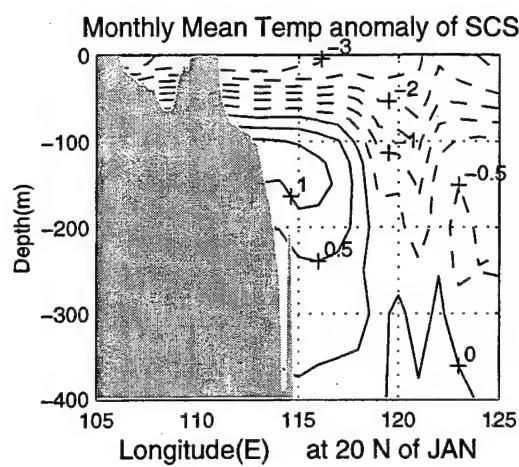


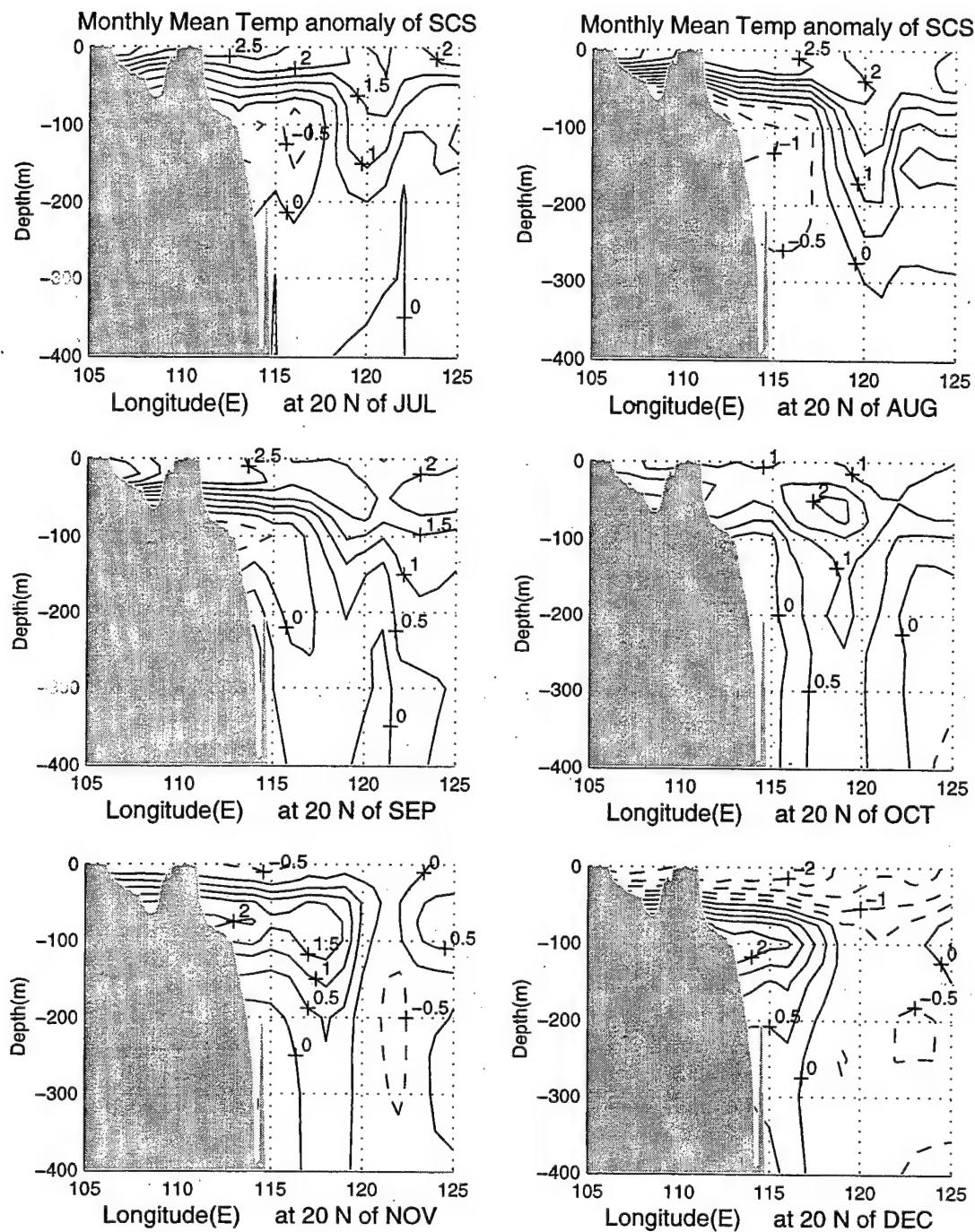


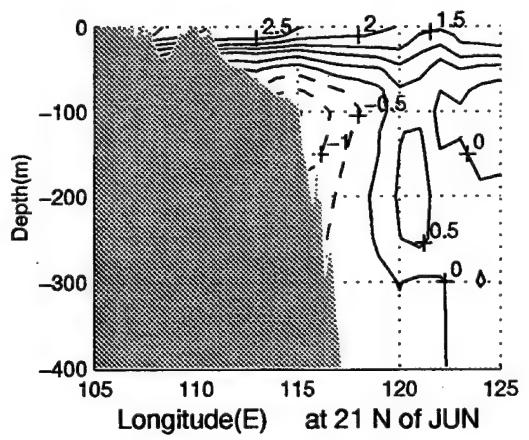
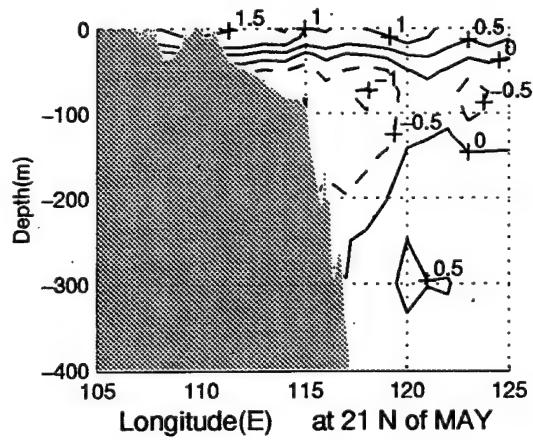
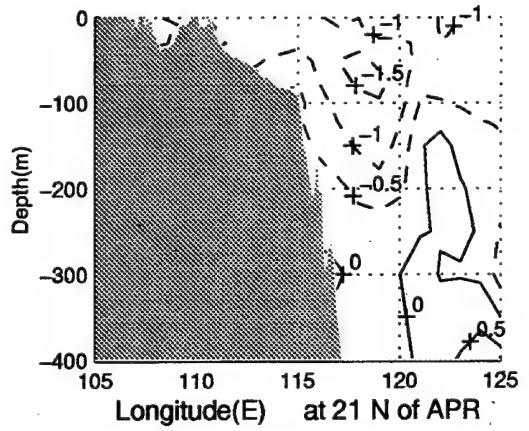
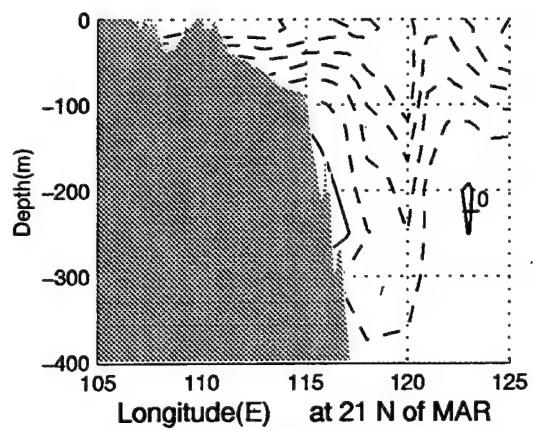
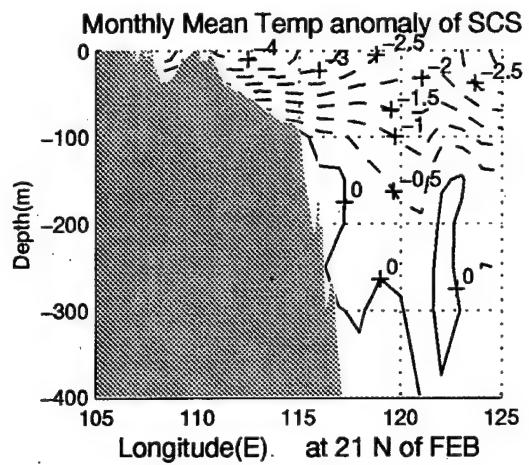
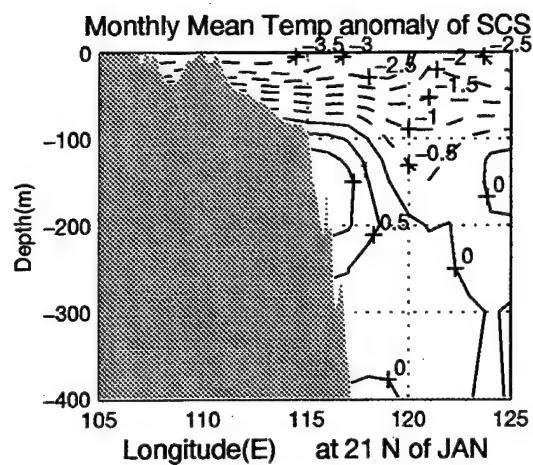


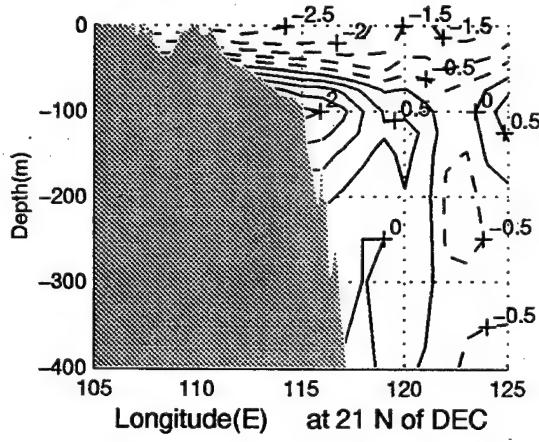
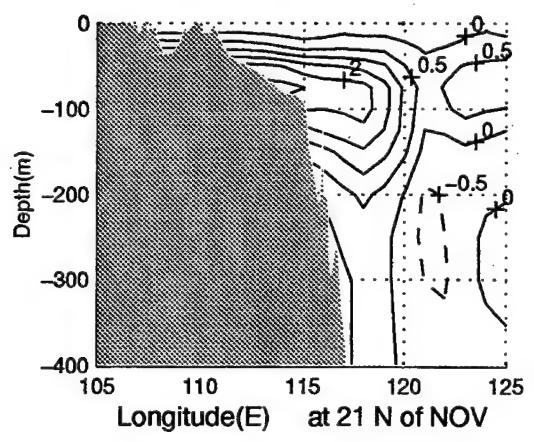
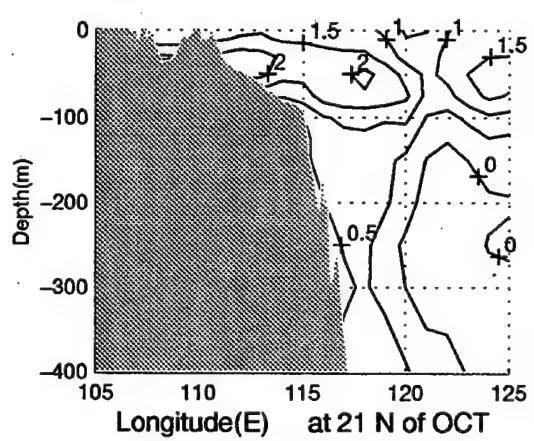
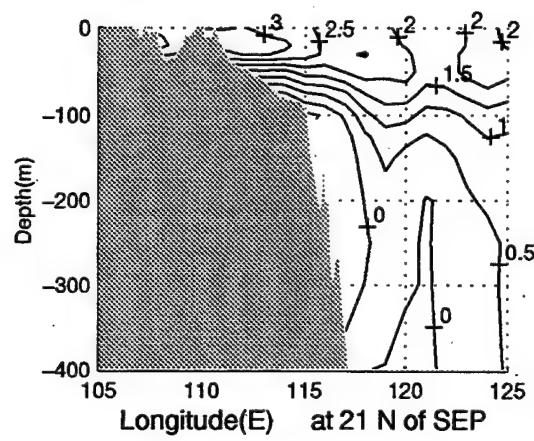
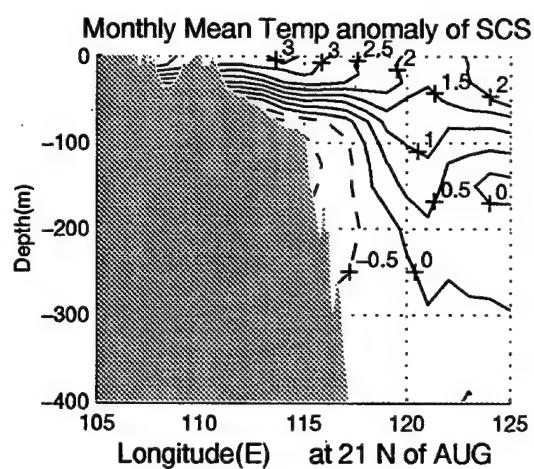
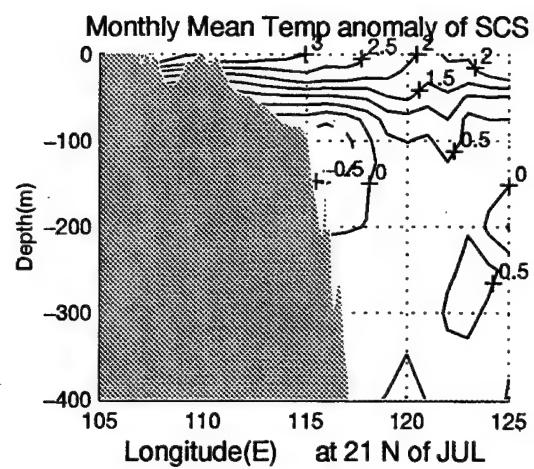


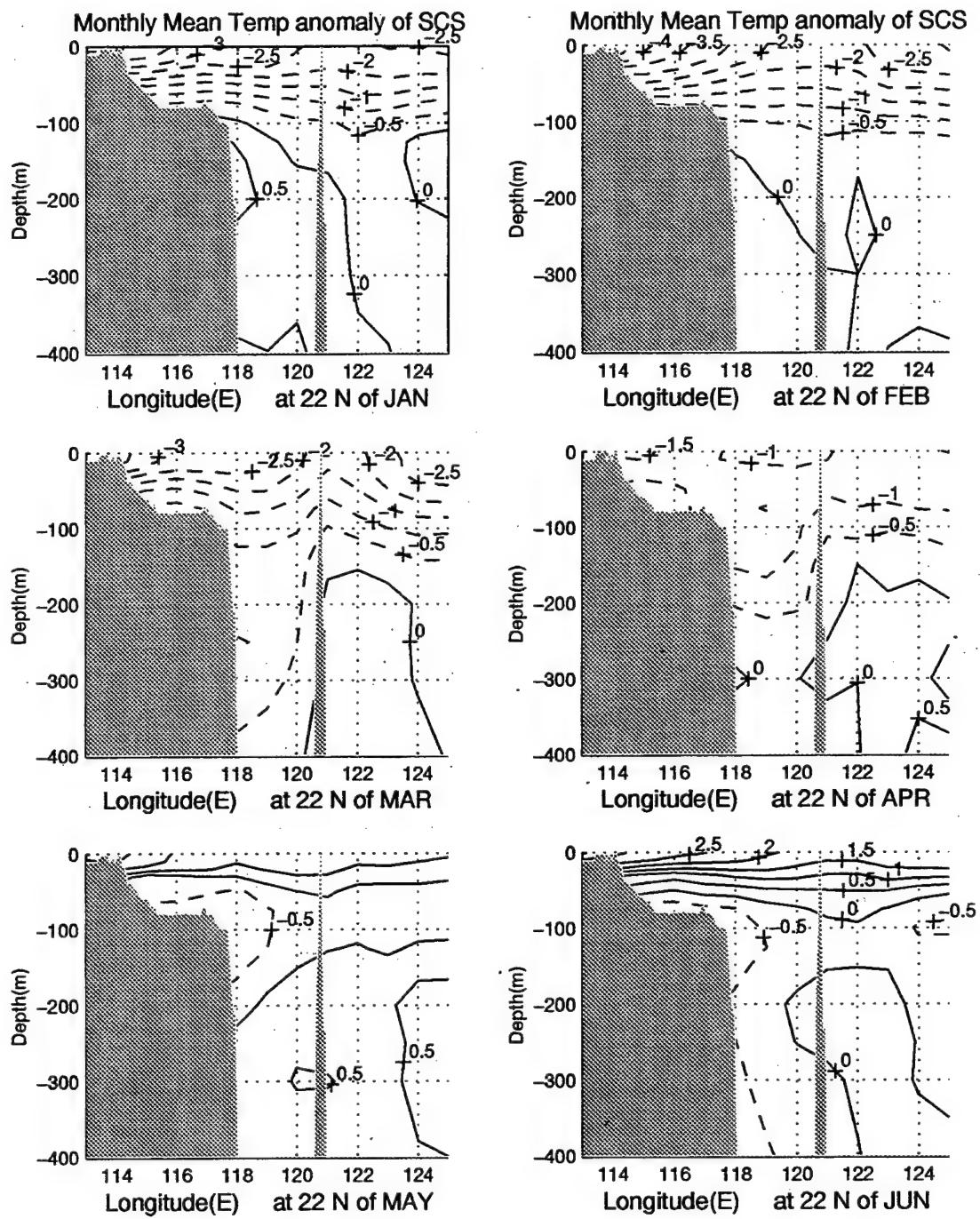


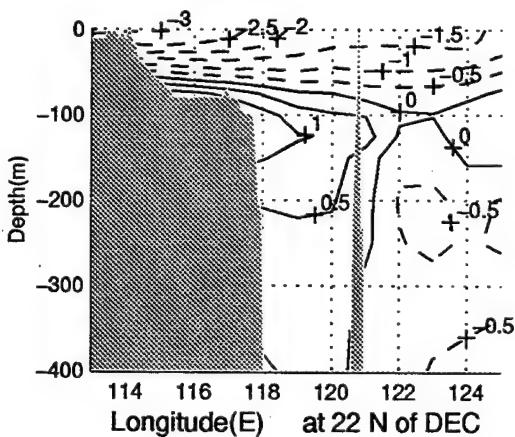
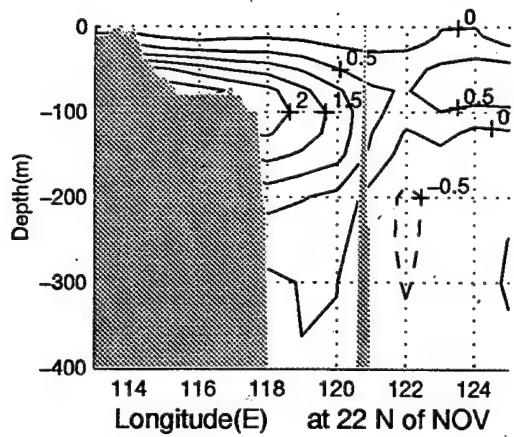
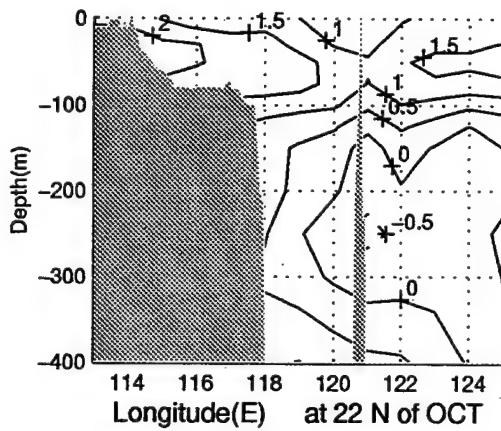
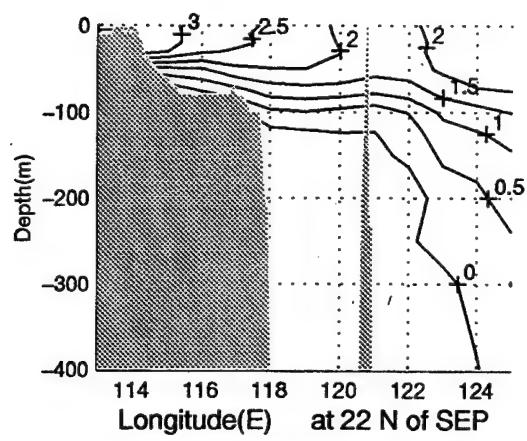
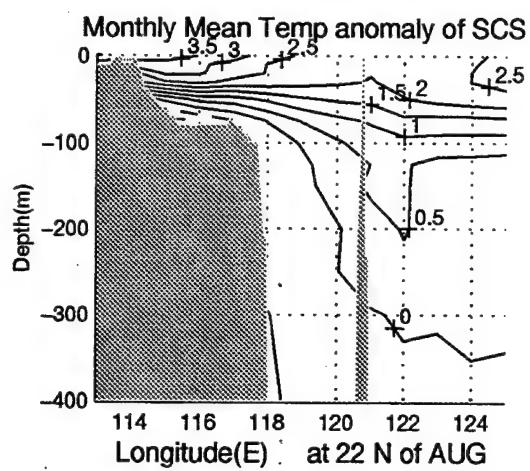
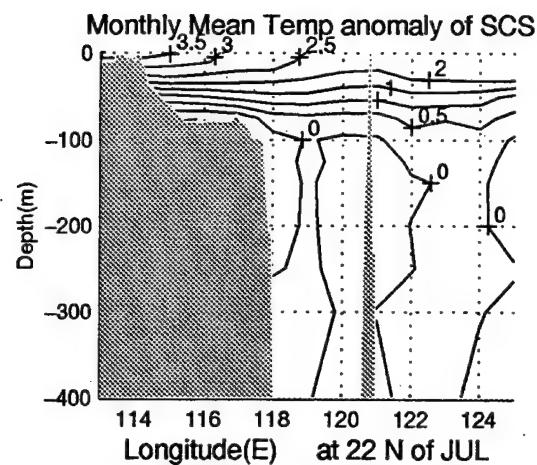


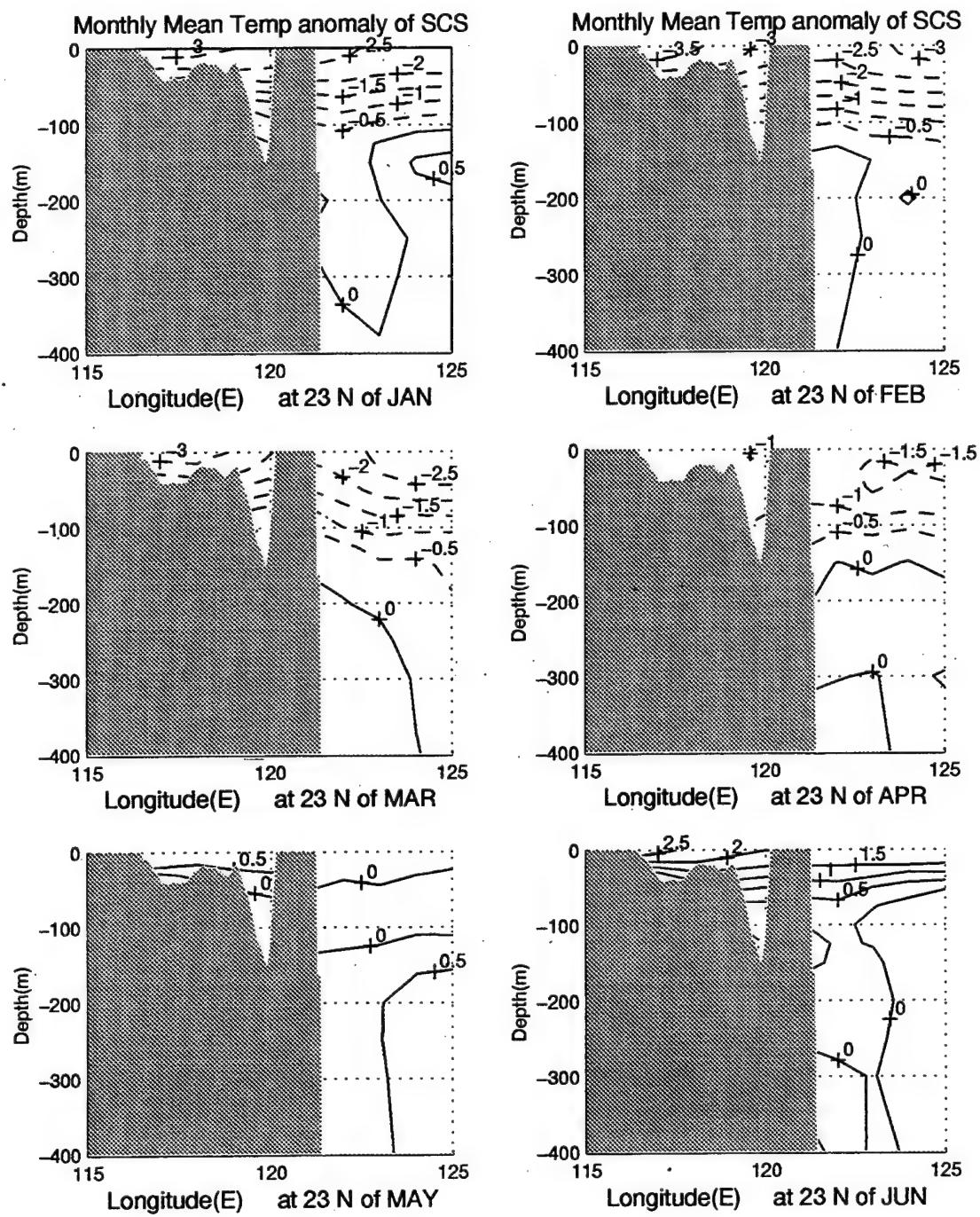


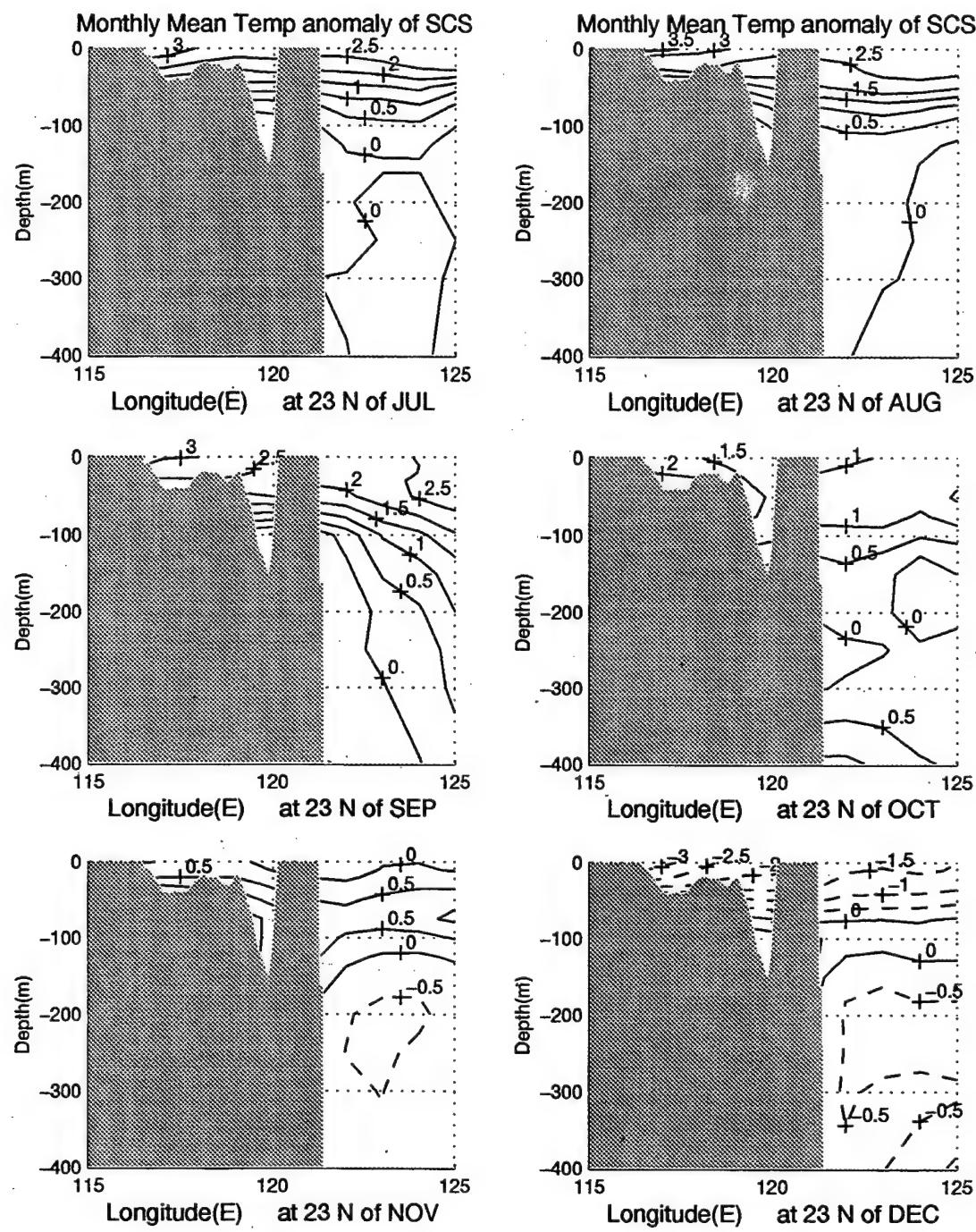


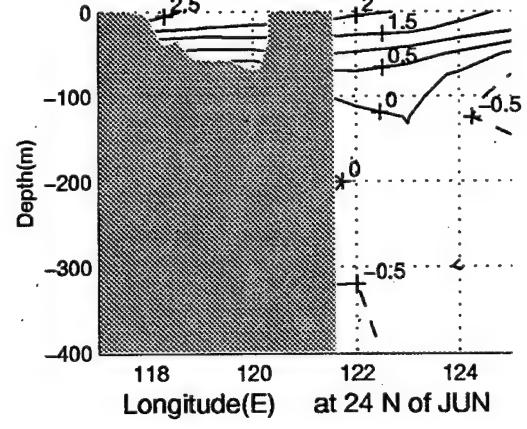
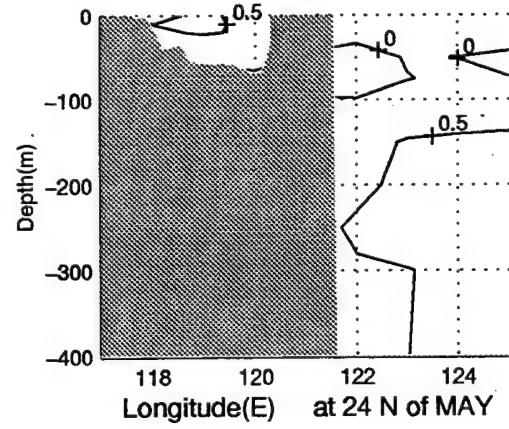
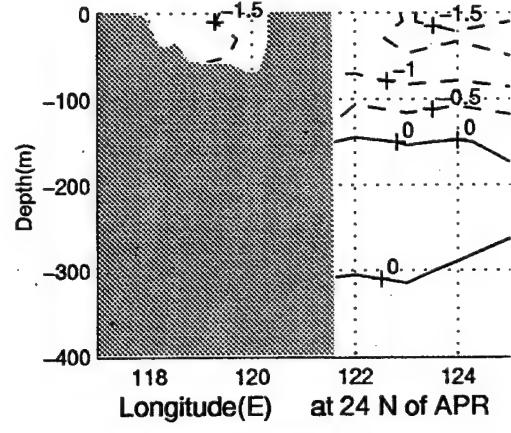
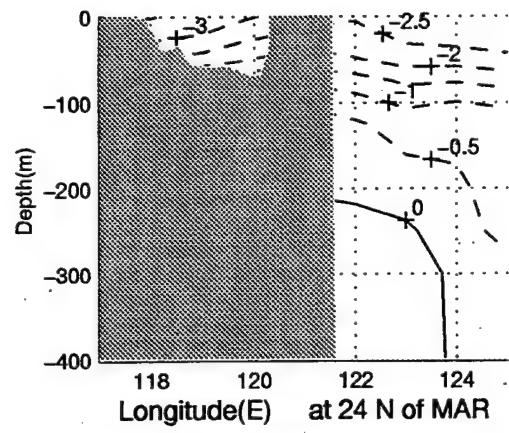
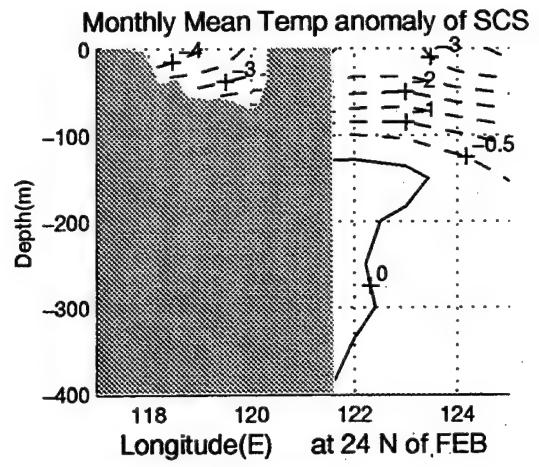
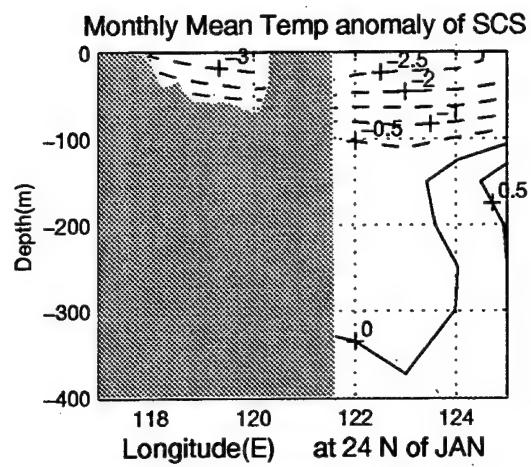


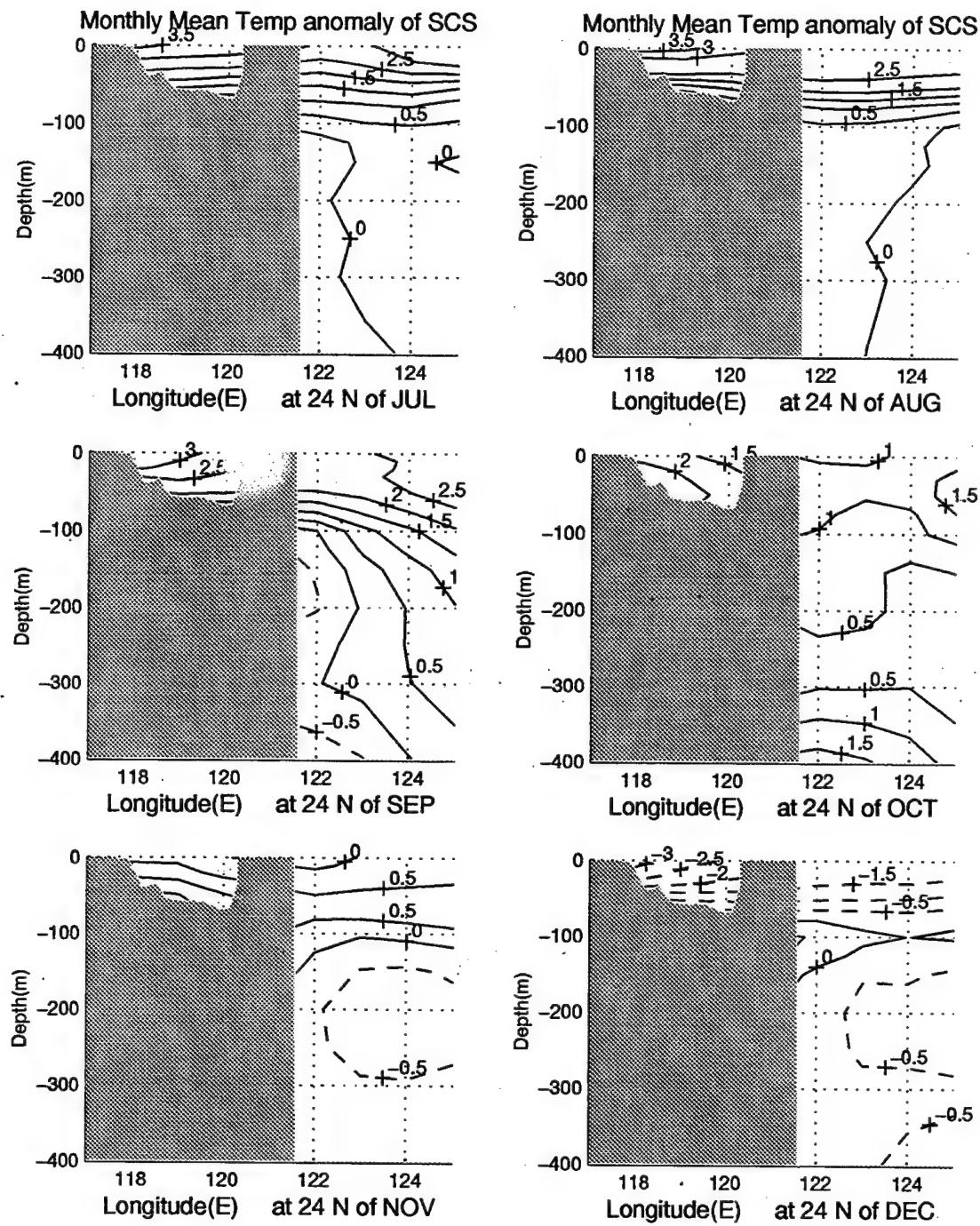


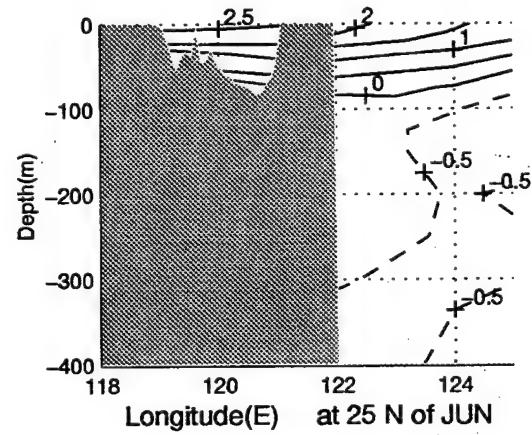
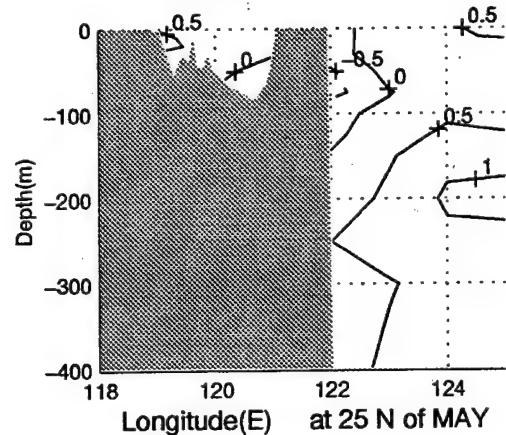
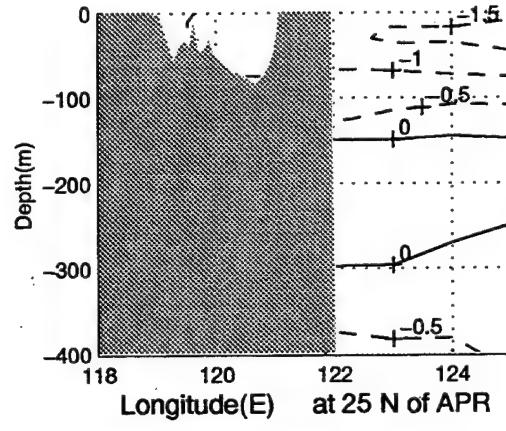
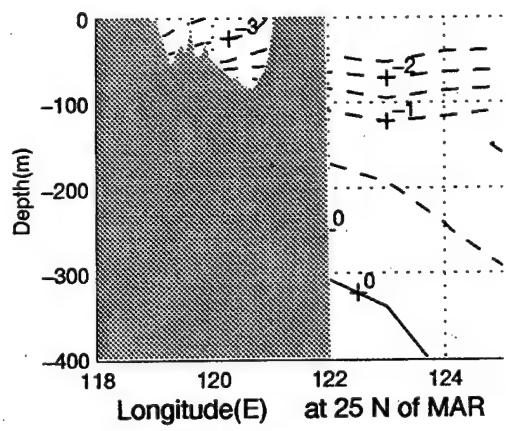
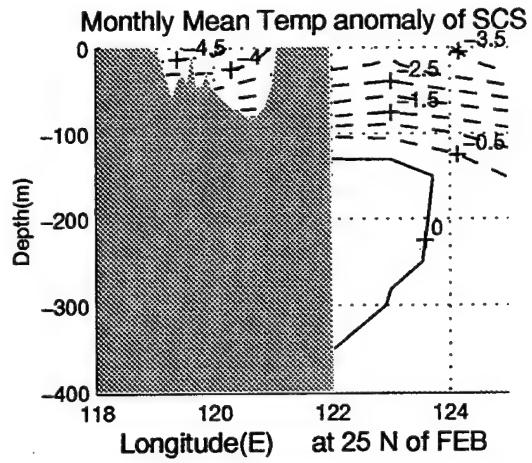
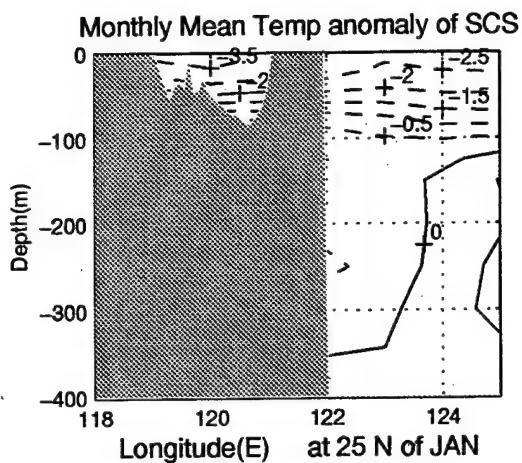


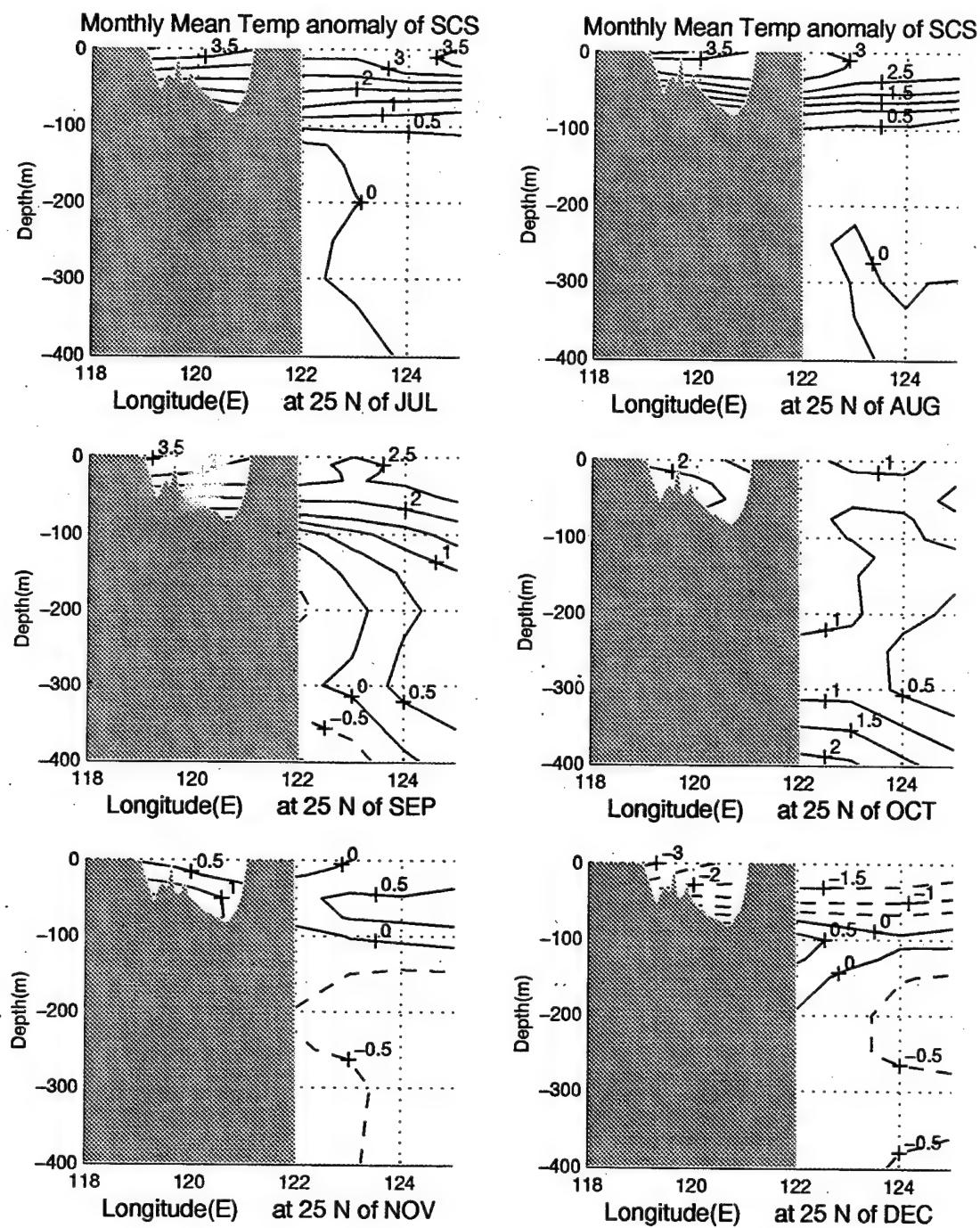




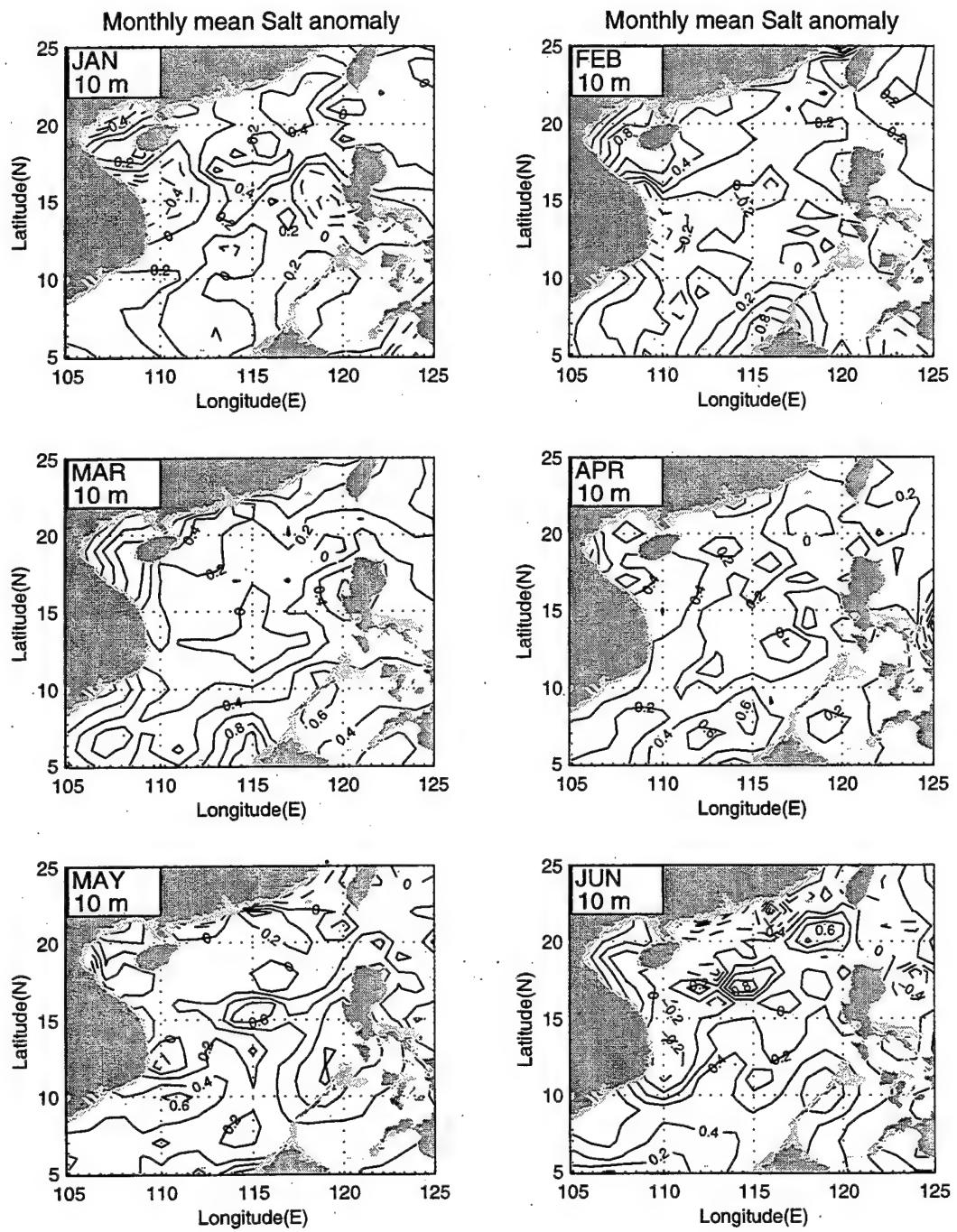


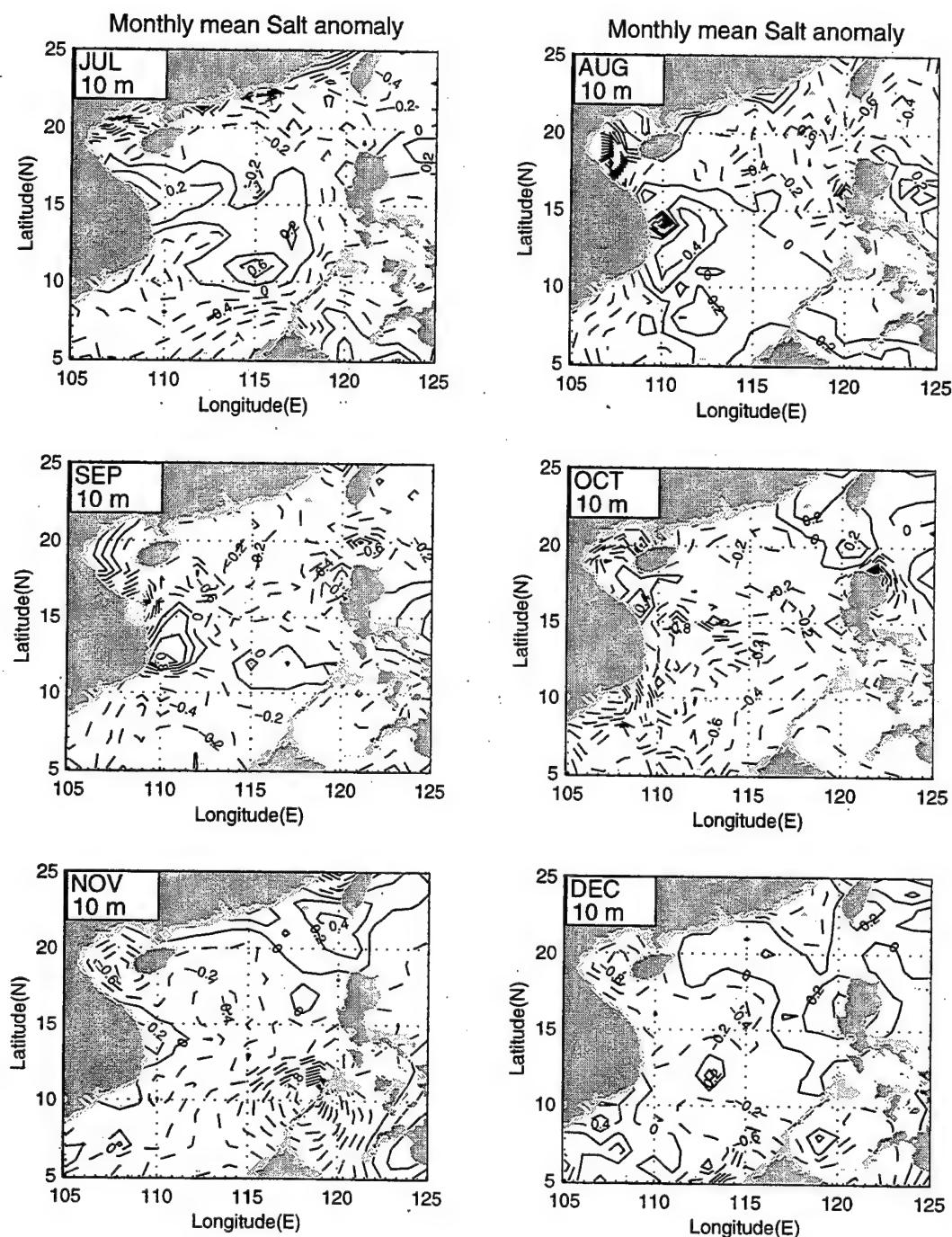


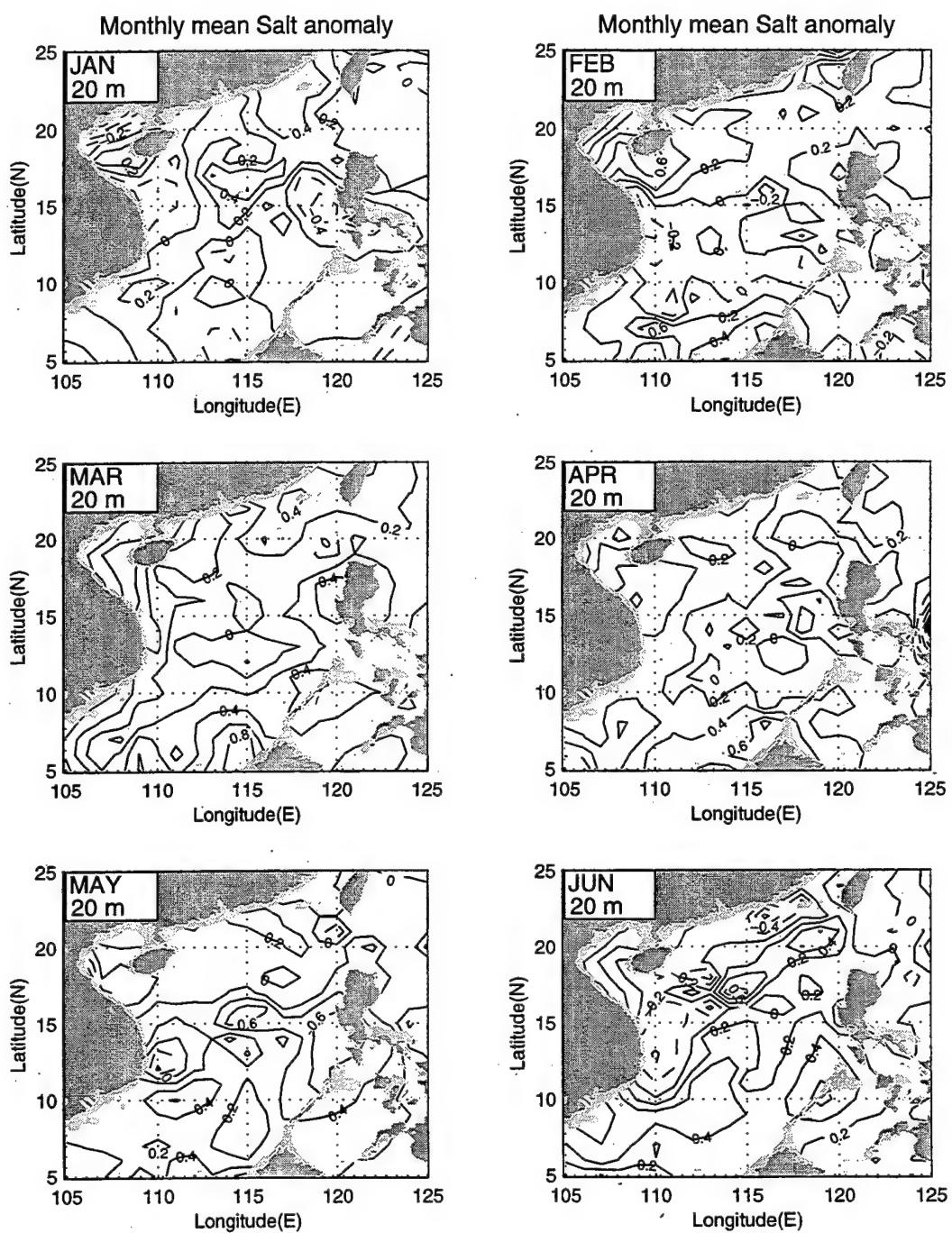


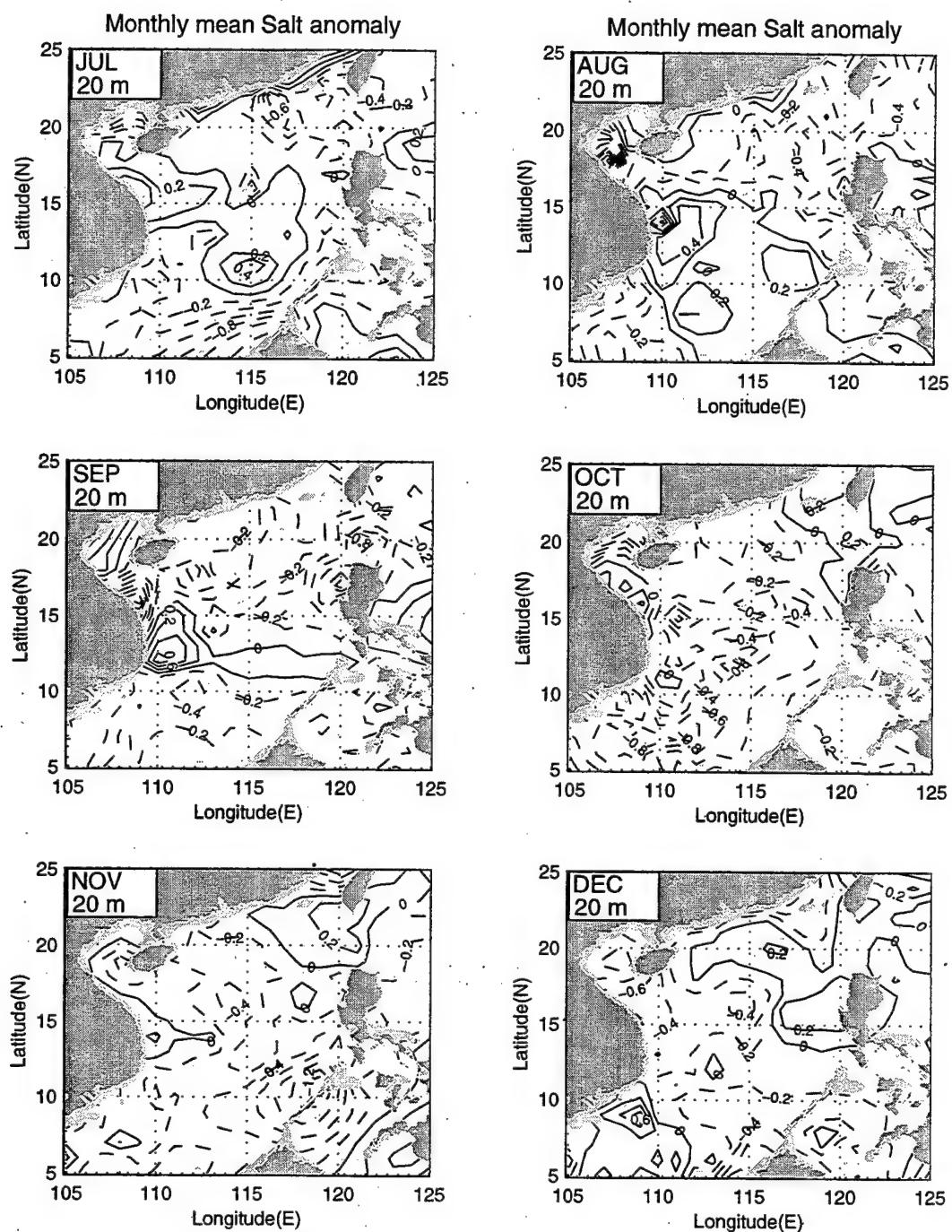


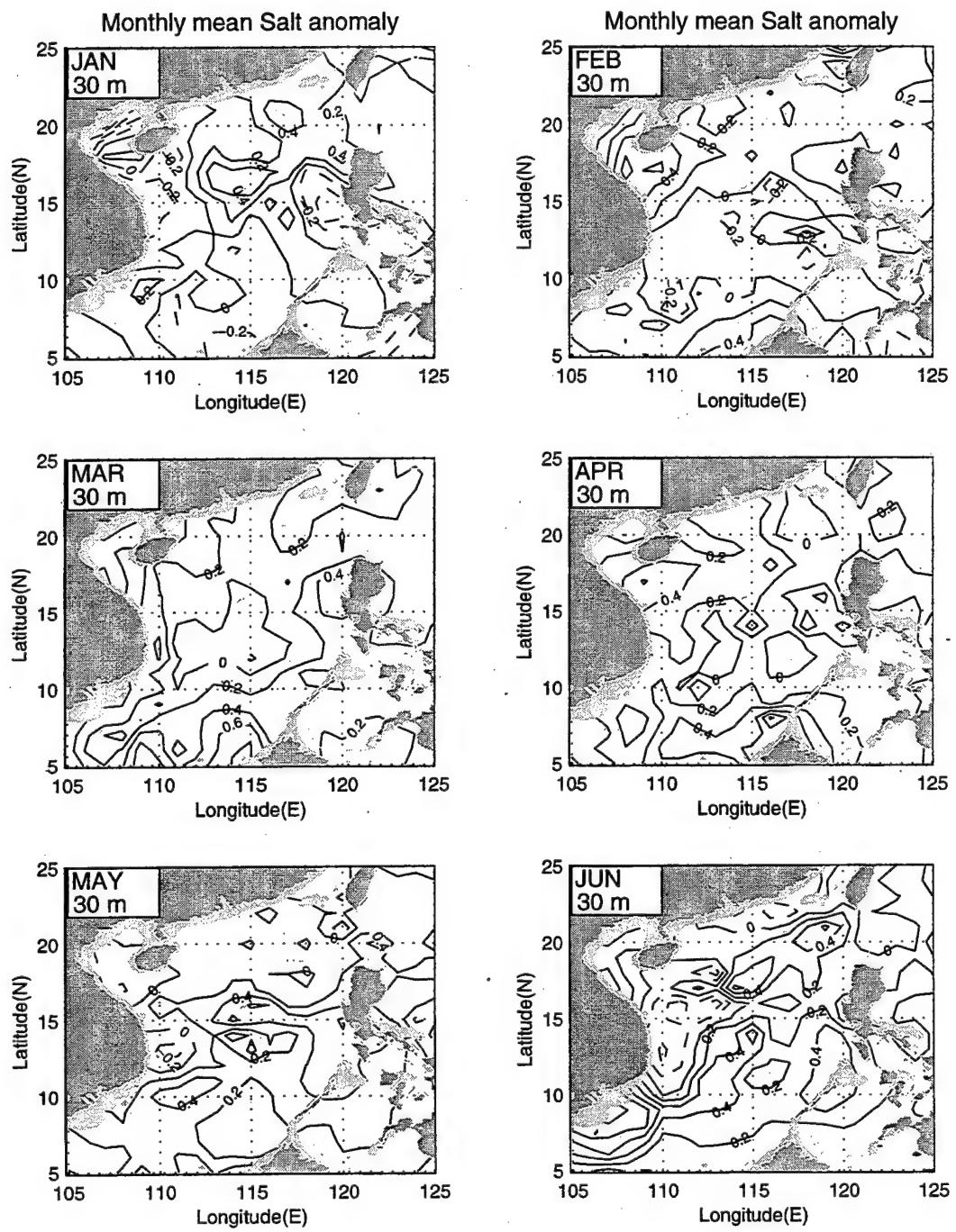
APPENDIX B. MONTHLY SALINITY ANOMALY

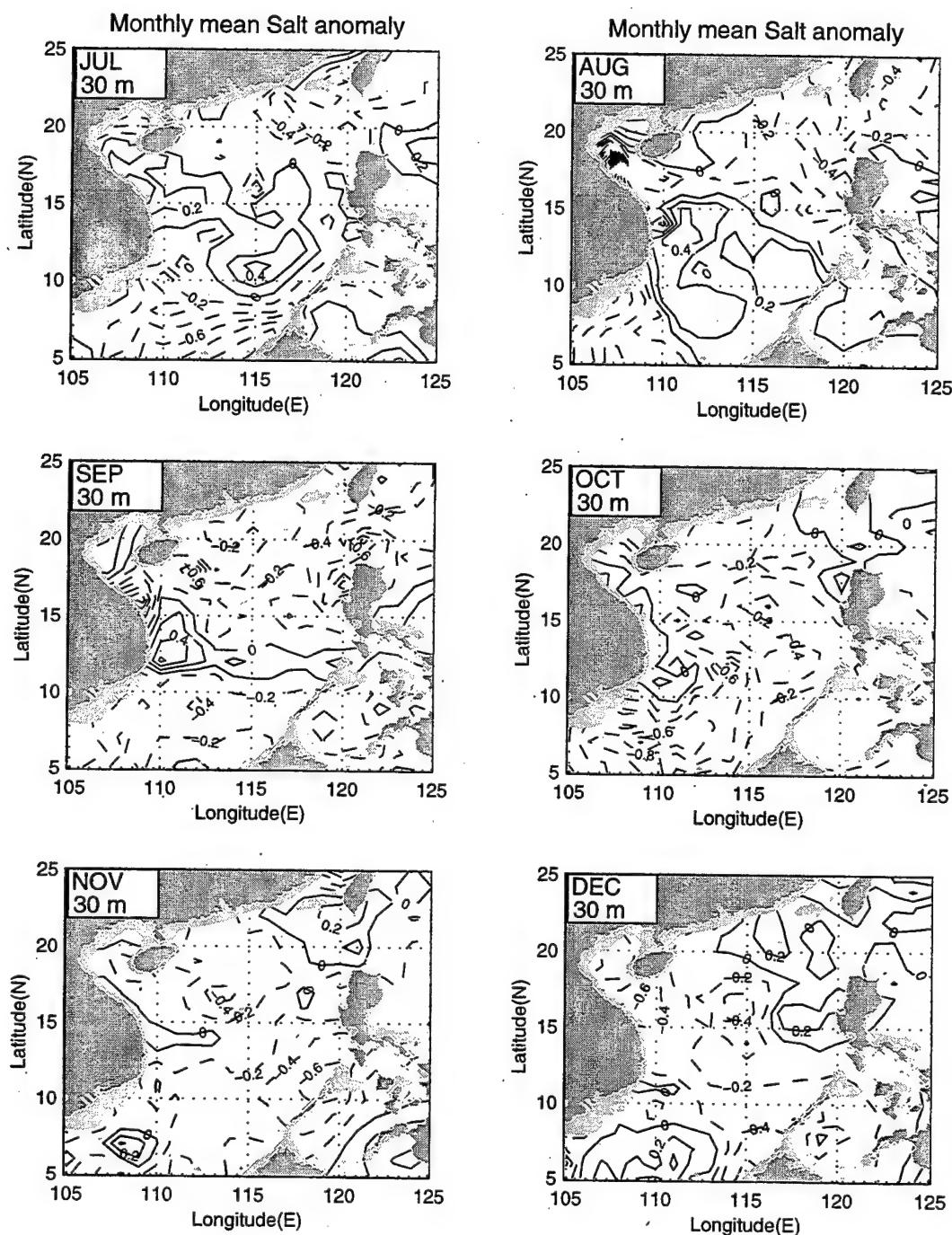


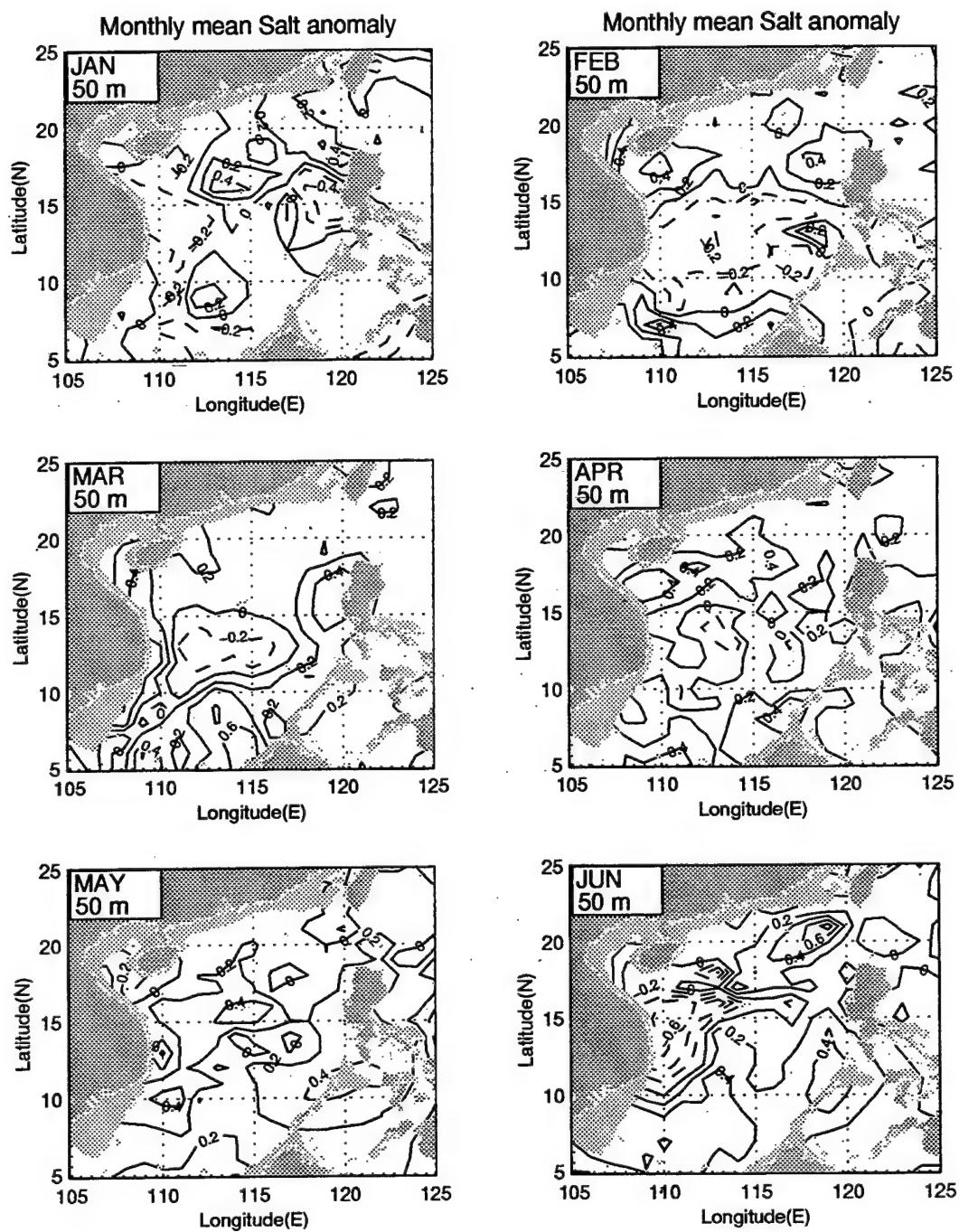


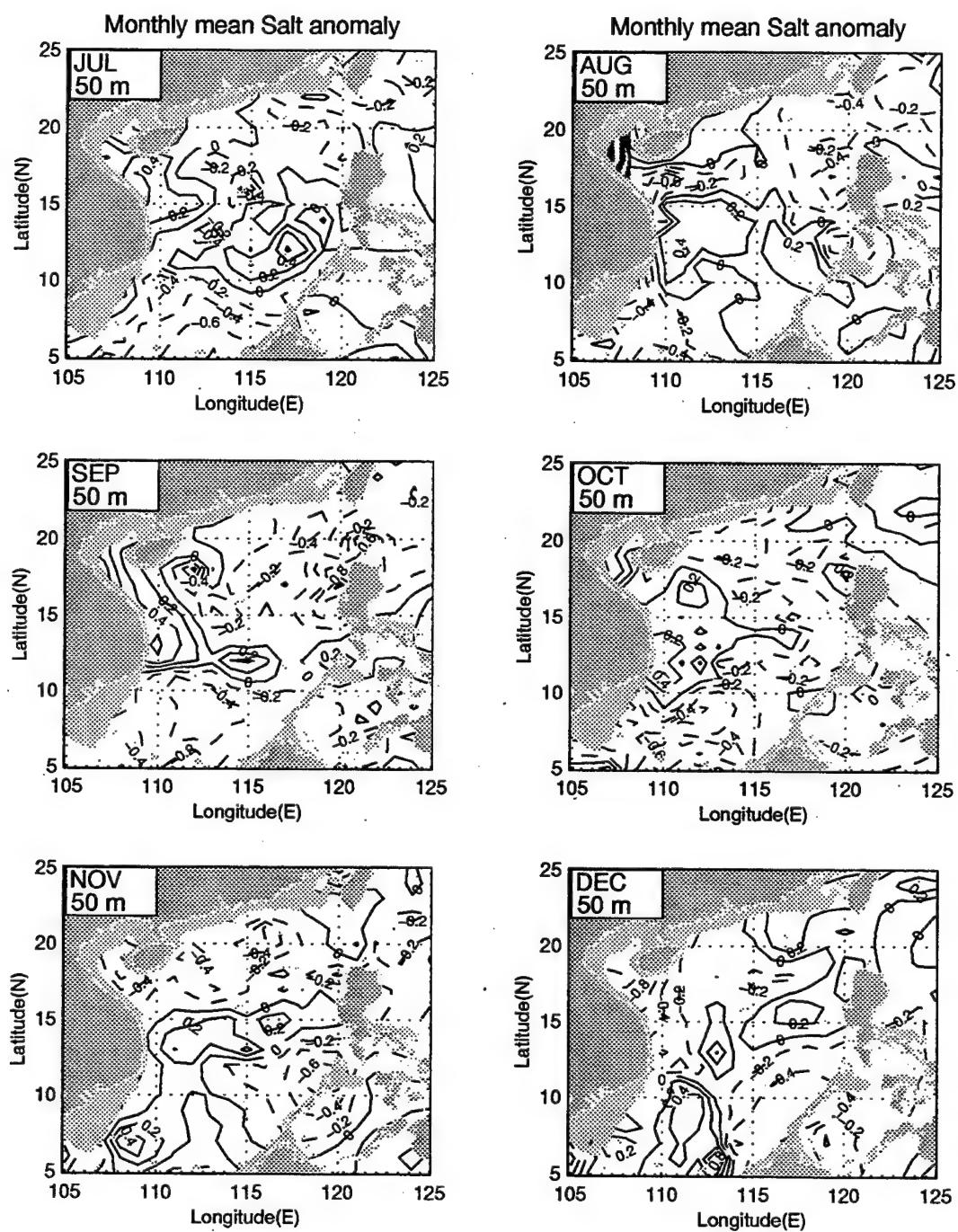


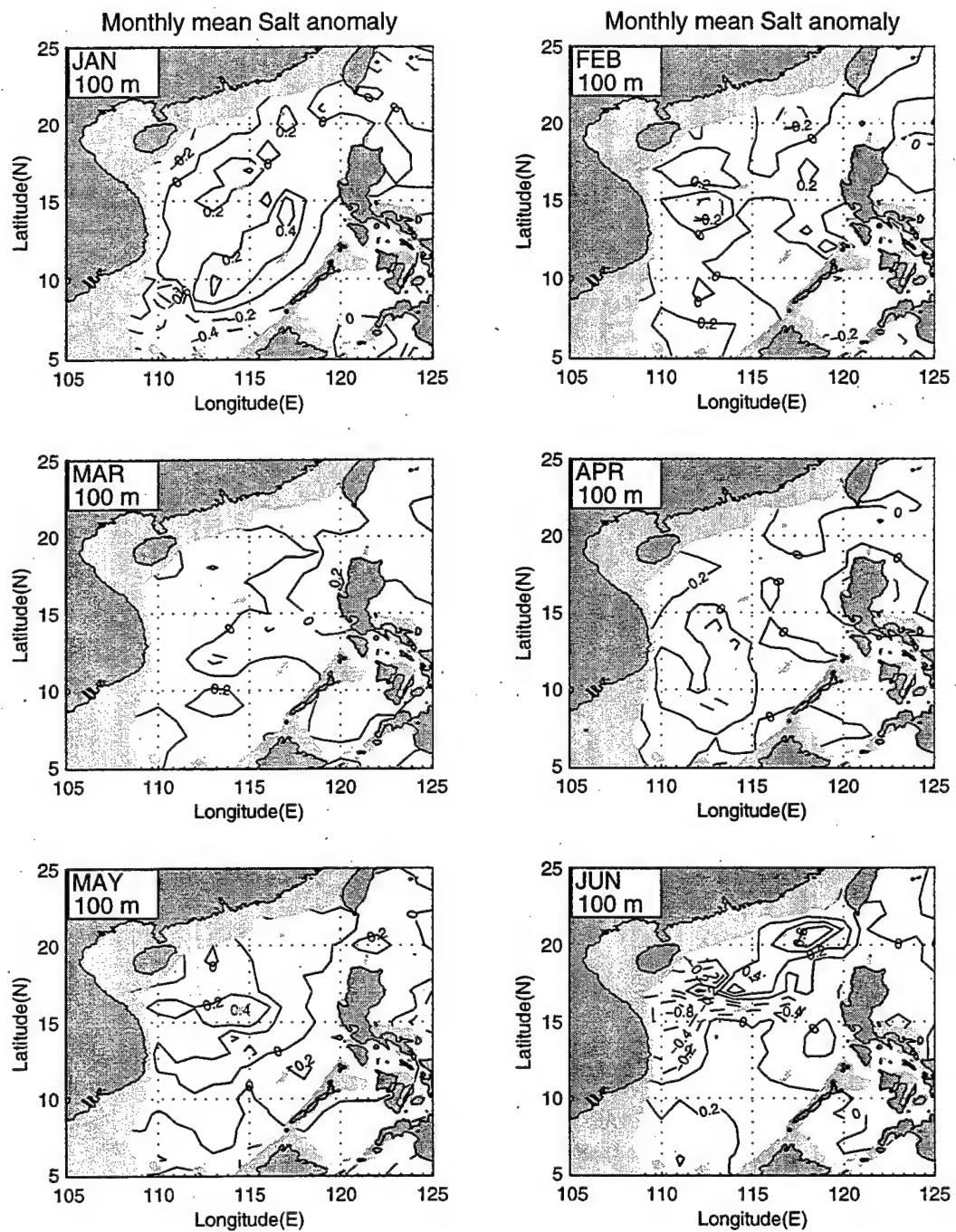


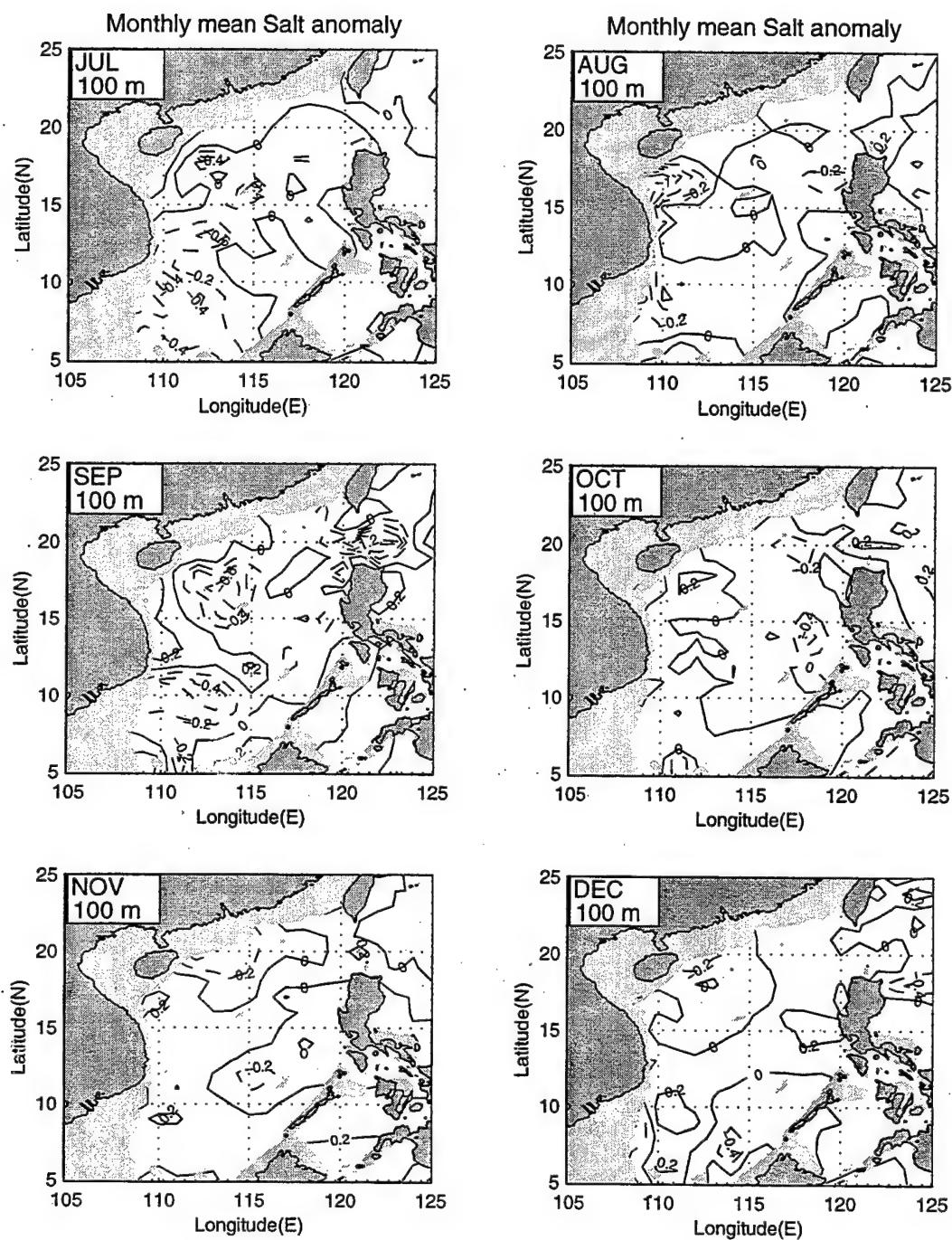


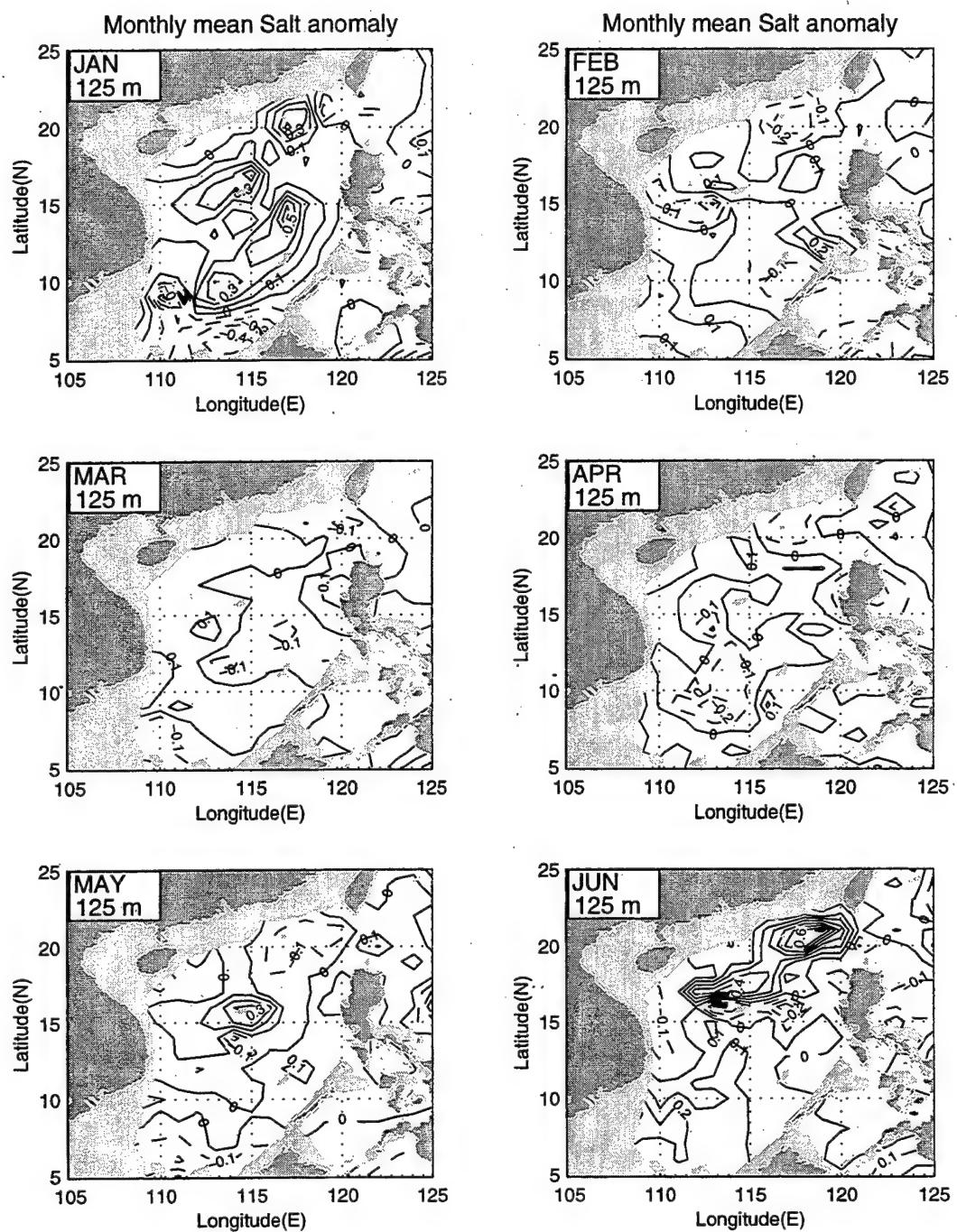


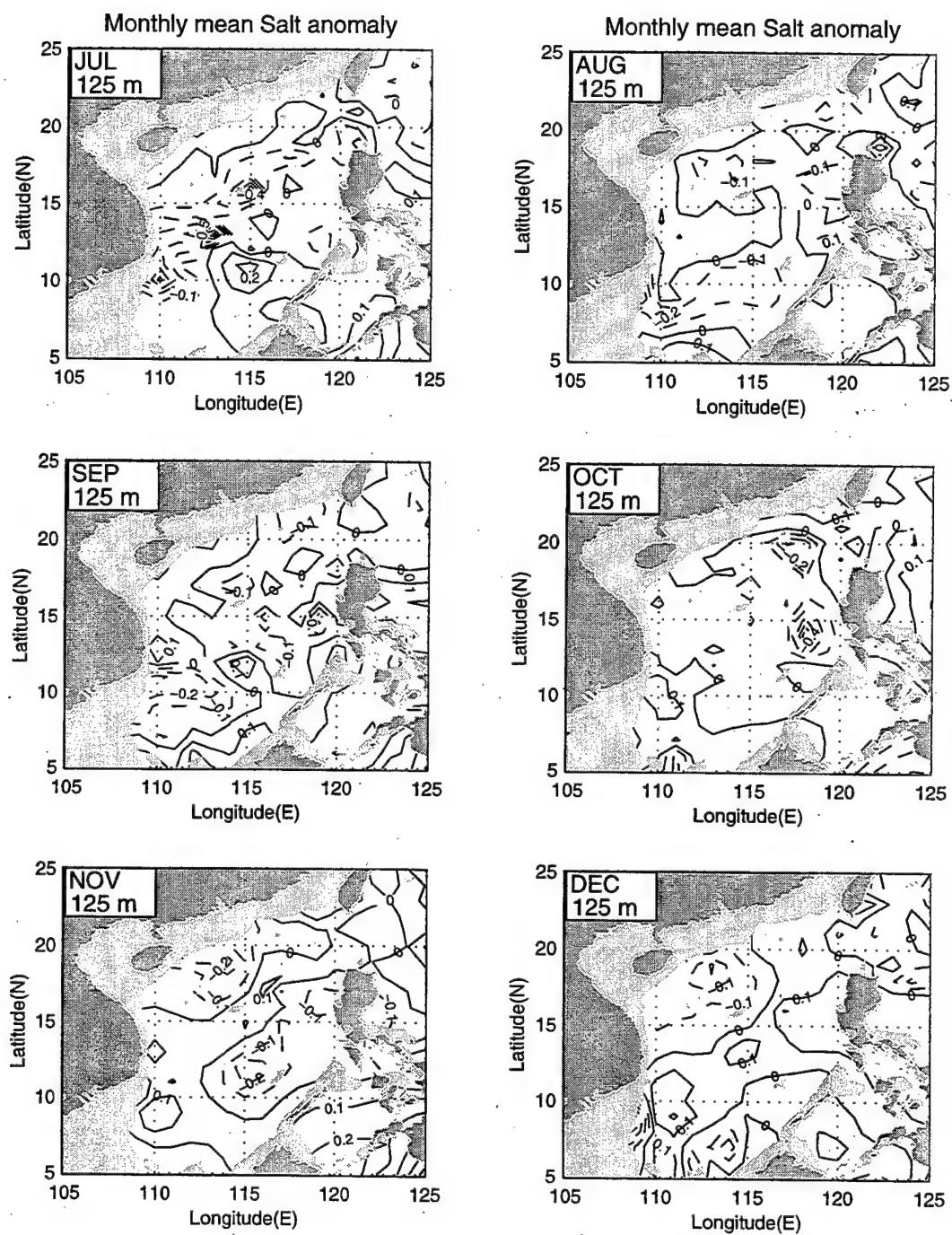


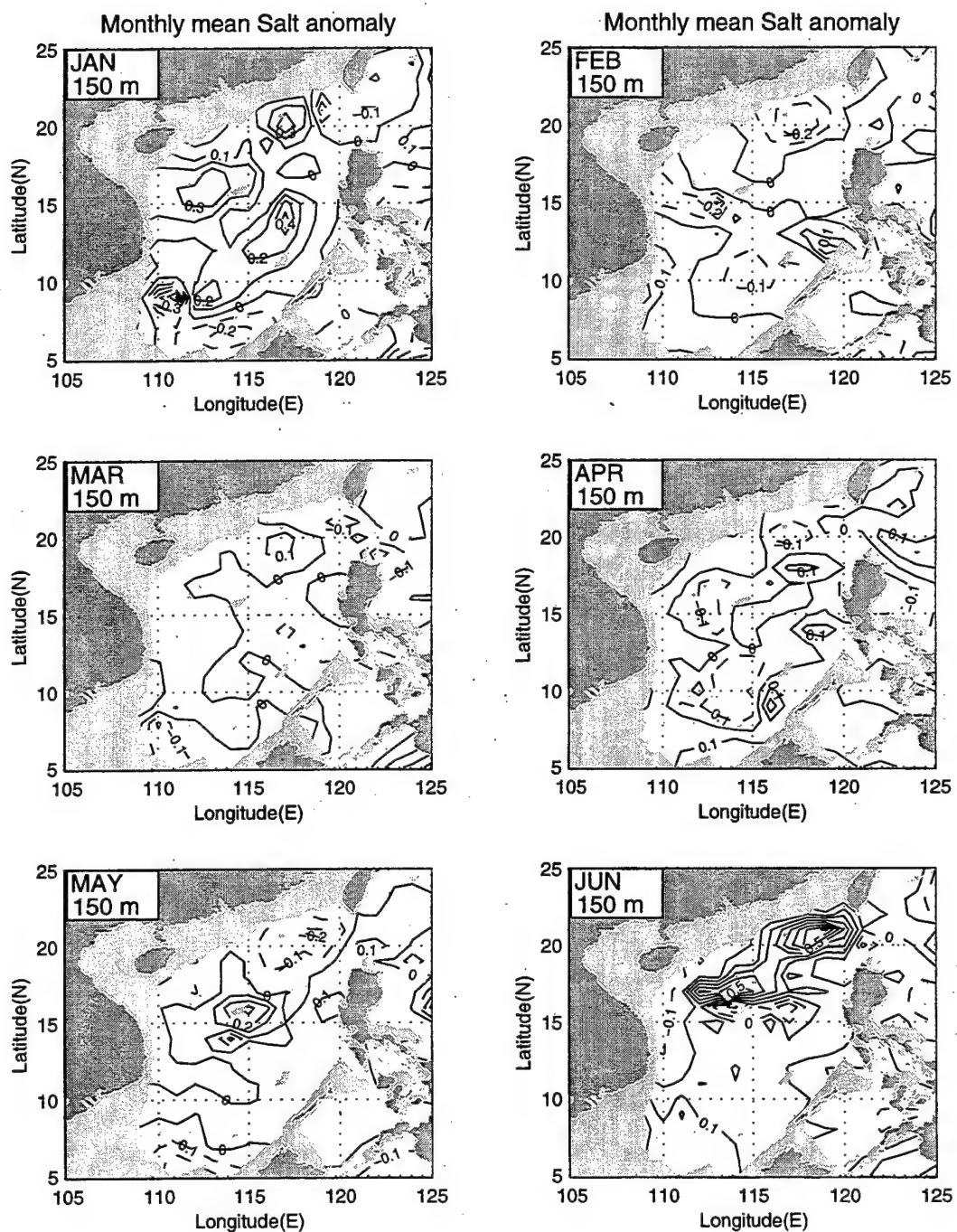


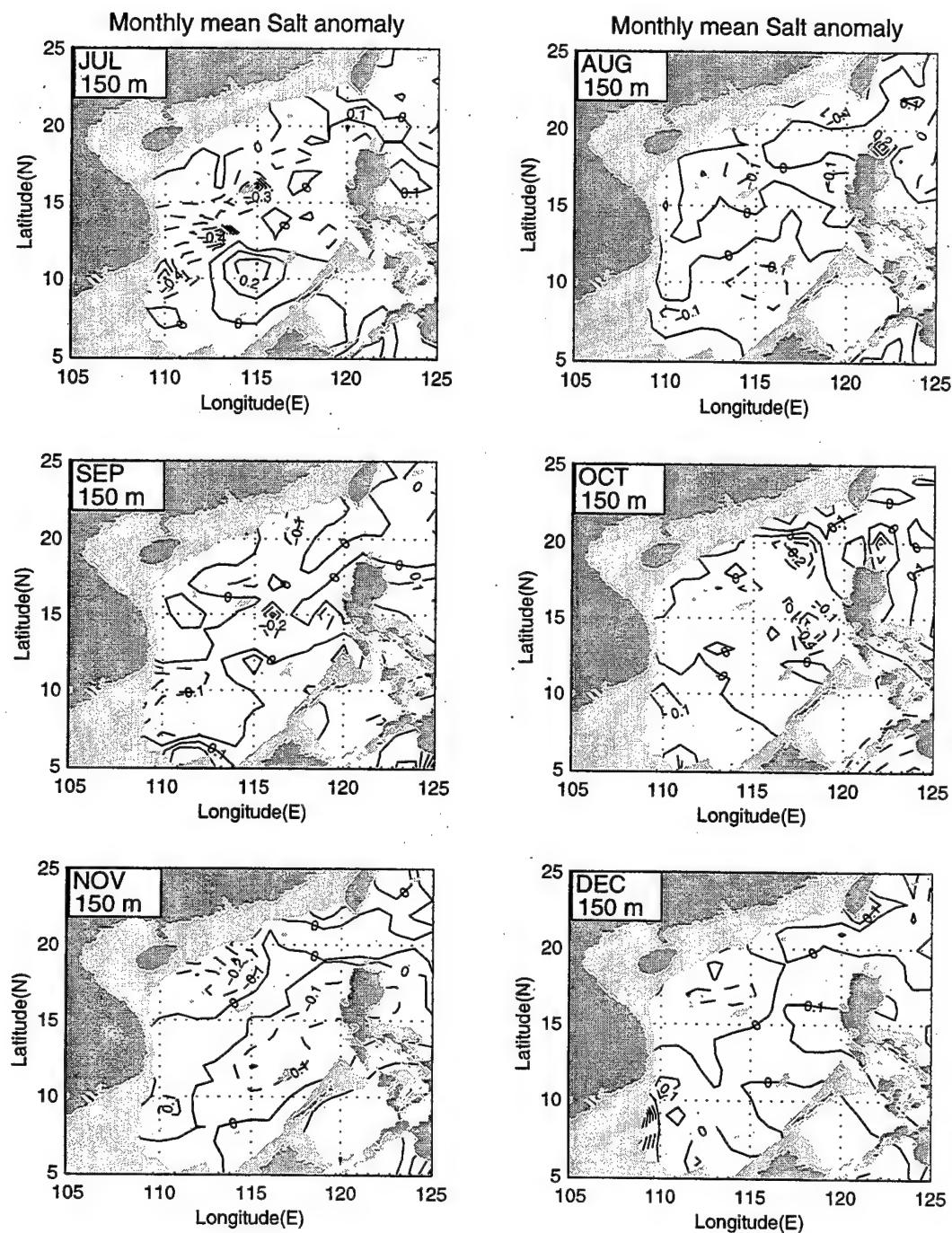


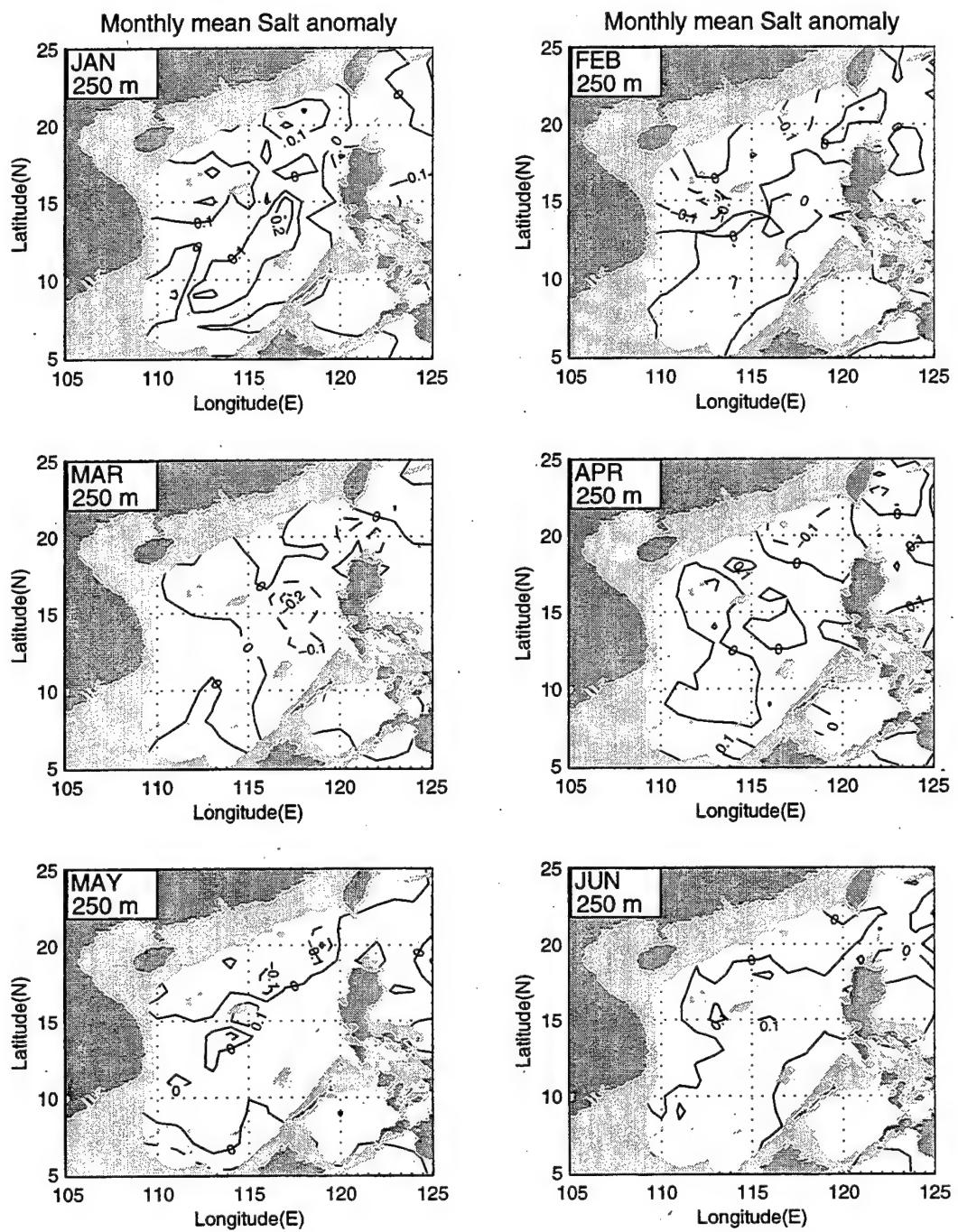


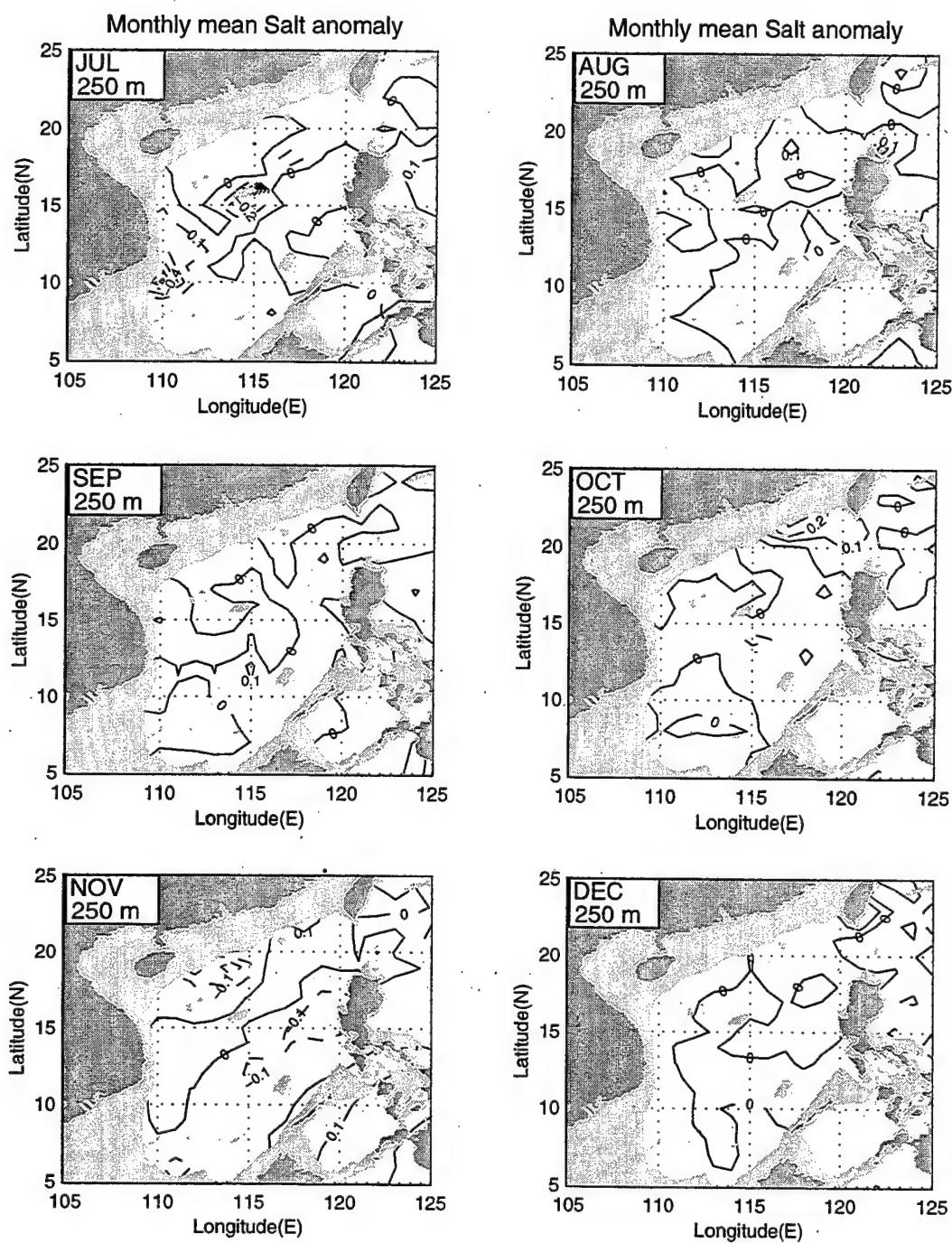


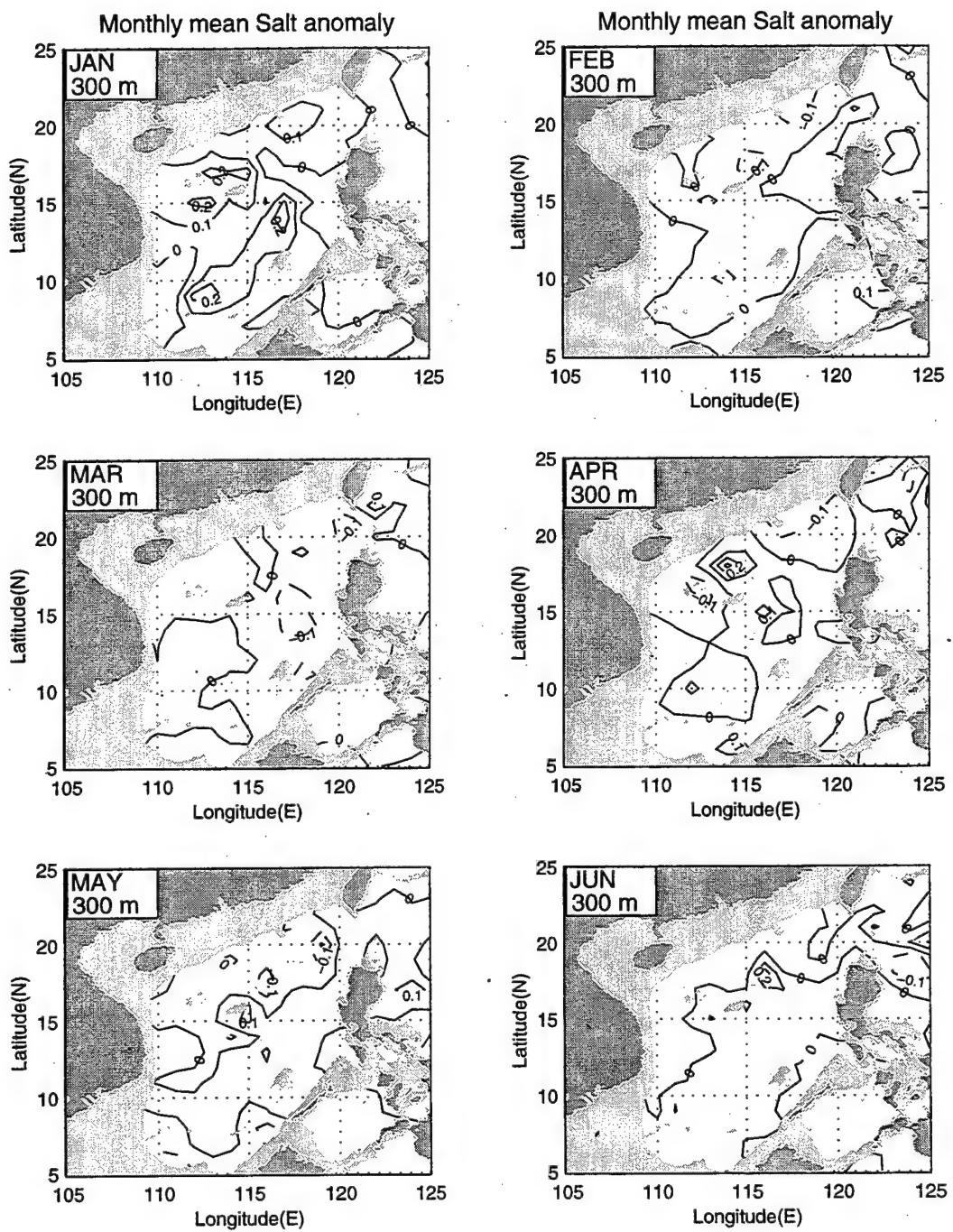


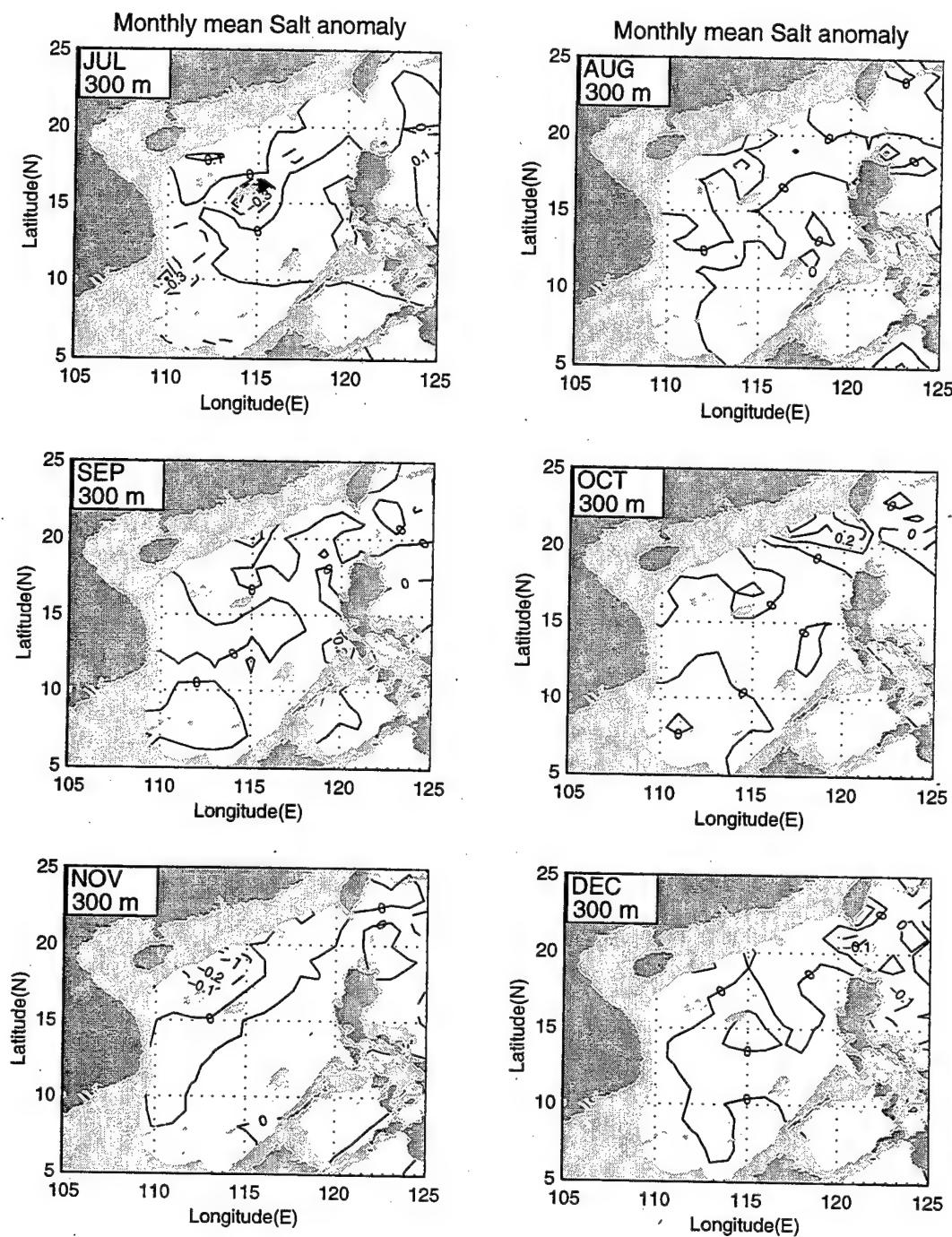


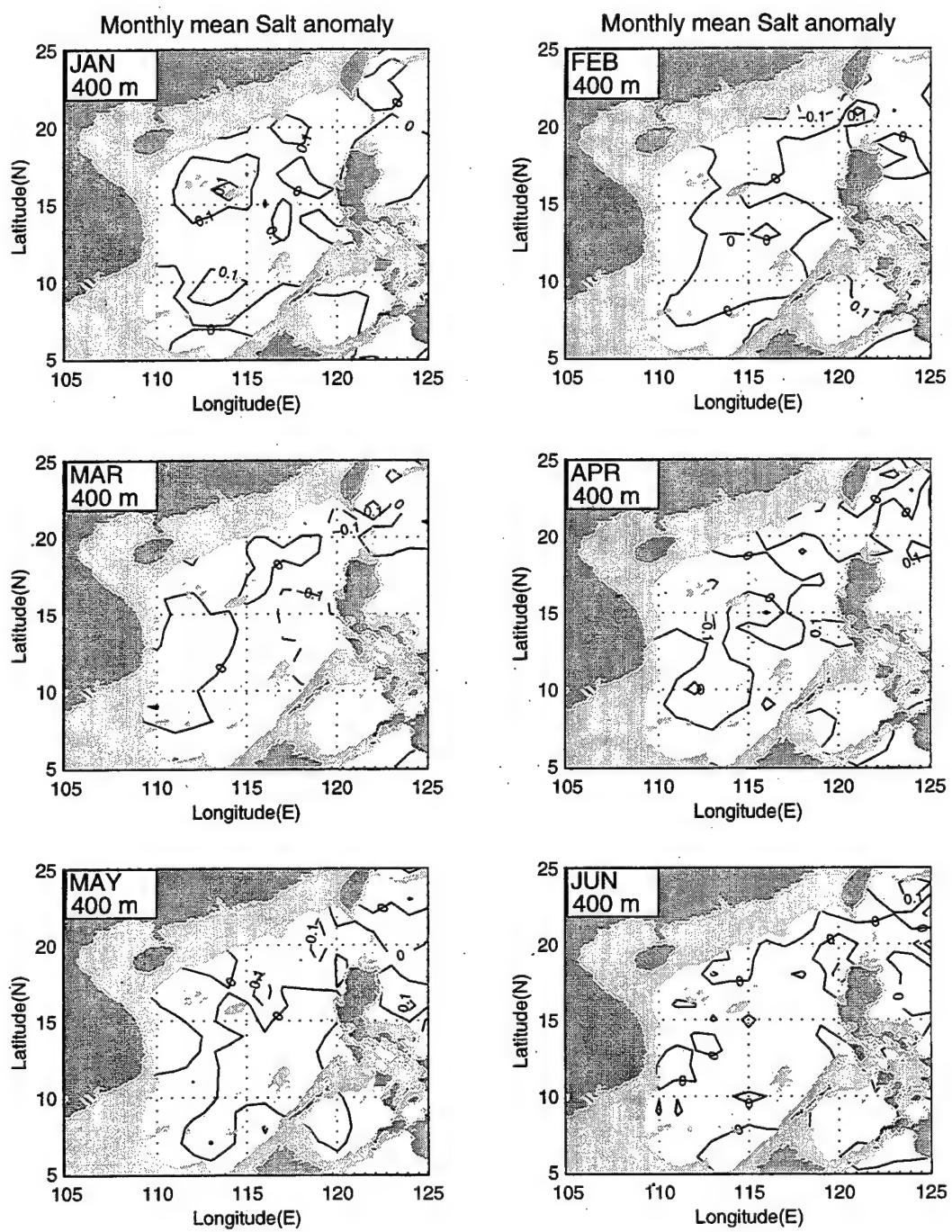


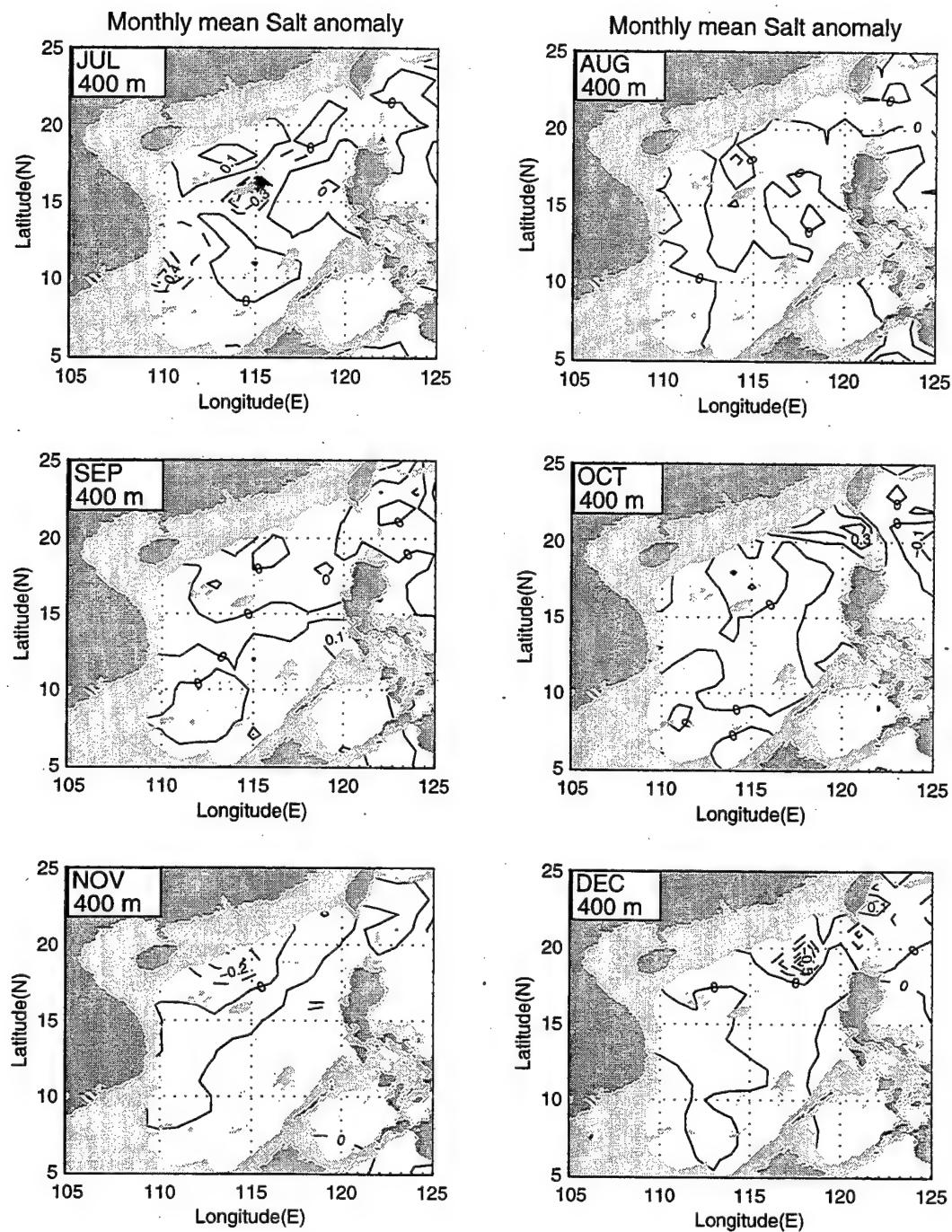


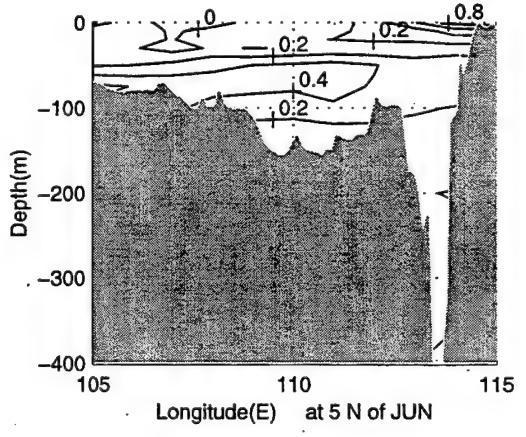
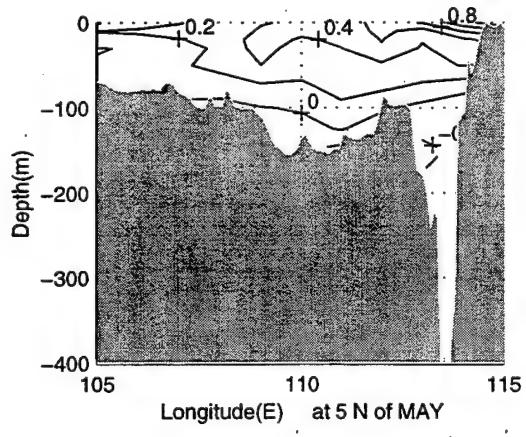
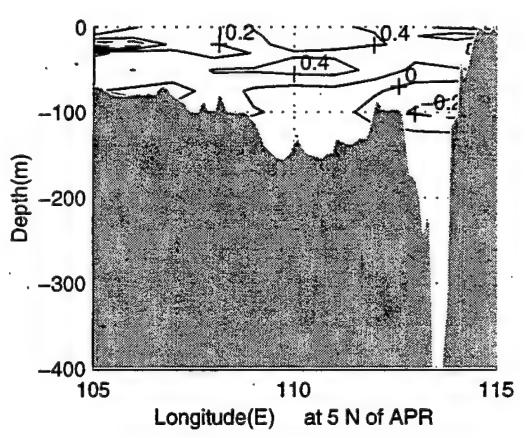
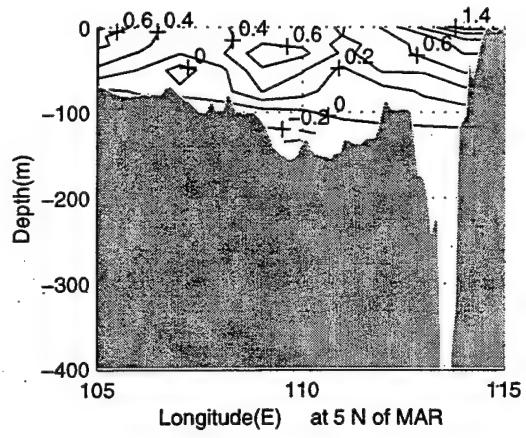
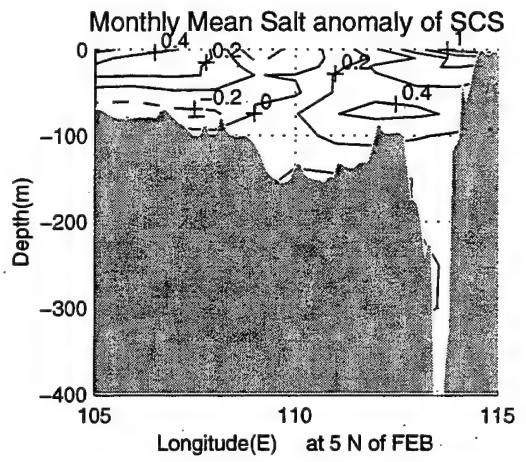
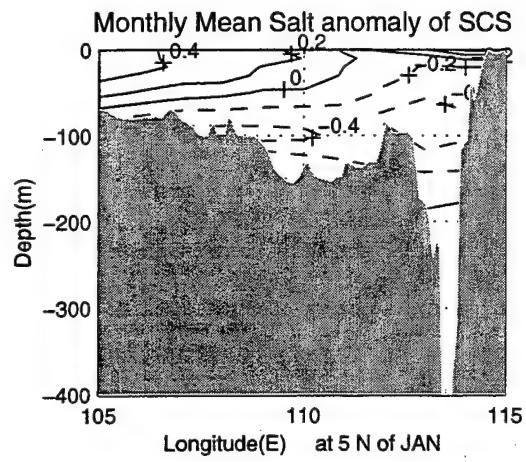


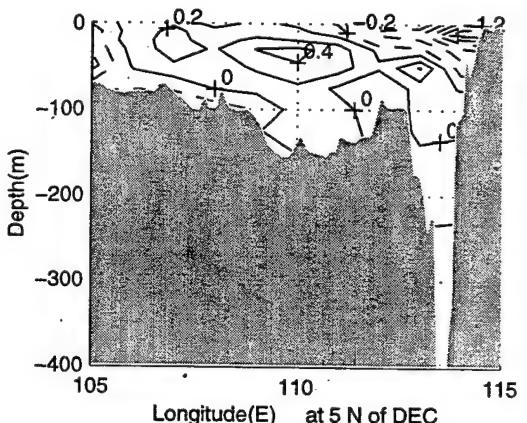
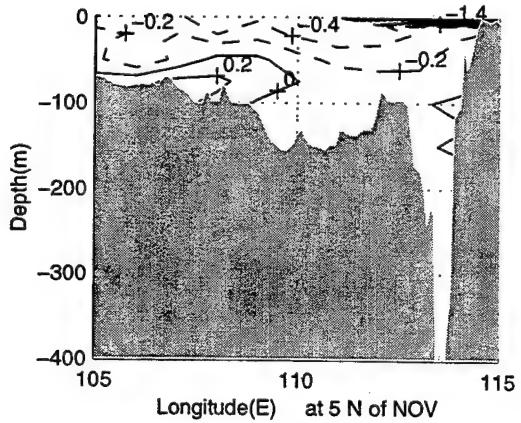
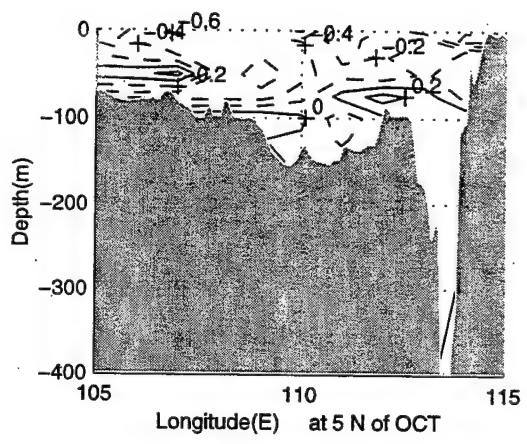
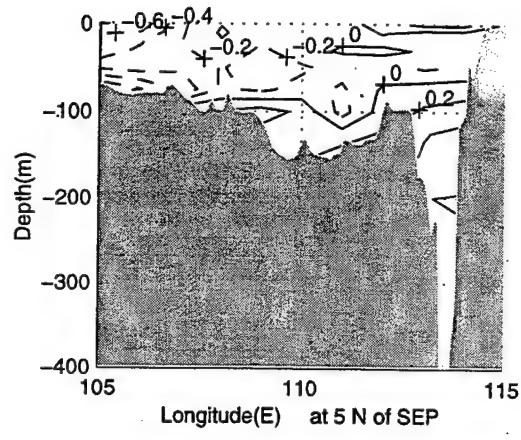
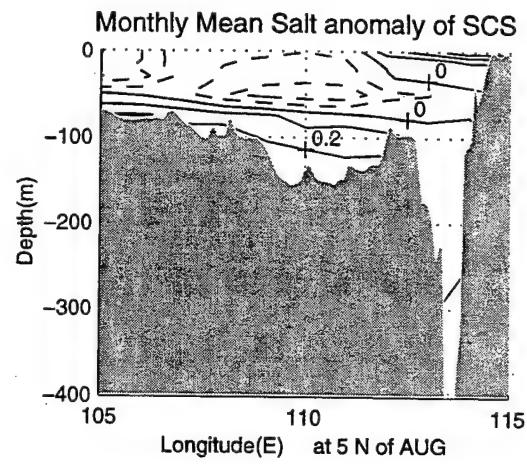
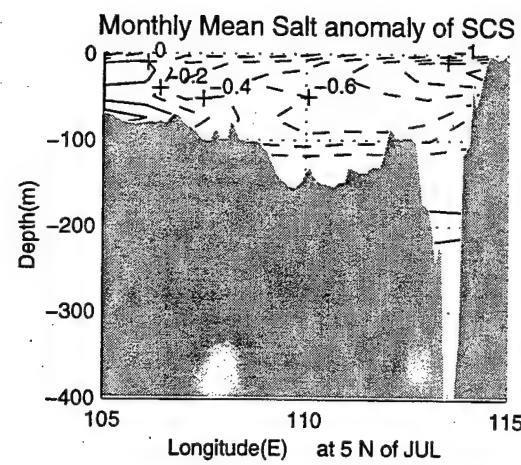


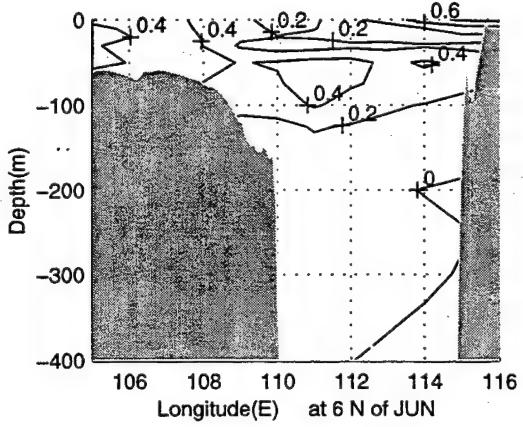
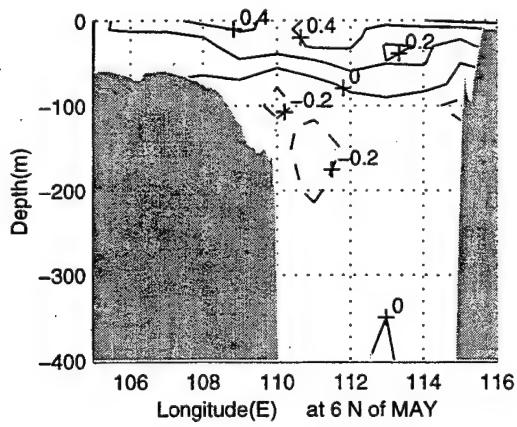
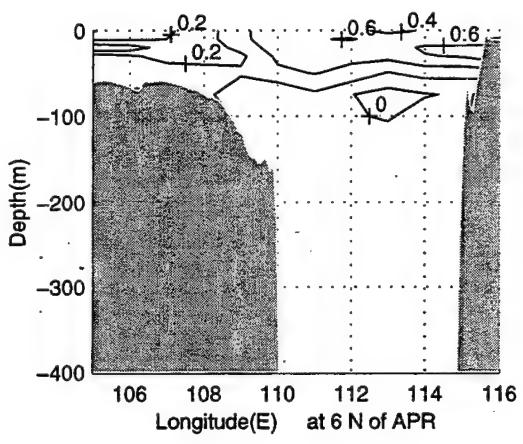
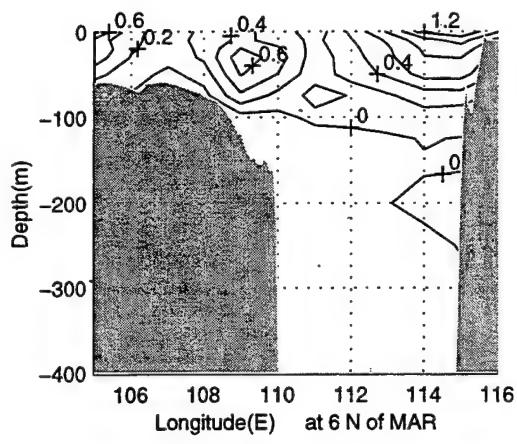
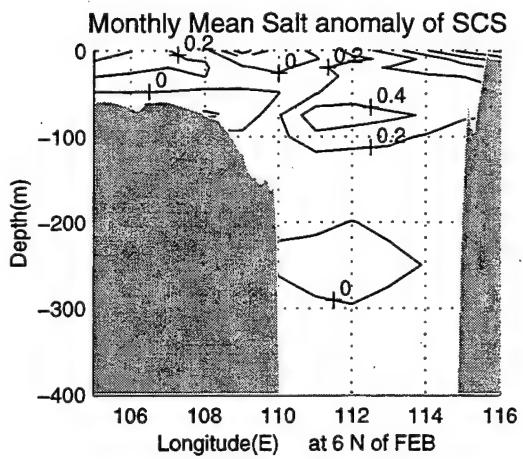
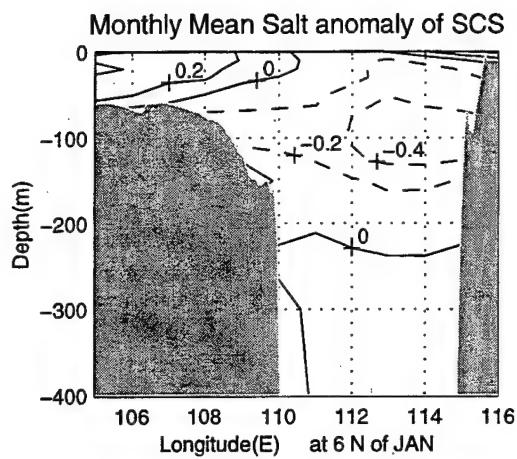


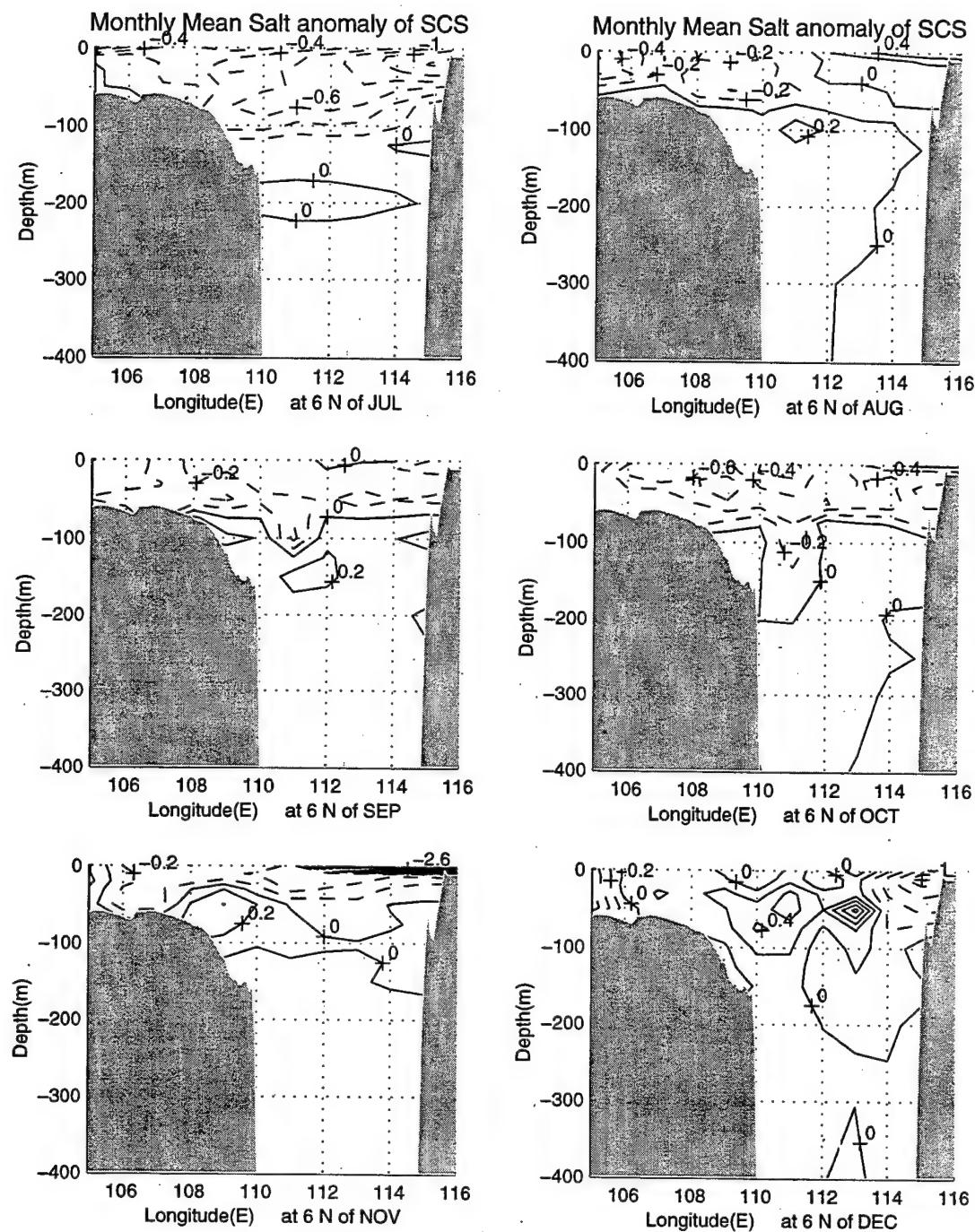


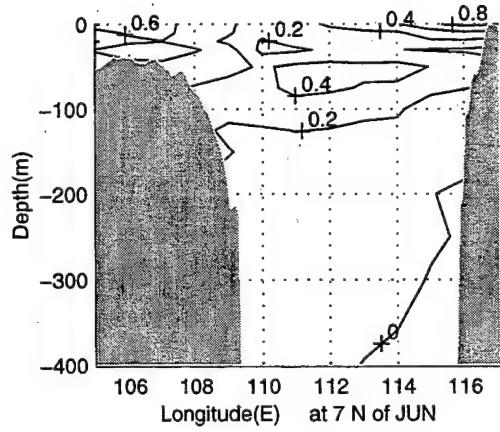
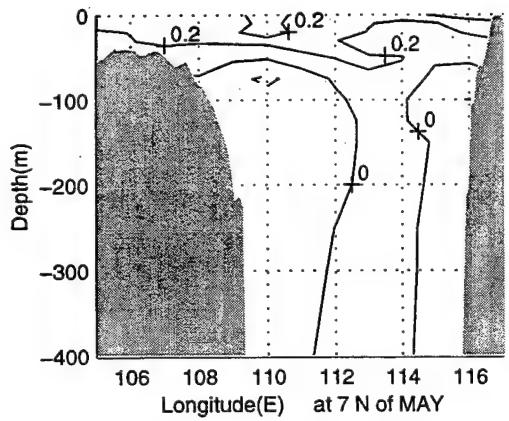
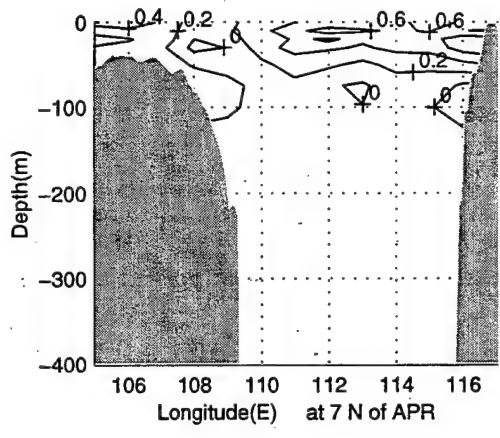
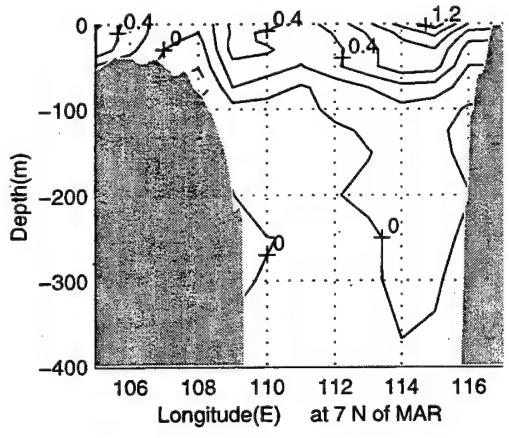
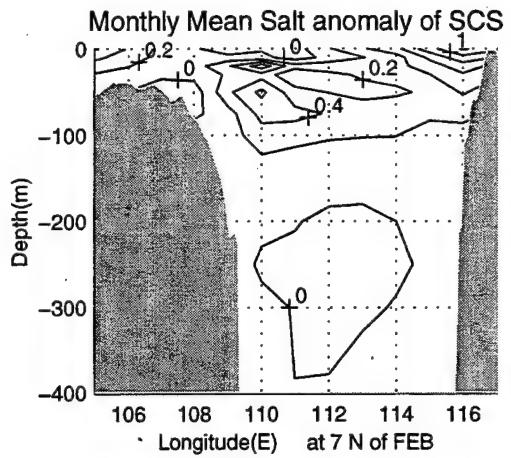
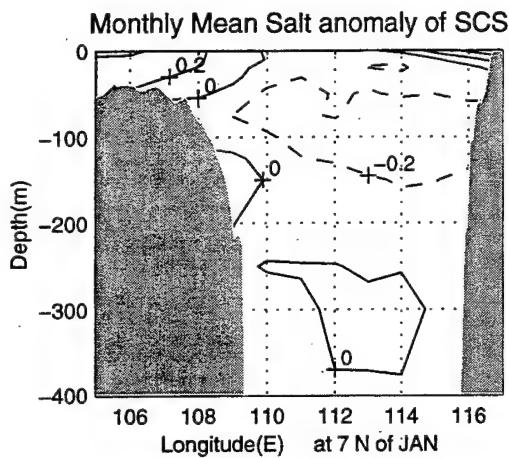


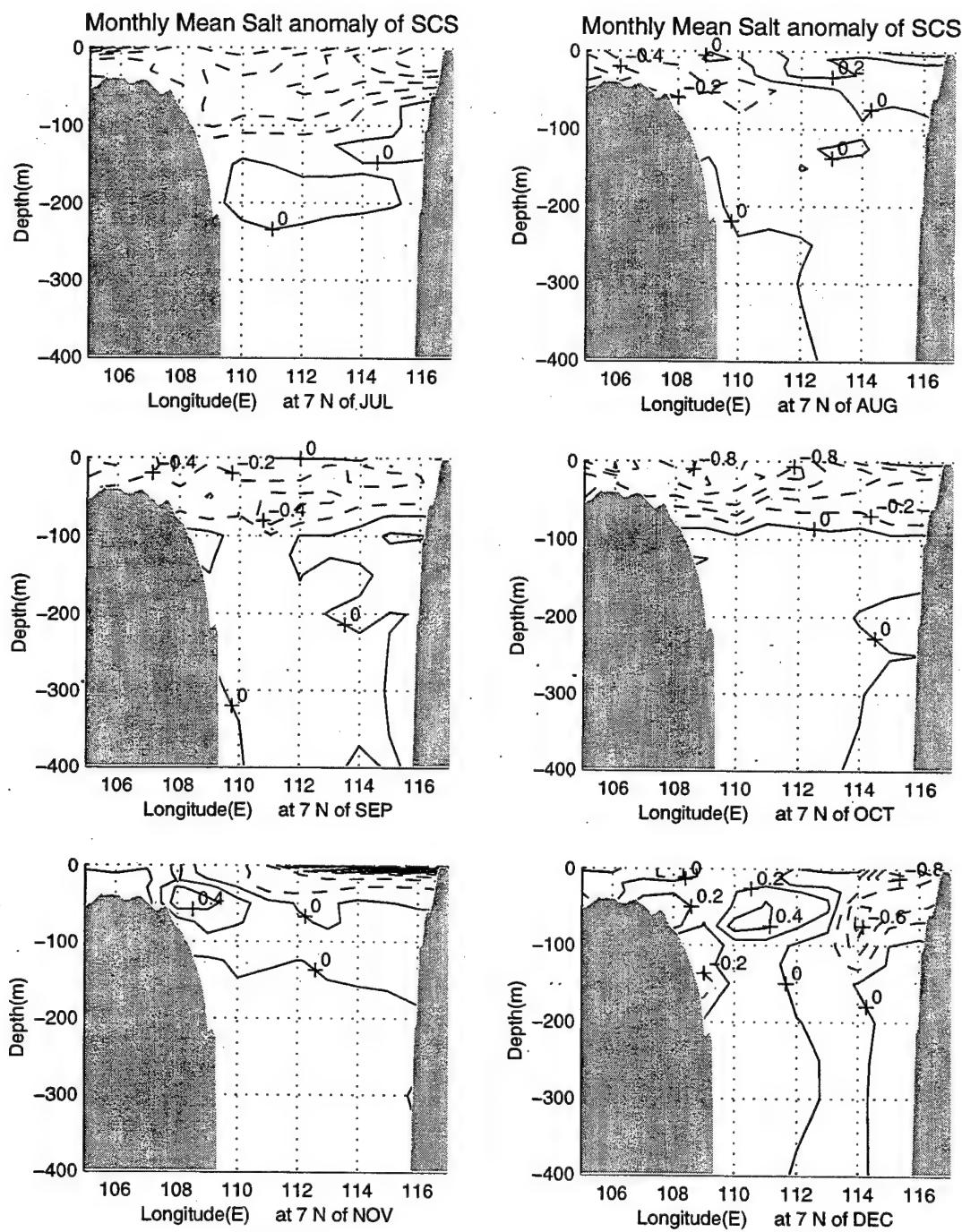


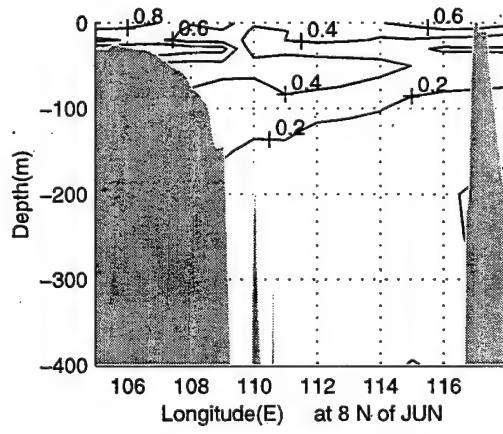
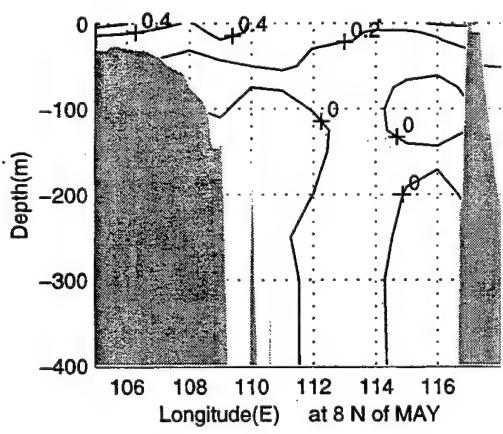
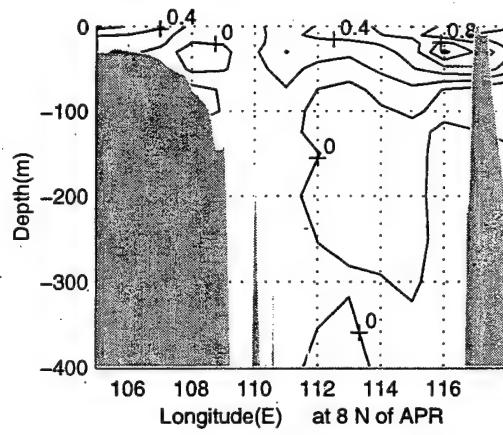
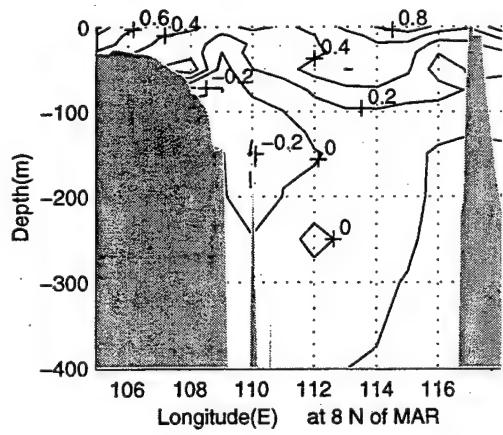
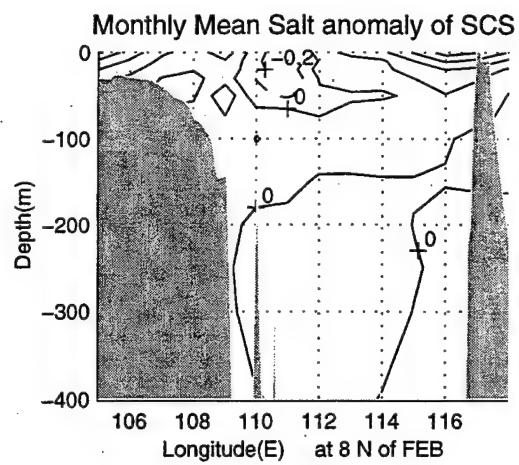
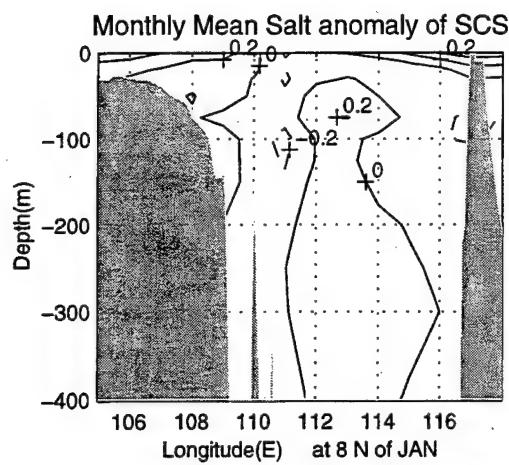


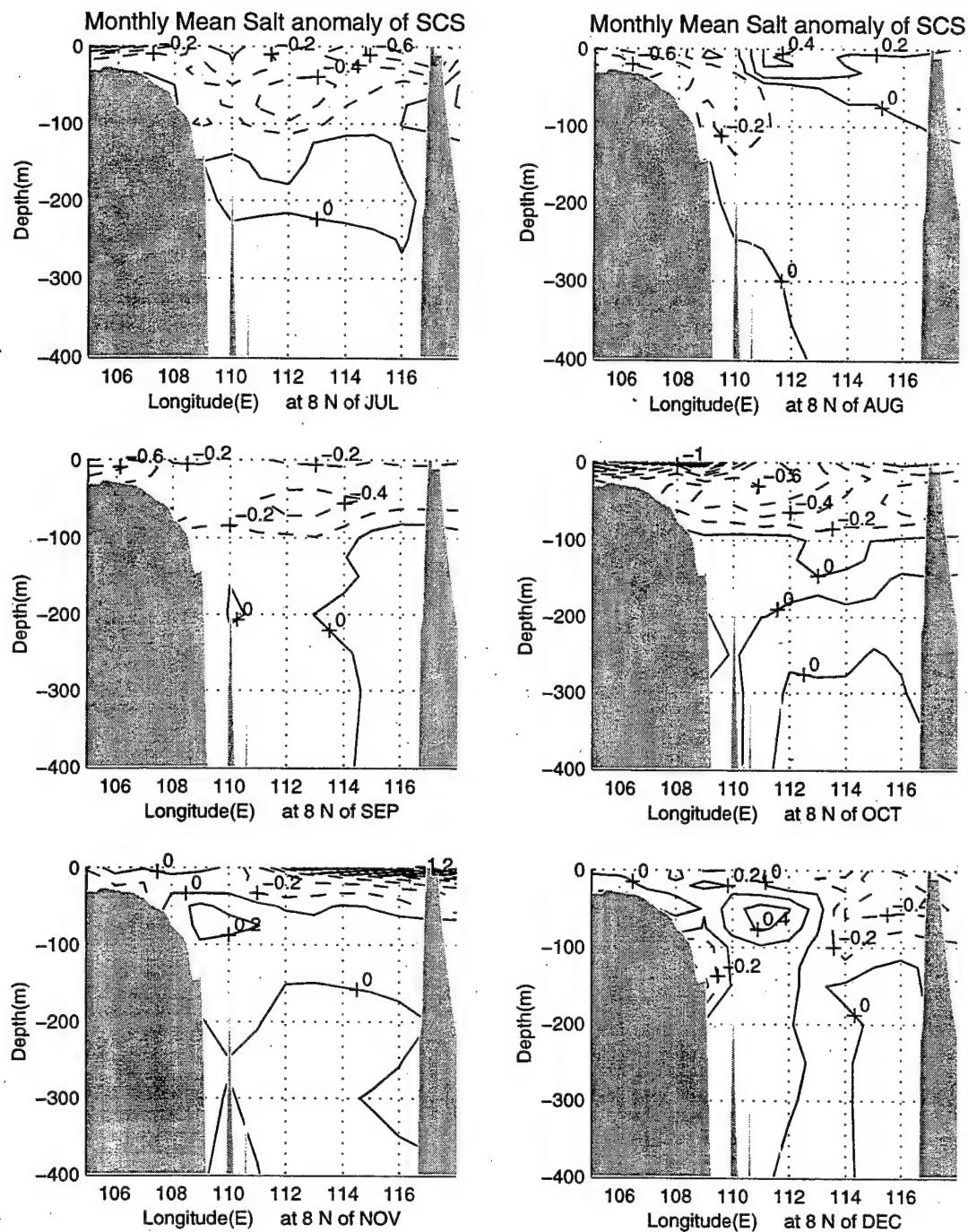


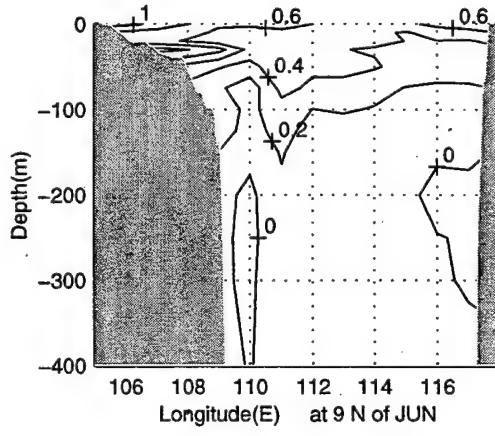
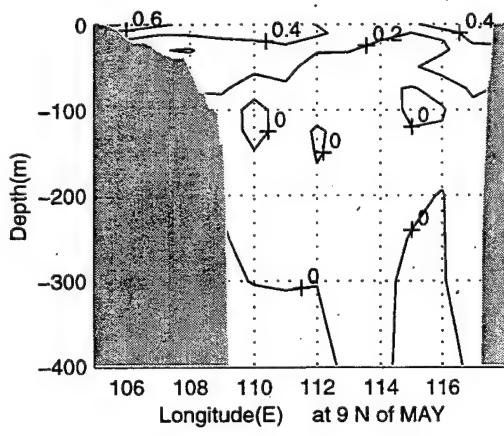
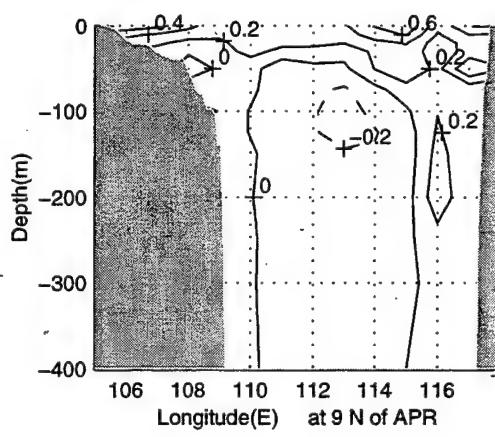
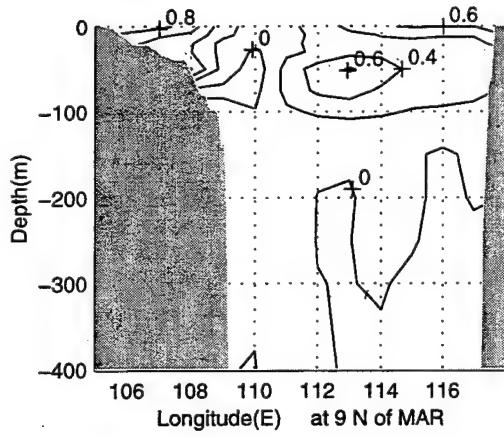
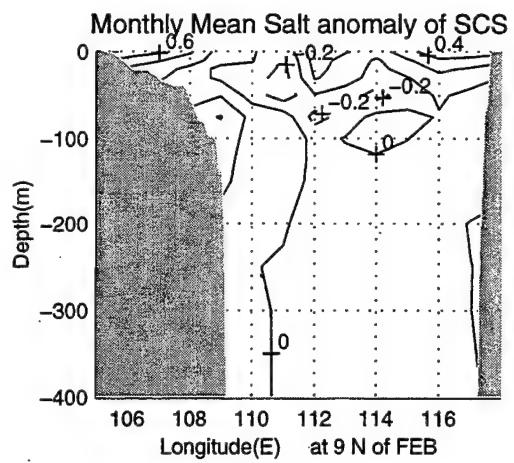
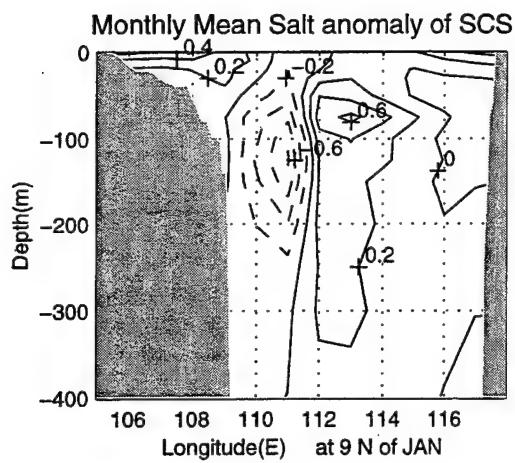


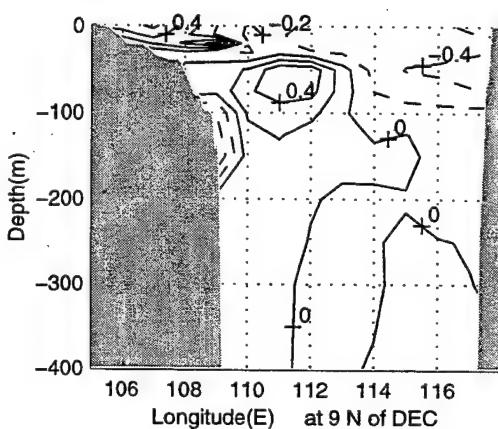
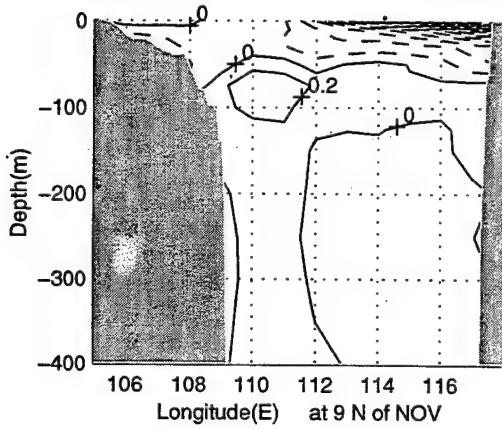
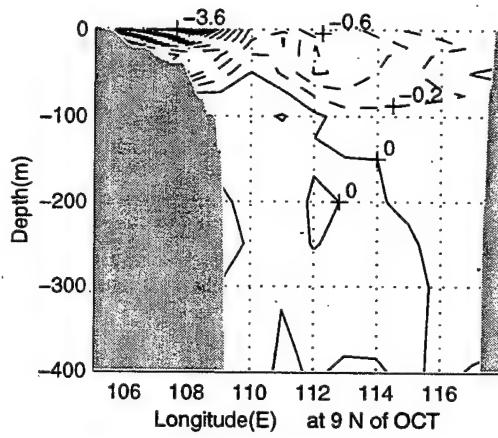
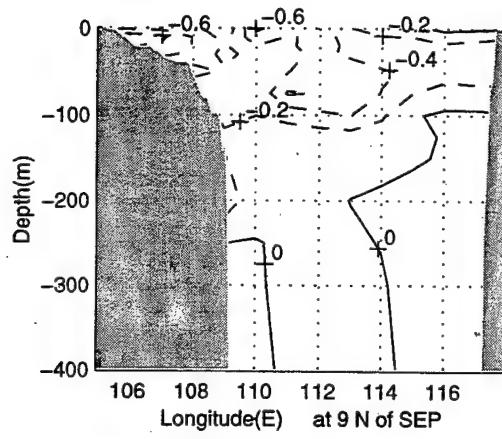
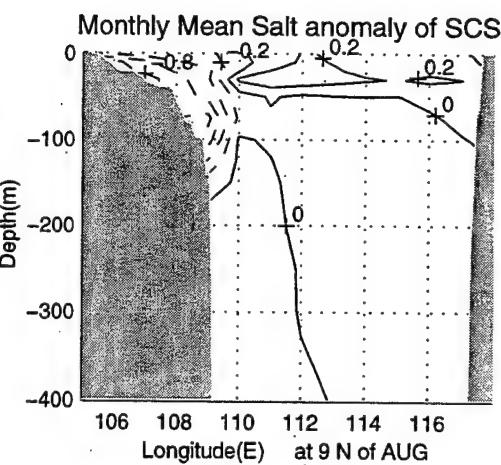
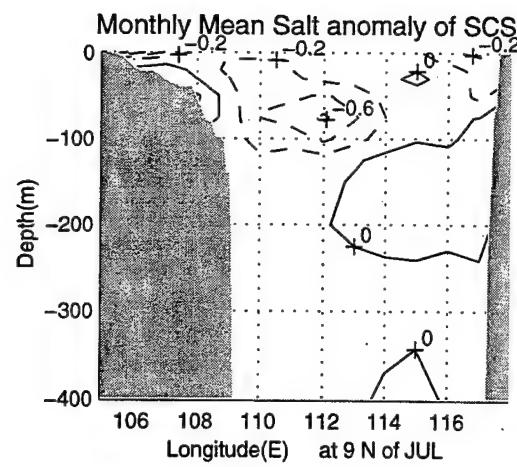


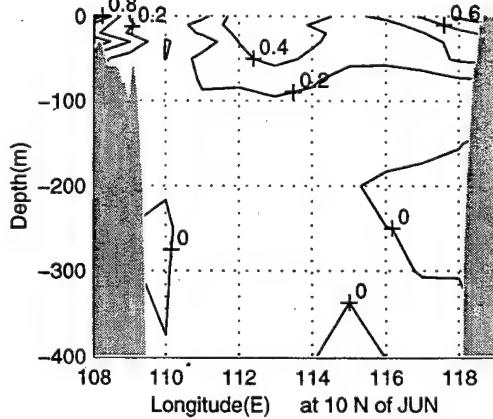
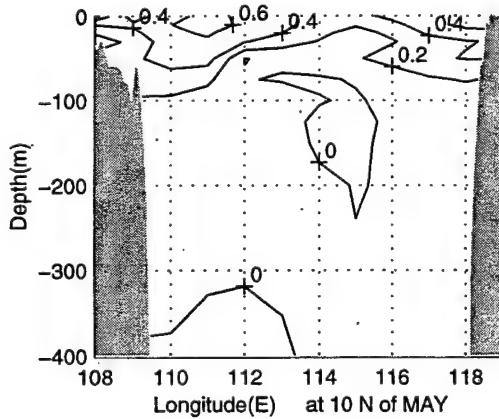
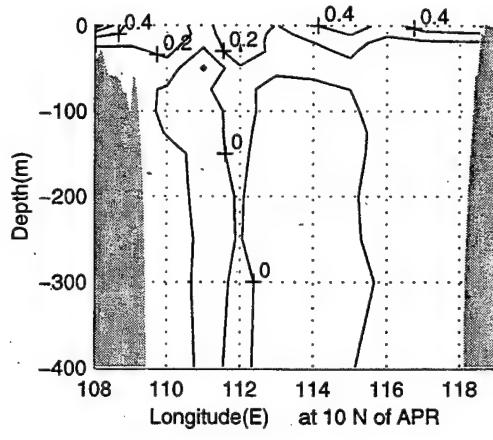
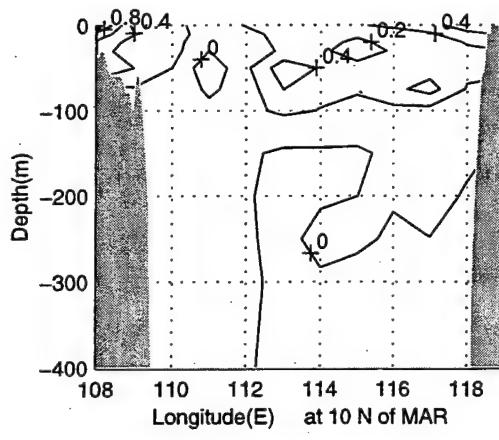
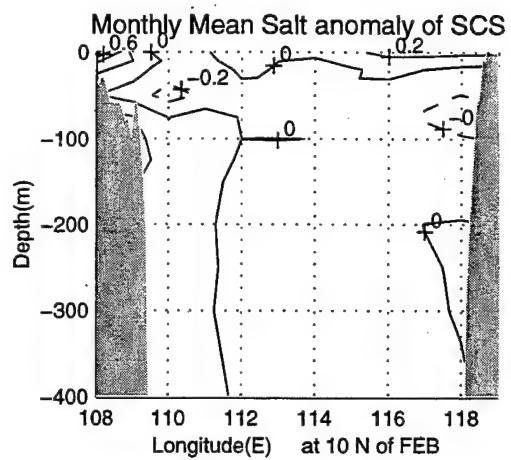
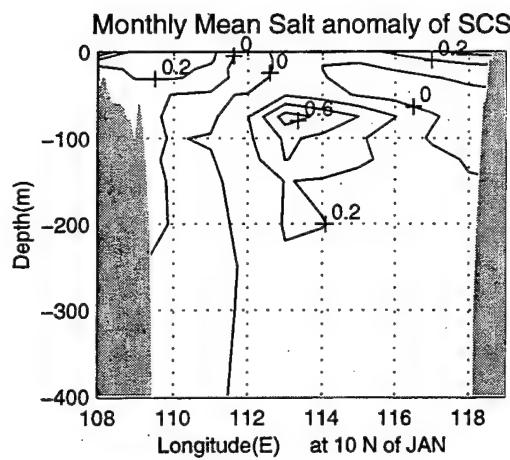


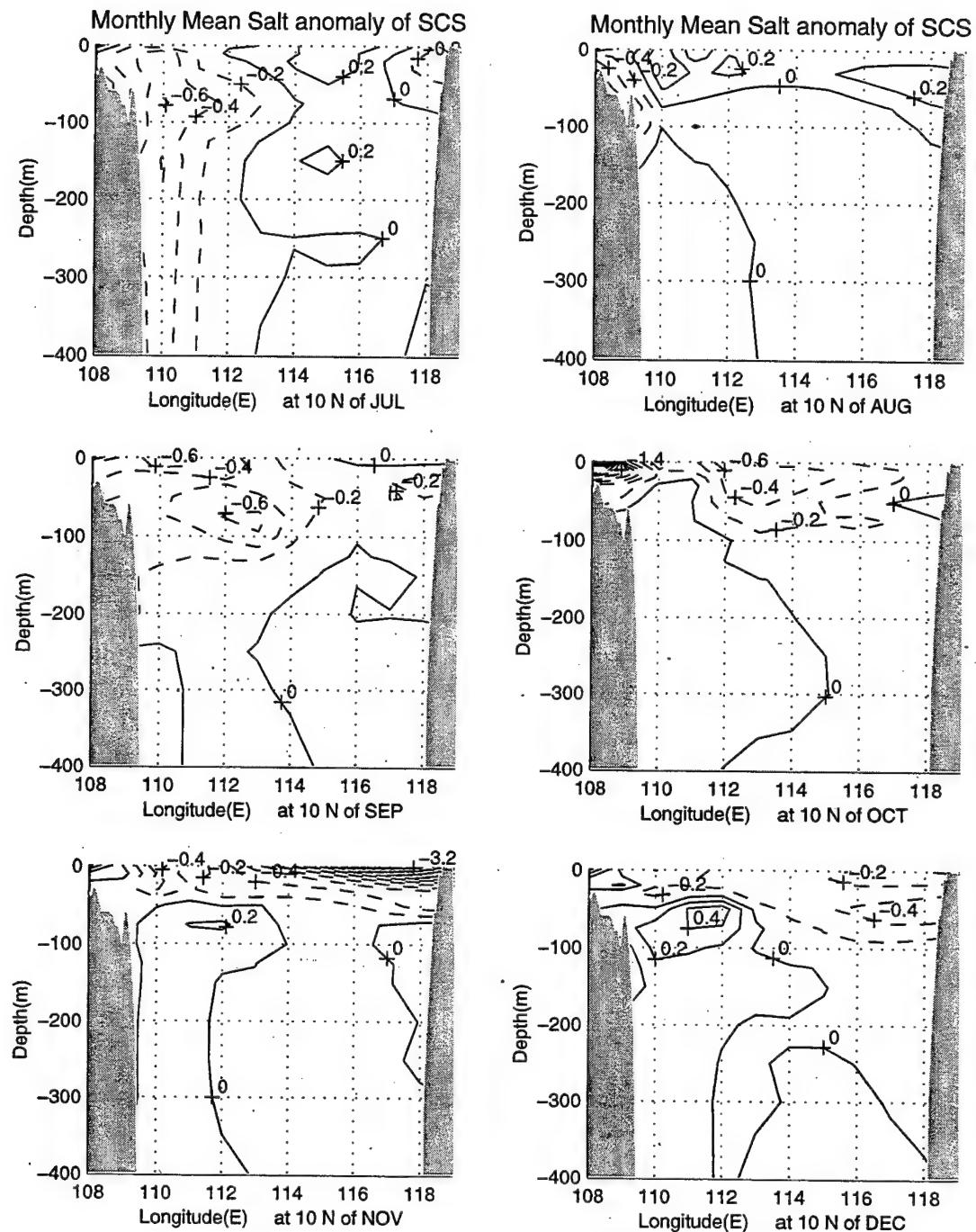


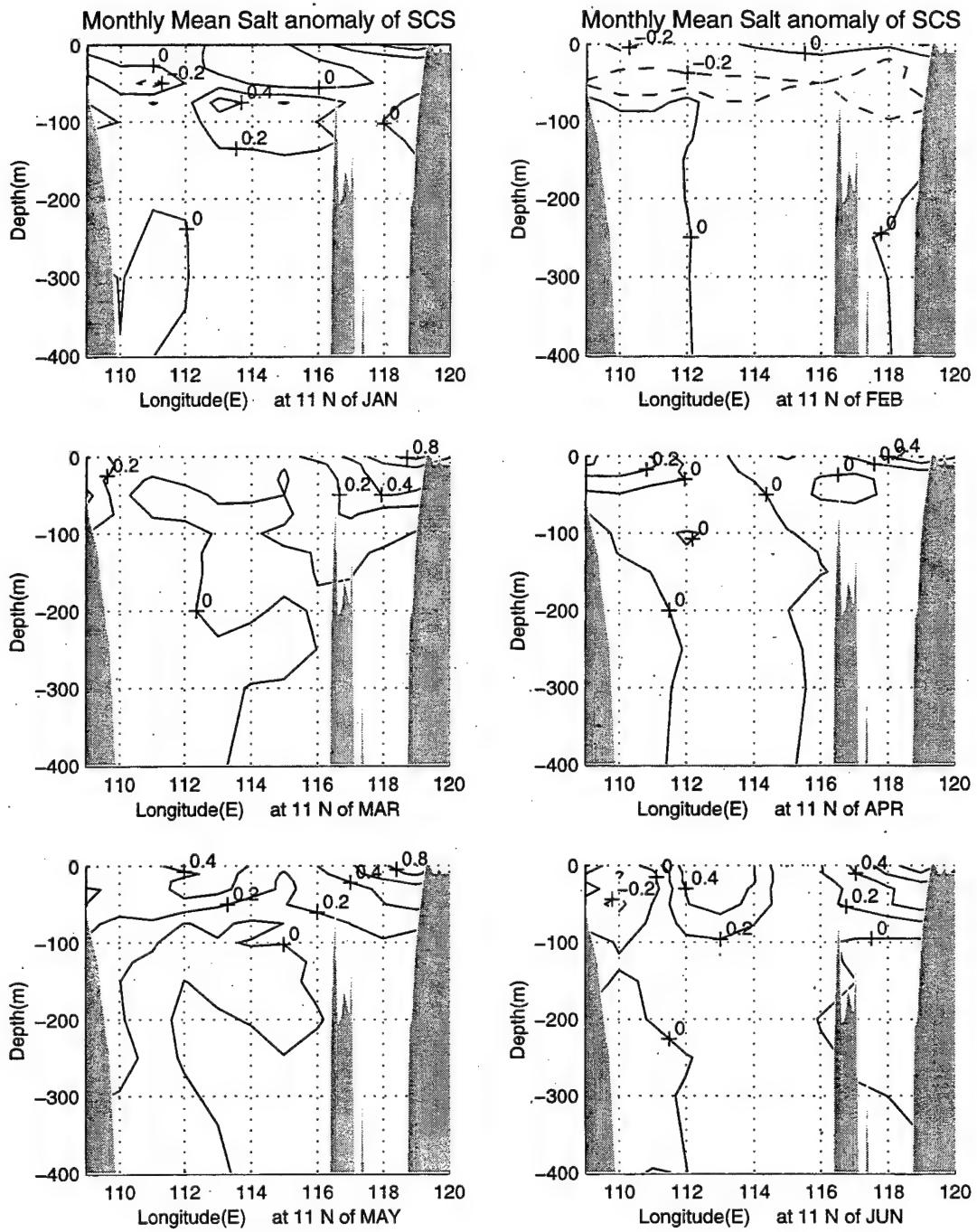


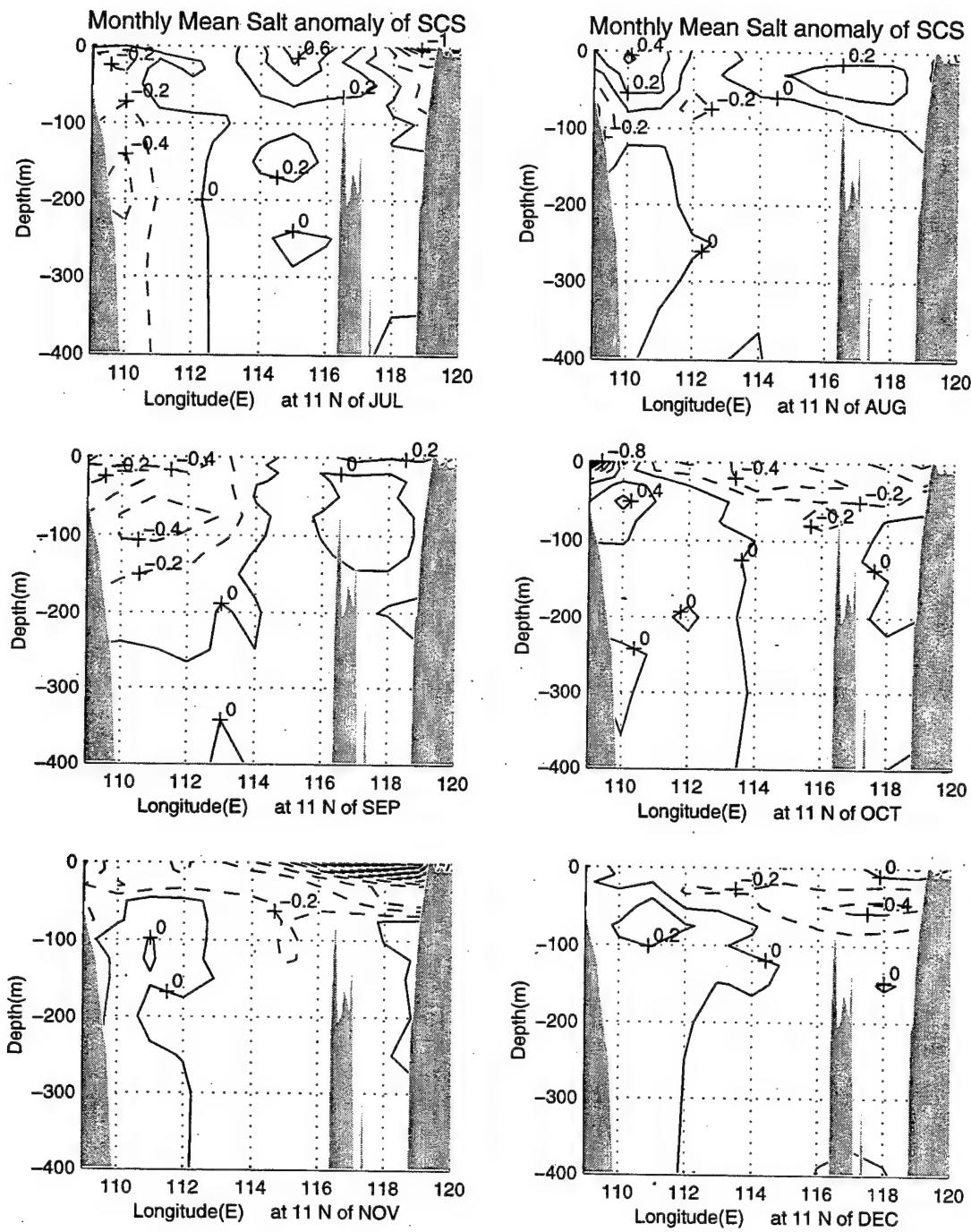


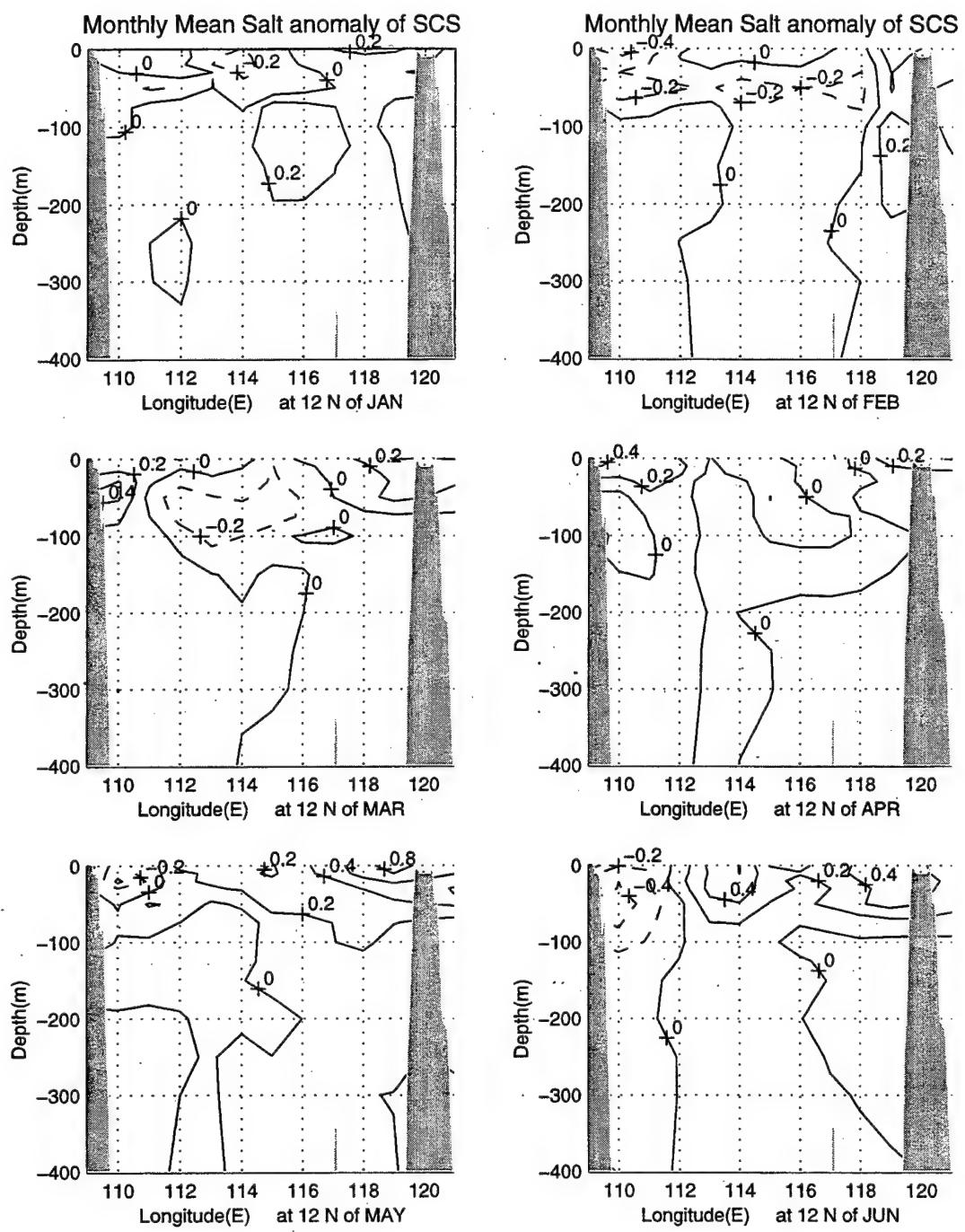


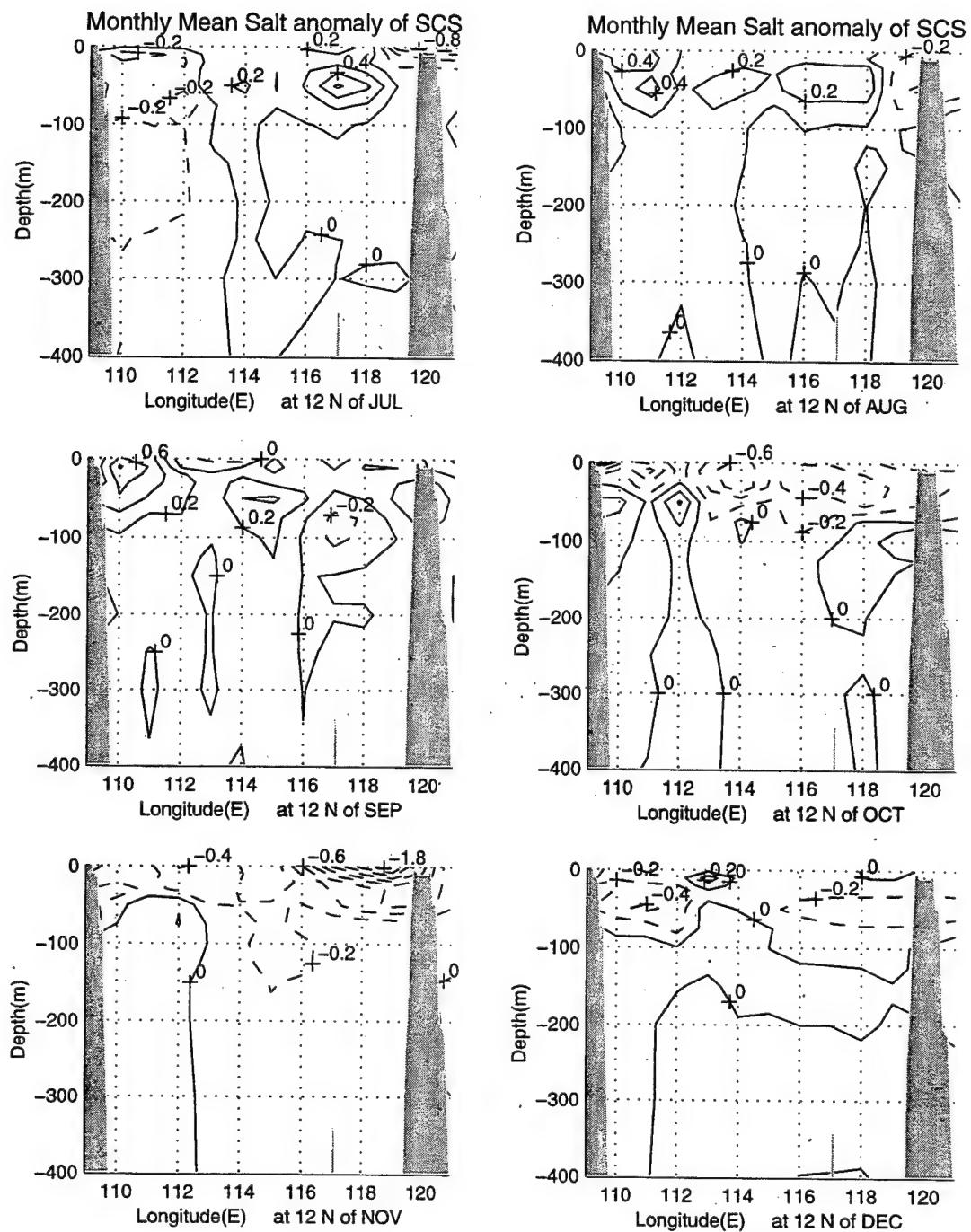


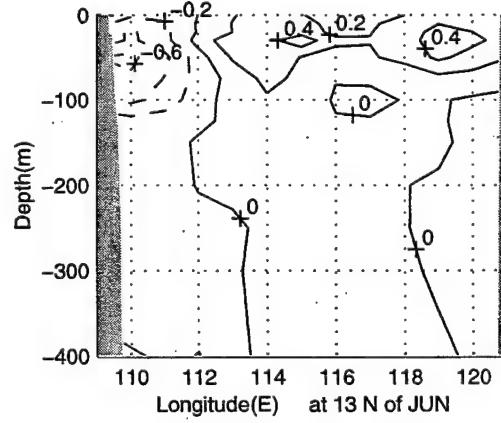
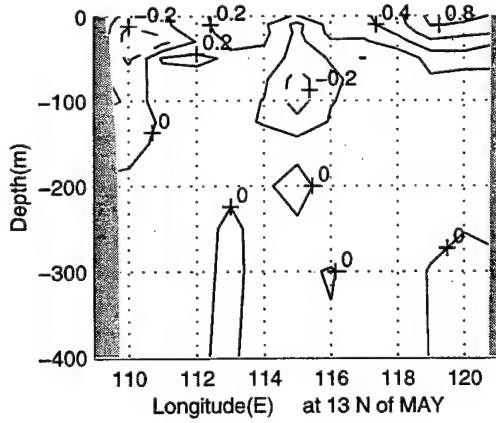
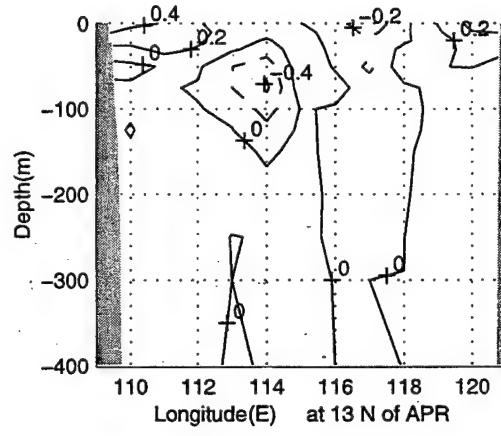
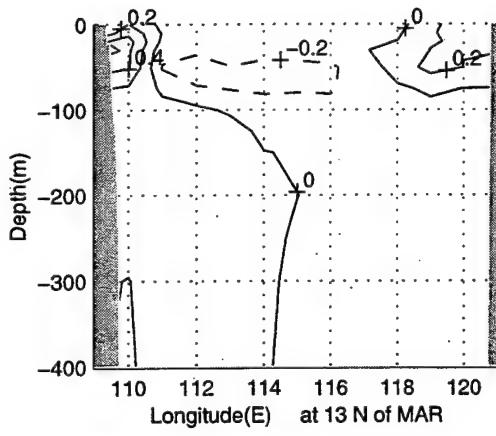
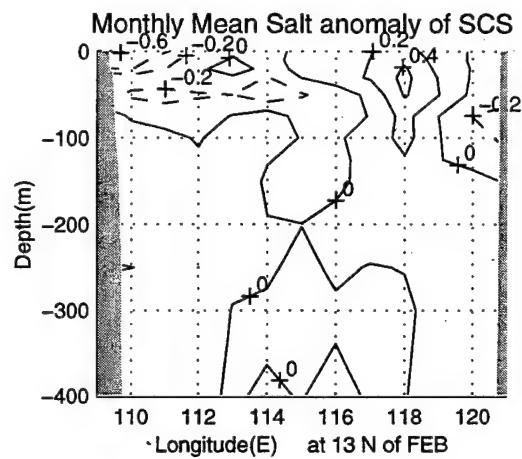
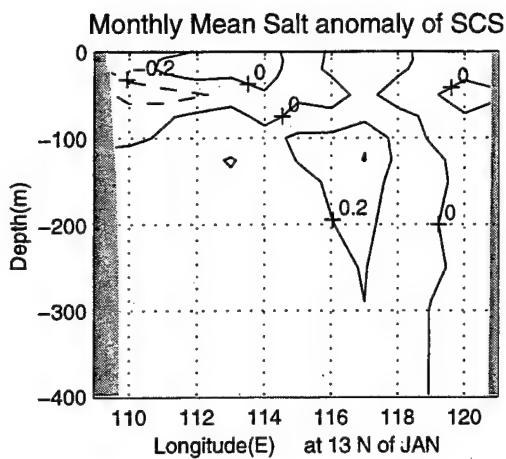


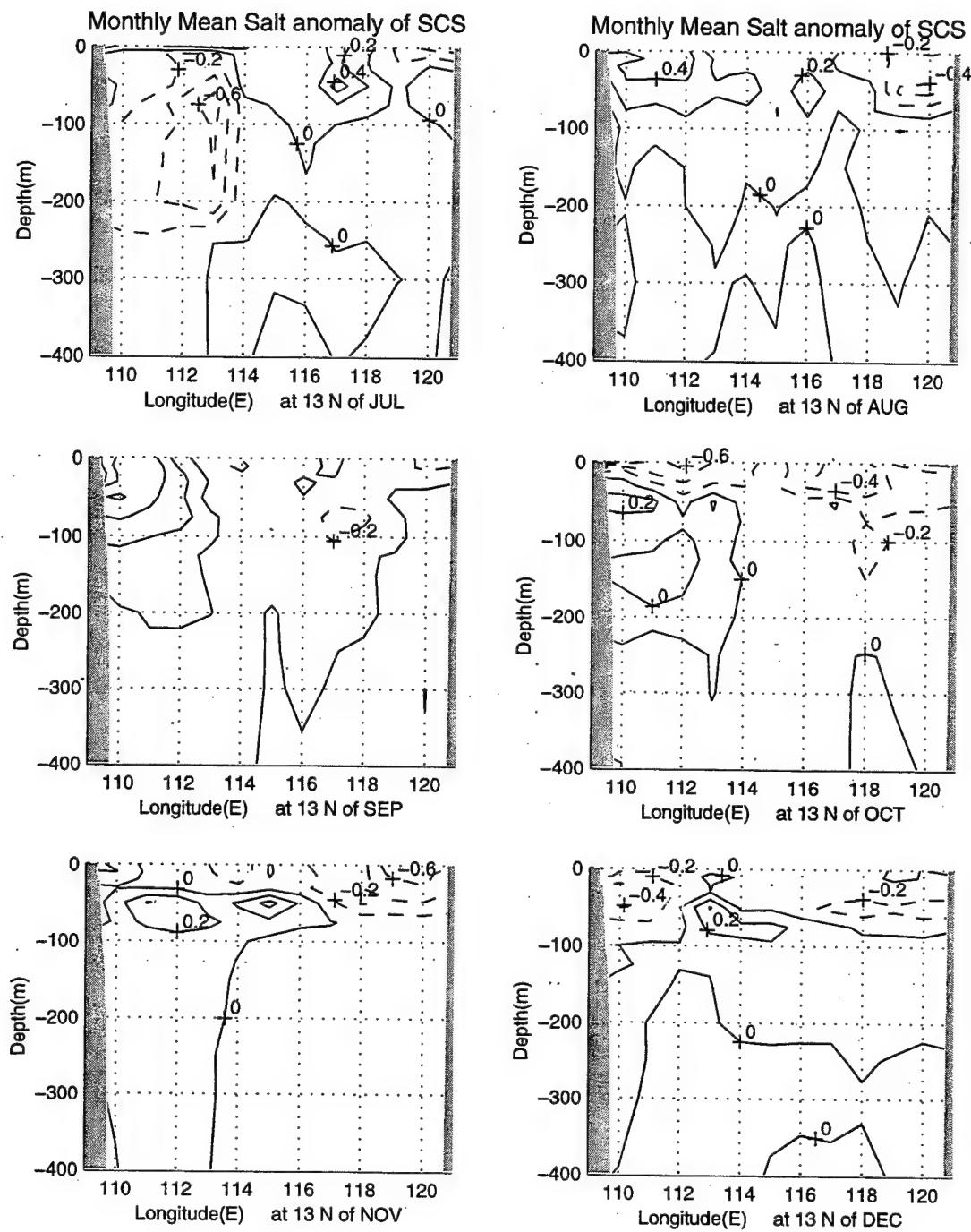


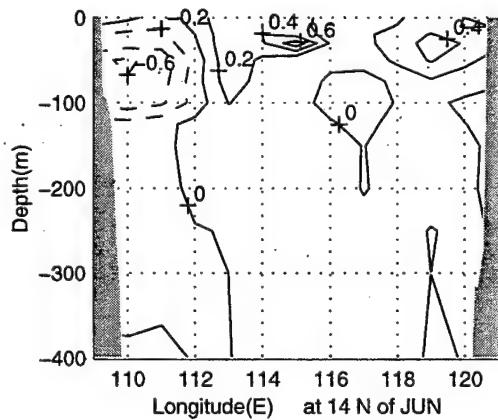
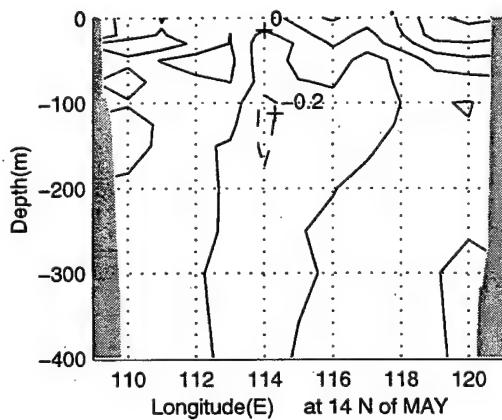
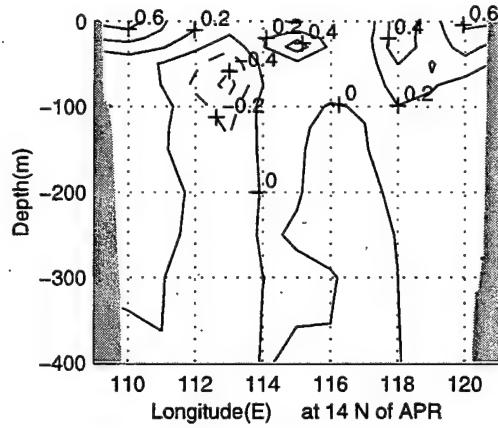
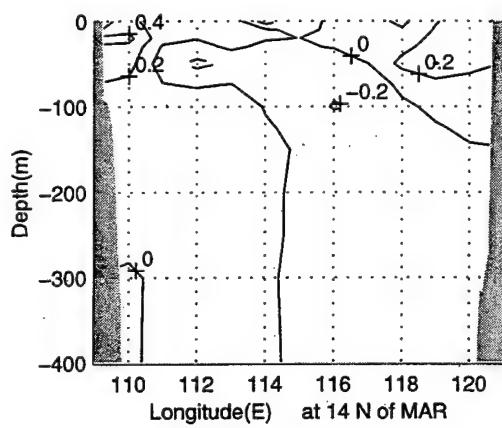
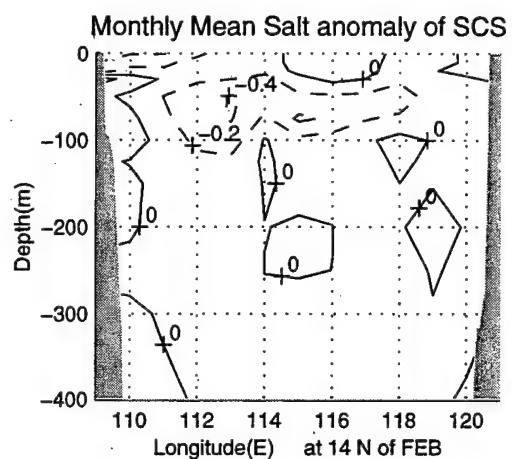
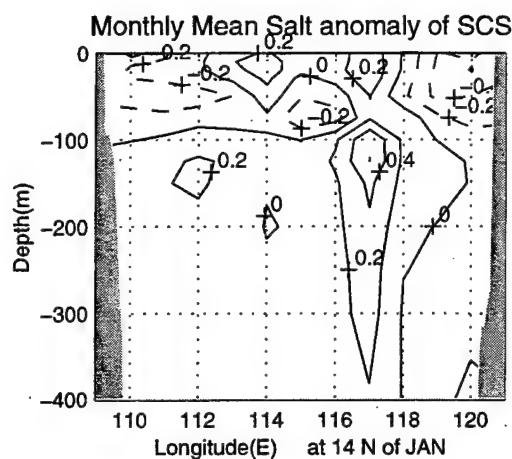


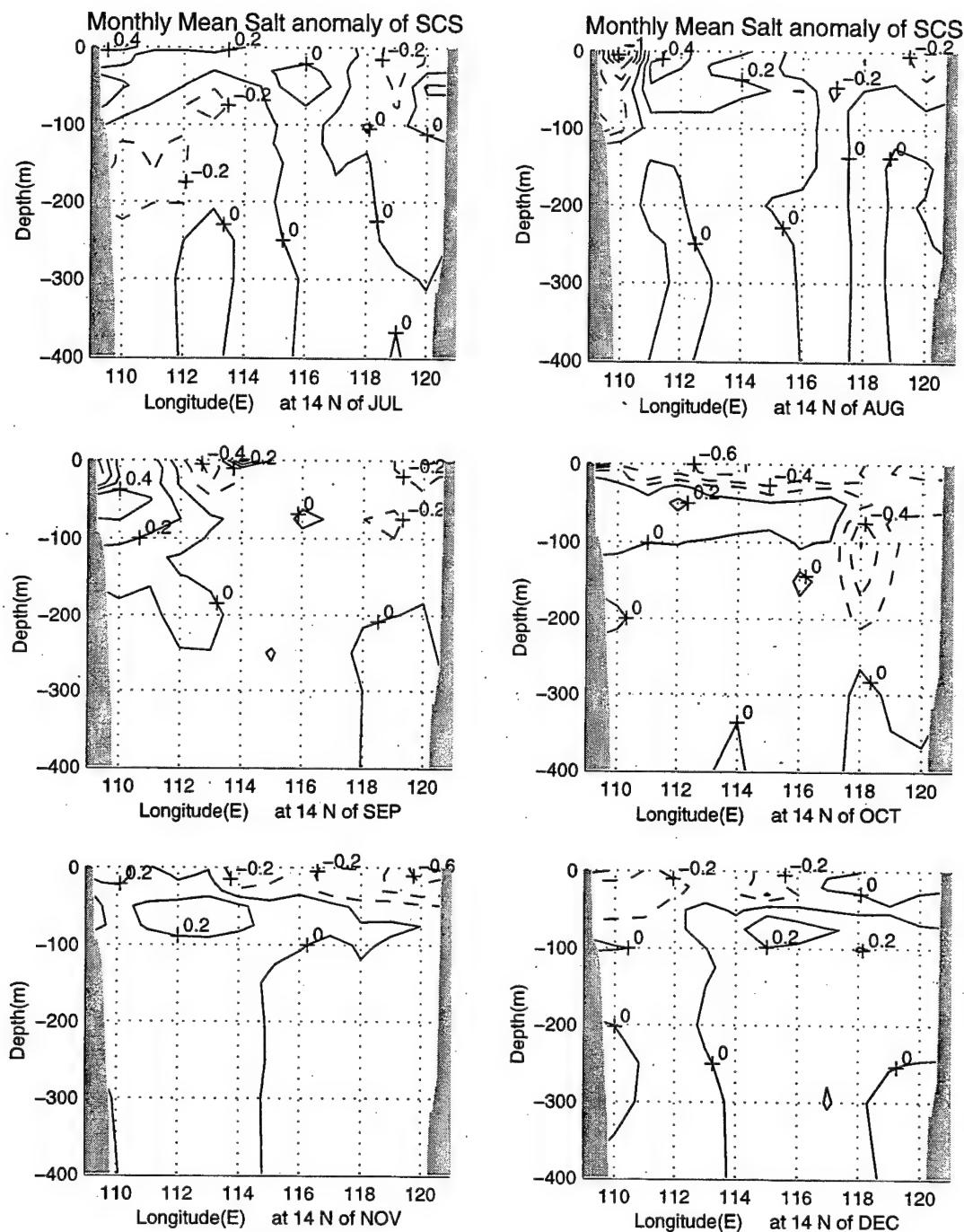


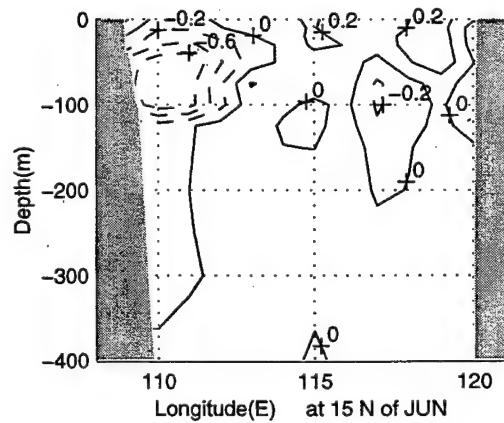
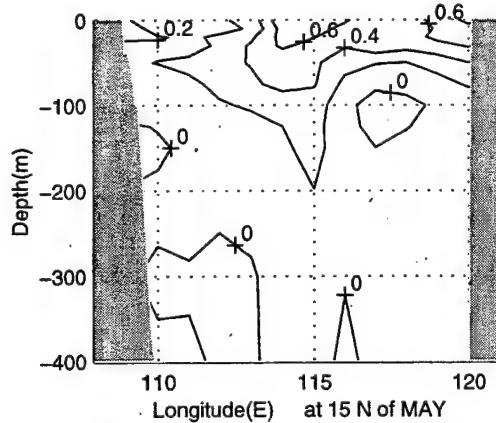
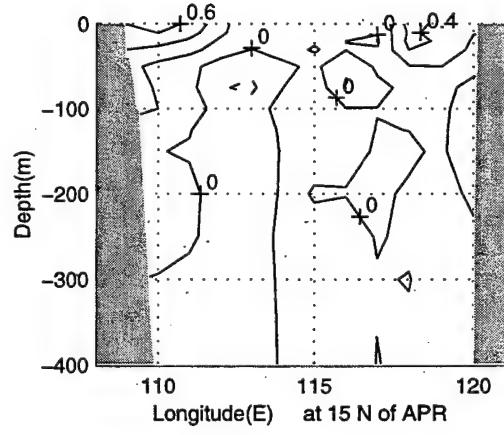
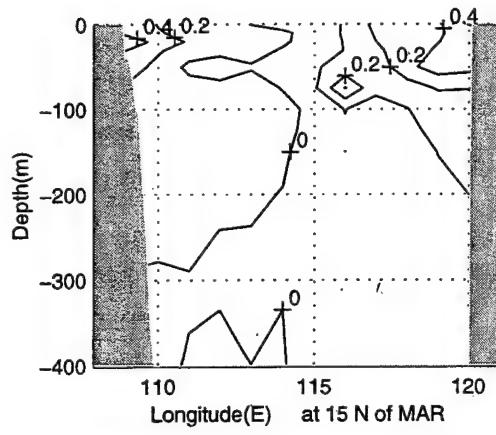
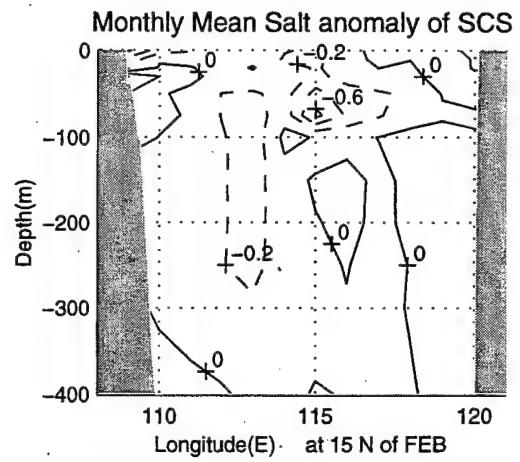
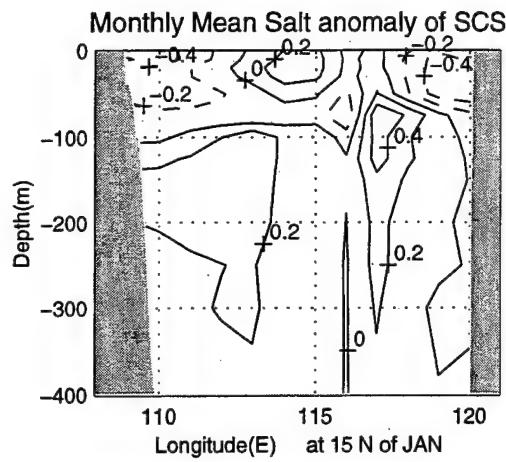


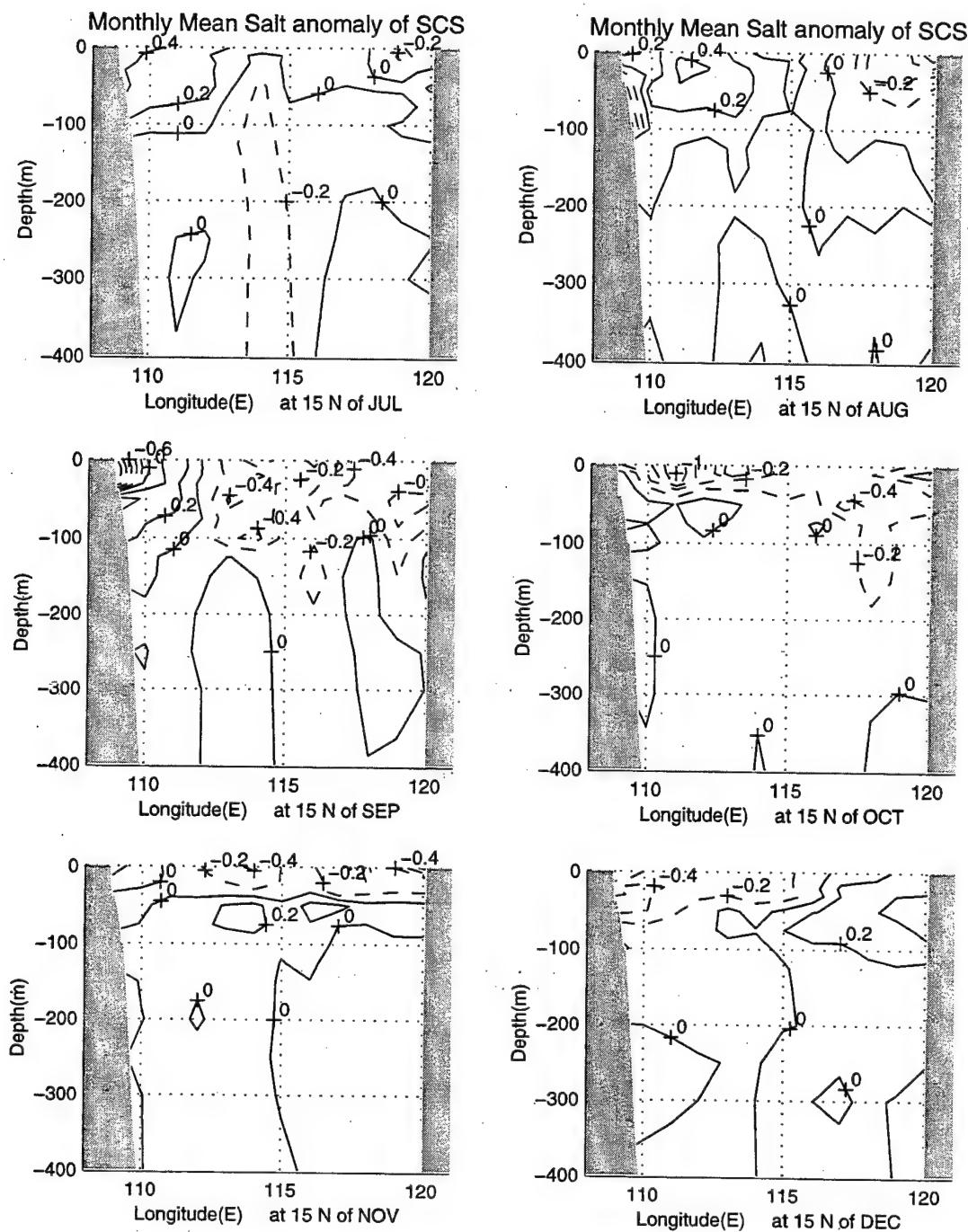


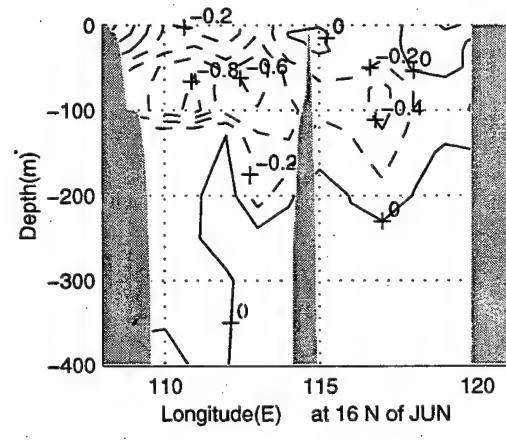
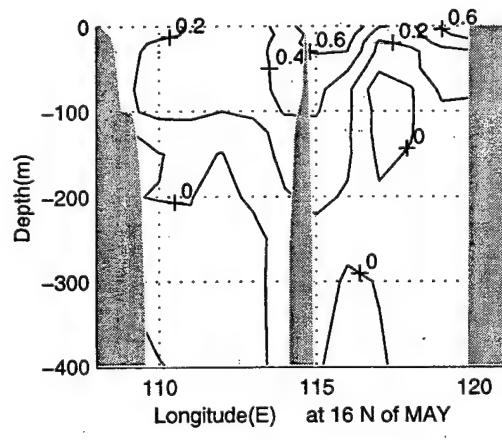
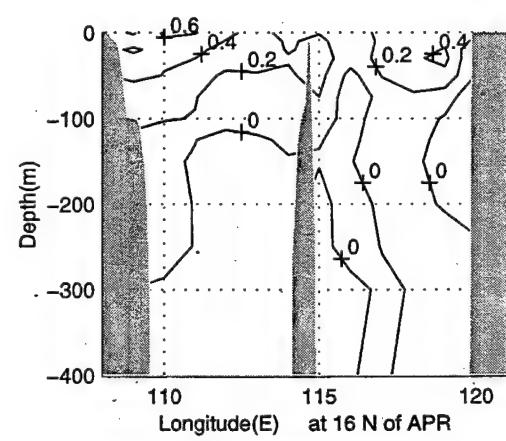
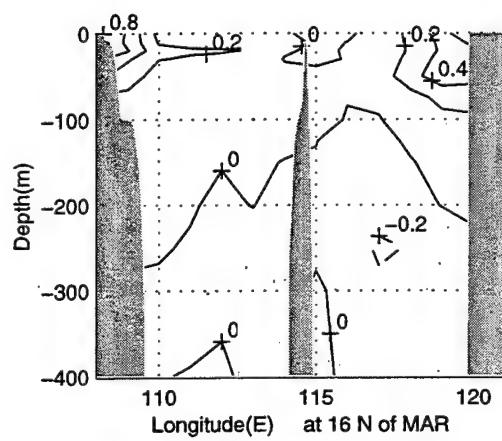
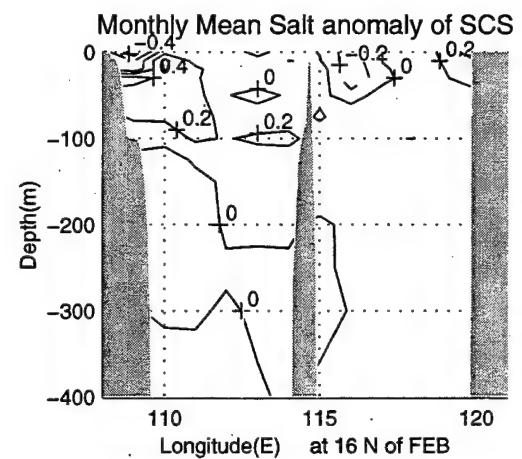
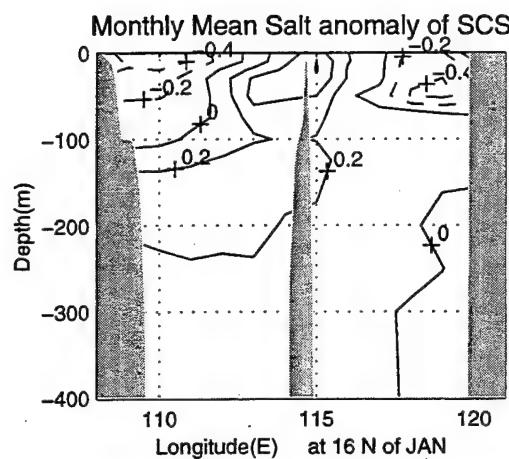


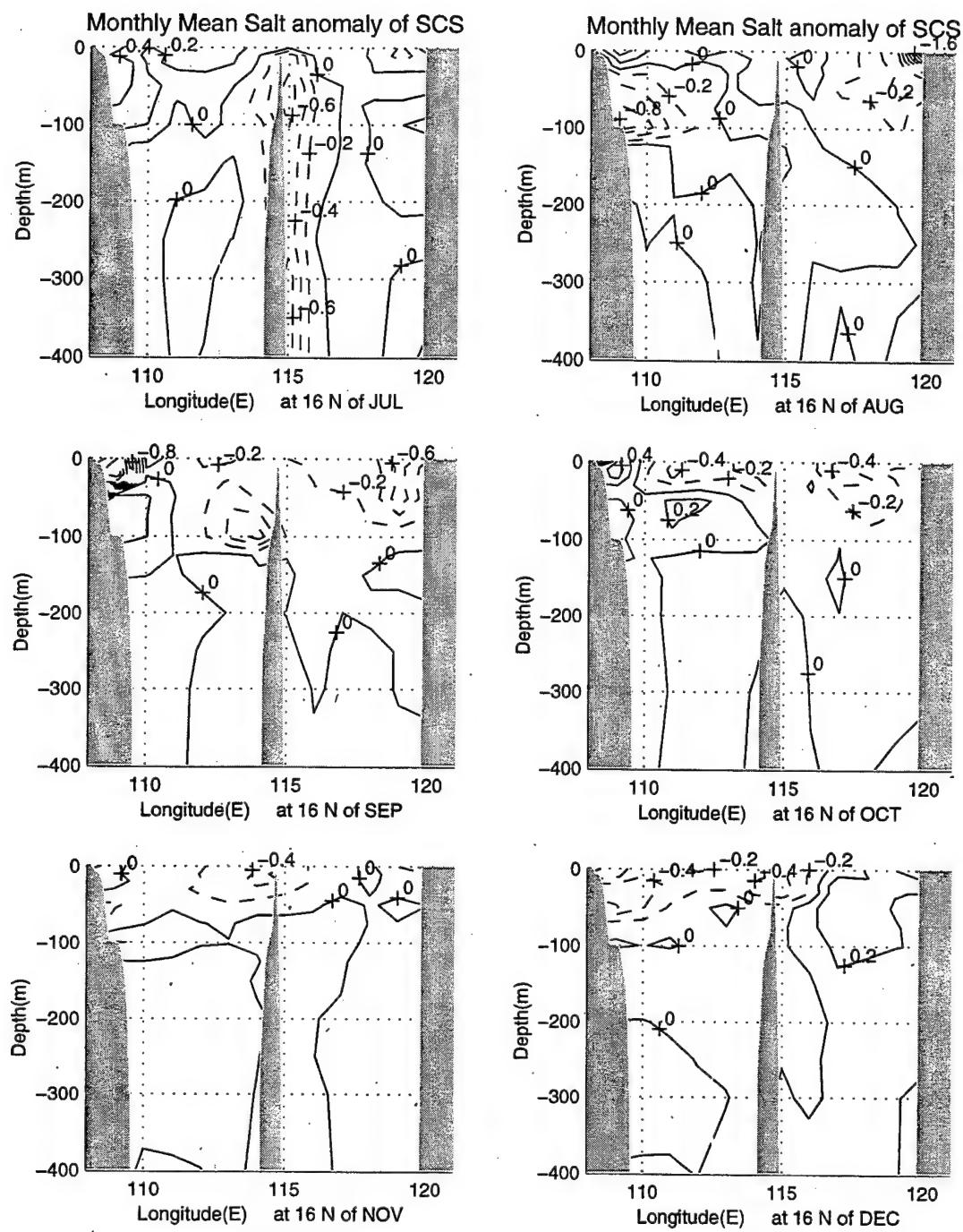


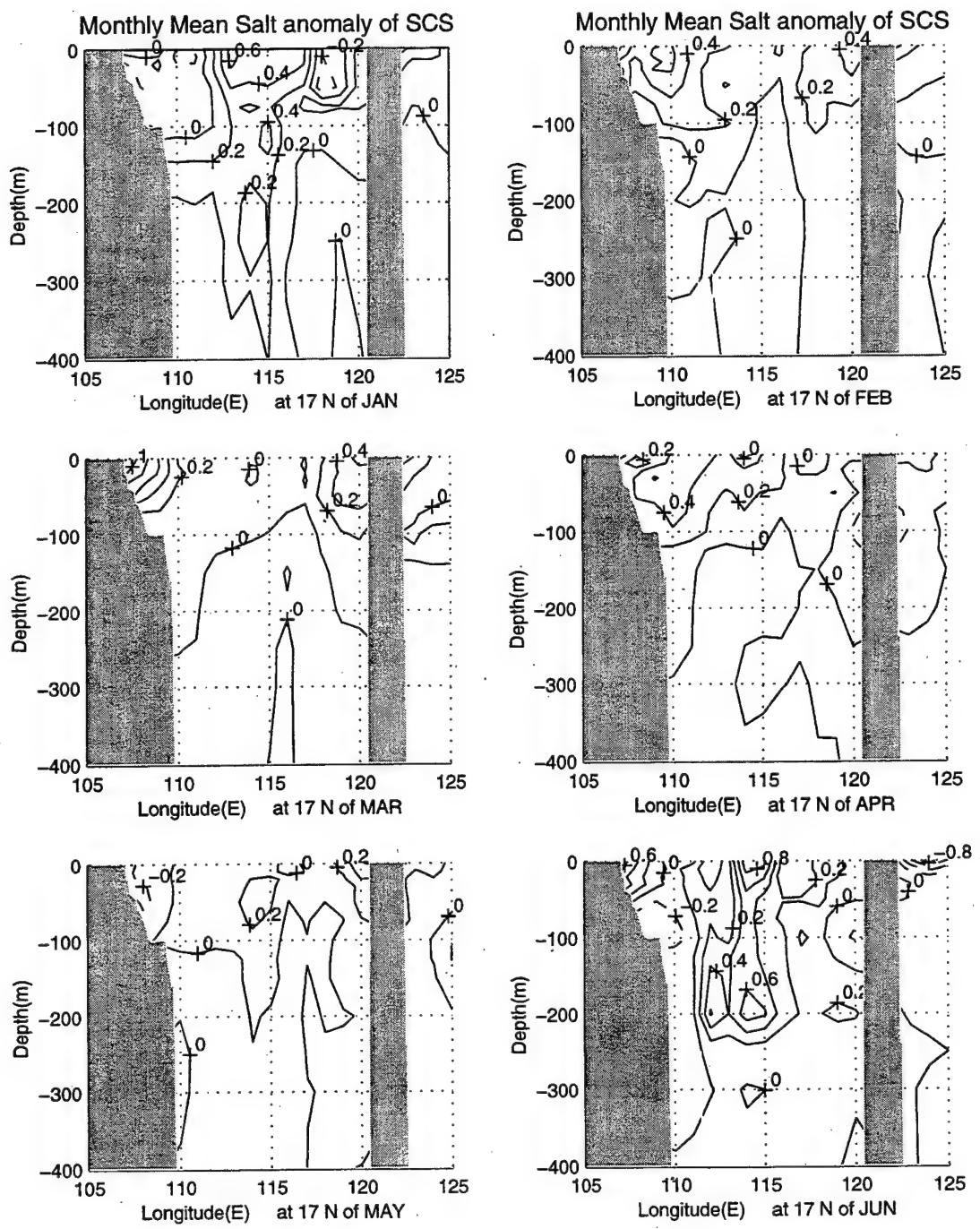


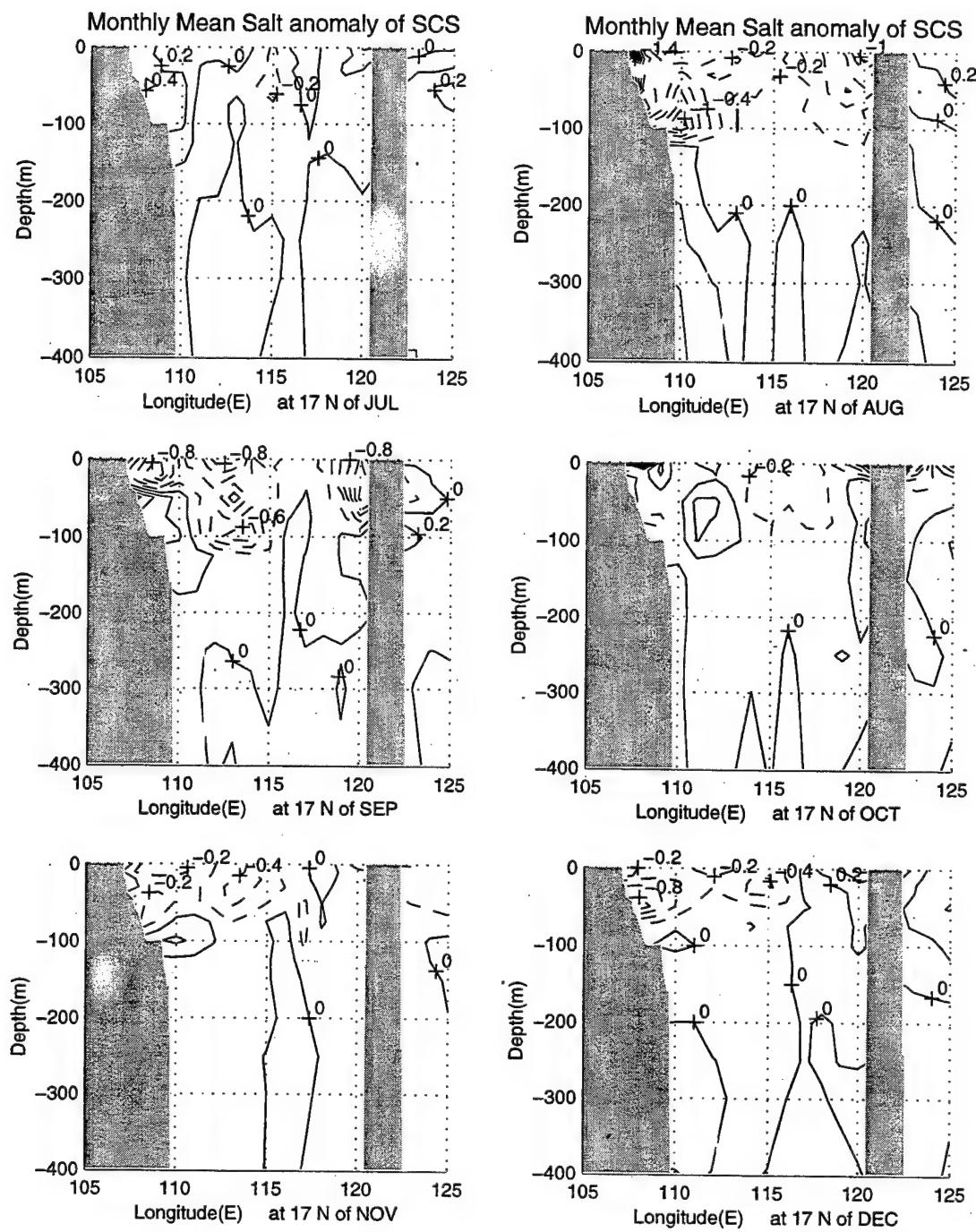


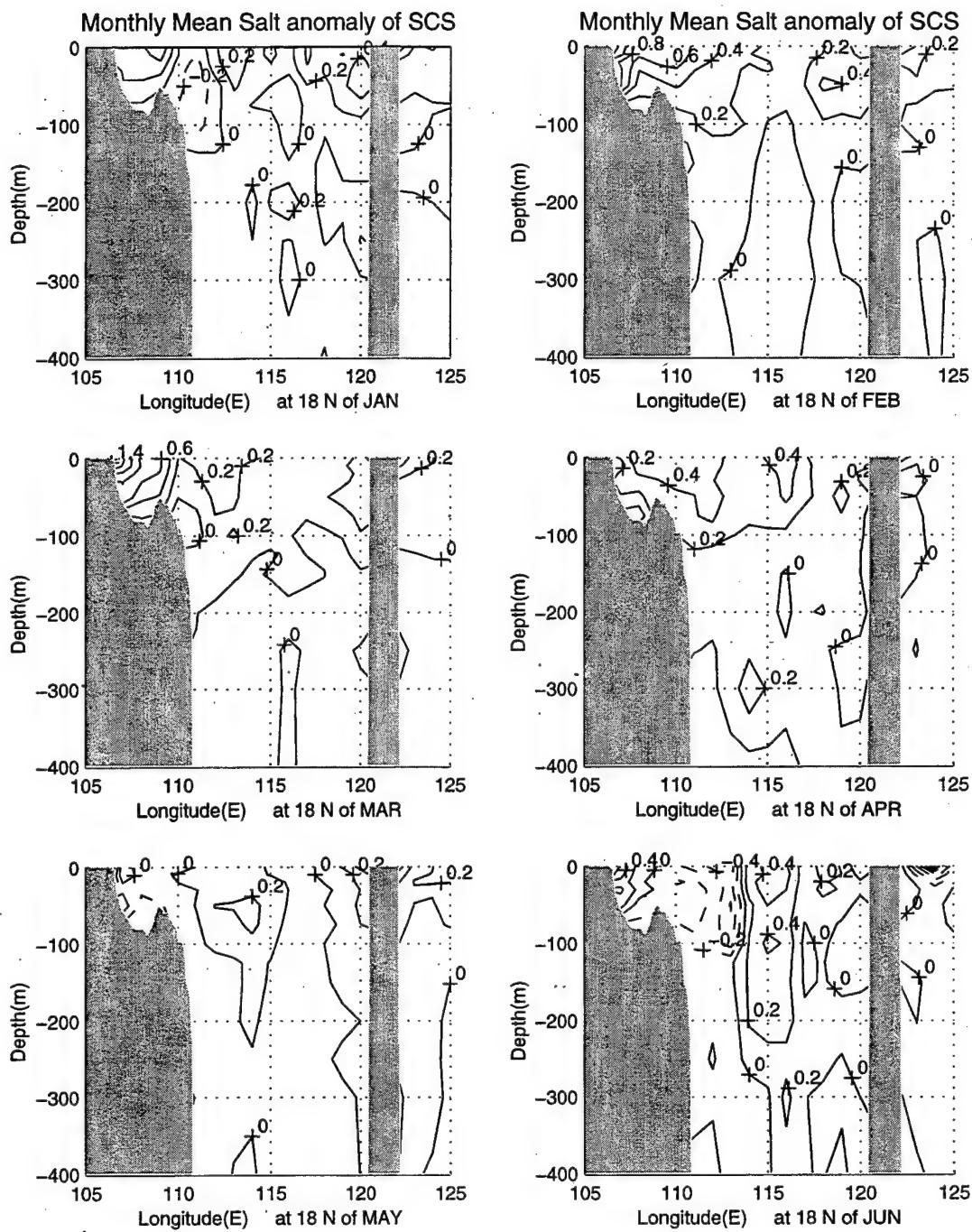


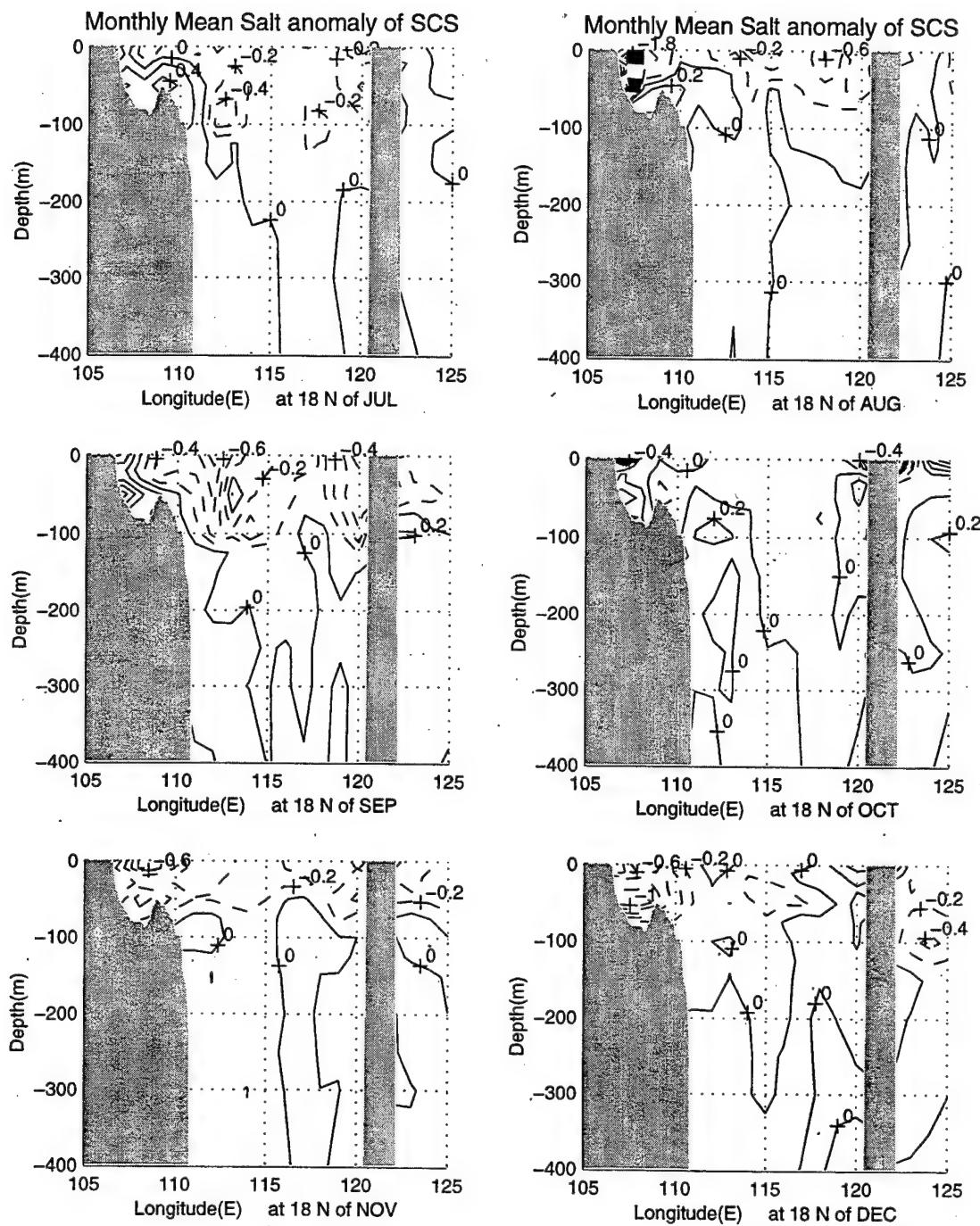


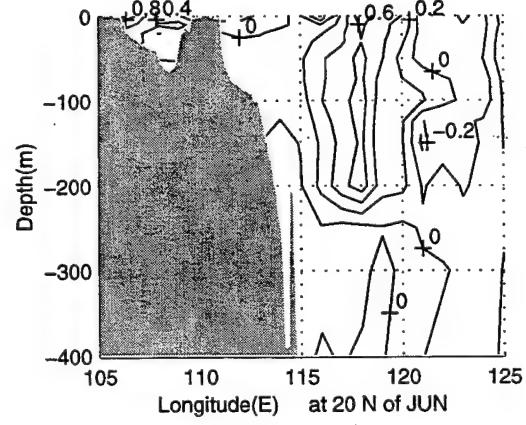
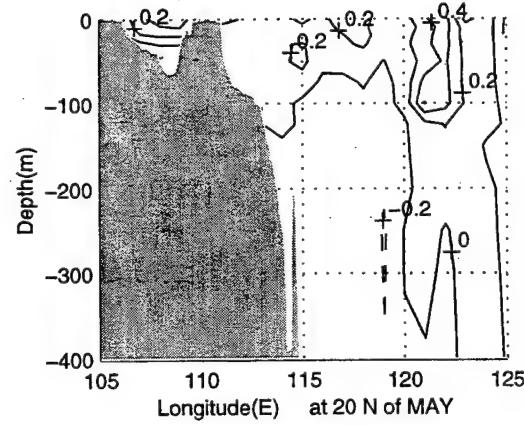
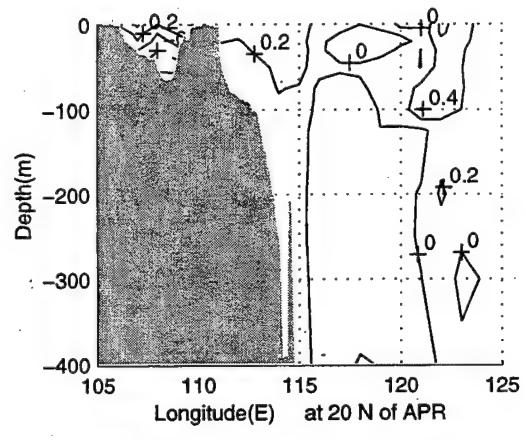
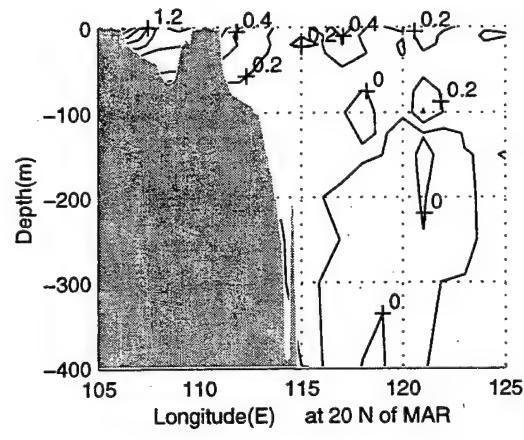
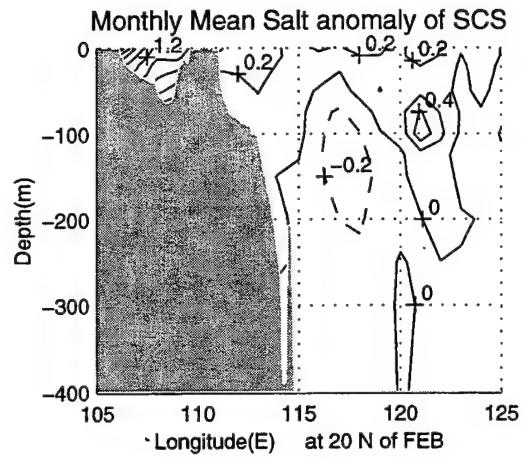
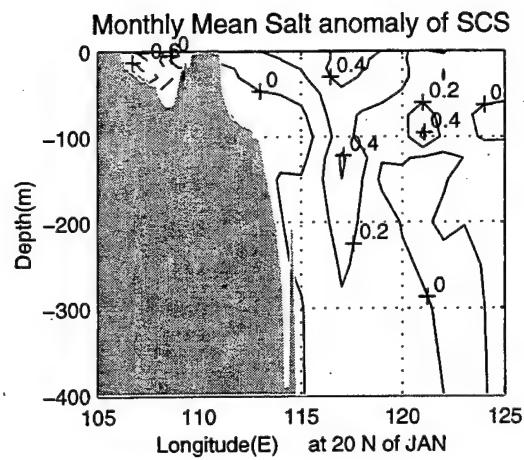


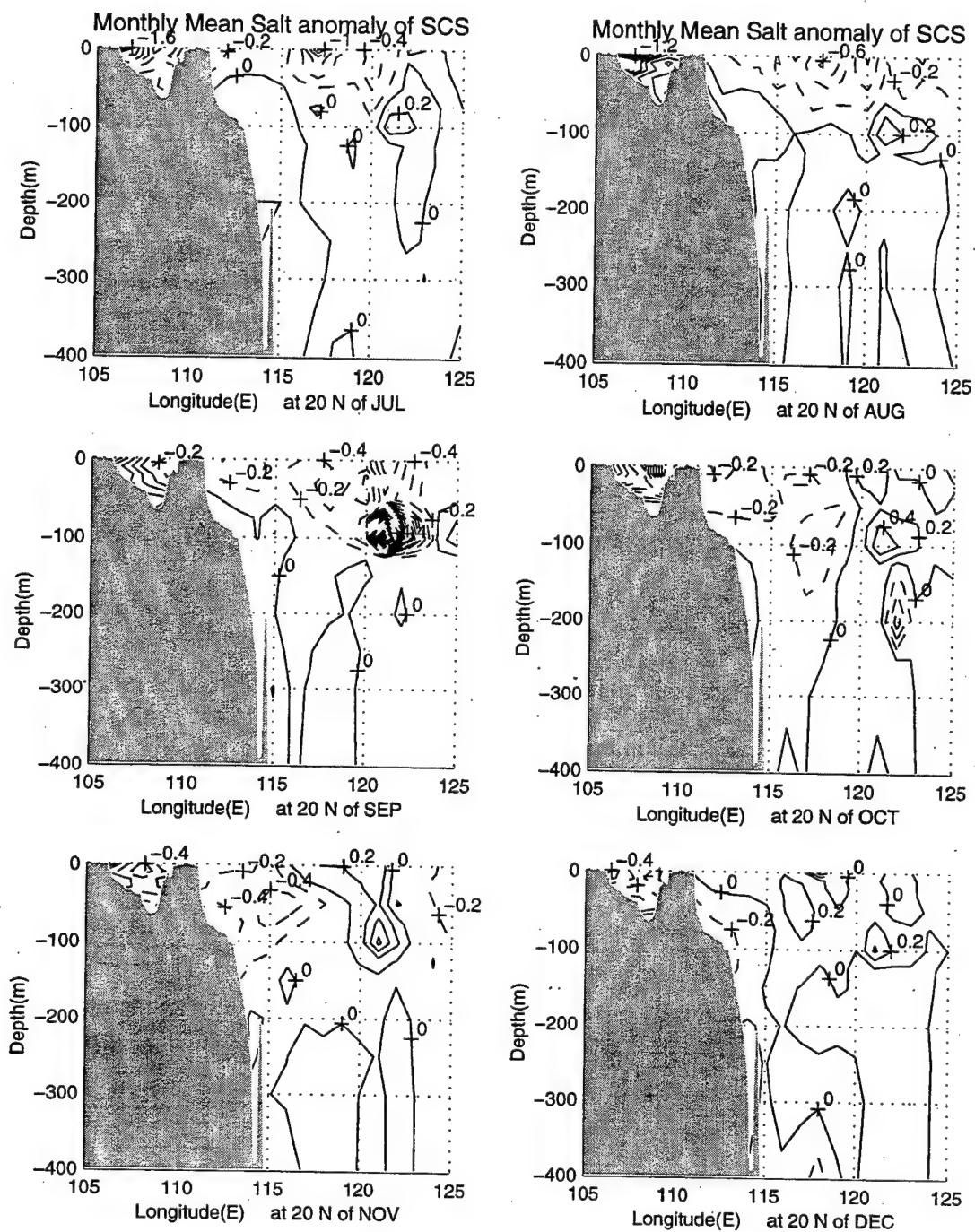


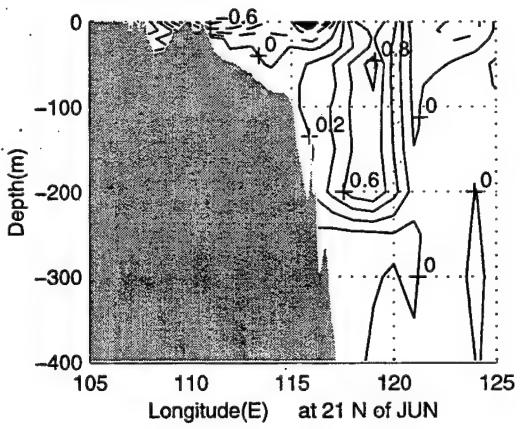
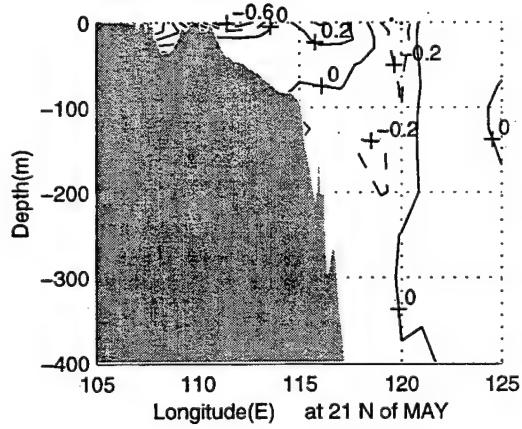
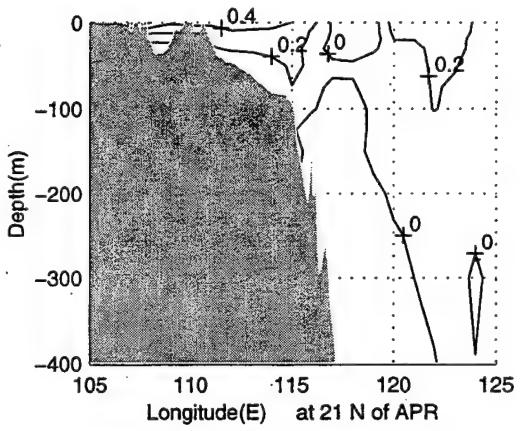
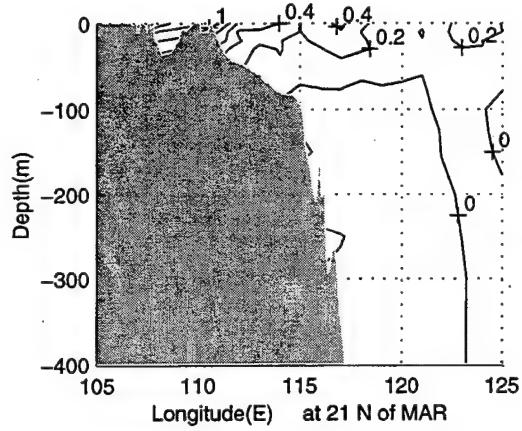
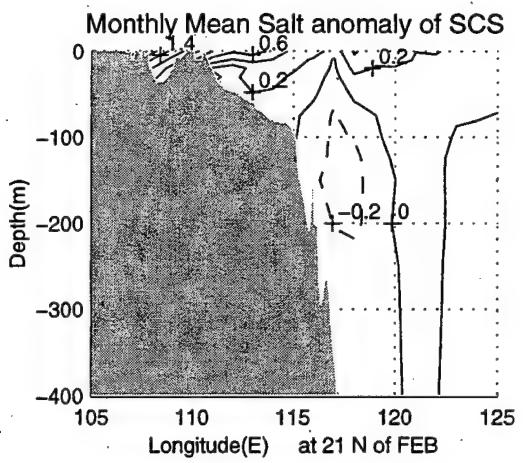
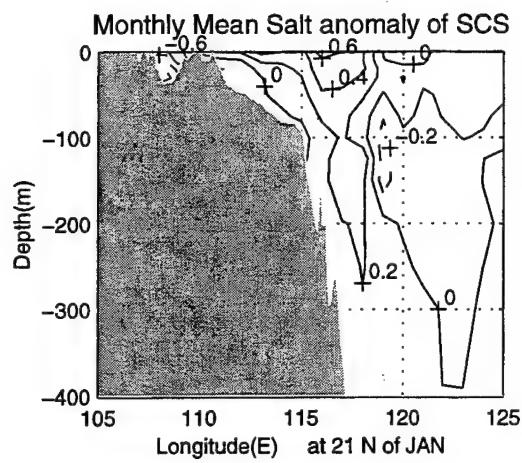


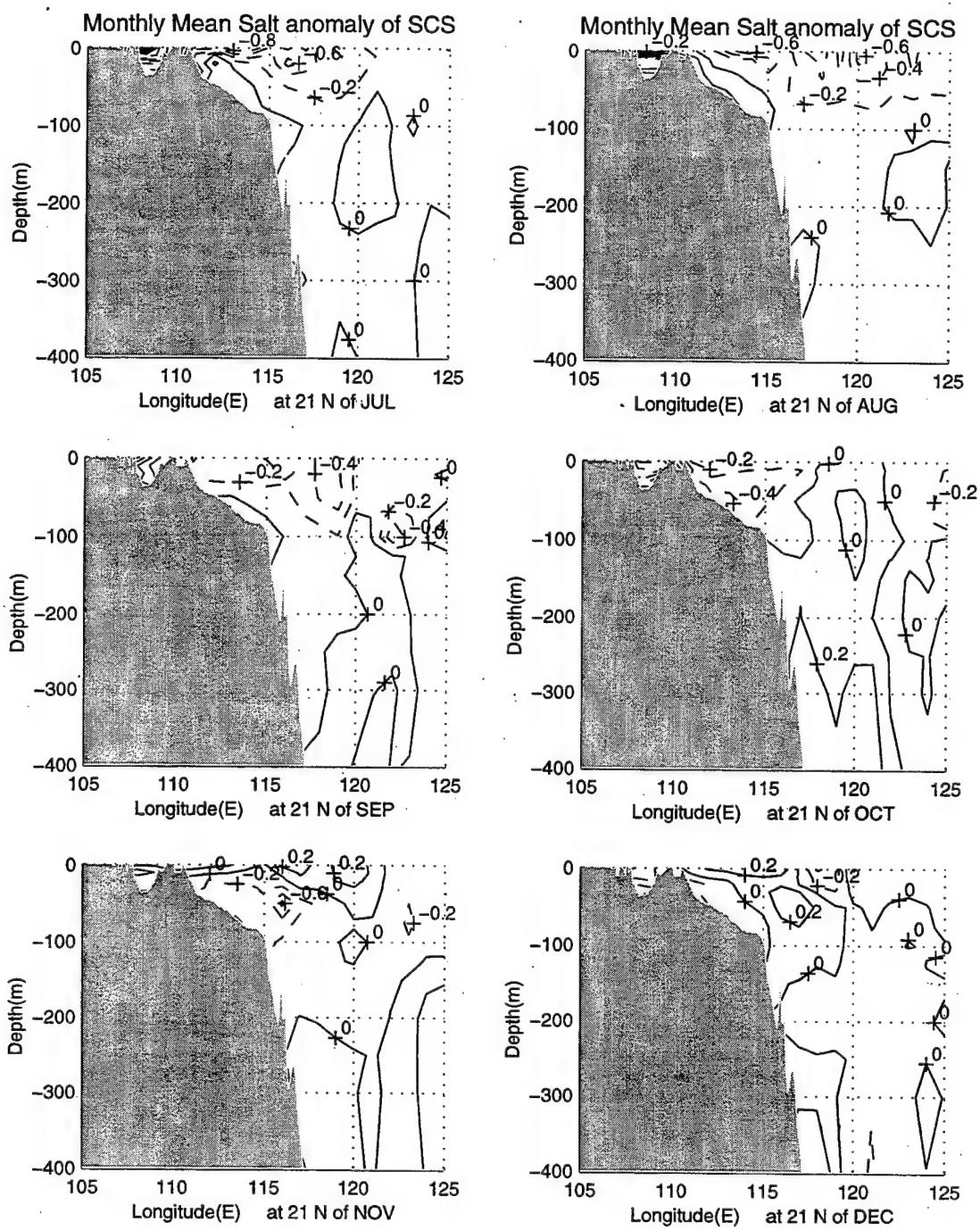


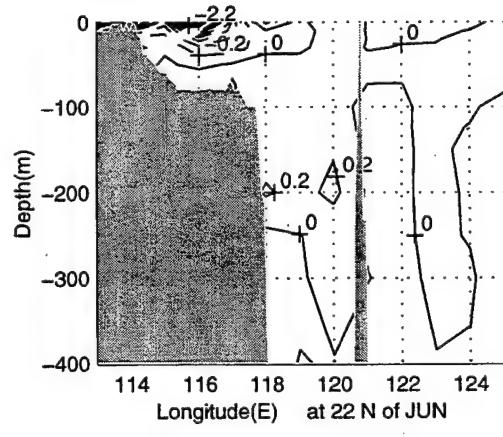
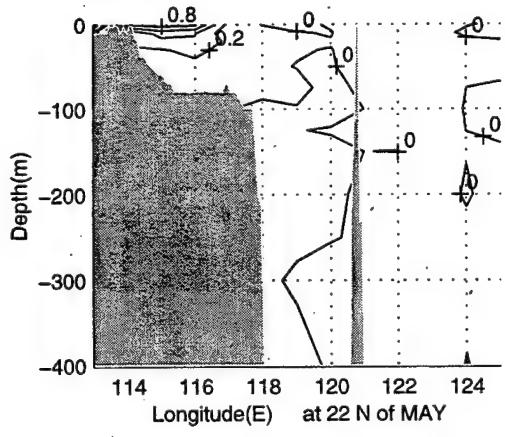
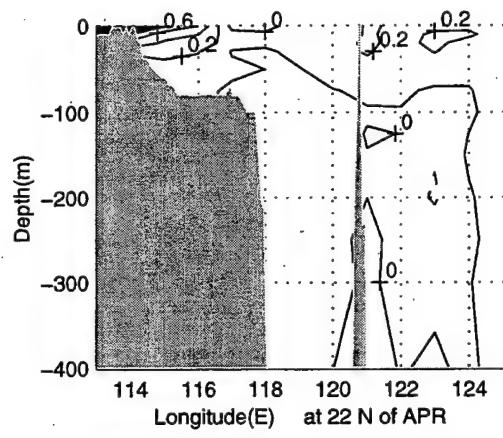
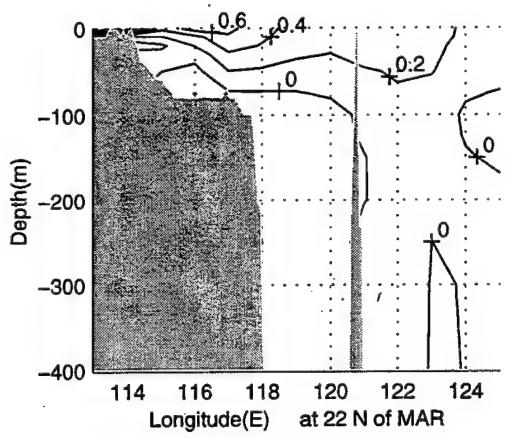
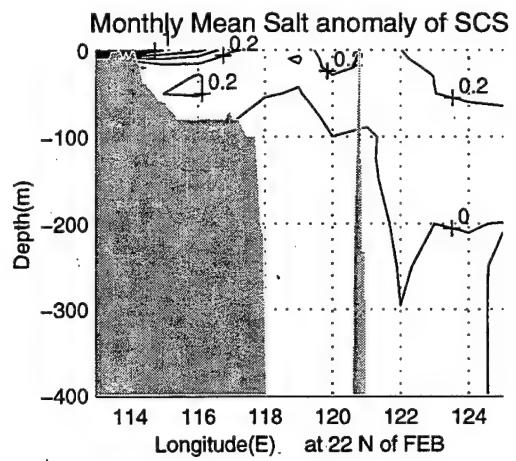
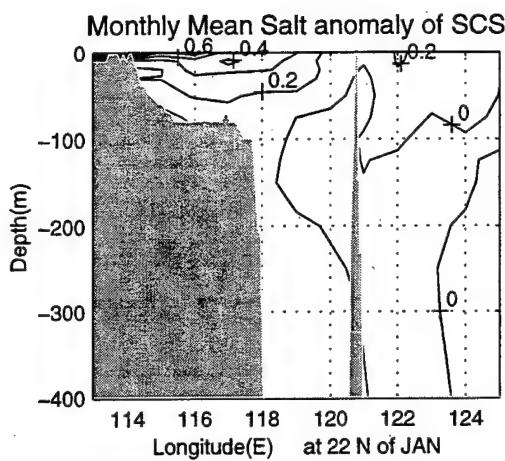


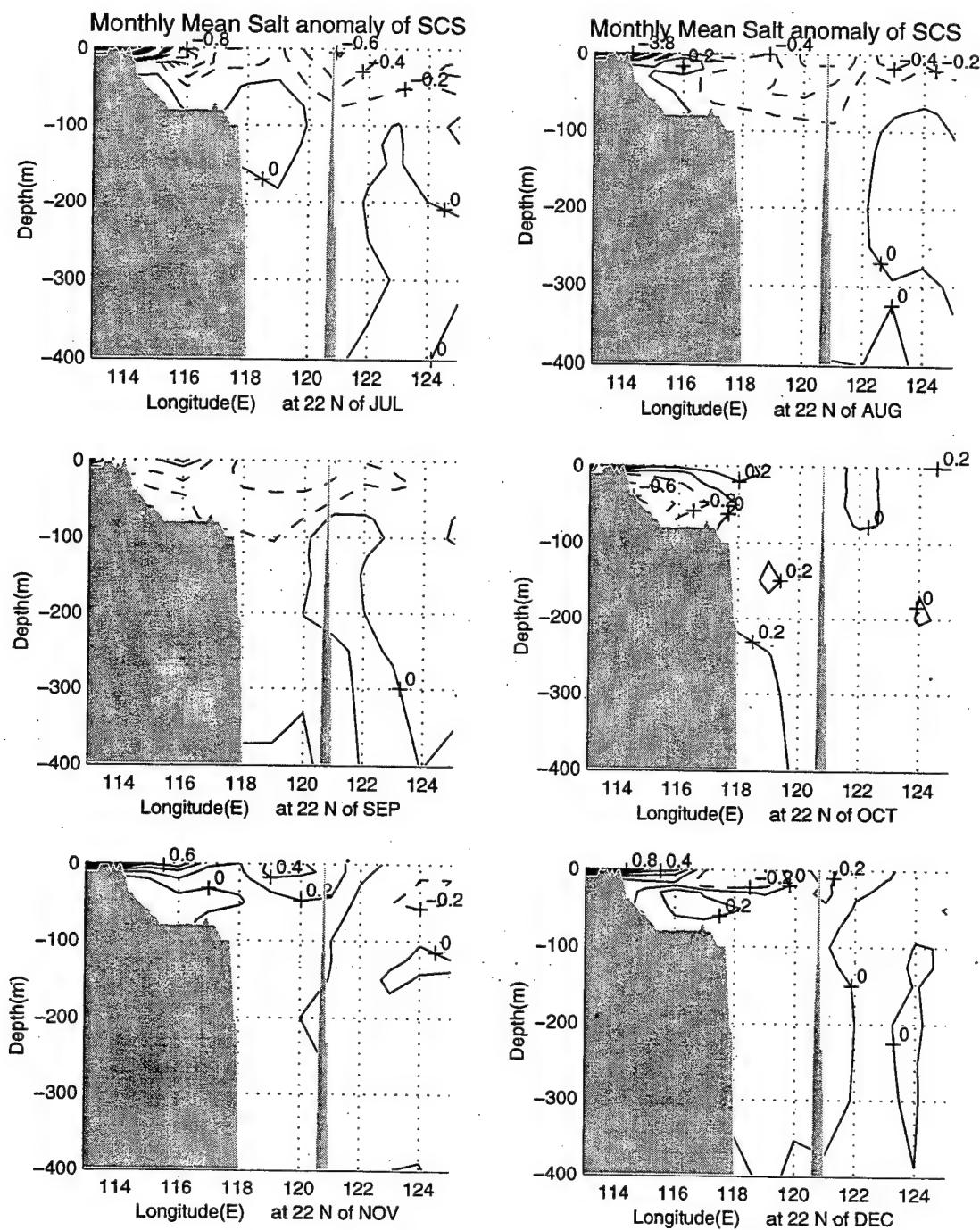


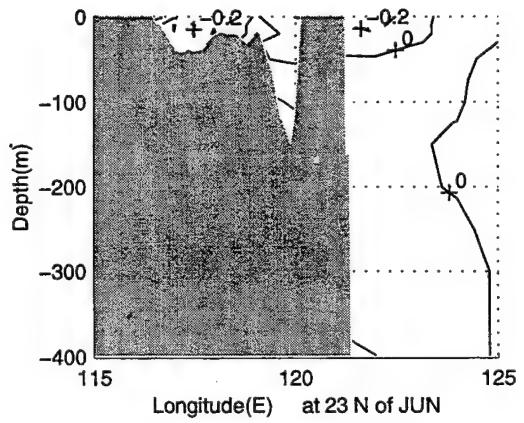
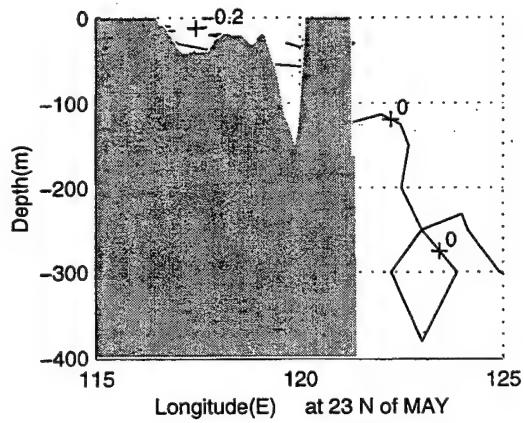
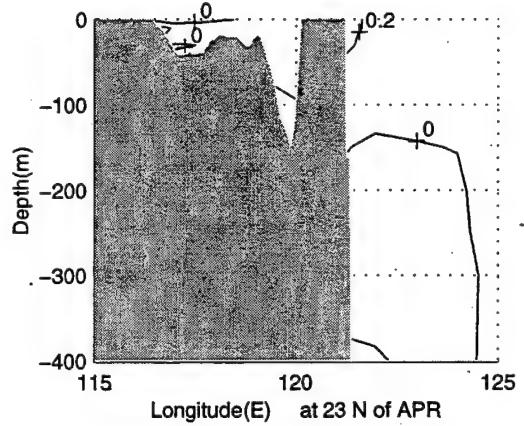
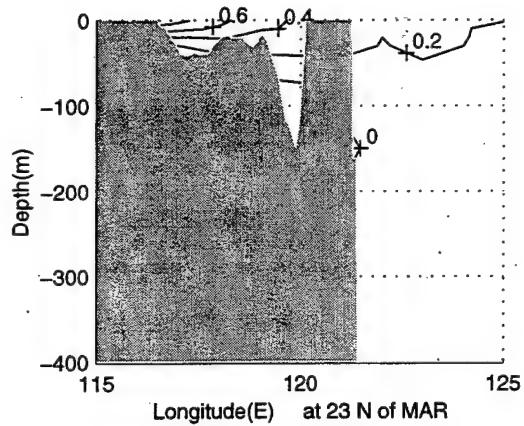
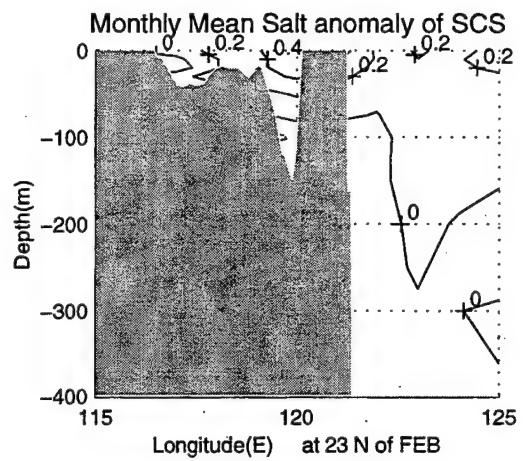
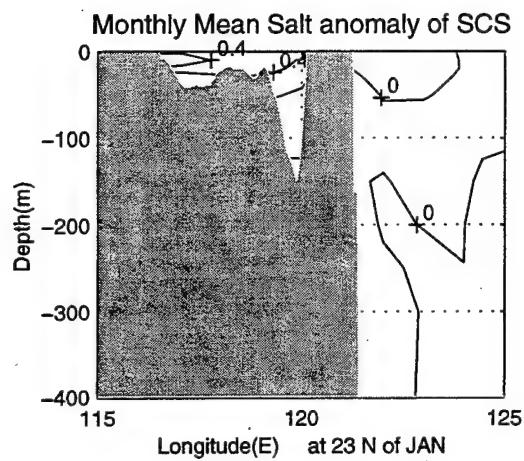


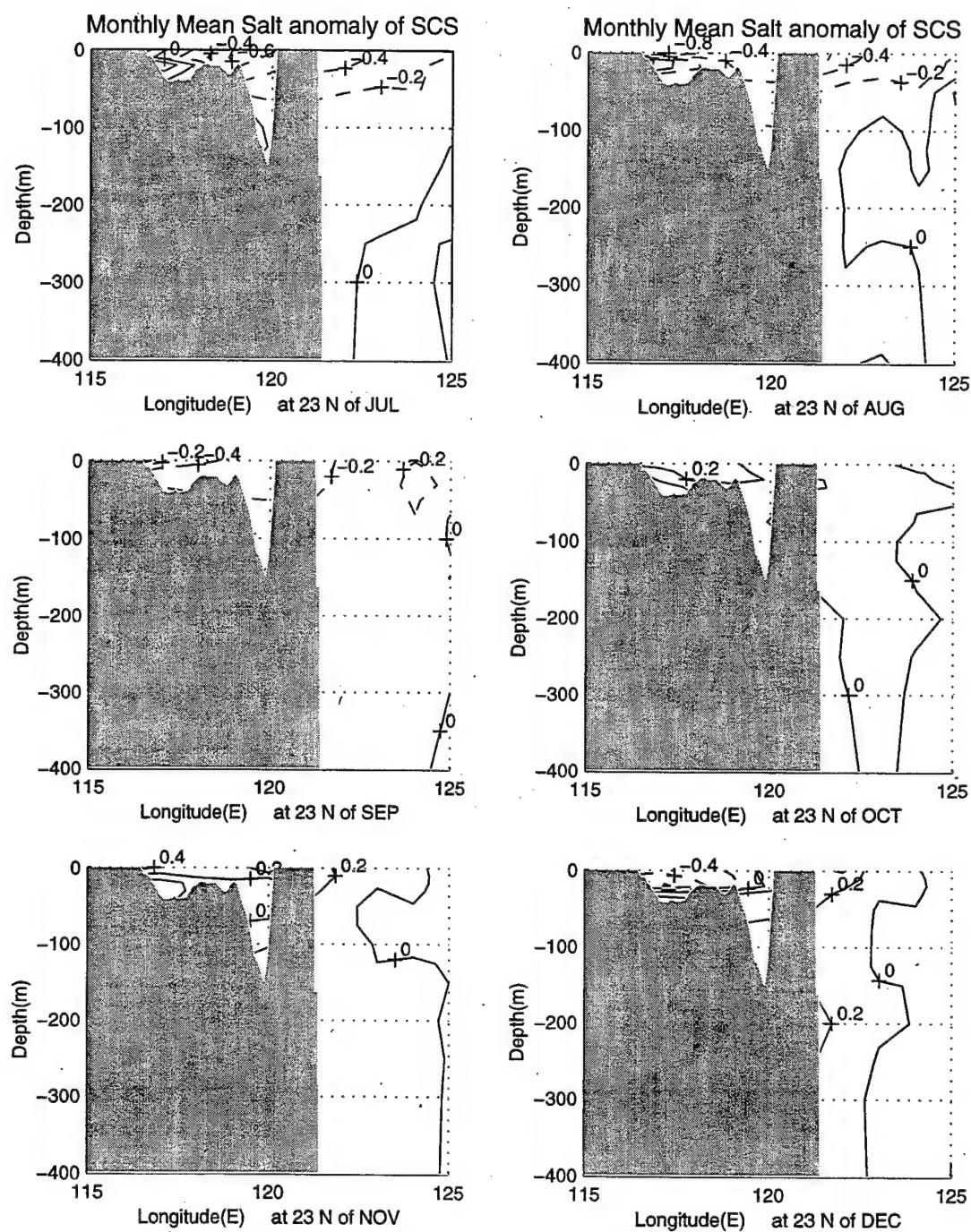


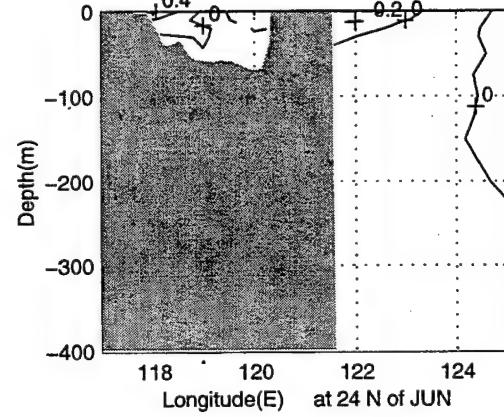
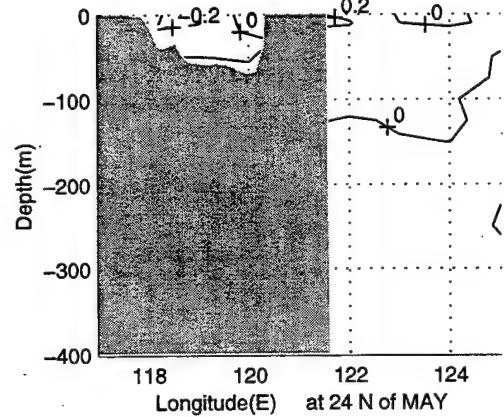
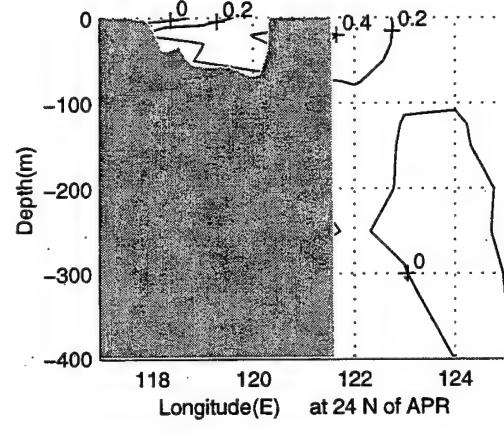
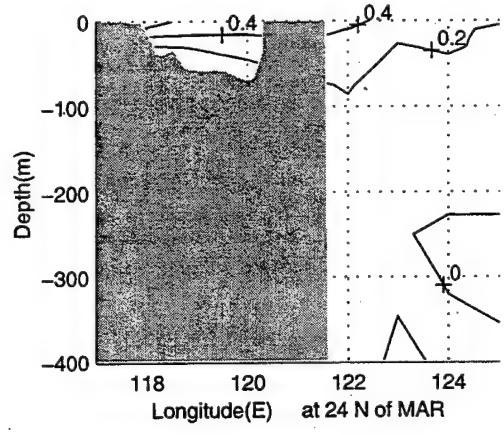
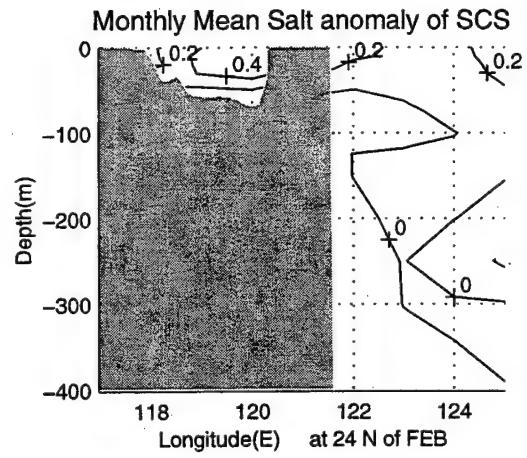
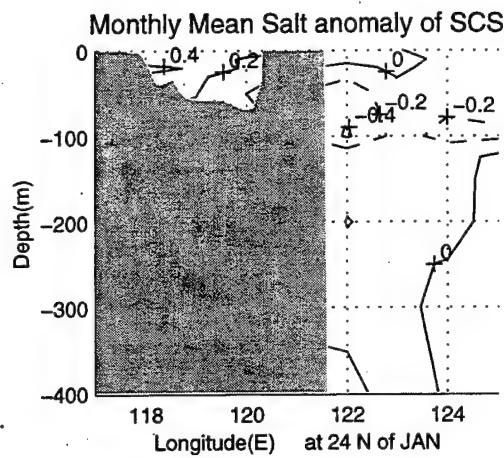


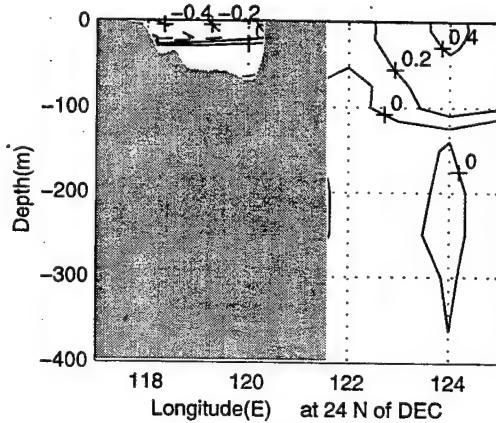
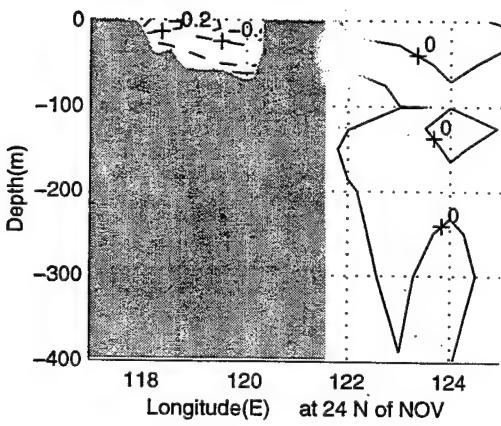
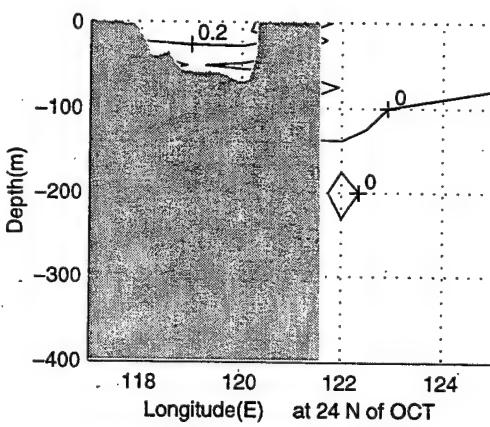
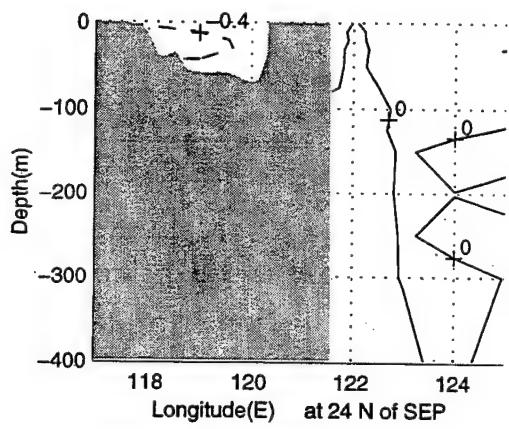
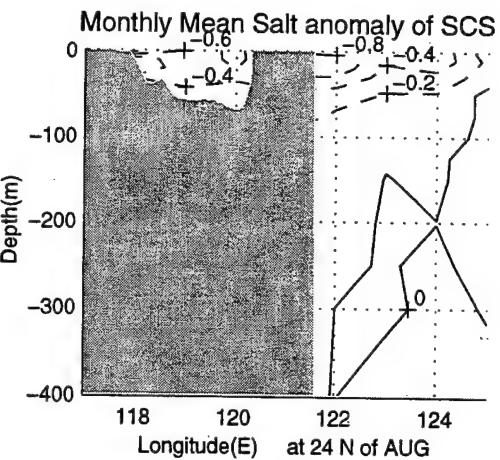
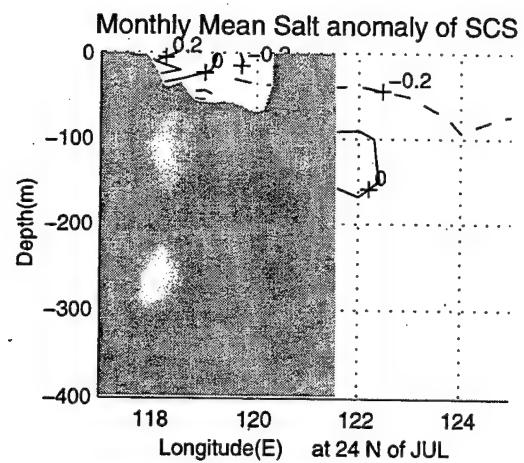


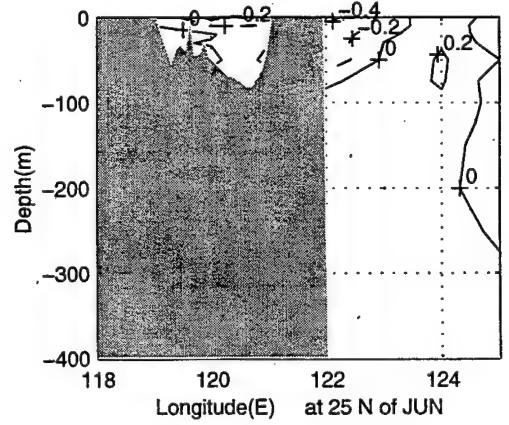
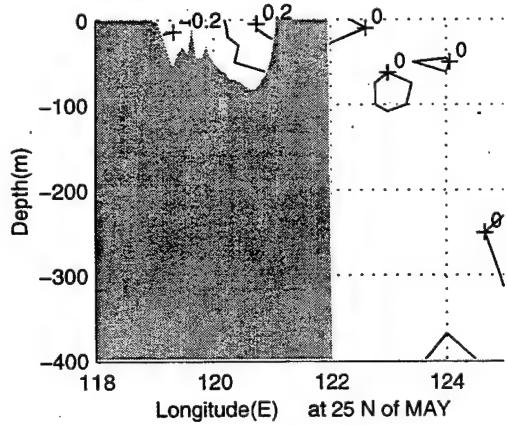
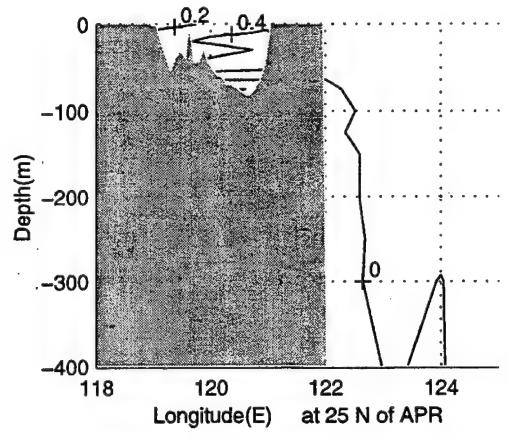
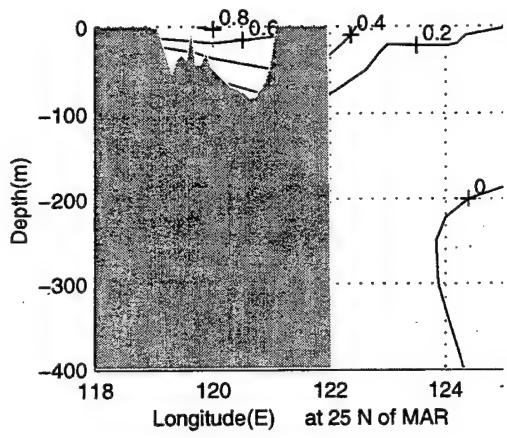
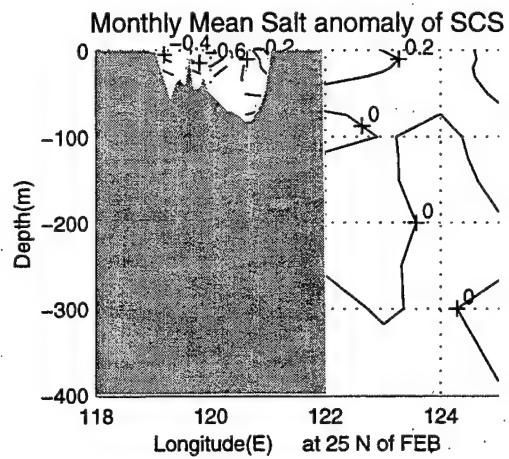
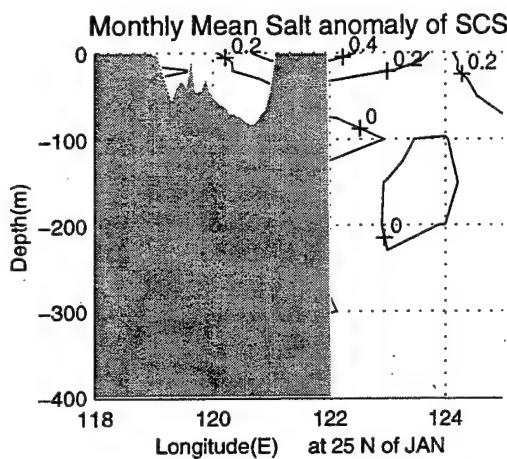


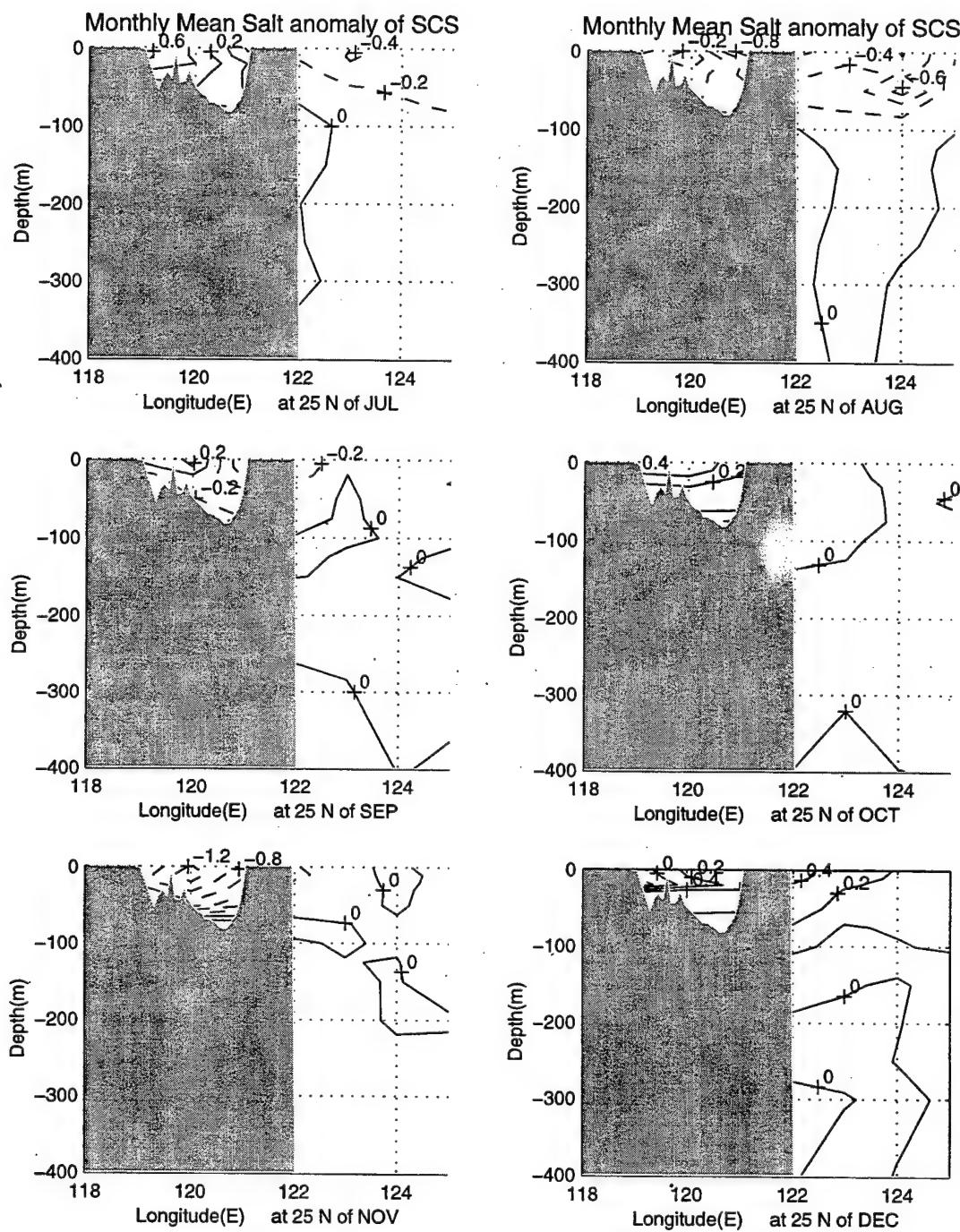






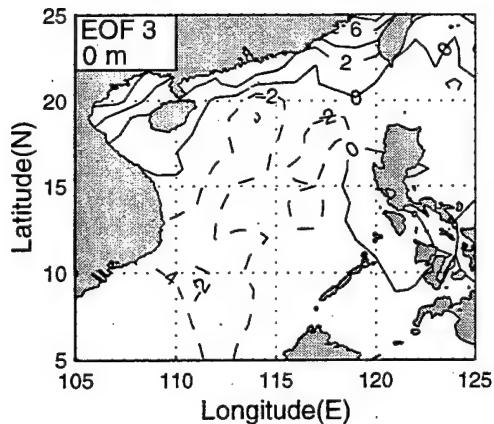




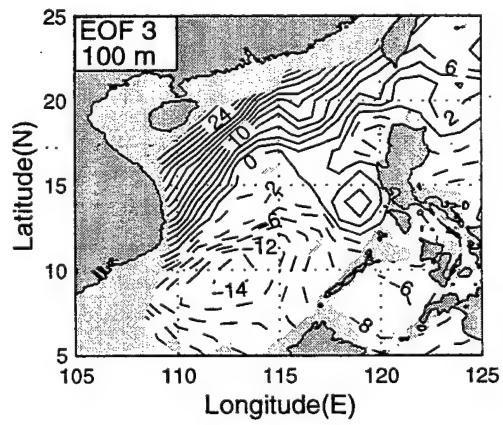
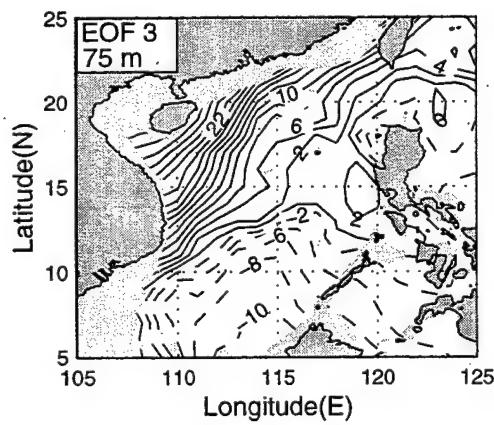
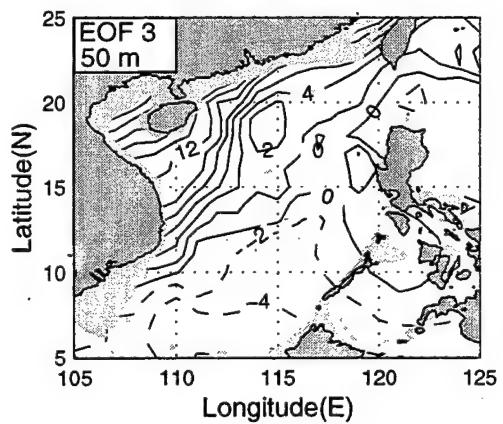
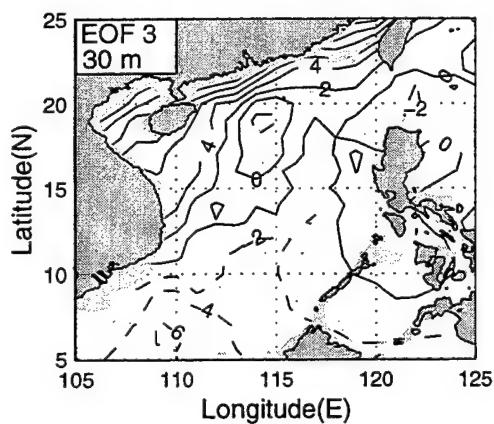
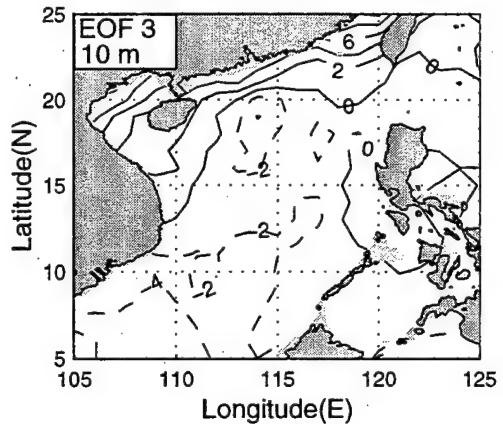


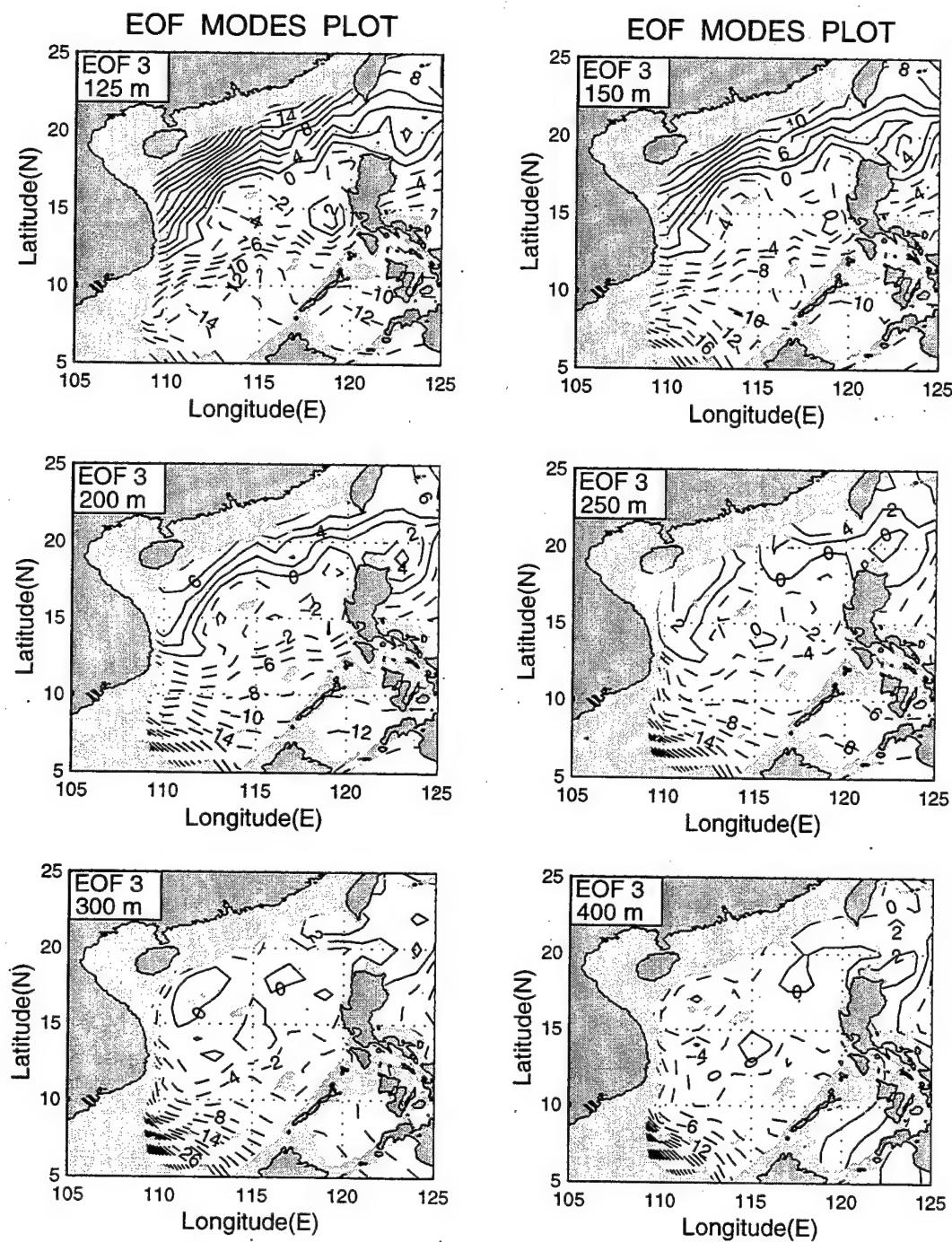
APPENDIX C. EOF 3~6 FOR TEMPERATURE ANOMALY

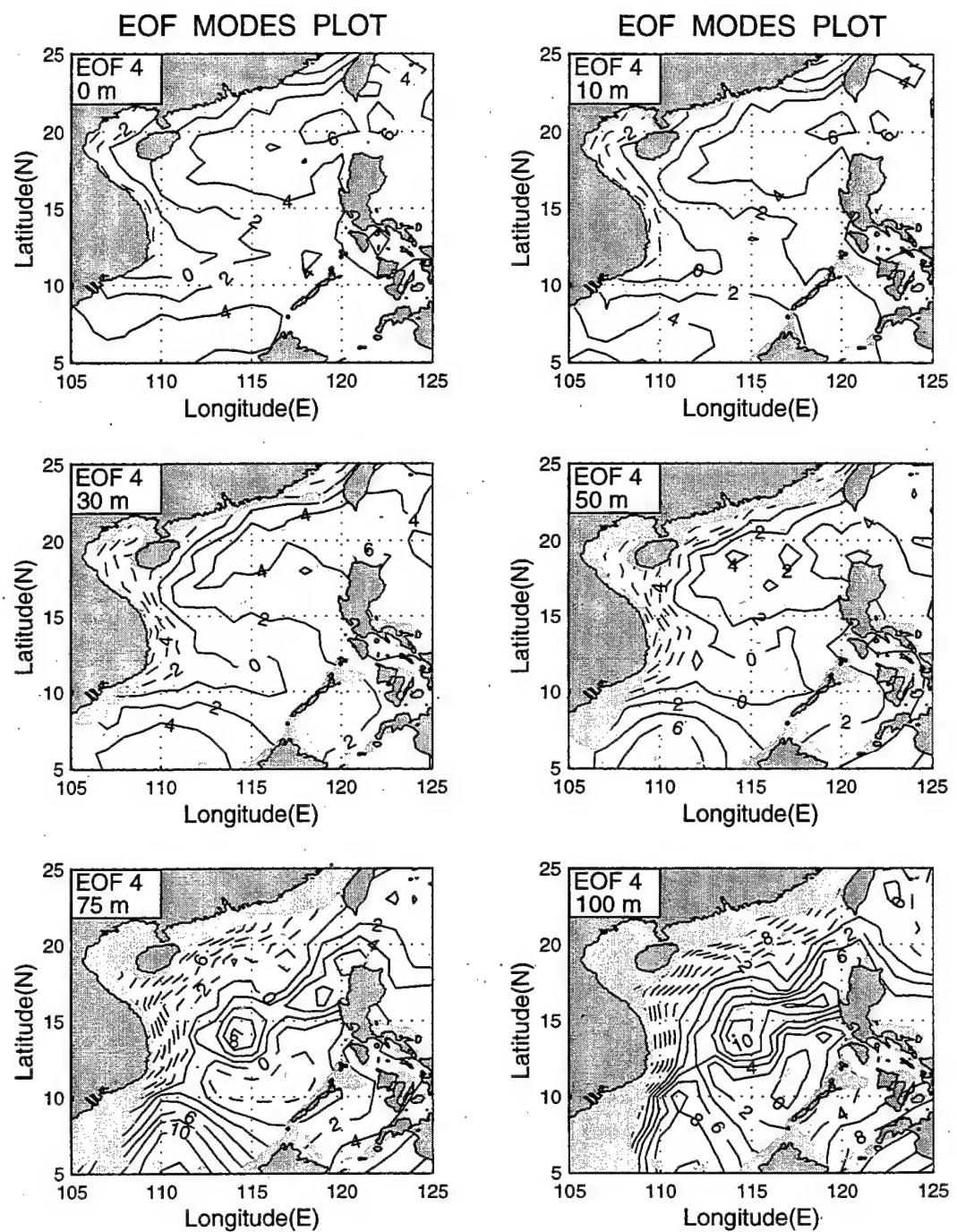
EOF MODES PLOT

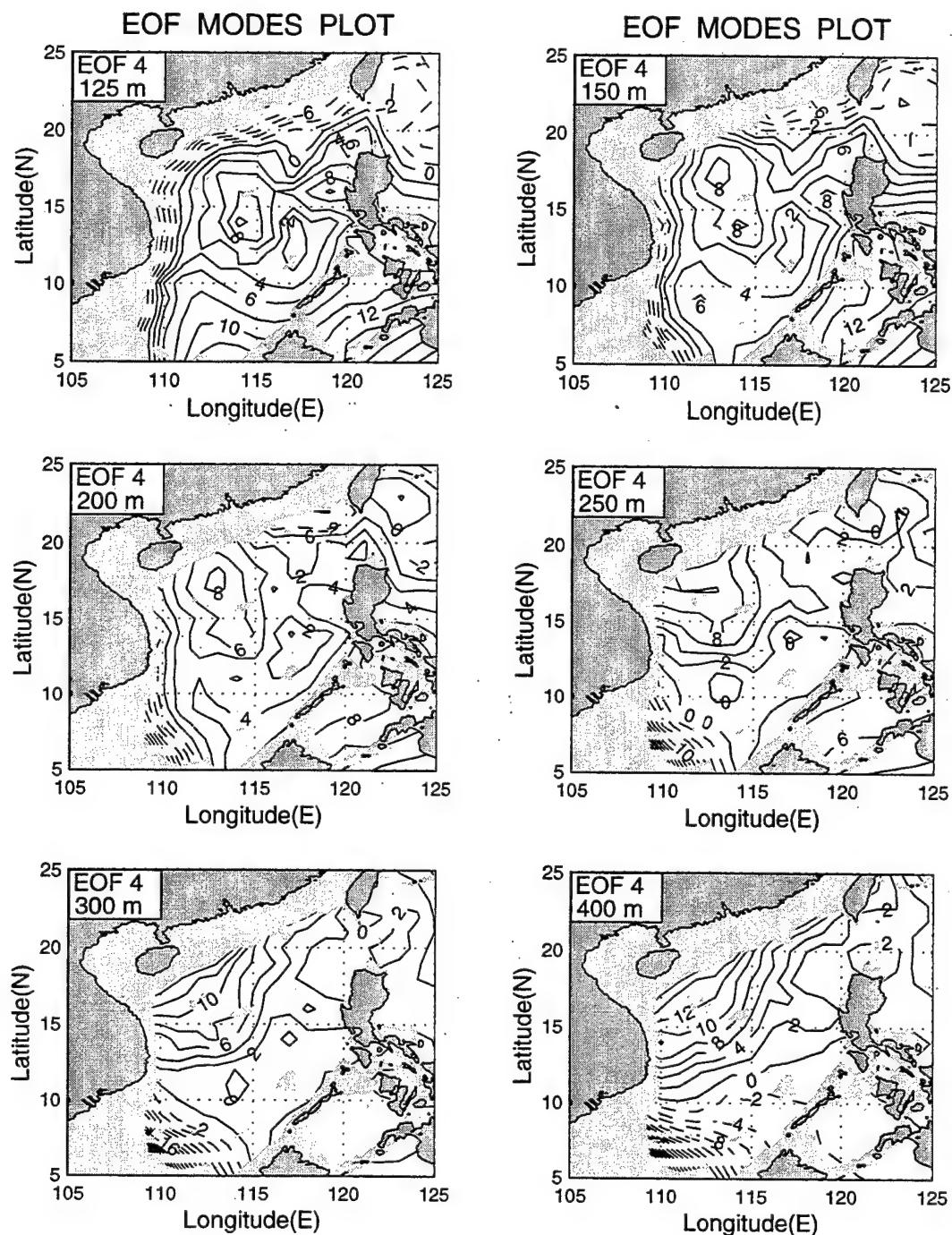


EOF MODES PLOT

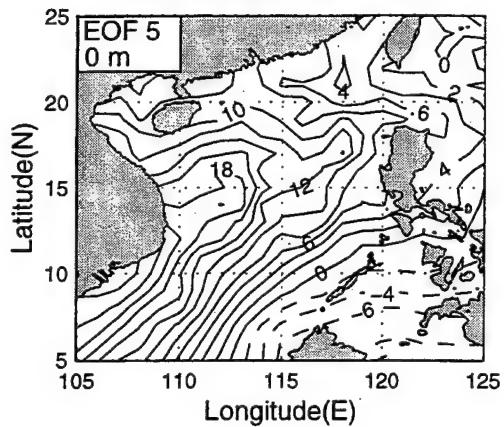




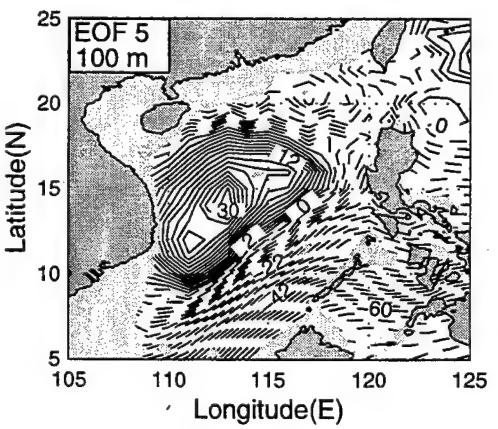
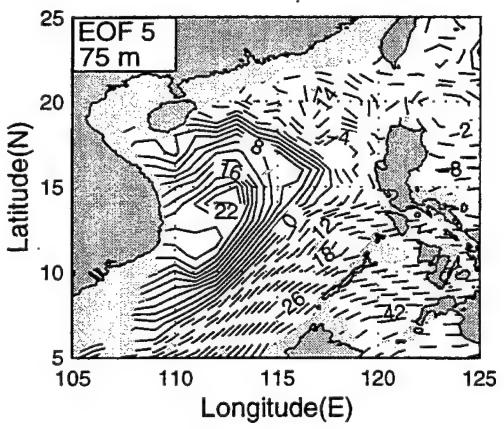
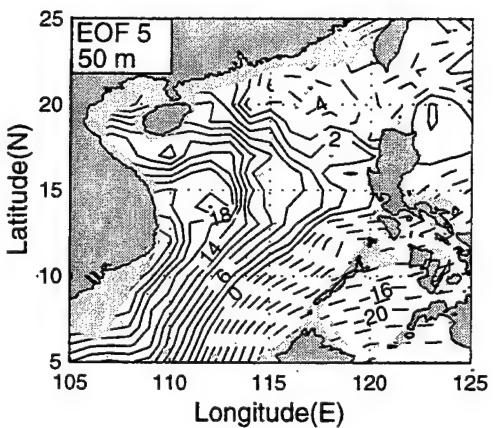
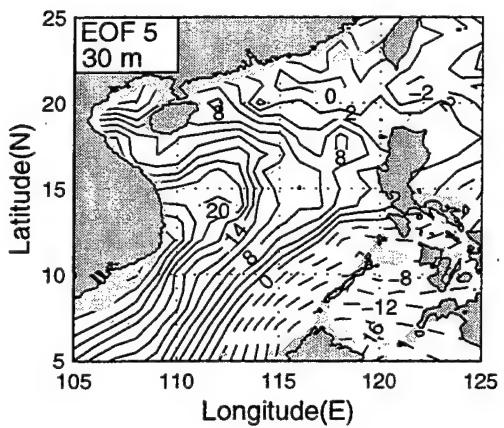
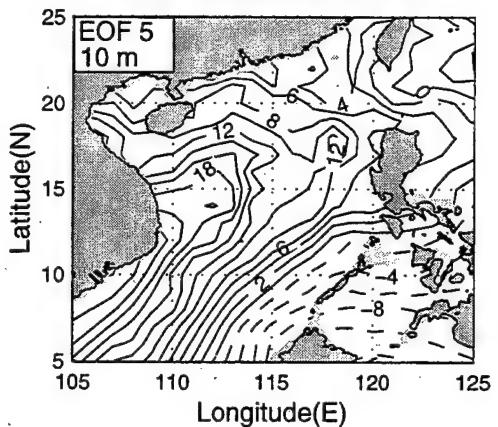


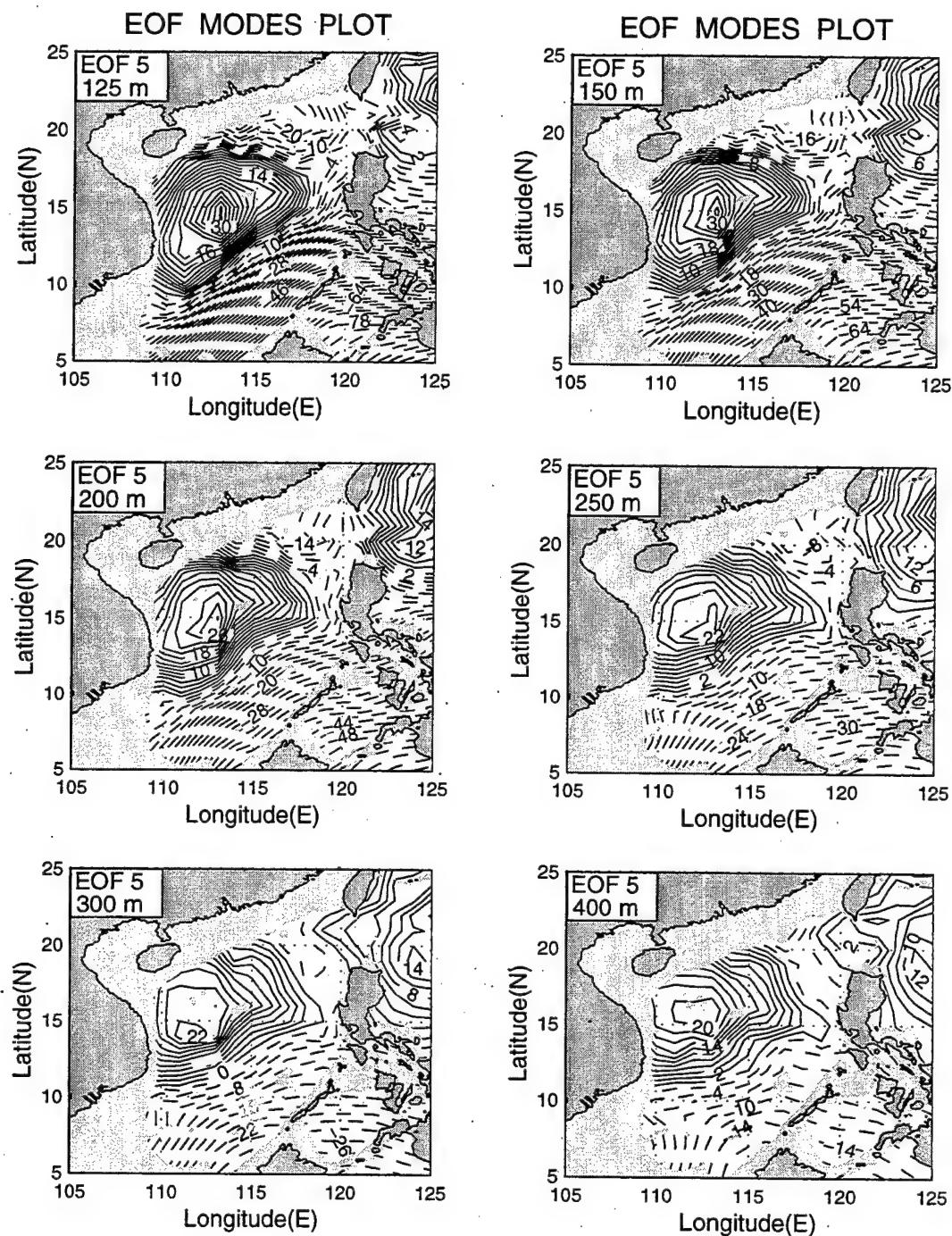


EOF MODES PLOT

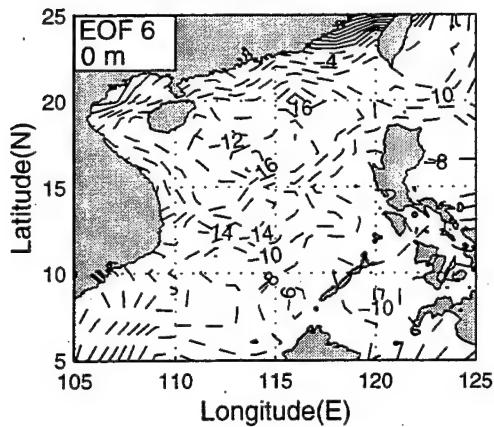


EOF MODES PLOT

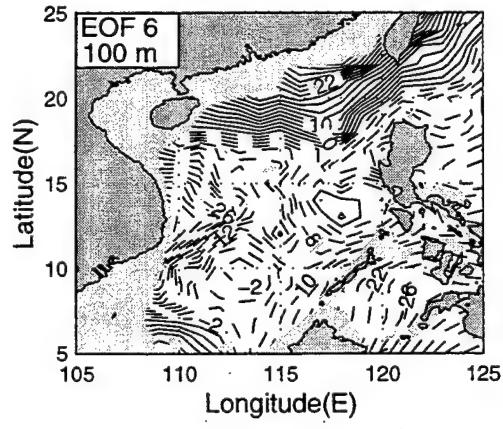
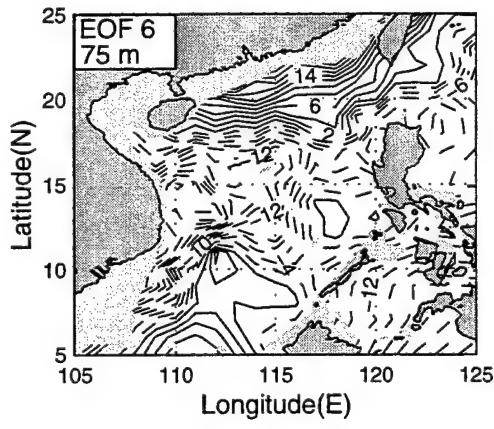
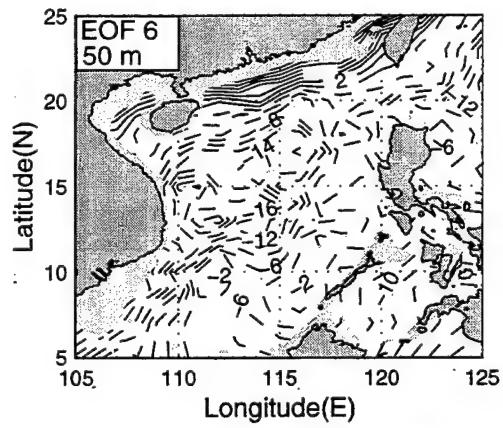
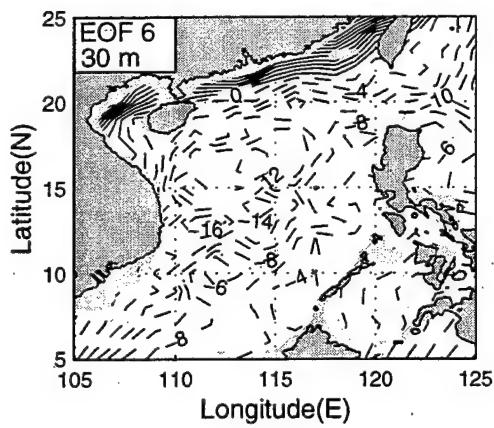
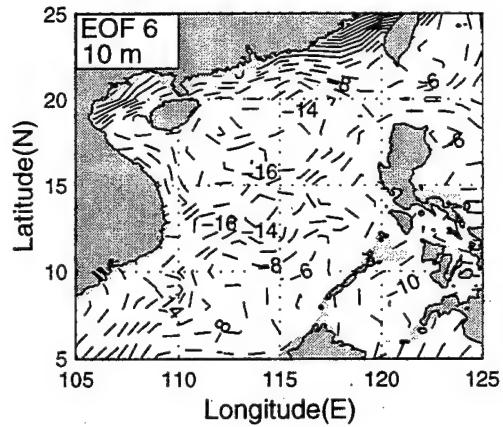




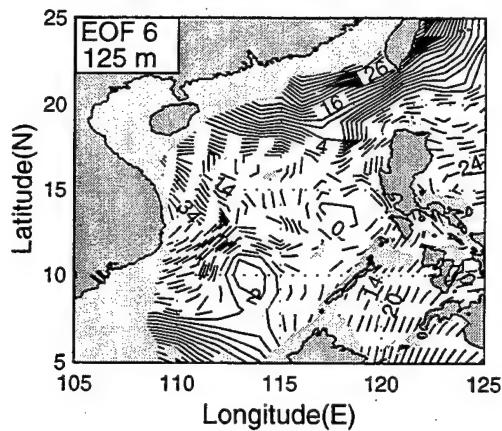
EOF MODES PLOT



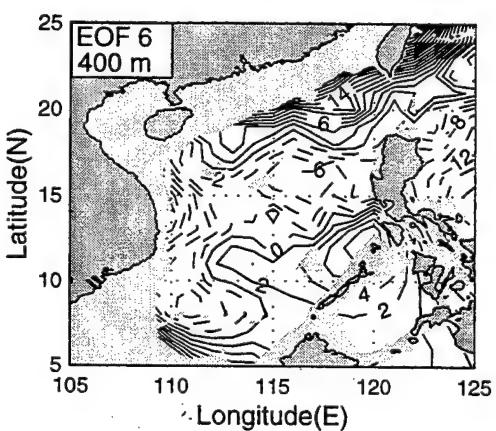
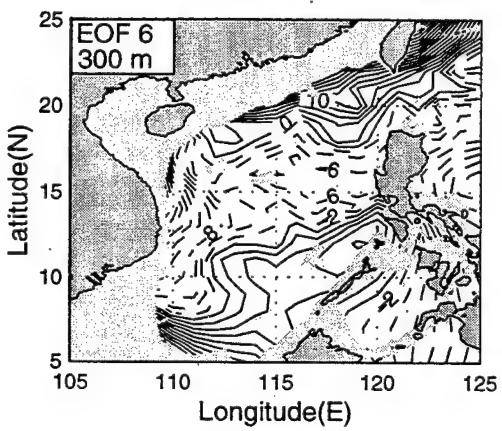
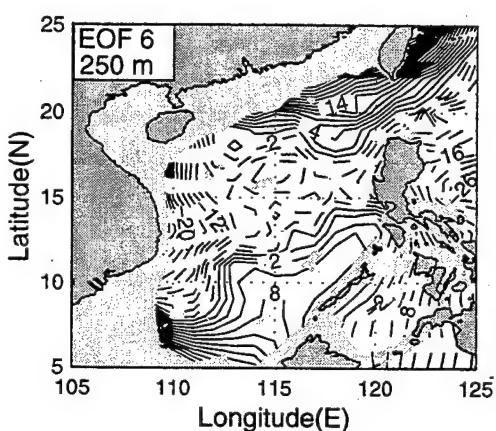
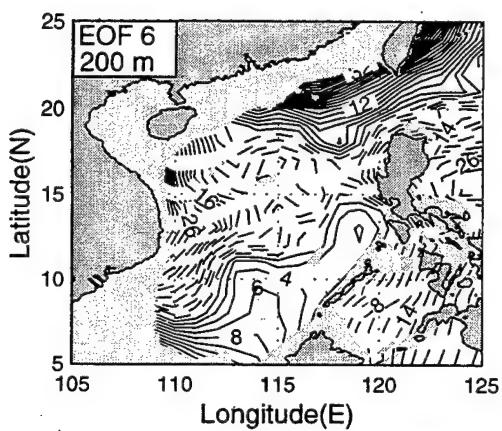
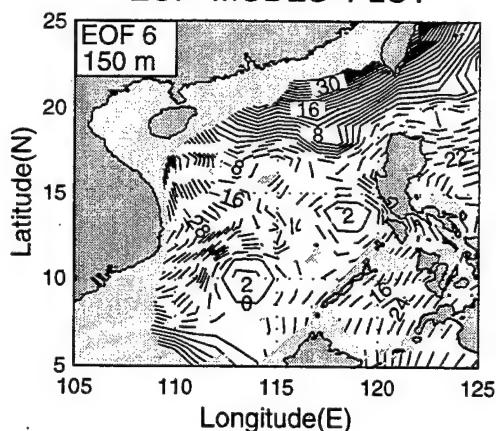
EOF MODES PLOT



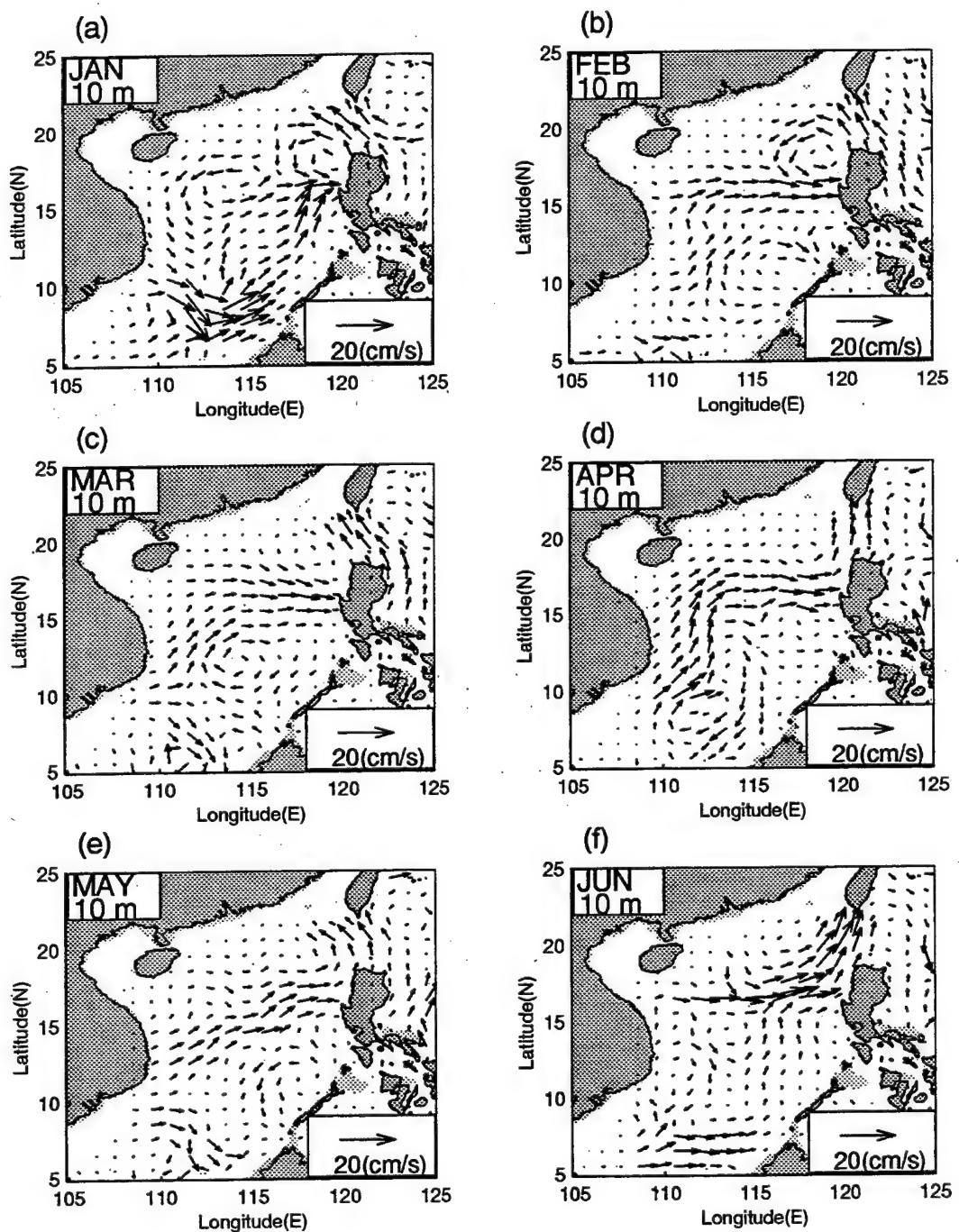
EOF MODES PLOT

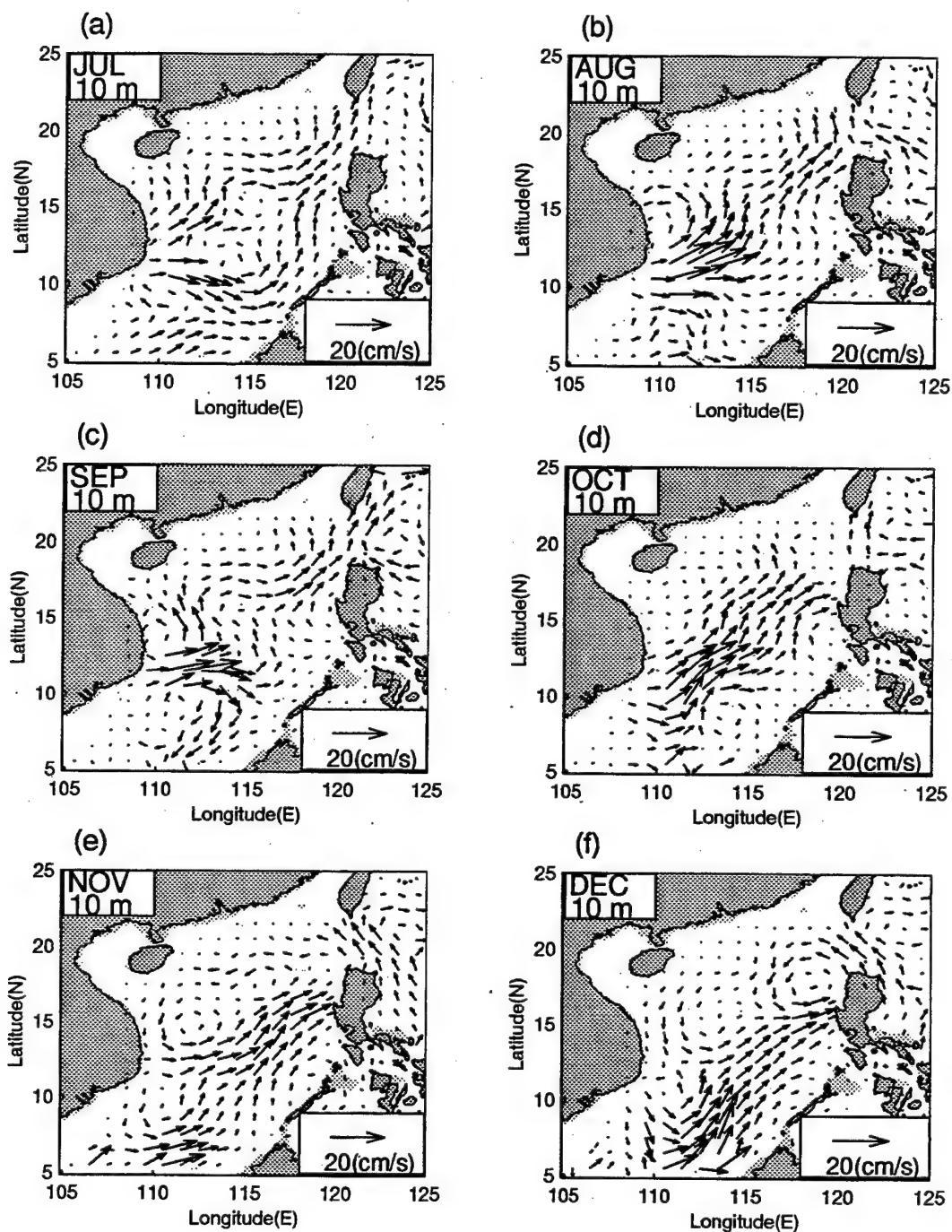


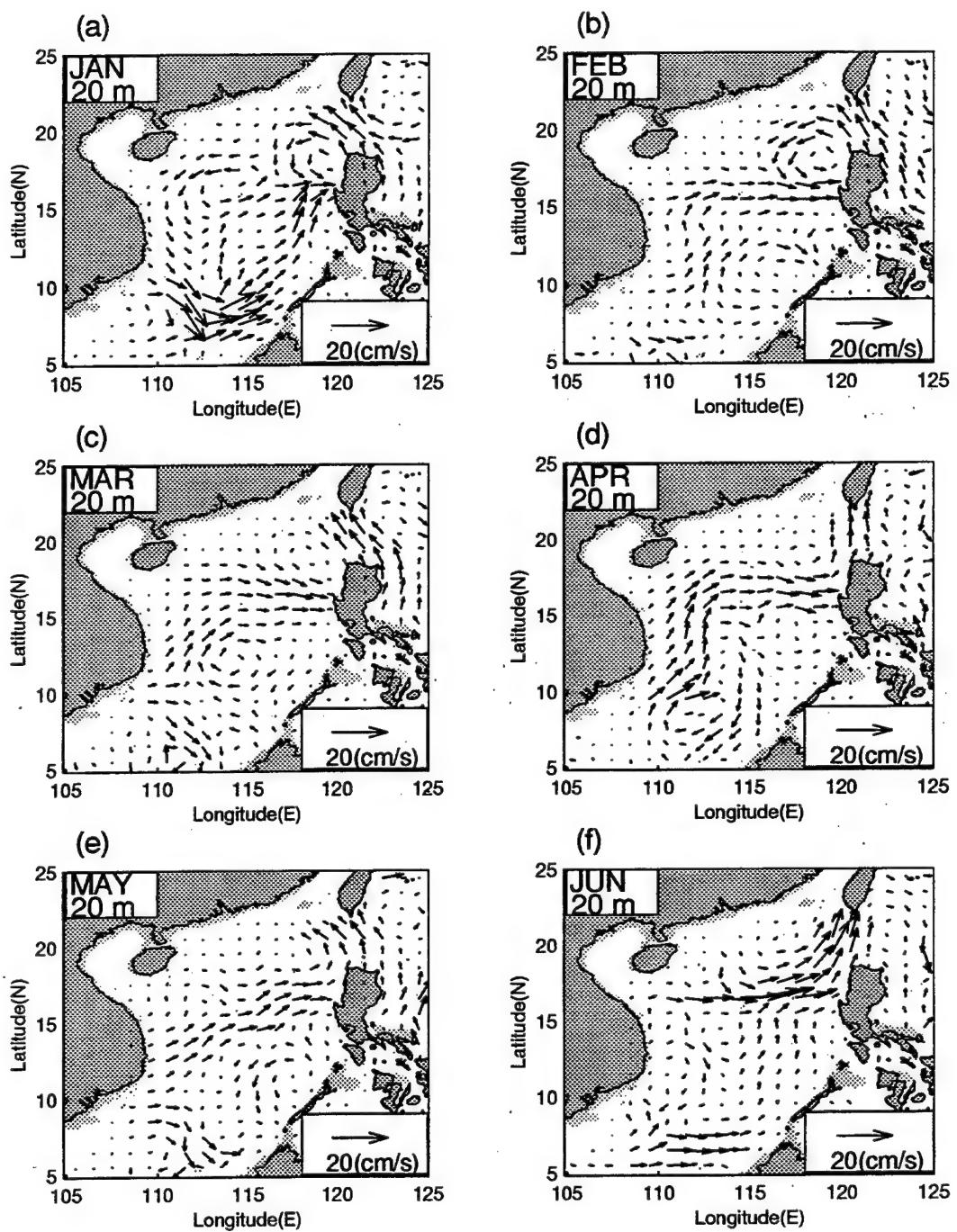
EOF MODES PLOT

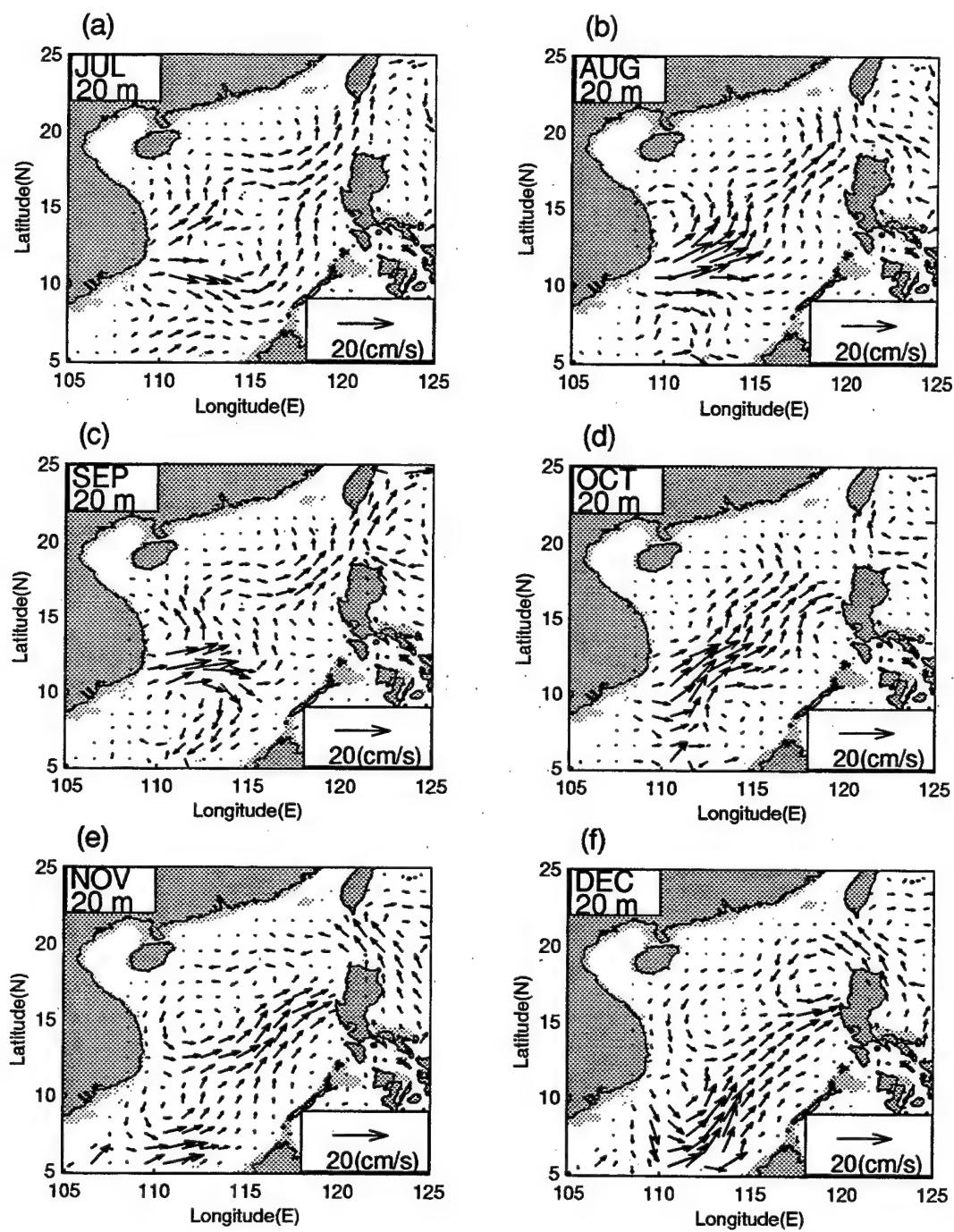


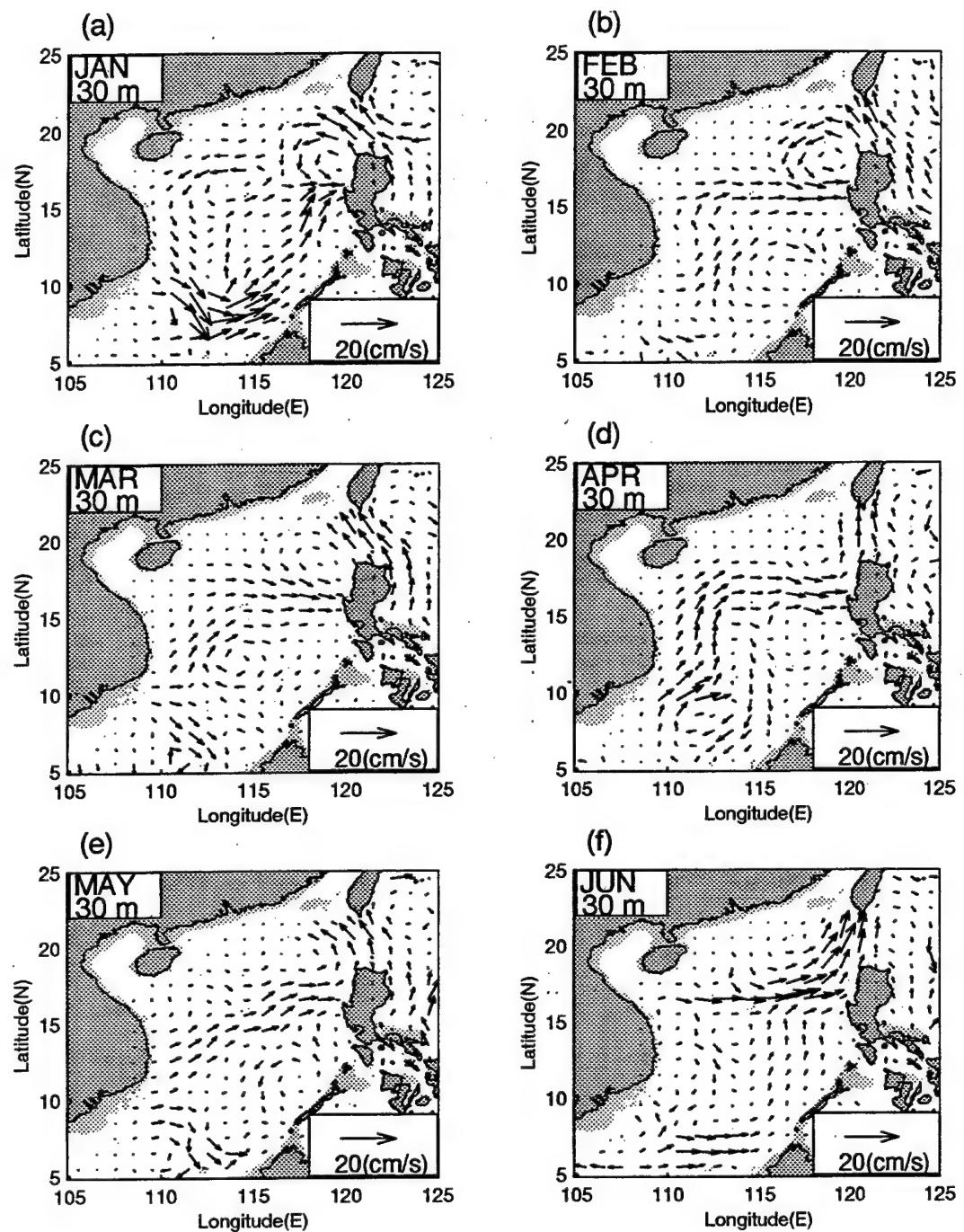
APPENDIX D. THE CIRCULATION PATTERNS

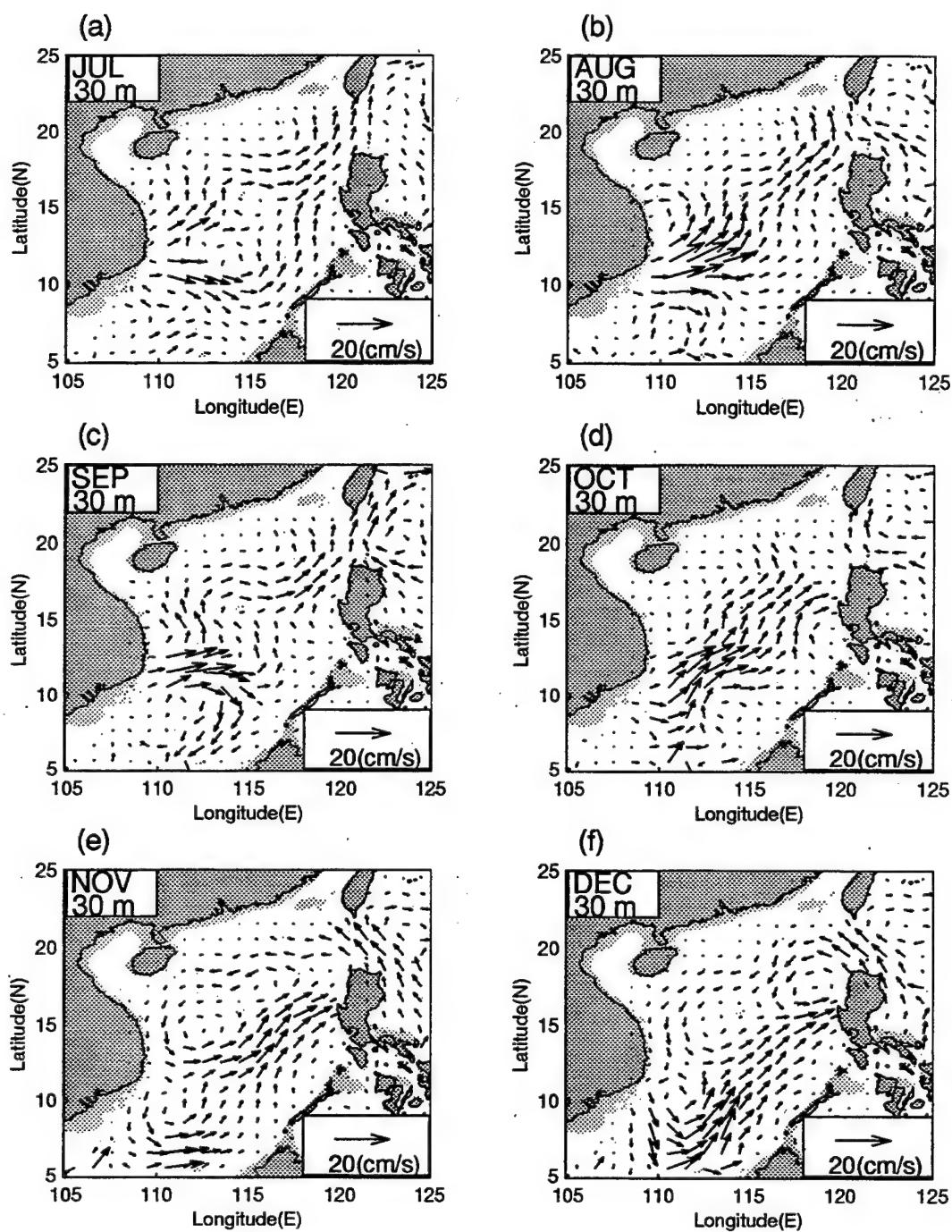


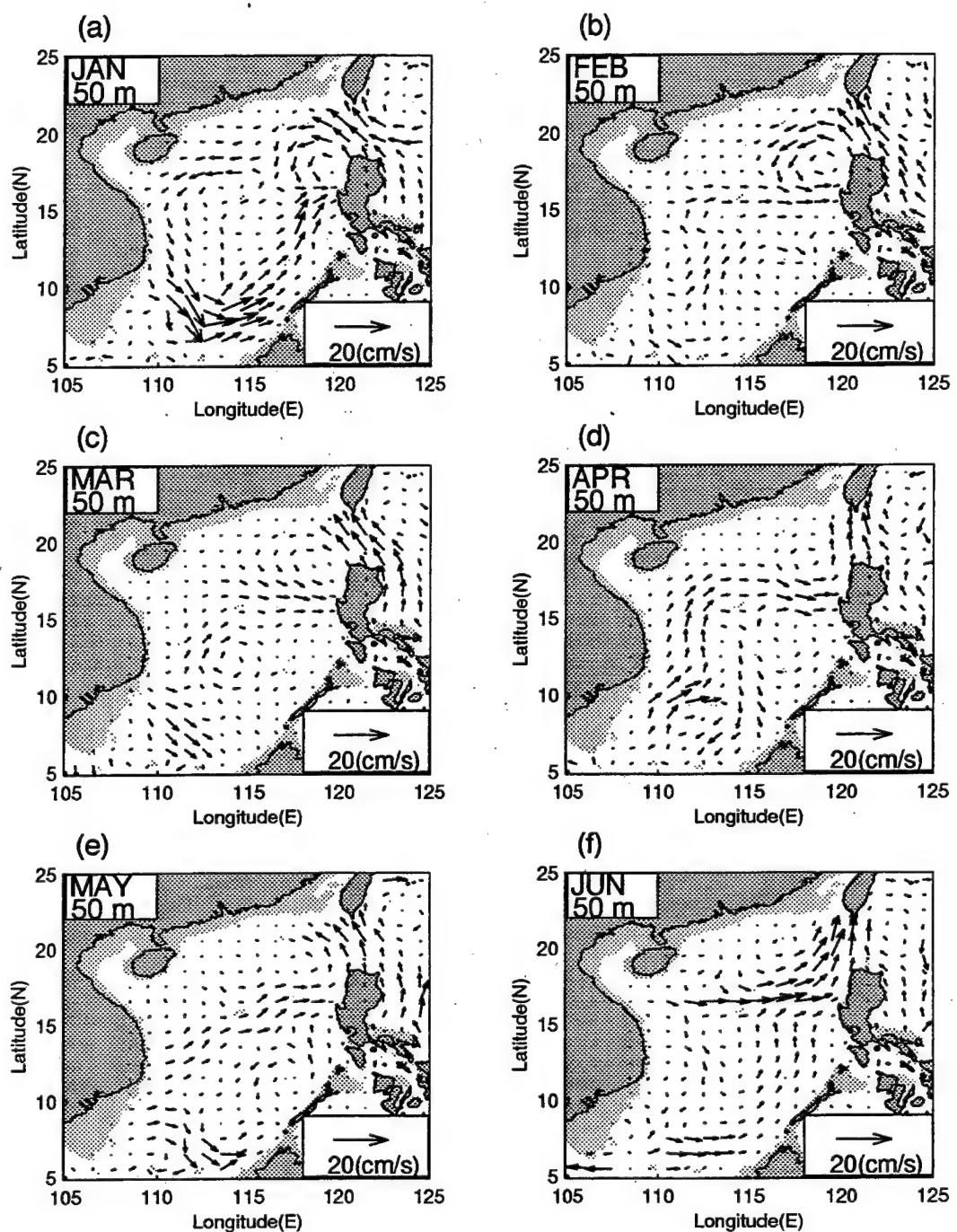


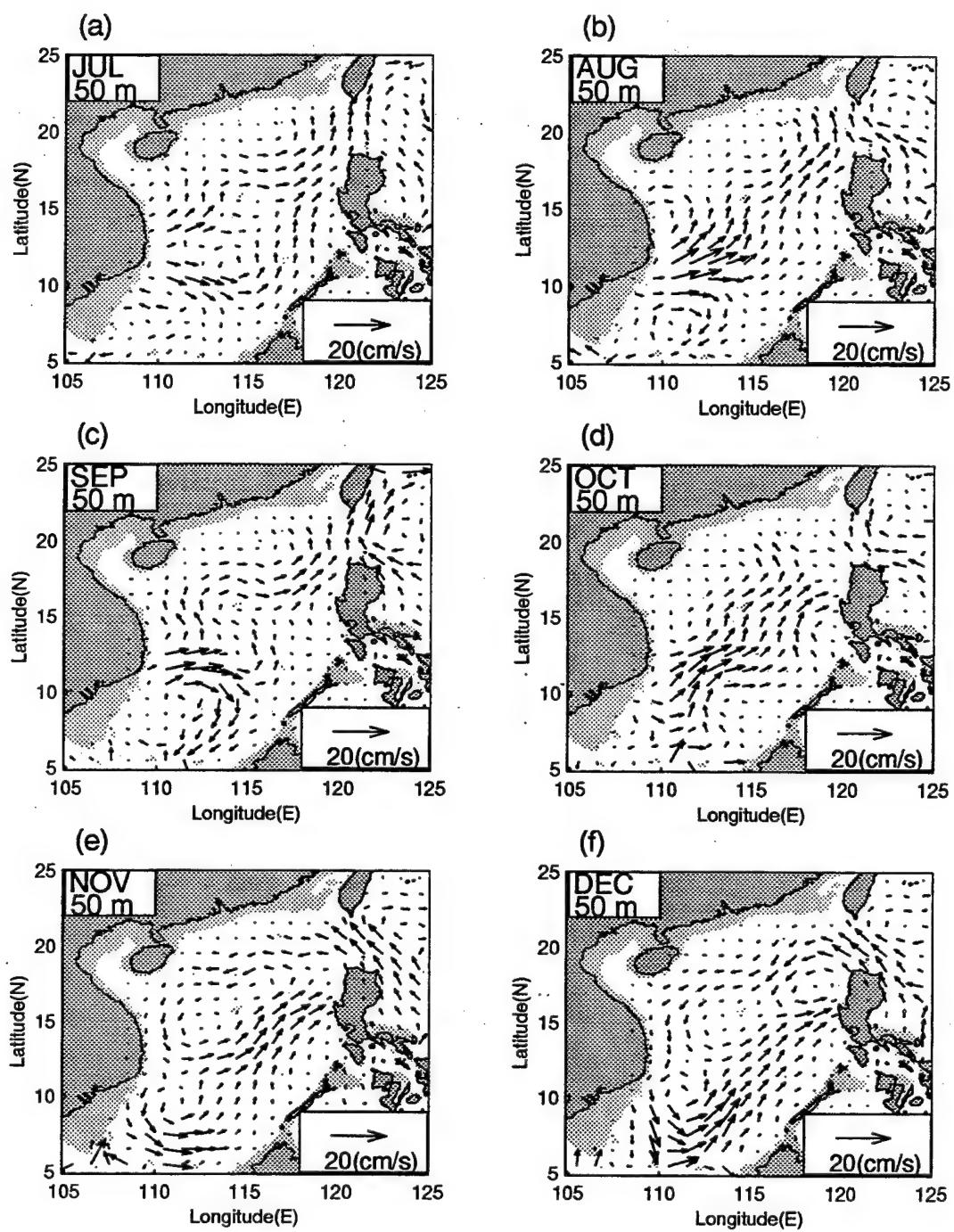


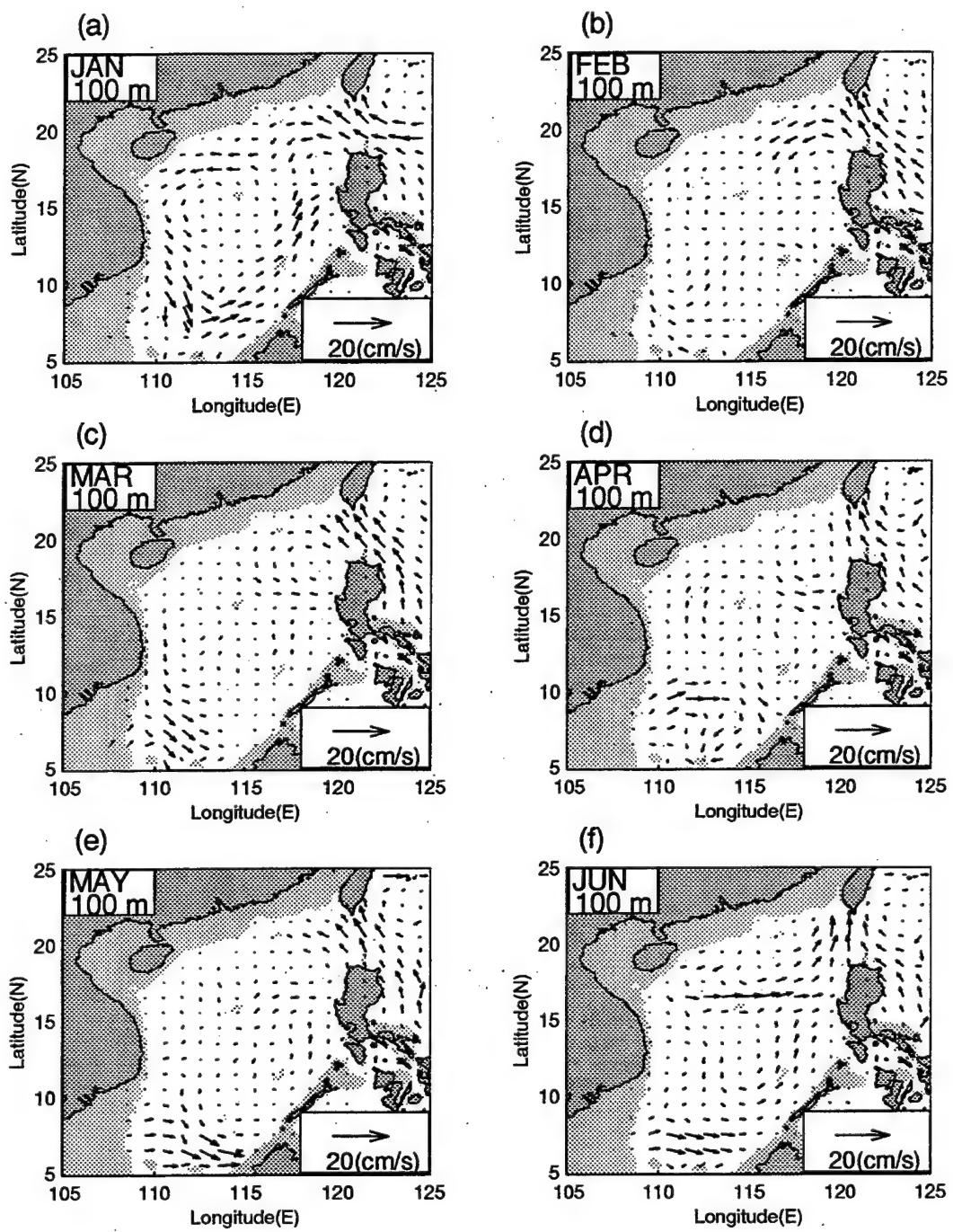


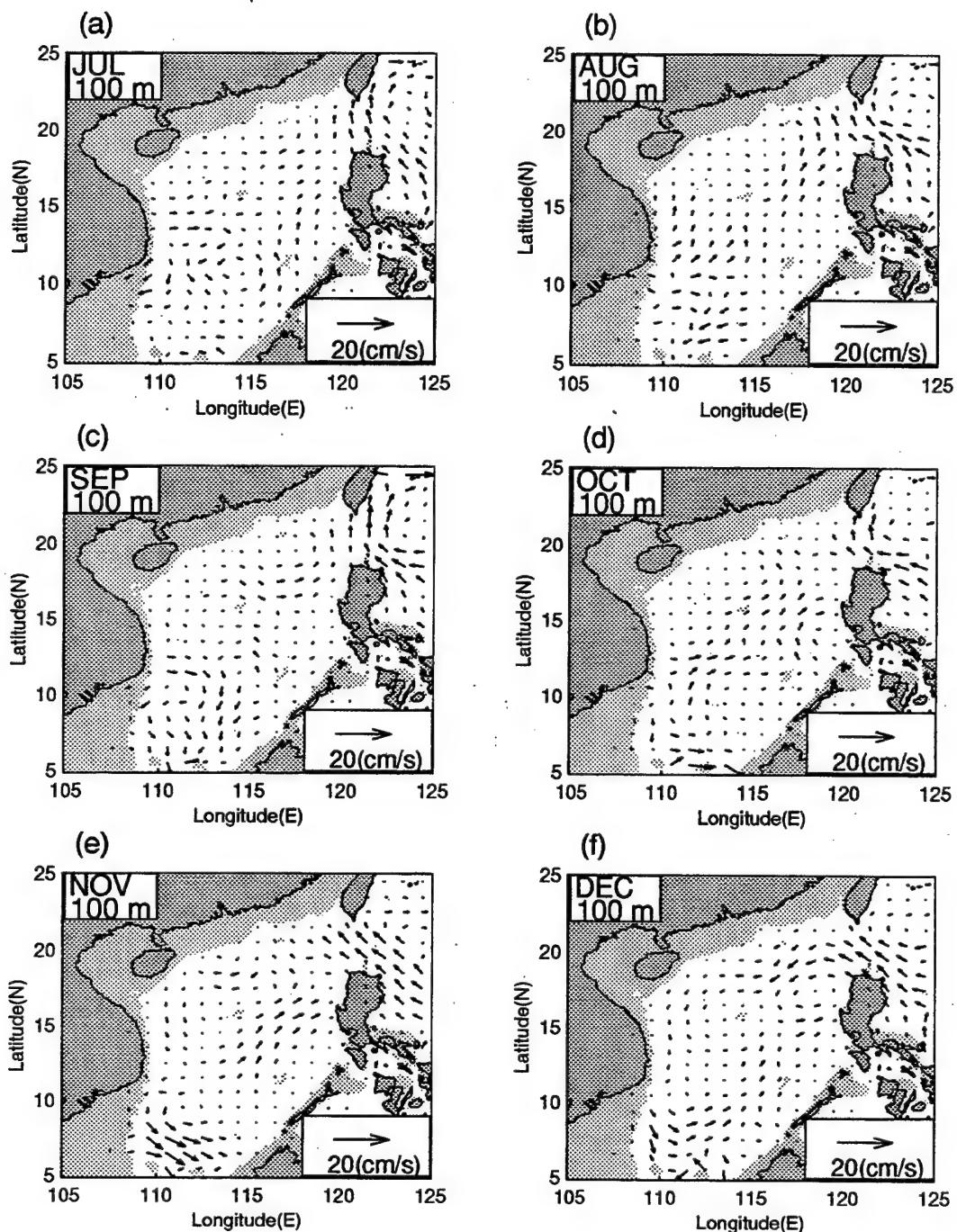


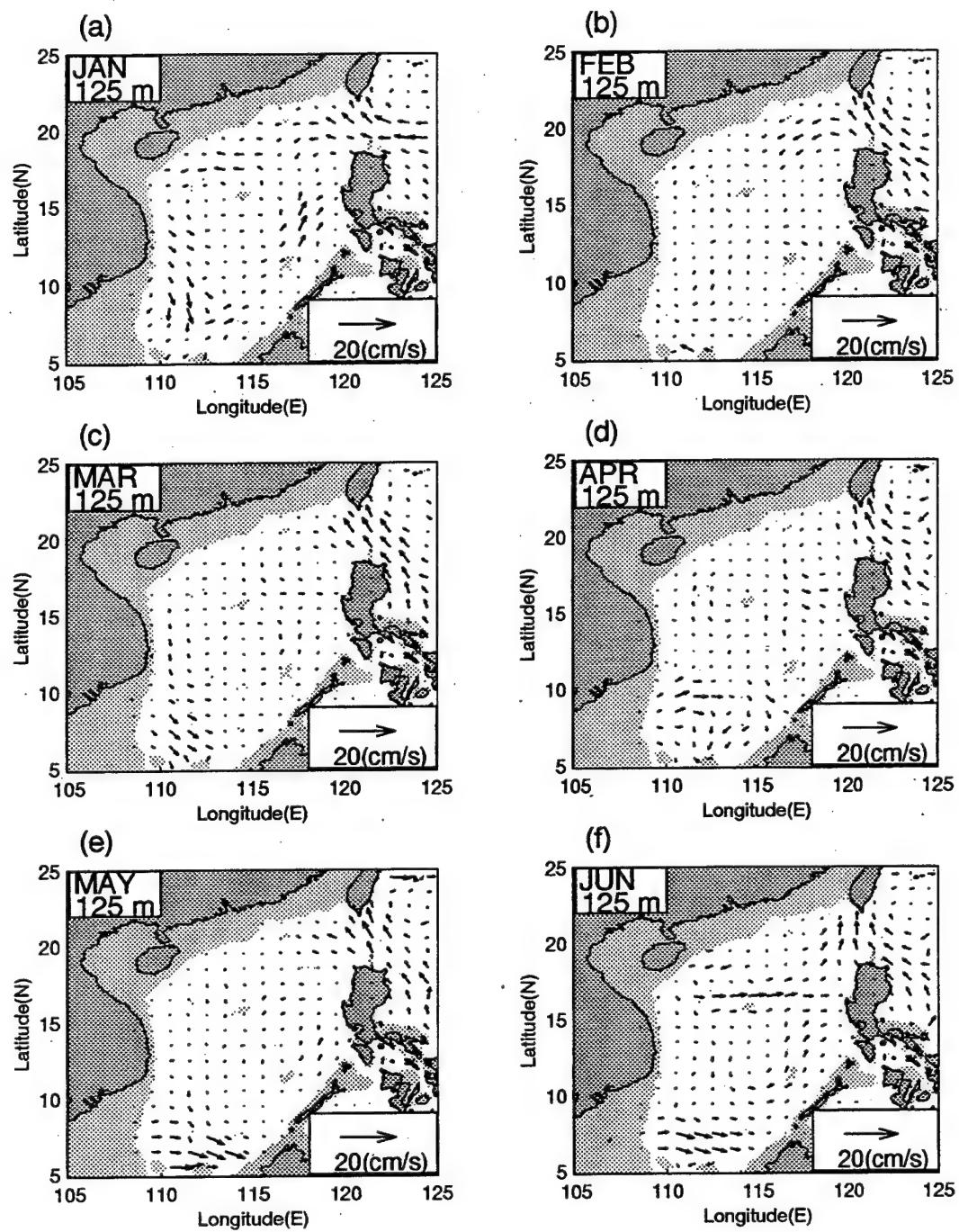


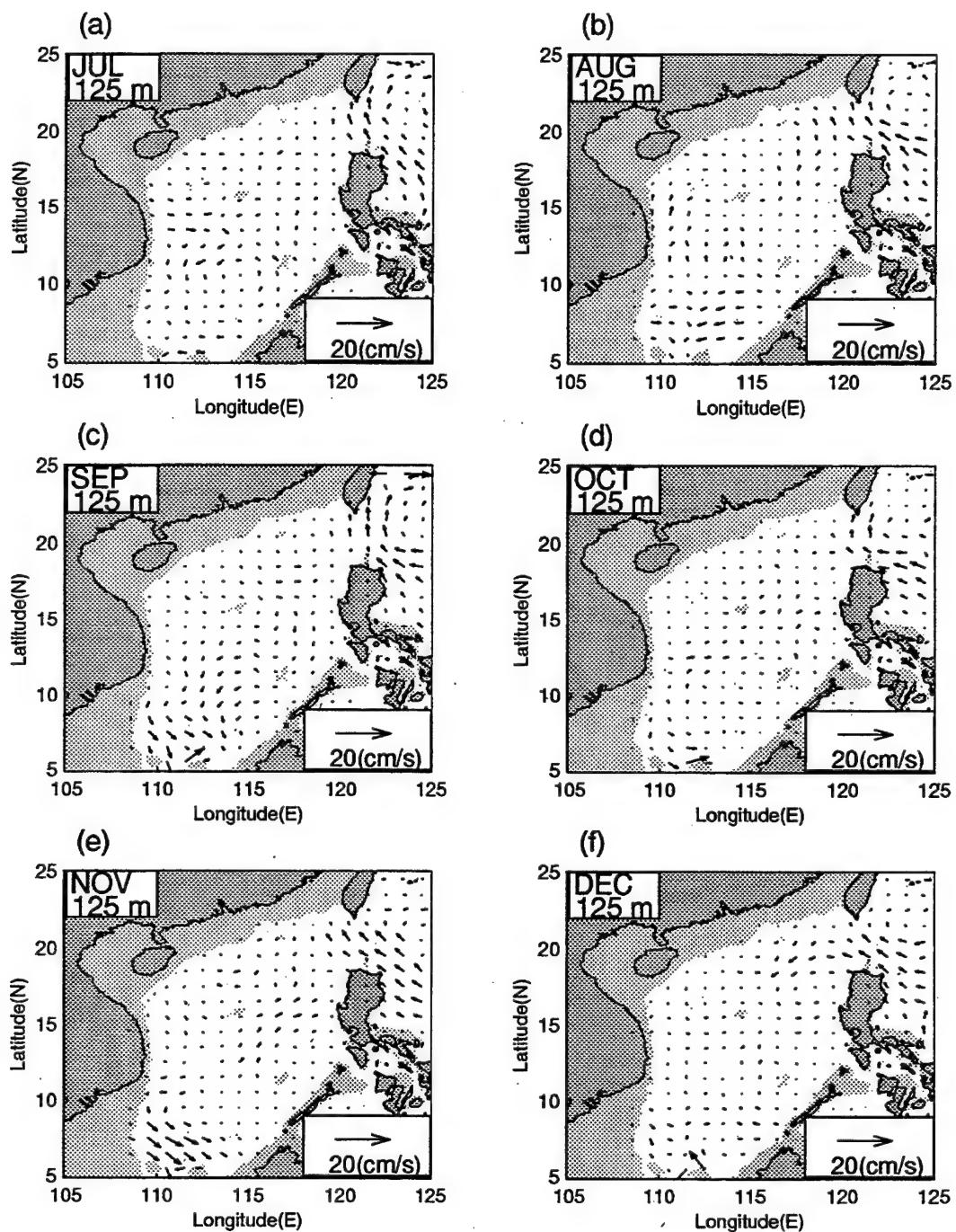


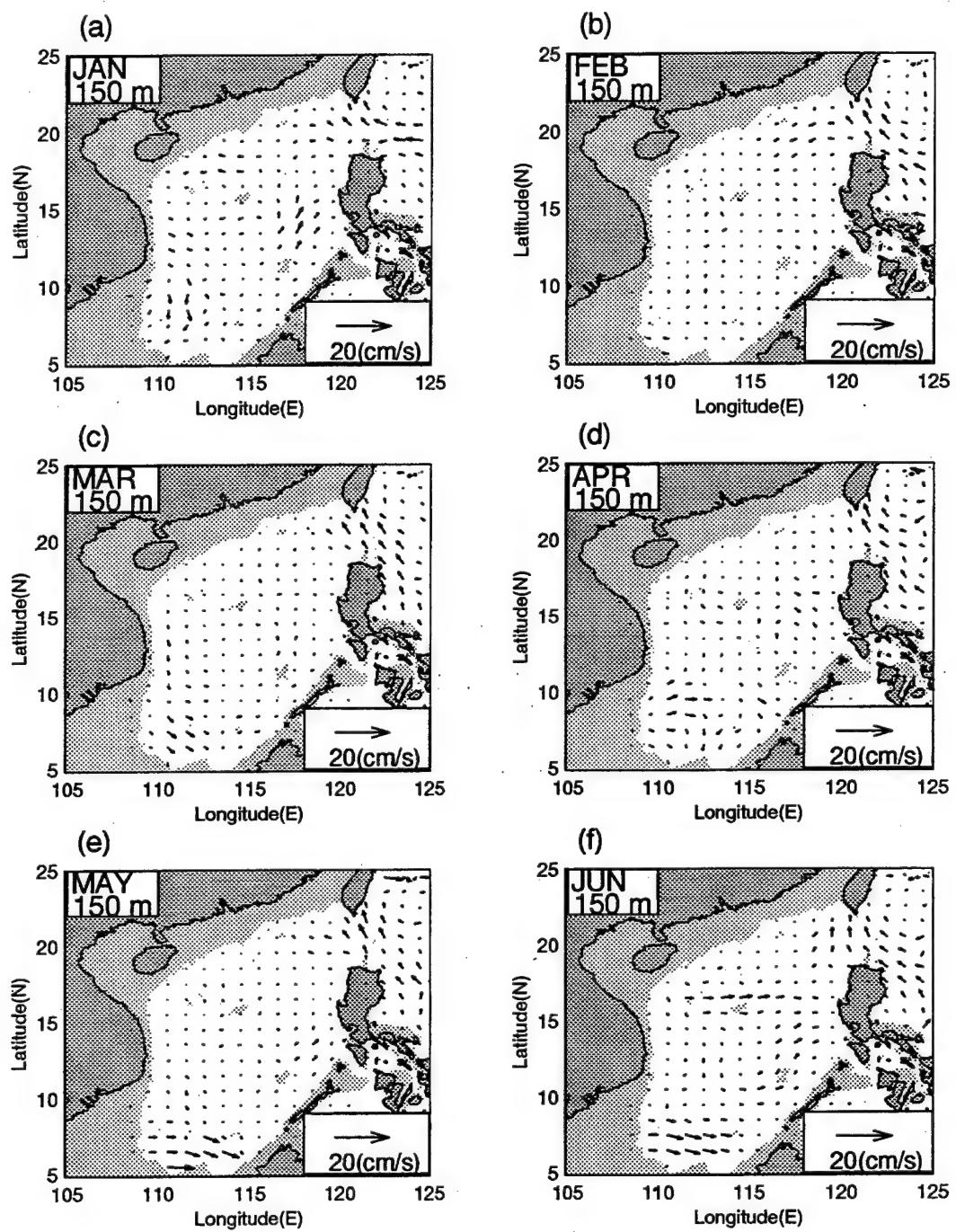


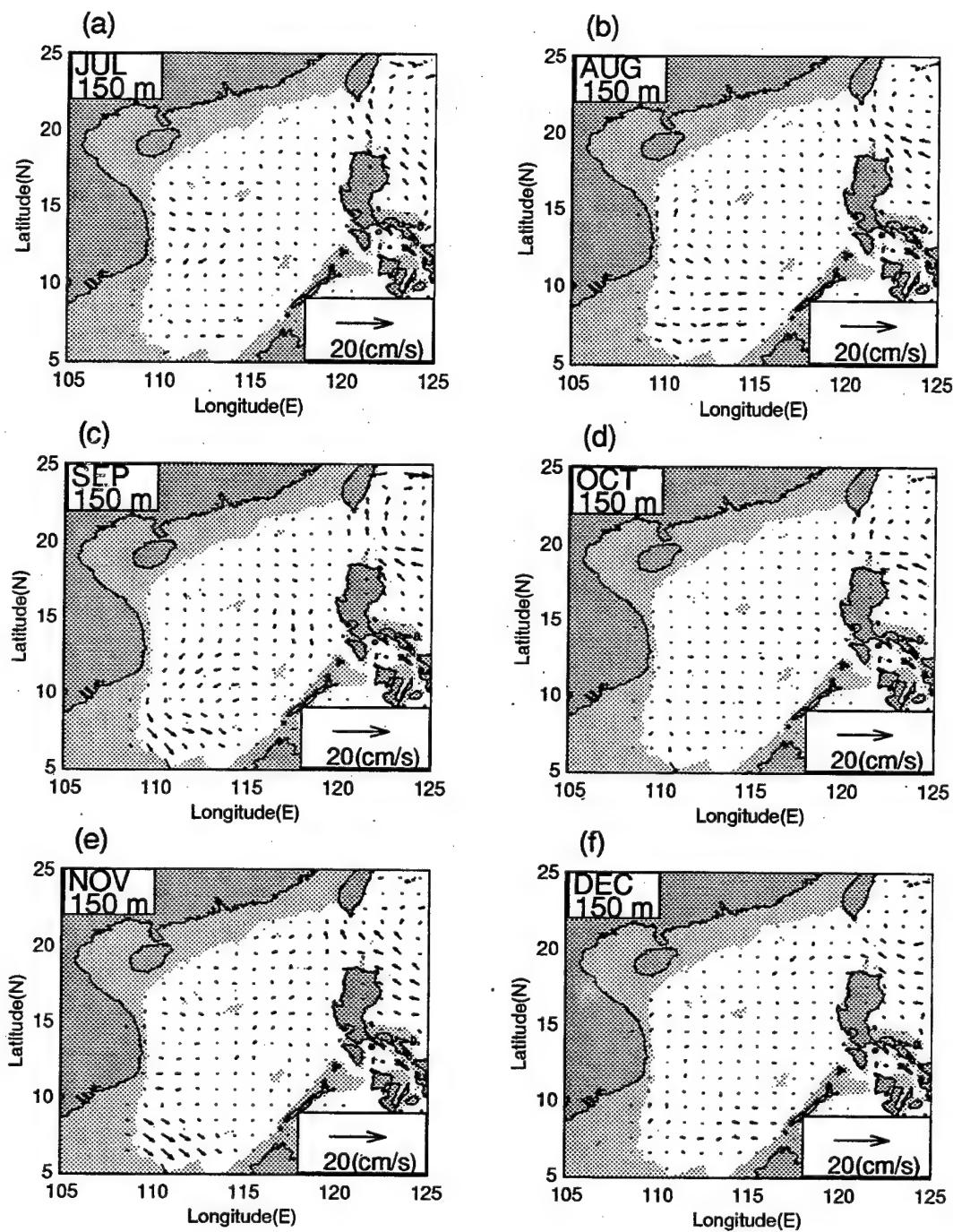


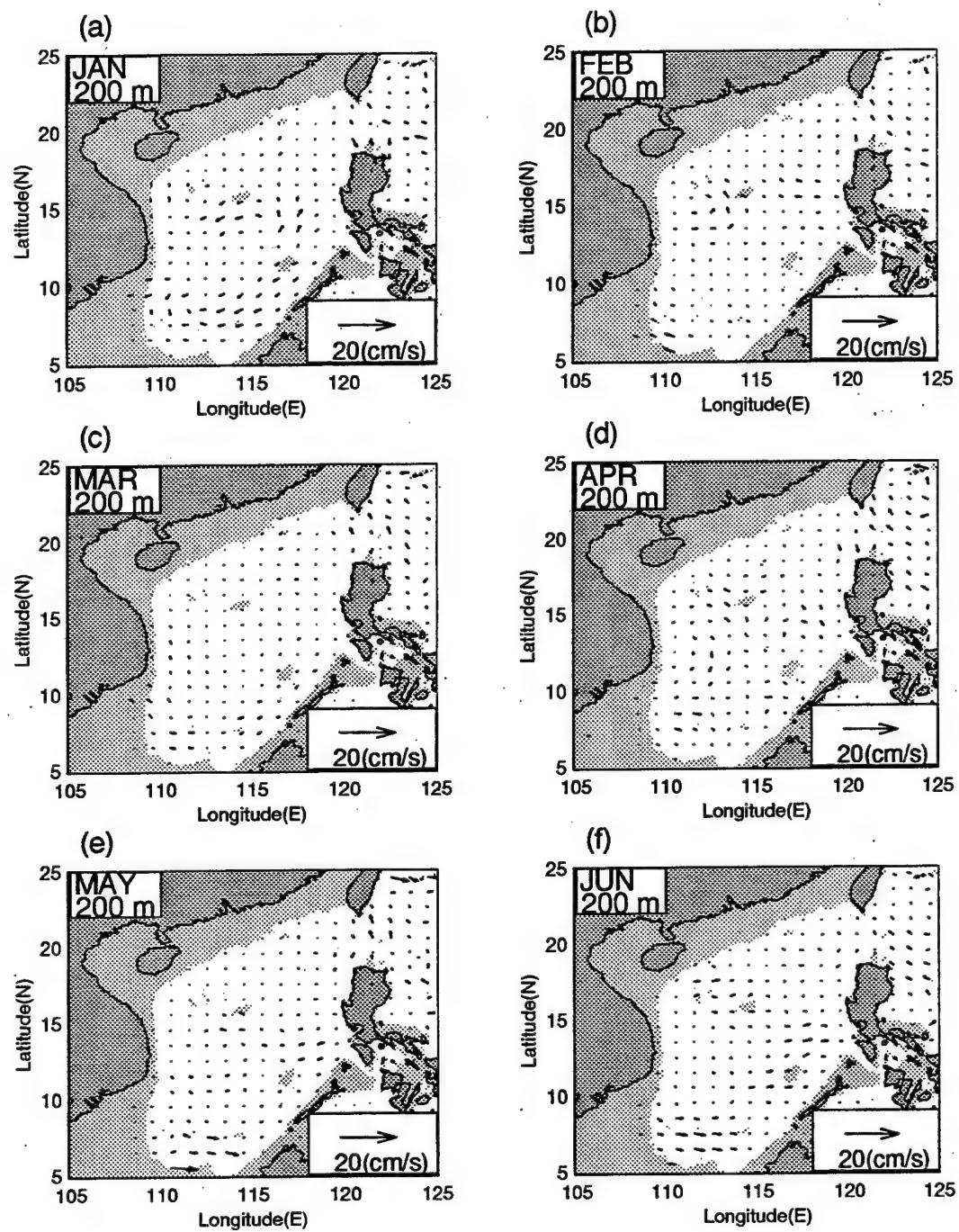


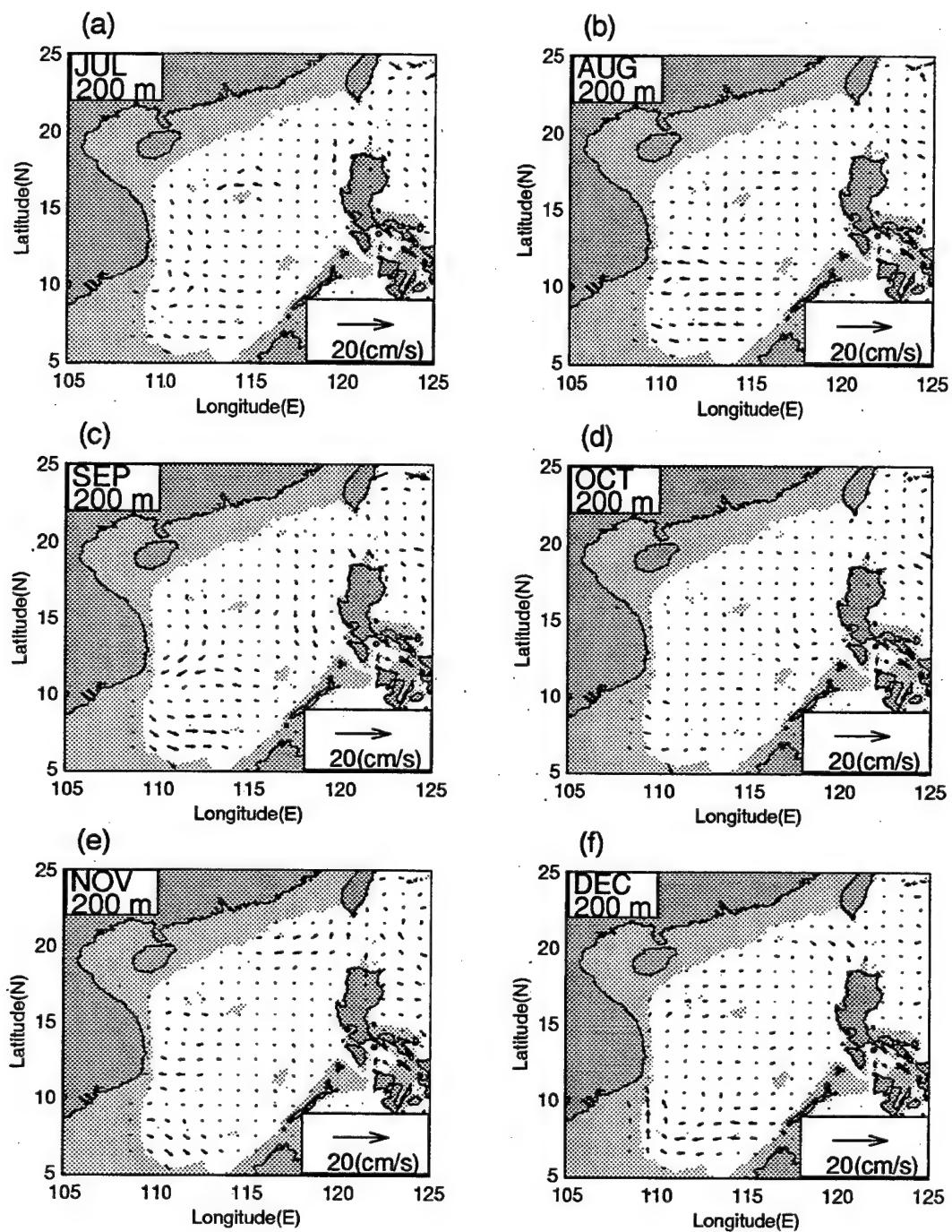


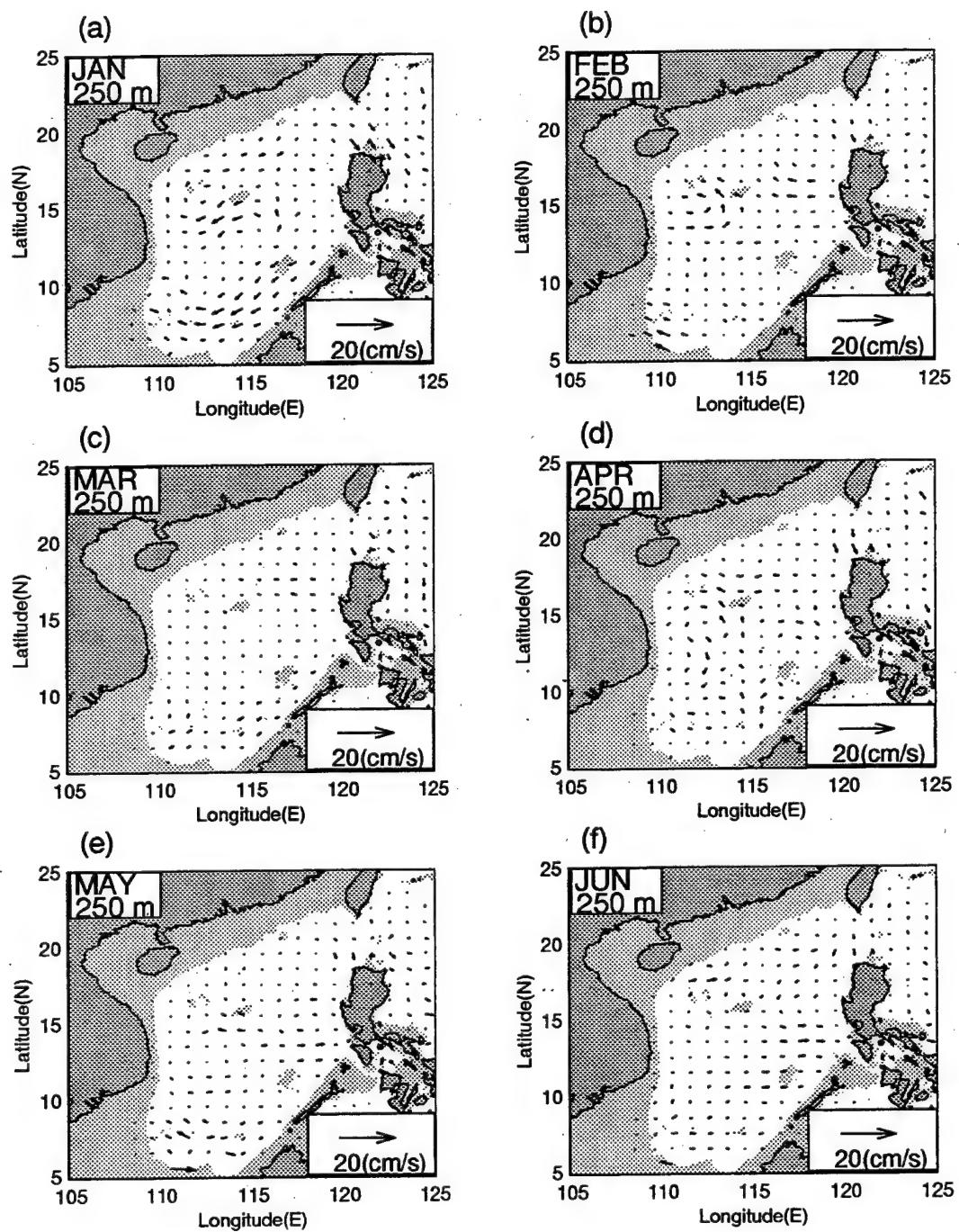


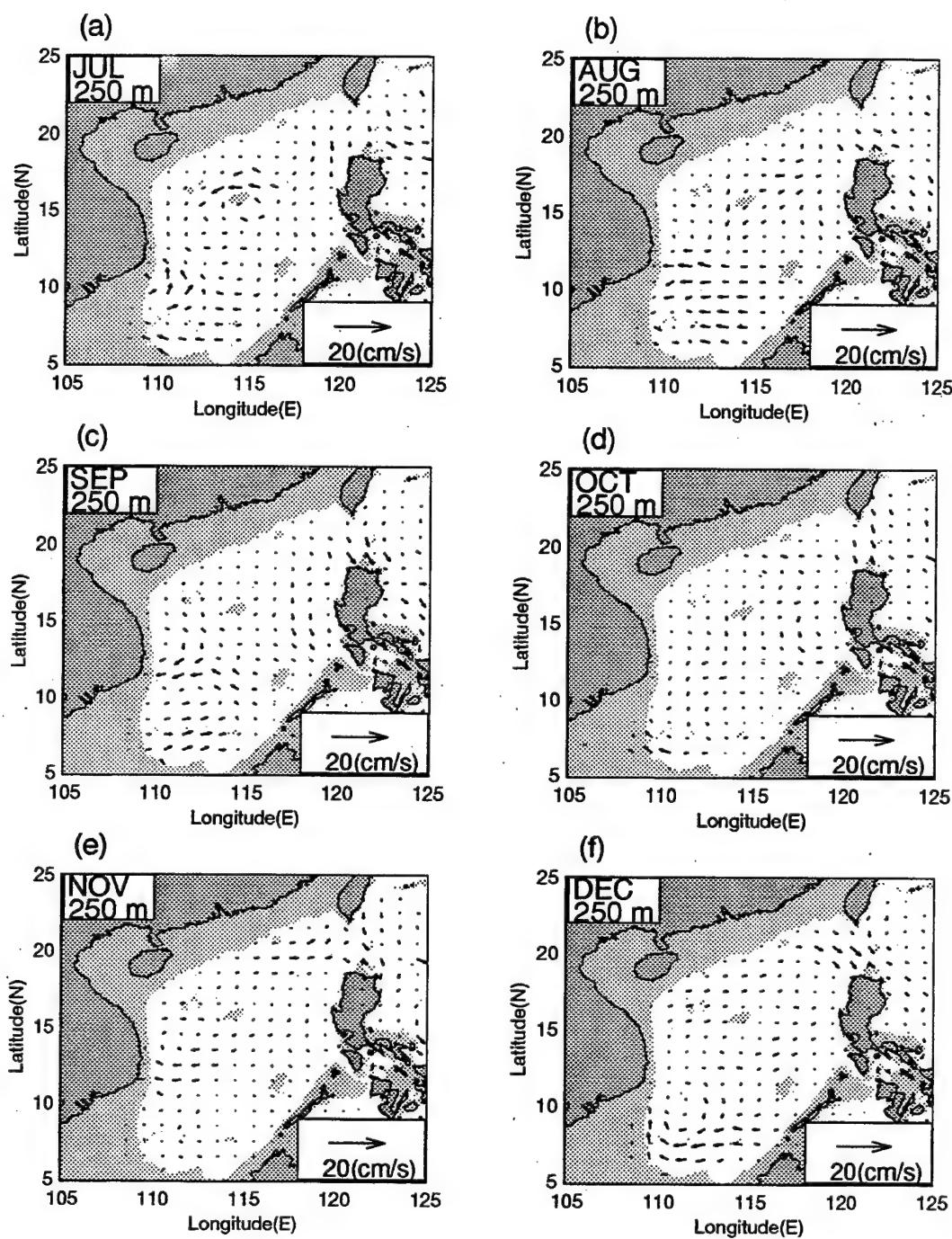


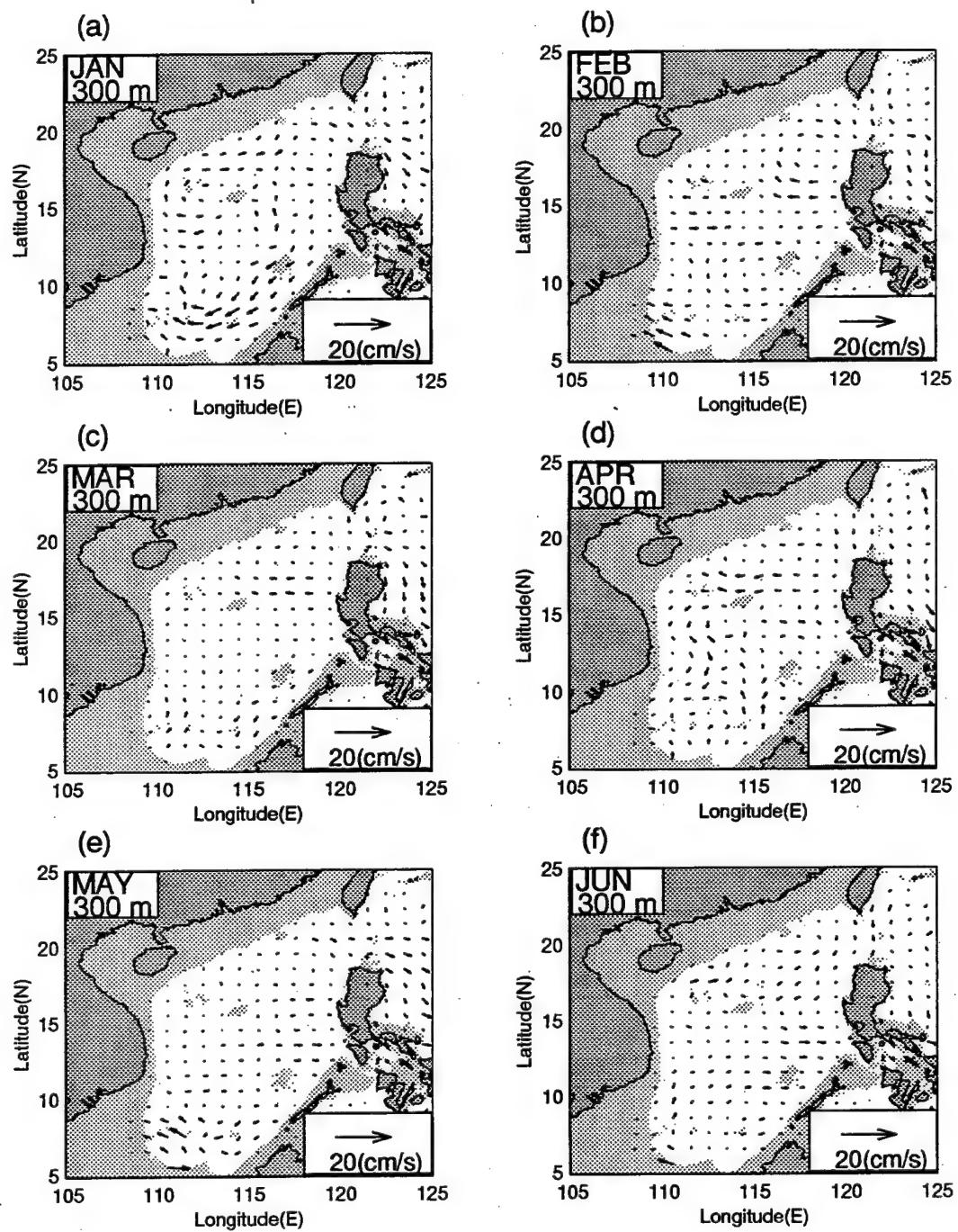


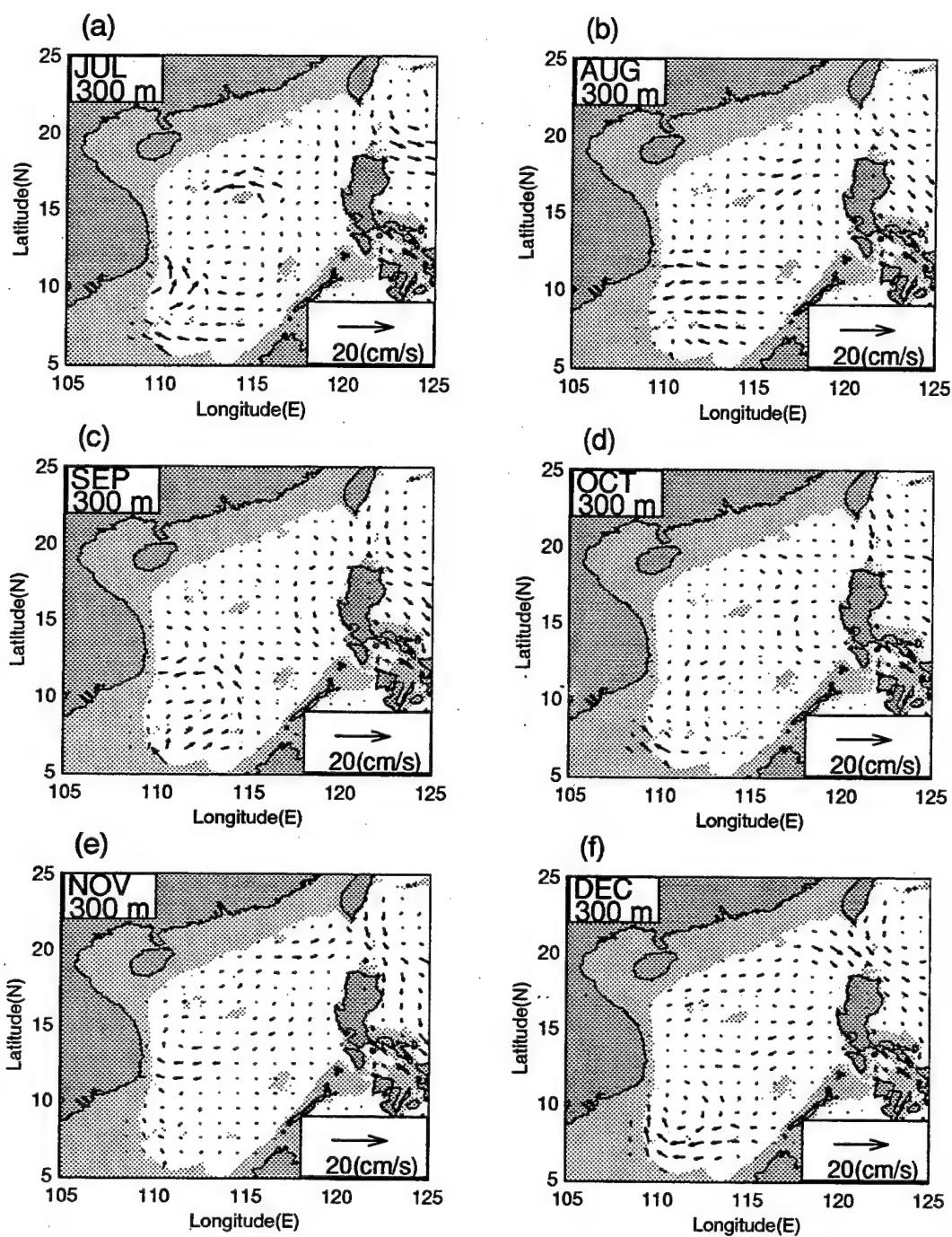












LIST OF REFERENCES

Bogden, P.S., R.E. Davis, and R. Salmon, 1993: "The North Atlantic circulation: combining simplified dynamics with hydrographic data", *J. Mar. Res.*, 51, 1-52.

Briggs, I. C., 1974: "Machine contouring using minimum curvature", *Geophysics*, 39, 39-48.

Cheang, B. K., 1980: "Some aspects of winter monsoon and its characteristics in Malaysia", *Res. Publ. No. 2*, Malaysian Meteorological Service, Kuala Lumpur.

Chu, P.C., Li, C.C., Ko, D.S. and Mooers, C.N.K., 1994: "Response of the South China Sea to seasonal monsoon forcing" Proceedings of the Second International Conference on Air-Sea Interaction and Meteorology and Oceanography of the Coastal Zone, American Meteorological Society, Boston, 214-215.

Chu, P.C. and Chang, C.P., 1995: "A case study of the South China Sea warm pool." paper presented at the *International CLIVAR-GOALS Workshop on Asian-Australian Monsoon Oceanography and Meteorology*, UCAR Joint International Climate Projects/Planning Office, Melbourne, Victoria, Australia, April 10-12.

Chu, P.C., 1995: "P vector method for determining absolute velocity from hydrographic data", *Mar. Technol. Soc. J.*, 29(3), 3-14.

Chu, P.C., Huang, M.J. and Fu, E.X., 1996: "Formation of the South China Sea warm core eddy in boreal spring", Proceedings of the Eighth Conference on Air-Sea Interaction, American Meteorological Society, Boston, 155-159.

Chu, P.C., Tseng, H.C., Chang, C.P. and Chen, J.M. 1997a: "South China Sea warm pool detected in spring from the Navy's Master Oceanographic Observational Data Set (MOODS)", *Journal of Geophysical Research*, 102, 15,761-15,771.

Chu, P.C., S.H. Lu, and Y.C. Chen, 1997b: "Temporal and spatial variabilities of the South China Sea surface temperature anomaly", *J. Geophys. Res.*, 102, 20,937-20,955.

Chu, P.C., S.K. Wells, S.D. Haeger, C. Szczechowski, and M. Carron, 1997c: "Temporal and spatial scales of the Yellow Sea thermal variability", *J. Geophys. Res.*, 102, 5,655-5,667.

Chu, P.C., C.W. Fan and W.J. Cai, 1998a: "Evaluation of P vector method using modular ocean model (MOM)", *J. Oceanogr.*, 54, 185-198.

Chu, P.C., C.W. Fan, C.J. Lozano, and J.L. Kerling, 1998b: "An airborne expendable bathythermograph survey of the South China Sea, May 1995", *J. Geophys. Res.*, in press.

Dale, W.L., 1959: "Winds and Drift Currents In The South China Sea.", *Malayan Journal of Tropical Geography*, 8, 1-31.

Davis, R., 1978: "On estimating velocity from hydrographic data", *J. Geophys. Res.*, 83, 5507-5509.

Edmons, N.L., 1996: "Studies of South China Sea circulation and thermal structure using a three dimensional numerical model", Master's Thesis, Naval Postgraduate School, Monterey.

Fan K.-L., and C.-Y. Yu, 1981: "A study of water masses in the seas of southernmost Taiwan", *Acta Oceanogr. Taiwan.*, 12, 94-111.

Huang, Qi-zhou and Wang, Wen-zhi, 1994: "Current characteristics of the South China Sea", in *Oceanology of China Seas*, edited by Z. Di, L. Yuan-Bo and Z. Cheng-Kui, 39-46, Kluwer, Boston.

Killworth, P., 1986: "A Bernoulli inverse method for determining the ocean circulation", *J. Phys. Oceanogr.*, 16, 2031-2051.

Levitus, S., 1984: "Climatological atlas of the world ocean", NOAA Professional Paper, 13, U.S. Government Printing Office, Washington D.C., 173 pp, 1984.

Li, C., 1994: "A numerical simulation of seasonal circulation in the South China Sea", Master's Thesis, Naval Postgraduate School, Monterey.

Love, A. E. H., 1927: "A treatise on the mathematical theory of elasticity", 4th ed. Dover Publ. Inc.

Needler, G.T., 1967: "A model for the thermohaline circulation in an ocean of finite depth", *J. Mar. Res.*, 25, 329-342.

SCSIO (South China Sea Institute of Oceanology, Academia Sinica), 1985: "Integrated Investigation Report on Sea Area of the South China Sea (II)", *Science Press, Bejing*, pp. 183-231 (in Chinese).

Schott, F., and H. Stommel, 1978: "Beta spirals and absolute velocities in different oceans", *Deep Sea Res.*, 25, 961-1010.

Shaw, P.-T. 1989: "The intrusion of water masses into the sea southwest of Taiwan", *J. Geophys. Res.* 94, C12, 18,213-18,226.

Shaw, P.-T. 1991: "The seasonal variation of the intrusion of the Philippine Sea water into the South China Sea", 96, C1, 821-827.

Smith, and Wessel, 1990: "Gridding with continuous curvatures splines in tension." *Geophysics*, 55, 293-305.

Soong, Y.S., Hu, J.H., Ho, C.R. and Niiler, P.P., 1995: "Cold-core eddy detected in South China Sea", *EOS Trans. AGU*, 345-347, 1995.

Stommel, H., and F. Schott, 1977: "The beta spiral and the determination of the absolute velocity field from hydrographic station data", *Deep sea Res.*, 24, 325-329.

Su, Y.S. and Weng, X.C., 1994: "Water masses in China Seas", in *Oceanology of China Seas*, edited by Z. Di, L. Yuan-Bo and Z. Cheng-Kui, 3-25, Kluwer, Boston, 1994.

Tseng, H.C., 1995: "South China Sea warm-core and cool-core eddies detected from the Navy's Oceanographic Observation Data Set (MOODS)", Masters thesis, Naval Postgraduate School, Monterey.

Timoshenko, S., and Woiniawsky-Krieger, S., 1968: "Theory of plates and shells: 2nd ed.", McGraw-Hill Book Co.

Tziperman, E., W.C. Thacker, R.B. Long, and S.-H. Hwang, 1992: "Oceanic data analysis using a general circulation model, 1, Simulations", *J. Phys. Oceanogr.*, 22, 1434-1457.

Uda, M., and T. Nakao, 1972: "Water Masses And Currents In The South China Sea And Their Seasonal Changes." In: *The Kuroshio-Proceedings of the 3rd CSK Symposium*, Bangkok, Thailand, 161-188.

Wessel, and Smith, 1992 "The GMT-SYSTEM Technical Reference and Cookbook."

Wunsch, C., 1978: "Dynamically consistent hydrography and absolute velocity in the eastern North Atlantic west of 50 °W determined from inverse method", *Rev. Geophys. Res.*, 16, 583-620.

Wunsch, C., 1994: "Dynamically consistent hydrography and absolute velocity in the eastern North Atlantic Ocean", *J. Geophys. Res.*, 99, 14,071-14,090.

Wyrki, K., Scientific results of marine investigations of the South China Sea and the Gulf of Thailand 1959-1961, *Naga Report*, Vol 2&3, the University of California Scripps Institution of Oceanography, 1961.

INITIAL DISTRIBUTION LIST

	No. Copies
1. Defense Technical Information Center 8725 John J. Kingman Rd., Ste 0944 Ft. Belvoir, VA 22060-6218	2
2. Dudley Knox Library Naval Postgraduate School 411 Dyer Rd. Monterey, CA 93943-5101	2
3. Chairman (Code OC/GD) Department of Oceanography Naval Postgraduate School Monterey, CA 93943-5002	1
4. Chairman (Code MR/WX) Department of Meteorology Naval Postgraduate School Monterey, CA 93943-5002	1
5. Professor Peter C. Chu (Code OC/CU) Department of Oceanography Naval Postgraduate School Monterey, CA 93943-5002	3
6. Professor Pierre-Marie Poulain (Code OC/PN) Department of Oceanography Naval Postgraduate School Monterey, CA 93943-5002	1
7. Chinese Naval Academy Library P.O. Box 90175 Tsoying, Kaohsiung Taiwan, R.O.C.	1
8. Department of Oceanography National Taiwan University 1 Roosevelt Road, Sec. 4 Taipei, Taiwan, R.O.C.	1

9. Department of Oceanography 1
National Chung Shan University
Ku Shan District,
Kaohsiung, Taiwan, R.O.C.

10. Commander Yu-Ming Li 1
4201 Wisconsin Ave, N.W.,
Washington D.C. 20016

11. Mr. Ping-Hong Chen 1
6th Floor, No. 1, Aly 55, Ln. 134,
Hsin-Yi Rd., Sec 3,
Taipei, Taiwan 106, R.O.C.

12. Lieutenant Commander Binbing Ma 3
14F 29 Der-Hsiang Road
Nan-Tzu District,
Kaohsiung, Taiwan, R.O.C.